1-1-1970

Studies on rheo-optical properties of low density polyethylene.

Akira Tanaka
University of Massachusetts Amherst

Recommended Citation

Tanaka, Akira, "Studies on rheo-optical properties of low density polyethylene." (1970). *Doctoral Dissertations 1896 - February 2014*. 938.
https://doi.org/10.7275/k48y-3e38 https://scholarworks.umass.edu/dissertations_1/938

STUDIES ON RHEO-OPTICAL PROPERTIES
OF
LOW DENSITY POLYETHYLENE

A Dissertation Presented
by
Akira Tanaka
//

Submitted to the Graduate School of the
University of Massachusetts in
partial fulfillment of the requirements for the degree of

DOCTOR OF PHILOSOPHY

October 1970

Major Subject: Polymer Science and Engineering

STUDIES ON RHEO-OPTICAL PROPERTIES
OF
LOW DENSITY POLYETHYLENE

A Dissertation Presented
by
Akira Tanaka

Approved as to style and content by:

Richard S. Stein
(Chairman of Committee)

Roger S Porter 10/20/70
(Head of Department)

(Member)

(Member)

October 1970

ACKNOWLEDGEMENT

The author wishes to express his sincere appreciation to Professor Richard S. Stein, thesis director, for guidance, patience and thoughtfulness throughout the course of this work.

Acknowledgement and thanks go to the Thesis Committee consisting of Dr. Richard S. Stein, Dr. Frank E. Karasz, Dr. William J. MacKnight and Dr. Seymour Newman. Their constructive comments in reviewing the thesis are appreciated.

Sincere thanks are due to a number of coworkers, particularly to Mr. D. A. Keedy, Mr. I. Kimura and Dr. B. W. Delf for the improvement of the dynamic x-ray apparatus and their discussions.

The author thanks Mrs. Sophia Kinney and Mrs. S. Hashimoto for typing the thesis and to Miss Helen Piekarski, Mrs. Candace Moule and Mrs. Sophia Kinney for providing secretarial work during the course of the work.

Thanks are extended to Professor S. Onogi, Professor R. S. Porter, Professor R. Lenz, Professor J. Ragle and Professor H. Stidham for their guidance and encouragement.

Computer calculations were carried out at the University of Massachusetts Research Computing Center.

Acknowledgement for financial assistance is made to the National Science Foundation and the Petroleum Research Fund of the American Chemical Society.

TABLE OF CONTENTS

CHAPTER I

CHAPTER II

CHAPTER III

Appendix A

CHAPTER IV

Appendix B

CHAPTER V

CHAPTER I

ABSTRACT

The orientational compliances of particular crystal axes by the dynamic x-ray diffraction, the dynamic strain-optical coefficient, by the dynamic birefringence and the dynamic mechanical properties were measured at several frequencies in the temperature region between 30° and 90°C for low density polyethylene with two different thermal histories, Q- (quenched) and H- (heat-treated) samples.

By combining the dynamic x-ray technique with the dynamic birefringence technique, one can estimate the amorphous and crystalline contributions to the strain-optical coefficient.

For both Q- and H-samples, the master curves for the mechanical loss tangent tanδ, the in-phase orientational compliances of the 110 and 200 crystal planes, C'_{110} and C'_{200}, and the in-phase strain-optical coefficient K' were obtained by applying the time-temperature superposition principle using only the horizontal shift. However, for K', both horizontal and vertical shifts were necessary. The master curve of tanδ and C'_a, C'_b and C'_c for Q-samples was quite different from that for H-samples, indicating that the deformation mechanisms related to these quantities might be quite different for the two samples.

The deformation mechanism for Q-samples might be mainly associated with the α_2 loss mechanism and that for H-samples might be mainly associated with the α_1 loss mechanism in the measured temperature region. The former may be interpreted by the floating rod-like model

of crystallites by Kratky (52), where activation energy was observed to be about 50 kcal/mole, and the latter may be related to the nature of the superstructure such as spherulites and therefore may be interpreted in terms of interlamella and intralamella contributions which include the tilting and twisting of lamella and also by the deformation of the spherulite from a sphere to an ellipsoid, for which the activation energy was observed to be about 25 kcal/mole.

The contribution of the crystalline part to the total in-phase strain optical coefficient K' was comparable with that of the amorphous part for Q-samples, but it was quite small for H-samples.

These measurements were also carried out for irradiated samples, which proved to be a rather complicated system. It can be only concluded that the irradiation might be more effective in affecting the intercrystalline contributions than the intracrystalline contributions.

CHAPTER II

INTRODUCTION

The mechanical properties of crystalline polymers are more complicated than those of amorphous polymers. This may depend upon the fact that crystalline polymers might involve many more different kinds of deformation mechanisms which are dependent upon morphological features such as degree of crystallinity, the size and shape of the spherulites and the mobility of amorphous chains connecting the crystallites.

Those relatively complicated deformation mechanisms may be resolved by the simultaneous observation of several kinds of optical quantities such as x-ray diffraction, birefringence, fluorescence, infrared, visible and ultraviolet dichroism and light scattering with mechanical properties. Each optical quantity is primarily sensitive to a particular aspect of the morphology. Therefore, combined use of two or more methods might be helpful to get information about the deformation mechanisms of crystalline polymers.

Many rheo-optical studies, where optical quantities are simultaneously observed with rheological quantities, have been carried out for several years (1-10).

In this thesis, dynamic x-ray diffraction and dynamic birefringence measurements on low density polyethylene were carried out for the purpose of the clarification of the so-called alpha loss mechanisms of polyethylene. There has been much recent speculation about the nature of the alpha mechanical loss mechanism of

polyethylene (11-25). The prevalent opinion appears to be that the reversible part of this loss peak consists of two components. One is a low temperature part, designated α_1, which is found to have an activation energy of the order of 25 kcal/mole on the basis of time-temperature superposition of dynamic mechanical spectra and of stress relaxation data. Another is a higher temperature part, designated α_2, which has a higher activation energy of the order of 45 kcal/mole.

For single crystals of polyethylene which are not annealed, only the α_2 mechanism is found and is dependent upon the thickness and thermal history of the crystal but independent of the state of compaction of the crystal mats (23,24) indicating its intracrystalline nature. Studies by Sinnott (19), Hoffman, et al. (20), and by Takayanagi (23) indicate that this α_2 peak may have more than one component and may partly result from internal motion within the crystal and partly from motion of the chain folds on the surface. Recent studies by Hideshima showing the effect of solvent on this peak indicate the probability of a surface contribution. The recent studies of Takayanagi, et al. (25), showing that the variation of the temperature of this peak with crystal thickness parallels the variation of the temperature at which the a-axis expansion coefficient of the crystal changes slope, demonstrates the connection between at least a part of the α_2 loss upon the internal motion within the crystal.

Upon annealing single crystals, Takayanagi and Matsuo (23) demonstrate that the α_1 loss peak is seen to appear. It has an activation energy of 25 kcal/mole similar to that found for this peak for

bulk crystallized samples in contrast to the value of 42 kcal/mole for the single crystal α_2 peak. Takayanagi indicates that this absorption may be associated with the mosaic structure which manifests itself after annealing the isothermally crystallized single crystals. The absorption may be interpreted in terms of internal friction between mosaic blocks although at present there is no direct evidence.

Although some theories and speculations about the alpha loss mechanism were proposed, there is no direct morphological evidence. Rheo-optical techniques may provide such a direct morphological evidence. Dynamic x-ray diffraction measurements may give the time-dependent orientability of a particular crystal plane and dynamic birefringence measurements may give the average time-dependent orientability over crystalline and amorphous phases. Therefore, combining the dynamic x-ray diffraction with the dynamic birefringence technique may give the contribution of amorphous and crystalline parts, respectively, to the total orientability, assuming the two phase model.

The morphology of polyethylene is usually spherulitic with preferred growth along a particular (the b) crystal axis, and so the b axis is directed along the radius with the a and c axes helicoidally oriented perpendicular to the b axis with more or less radial order (27). The size and perfection of the spherulites which are most important factors in our understanding of the alpha loss mechanism are dependent upon linearity, molecular weight and its distribution of the polyethylene and the thermal history.

CHAPTER III

SAMPLE CHARACTERIZATION

Sample Preparation

Low density polyethylene (Monsanto Research Special No. AA-1933, Grade 910, M.I. = 7.0) was used as samples in this study. The gel permeation chromatography data, which was carried out in Monsanto Research Laboratory, showed that the number average and weight average molecular weights were 1.67×10^4 and 6.20×10^5 ($\overline{M}_w/\overline{M}_n = 37.0$) as shown in Appendix A. Films with 20 - 25 mils thickness were prepared for dynamic x-ray measurements and those with 3 - 5 mils thickness were prepared for dynamic birefringence as follows.

Q-Samples (Quenched L.D.P.E.).

Pellets of the low density polyethylene were melted for 10 minutes and pressed for 5 minutes at 155°C at a pressure of 10,000 p.s.i. in a laboratory press equipped with heating plates. The samples were then removed from the press and quenched by plunging into a dry-ice and ethanol bath. The films thus prepared were called Q-samples.

H-Samples (Heat-Treated L.D.P.E.).

Films were prepared by making the heat treatment for one hour at 95°C on Q-samples and freely cooled down to room temperature holding in the laboratory press.

Irradiated L.D.P.E.

(a) Q-I-10 and Q-I-30 Samples.

Films were prepared by making β-ray irradiation with doses of 10 Mrads. (Q-I-10 samples) and 30 Mrads. (Q-I-30 samples), respectively,

to Q-films at room temperature by van der Graff.

(b) H-I-10 and H-I-30 Samples.

Films were prepared under the same conditions as used in the preparation of Q-I-10 and Q-I-30 samples, not from Q-samples but from H-samples.

Sample Characterization

Density.

The density of the films used in this study was measured by the floatation method in water-ethanol mixture at room temperature and the weight and volume fractions of the degree of crystallinity in percent, X_c^w and X_c^v, were calculated by the equations:

$$X_c^w = \frac{\rho_c \cdot (\rho - \rho_a)}{\rho \cdot (\rho_c - \rho_a)} \times 100 \qquad (1)$$

$$X_c^v = \frac{\rho - \rho_a}{\rho_c - \rho_a} \times 100 \qquad (2)$$

where ρ is the measured density and ρ_a and ρ_c are, respectively, the densities of the amorphous and crystalline regions and were assumed to be (33)

$$\rho_a = 0.852 \qquad (3)$$

$$\rho_c = 1.00 \qquad (4)$$

The results are shown in Table I.

TABLE I

Density and Crystallinity

Sample	Density (g/cm^3)	Crystallinity (%) Weight Fraction	Volume Fraction
Q	0.914	45.8	41.9
Q-I-10	0.913	45.2	41.2
Q-I-30	0.911	43.7	39.8
H	0.921	50.5	46.6
H-I-10	0.917	47.9	43.9
H-I-30	0.920	50.0	46.0

The irradiation might cause crosslinking in both amorphous and crystalline regions. Crosslinking in the amorphous region may increase the density because of compaction of chains. On the other hand, that in the crystalline region may decrease the density because of more or less destruction of crystalline structures. It was observed that: (1) heat-treated samples had higher density than quenched samples, (2) the density of quenched samples decreased with increasing irradiation dose, and (3) the density of heat-treated samples seemed to have a minimum at the vicinity of 10 Mrads. of irradiation dose.

β-ray irradiation might preferably attack imperfect crystalline regions at the earlier stage of irradiation and afterward may attack the amorphous state. Therefore, higher doses of irradiation than 30 Mrads. may give the higher density even for quenched samples. The results may suggest that quenched samples have much more imperfect crystalline portions than heat-treated samples, which was also observed

in D.S.C. and photographic light scattering measurements discussed later, and also that thermal treatment of the samples is more effective to change the perfectness of crystalline structure than the irradiation with 30 Mrads.

Temperature Dependence of Crystallinity and Lattice Spacing of Crystal.

The x-ray diffraction scan of the low density polyethylene (L.D.P.E.), which is a plot of scattered x-ray intensity versus scattering angle, showed two Bragg crystalline reflections and also one very broad liquid-like peak in the region of Bragg angle (2θ) between 12° and 28°, as shown in Figure 1. Figure 1 shows that of H-sample. Those of other samples, including both unirradiated and irradiated samples, showed quite the same pattern. From the diffraction scans, x-ray apparent degree of crystallinity was calculated under the following assumptions.

1. The summation of the background and incoherent scattering intensities is approximated by the baseline of the diffracted intensity between the Bragg angle of 12° and 28°.

2. The amorphous peak is symmetric about the peak maximum.

3. There is no contribution of the 110 and 200 plane peaks to the amorphous peak at lower Bragg angle than the amorphous peak maximum.

4. The area subtracted the amorphous peak area (A_a) and the background and incoherent scattering areas from the total observed intensity is the summation of the 110 and 200 plane peak areas (A_c).

5. The apparent degree of crystallinity, X_c^x, is expressed by the following equation.

$$X_c^x = \frac{A_c}{A_c + A_a} \times 100 \qquad (5)$$

It was then normalized by the degree of crystallinity, $X_c^w(T_o)$, obtained from density method at room temperature, T_o, as follows.

$$X_c^w(T) = \frac{X_c^w(T_o)}{X_c^x(T_o)} \cdot X_c^x(T) \qquad (6)$$

Although many methods have been proposed for determining the crystallinity from the x-ray technique (34,35,36), the value of the degree of crystallinity thus obtained can be good enough to estimate the temperature dependence of crystallinity of samples, which are shown in Figures 2 - 4.

The crystallinities of both quenched and heat-treated samples decreased monotonously with increasing temperature, as shown in Figure 2. Irradiated samples had less tendency for the crystallinity to decrease with increasing temperature than original Q- and H-samples. Crosslinking caused by the irradiation may work to decrease the thermal agitation of amorphous chains and prevent melting of crystallites.

Lattice spacing changes of crystal with temperature were also examined from the Bragg angle, θ, at the peak of x-ray diffraction scan by the following equation.

$$d_i = \frac{\lambda}{2 \sin \theta_i^{max}} \quad (7)$$

where d_i is the lattice spacing (Å) and θ_i^{max} is the i-th Bragg angle at the maximum of the peak. λ is the wavelength of x-ray (1.54Å). The results for the 200 plane (the a-axis) are shown in Figures 5 - 7. They show that (1) the value of the (100) plane spacing of heat-treated samples was smaller than for the quenched samples and second run, after being slowly cooled down to the room temperature from 95°C, for quenched samples was almost the same as for heat-treated samples. (2) The inflection point in the plot of the (100) plane spacing against temperature was recognized at about 70°C for the quenched samples. For the irradiated samples, no inflection point was observed because of the low angular resolution due to using a relatively wide slit (4mm receipt slit). (3) The (100) plane spacings of irradiated samples were almost the same value as the original samples within the error of measurement as shown in Figures 6 and 7.

The results may suggest that the quenched samples have less perfectness of crystalline structure than the heat-treated samples and that irradiation may not be so effective as thermal treatment of bulk crystallized L.D.P.E. samples. More accurate results could be obtained from the measurement by use of narrow slit and high intensity x-ray source.

The (110) plane spacings of those samples were observed to be constant or show little increase with increasing temperature.

A degree of crystallinity is in principle obtainable by determining any crystallinity-dependent quantity. For example, x-ray, IR, DSC, density and NMR techniques are used. Usually the assumption is made that a semicrystalline polymer is a simple two-phase structure of perfectly crystalline and amorphous regions. This means that lattice imperfections and interfacial effects which may not be described by a simple two-phase model are neglected. Since real polymers do not exactly conform to this assumption, degrees of crystallinity obtained from different techniques may be different and may have different temperature dependence. That is, the measured degree of crystallinity may depend upon how the observed properties depends upon the contributions of ordered or totally or partially disordered regions.

The degree of crystallinity obtained by the differential scanning calorimetry (DSC) technique was normalized by the degree of crystallinity from the density method as follows and is plotted as a function of temperature in Figure 2.

$$X_c^{app}\ (T) = \frac{\int_{T_o}^{T} C_p(T)\ dT}{\int_{T_o}^{T_m} C_p(T)\ dT} \times 100 \qquad (5')$$

$$X_c(T) = \frac{X_c^w(T_o)}{X_c^{app}(T_o)} \cdot X_c^{app}(T) \qquad (6')$$

where C_p is the heat capacity, T_o is the temperature at which crystallites begin to melt, $X_c^w(T_o)$ is the degree of crystallinity obtained from the density method at temperature T_o, X_c^{app} is the apparent crystallinity from the DSC method [Equation (5')], and $X_c(T)$ is the normalized crystallinity. It is observed that the temperature dependence of the degree of crystallinity from the DSC method is different from that obtained from the x-ray method. This is the behavior which was observed by Dole et al. (76), where the decrease in degree of crystallinity with increasing temperature is not as great as is calculated by the x-ray method. The difference may arise from different definitions of the crystalline region. The x-ray method used here is affected by a loss in intensity resulting from the thermal vibrations and lattice imperfections in the amorphous regions. Therefore the crystallinity from the x-ray method may give a smaller crystallinity than that from the DSC method under conditions where crystals become disordered as at higher temperatures.

Although many methods for determining the crystallinity from the x-ray technique have been proposed, they may be divided into mainly two types. The first consists of such techniques as those proposed by

Hermans and Weidinger (35,76) and Krimm and Tobolsky (77), which are based upon the principle that the ratio of amorphous peak intensity (or area) to that in the molten state is proportional to the amorphous content, and that the amorphous peak intensity (or area) in the molten state equals that in a low temperature. The second type are those proposed by Mathews et al. (34), by Aggarwal et al. (78), and by Bryant et al. (79), in which the crystallinity is given by

$$X_c^w = \frac{I_{110} + I_{200}}{I_{am} + I_{110} + I_{200}} \tag{7'}$$

where I_{am}, I_{110} and I_{200} are, respectively, intensities (or areas) of the amorphous, 110 and 200 plane peaks. In the calculation, it is assumed that the scattering powers from amorphous and crystalline regions equal each other or that the correction factor for different scattering power between the amorphous and crystalline regions is made as follows:

$$X_c^w = \frac{a_1 I_{110} + a_2 I_{200}}{a_o I_{am} + a_1 I_{110} + a_2 I_{200}} \times 100 \tag{8'}$$

where a_o, a_1 and a_2 are correction factors for the amorphous, 110 and 200 plane peaks.

Generally speaking, the latter leads to a higher crystallinity than the former.

Ruland (80) noted that even an entirely crystalline substance shows diffuse coherent scattering and a loss in intensity of the diffraction peaks due to thermal vibrations and lattice imperfections. This is expressed by

$$X_{cr} = \frac{\int_0^\infty s^2 I_{cr}\, ds}{\int_0^\infty s^2 I\, ds} \qquad (9')$$

where X_{cr} is the crystallinity, s is the magnitude of reciprocal space vector, I_{cr} and I are crystalline and total coherent scatterings, respectively, and K is the term for lattice imperfections and is expressed as

$$K = \frac{\int_0^\infty s^2 \overline{f^2}\, ds}{\int_0^\infty s^2 \overline{f^2}\, D\, ds} \qquad (10')$$

where $\overline{f^2}$ is the mean square scattering factor of atoms and D is the lattice imperfection factor, which may be given by a Gaussian distribution.

$$D = e^{-ks^2} \tag{11'}$$

where k is the constant. Roughly speaking, other methods previously described may correspond to the crystallinity at K = 1 (or D = 1 or k = 0). K might strongly depend upon temperature. One might say that other methods may neglect a loss in intensity of the diffraction peaks due to the thermal vibrations and lattice imperfections, or they may define an ideally ordered lattice crystal as crystalline. Therefore in methods except Ruland's method, the crystallinity may show the same tendencies for temperature change, where relatively rapid decrease in the crystallinity with increasing temperature may be observed as compared with the DSC method. According to Ruland's data for linear polyethylene at 20 - 25°, the crystallinity was evaluated to be about 10% higher than for other methods, when the region of s between 0.1 and 0.35 was chosen ($2\theta = 9° \sim 31°$) for averaging. The crystallinity by Ruland's method may show the different temperature dependence from those by other conventional methods because the lattice imperfection factor may be a function of temperature. Thus if such effects are taken into account, the degree of crystallinity from the x-ray method may become close to that obtained from the DSC method.

Thermal Properties.

Melting behavior was studied with a Perkin Elmer Differential Scanning Calorimeter (37) (D.S.C.-1B). Experiments were carried out with 5°C/min. heating and cooling rates. Thermograms are shown in Figures 8 - 10 where the first run cooling process was followed after being kept for 5 minutes at 415°K and the second run heating process after being kept for 5 minutes at 300°K.

The following observations were made:

1. Figure 8 shows that the heating curve of the first run for quenched samples (Q) had a broader peak with the peak maximum of higher temperature compared with that of heat-treated samples (H). This may indicate that quenched samples had both more complete and less complete crystallites with a broad distribution, but that by heat-treatment crystallites with a relatively narrow distribution of a certain degree of completeness might be formed as the result of growth of spherulitic structure.

2. Curves of the first run cooling and the second run heating for quenched samples were quite similar to those for heat-treated samples. This may indicate that the same thermal history from the molten state might give the same thermograms and morphology.

3. The first run heating curve for Q-series samples shows in Figure 9 that the melting peak shifted to lower temperature with increasing irradiation dose. This may indicate that irradiation might cause less order of crystallites. For H-series samples, the result was rather complicated, as shown in Figure 10. The first run

heating curve of H-I-30 samples had a peak maximum at a higher temperature than did the original H and H-I-10 samples. The irradiation process must cause higher order of crystallites. This extraordinary behavior may be understood by one of the following interpretations: (a) a relatively low molecular weight material resulting from degradation by irradiation might crystallize with high order of perfection or (b) heat generated during irradiation might cause a kind of annealing.

It seems that these tendencies for the H-series samples may be larger than for the Q-series samples because irradiation may attack the amorphous region rather than imperfect crystalline region. This may be supported from the result of density measurements that the density monotonously decreased with increasing irradiation dose for the Q-series, but that it decreased at 10 Mrads. of dose and then increased at 30 Mrads. of dose for the H-series. Another support is that in the curves of the first run cooling and the second run heating, Q-I-30 had exothermic and endothermic peak maxima at lower temperature than did H-I-30, as shown in Figures 9 and 10. This may suggest that for the Q-I-30 samples, the crystallization process might be delayed as the result of crosslinking occurring not only in an amorphous region but also in an imperfect crystalline region.

It was observed from the first run cooling curve of both Q- and H-series (Figures 9 and 10) that the maximum temperature and peak height of the exothermic peak decreased with increasing irradiation dose. This may indicate that the higher dose of irradiation could

cause more crosslinking. In other words, irradiation has the effect of lowering both the melting point and the degree of crystallization for the bulk samples crystallized from molten state after irradiation.

Photographic Light Scattering.

H_v light scattering patterns were taken by the apparatus (46, 72) shown in Figure 11 where the light beam [laser (He-Ne Gas Laser, Spectra-Physics 130)] was well collimated and the polarization axis of the analyzer was perpendicular to that of the laser beam. The pinhole type slit with a diameter of 1mm was used in this observation. Films with thicknesses of 20 - 22 mils were placed between glass plates. A silicone oil with a refractive index (n) of 1.533 was used to minimize the surface scattering. All pictures were taken with the same exposure time of a half second by using Polaroid films (ASA 3000).

Figure 12 shows the H_v light scattering patterns for undeformed samples. They showed the so-called "four leaf clover" pattern which has been shown to arise from spherulitic structure. The patterns for both H- and Q-samples show, more or less, a tendency of the "tennis racket" shape (38) characteristic of spherulites having internal disorder (39,40) or disorders at their boundaries (38). The intensity of the scattered light for all samples was very weak compared with that from high density and also low density polyethylene crystallized at higher temperature. This may suggest that relatively small and imperfect spherulites were formed in both Q- and H-series samples as compared with others.

According to the model calculation (41), the relationship between the scattering angle, θ^*_{max}, in the medium at which H_v intensity becomes maximum and the radius of spherulite (sphere), R, is expressed by the equation

$$4.1 \cong R \left(\frac{4\pi}{\lambda^*}\right) \sin\left(\frac{\theta^*_{max}}{2}\right) \tag{8}$$

where λ^* is a wavelength of light in the medium and expressed by the following equation

$$n = \frac{\lambda^{o}}{\lambda^*} \tag{9}$$

where λ^{o} is the wavelength of light in air (6328Å) and n is the refractive index of the polymer. θ^*_{max} is the scattering angle within the sample related to the observed scattering angle, θ_{max}, by the equation

$$n = \frac{\sin\,\theta_{max}}{\sin\,\theta^*_{max}} \tag{10}$$

which corrects for the change in scattering angle resulting from refraction at the sample-air interface.

The validity of the equation was proved from the agreement between spherulite sizes measured by the microscope and by the light scattering method (41) and therefore the radius of the spherulite, R,

could be calculated by using Equations (8) - (10). It is assumed in the calculation that the scattering arises from an isolated homogeneous anisotropic sphere in an isotropic medium. In the actual system, the spherulites may fill the sample space and may interfere with each other and also may have internal disorders in terms of both orientation and anisotropy (39,40). The effect of interparticle interference (42) and truncation (43) and the effect of such internal heterogeneities (39,40) on the scattered intensity distribution have been recently shown to hardly shift the peak position, θ^*_{max}, at which the maximum H_v intensity is observed. Consequently, these effects may not significantly affect Equation (8) and therefore the measured size of the spherulite. A spherical type of disorder has also been proposed (38) involving disorder of the spherulite anisotropy at the spherulite boundary where the anisotropy gradually decreases. The peak position, θ^*_{max}, is quite sensitive to such disorder and a modification of Equation (8) may be required.

The values obtained for spherulite sizes are listed in Table II.

TABLE II

Size of Spherulite

Sample	R(μ)	Sample	R(μ)
Q	2.00 ± 0.20	H	2.40 ± 0.20
Q-I-10	1.50 ± 0.20	H-I-10	1.61 ± 0.20
Q-I-30	1.95 ± 0.20	H-I-30	2.23 ± 0.20

It was rather difficult to find the maximum point of the intensity of scattered light in such pictures and therefore personal observing error might be large, which was estimated to be ± 0.20μ. For the purpose of determining the accurate average size of the spherulite, the intensity distribution must be measured photometrically. It was observed that the four leaf clover patterns of Q-series were much larger than those of H-series specimens. This means that the average size of spherulite of the H-series was larger, as shown in Table II, indicating that the heat-treatment process was fairly effectiving in reforming the spherulitic structure with larger size and with greater completeness. Q-I-10 and H-I-10 samples show extraordinary patterns where the average spherulite sizes were smaller than those of other samples. This is hard to understand. It is probably due to some different and unexpected thermal condition at the irradiation process or the film preparation process.

Figure 13 shows the H_v light scattering patterns for undeformed and deformed (15, 30 and 50%) originally quenched and heat-treated samples. In the figure, the direction of stretching (S.D.) is shown. Upon stretching the samples, the scattering patterns were elongated in a direction perpendicular to the stretching direction indicating a change of the spherulite stretching direction as has been previously observed (41,72). The four leaf clover scattering patterns characteristic of spherulitic structure remain up to 80% stretching, at least, indicating that the spherulitic structure may be maintained up to such elongations without having a prominent disruption at the

boundary or in the equatorial part of the spherulite. The change of the patterns for the Q- and H- samples are similar to each other indicating that there are not appreciable differences in the deformation of the spherulite as a whole. However, the details of the deformation mechanism, such as the internal reorientation processes of crystallites, may depend upon thermal history and may be different for the Q- and H- samples.

APPENDIX A
CALCULATION OF GEL PERMEATION DATA

```
GRADE-0910       LOT AA1933                 DATE-07/06/70    GPC NO.-  4664
                                                                                4664

SOLVENT-TCB TEMP.135C  CONC..10  TIME-120S.
COLUMN SET -  69- 8-A          COLUMNS-10E7-10E6-10E4-10E3-

EXP. ETA       ETA-K        ETA-A         A(0)
 0.900       .0004500      0.725      -0.11635D 02

COUNT BEGIN.   COUNT FINISH    BASE BEGIN.   BASE FINISH    CDELTA
    20             32             20.9          19.6         0.150

  COUNT      HT.      CUM.HT.      MOL.WT.     COR.HT.  LOG MWT
  31.87      0.0        0.C          773.       0.0     2.8882
  30.87      1.8        0.47        1372.       2.03    3.1375
  29.88      6.5        3.14        2719.       6.29    3.4344
  28.88     13.9       10.28        5958.      11.84    3.7751
  27.89     20.8       22.42       14356.      16.00    4.1570
  26.89     26.1       39.23       37545.      18.57    4.5746
  25.89     24.3       57.41      104103.      16.45    5.0175
  24.90     18.3       72.39      296281.      12.35    5.4717
  23.90     14.7       83.95      837195.      10.14    5.9228
  22.91      9.8       92.79     2268765.       7.15    6.3558
  21.91      4.3       97.76     5711167.       3.46    6.7567
  20.91      1.3       99.60    12950323.       1.21    7.1123
  19.92      0.0      100.00    25681200.       0.0     7.4096

    MN             MW             MZ            MZ+1
  16739.         620055.        5810686.       11094650.

  SIGMA N        SIGMA W        SIGMA Z        MW/MN
  100494.        1794011.       5541070.        37.04

   FLAT           SKEW          MZ*MZ+1/MW
  -0.637          0.279        103970608.

   LAMBDA        CHAIN LGT.     ME/100C        CALC. ETA
  0.000539          0.0           0.0            0.900
```

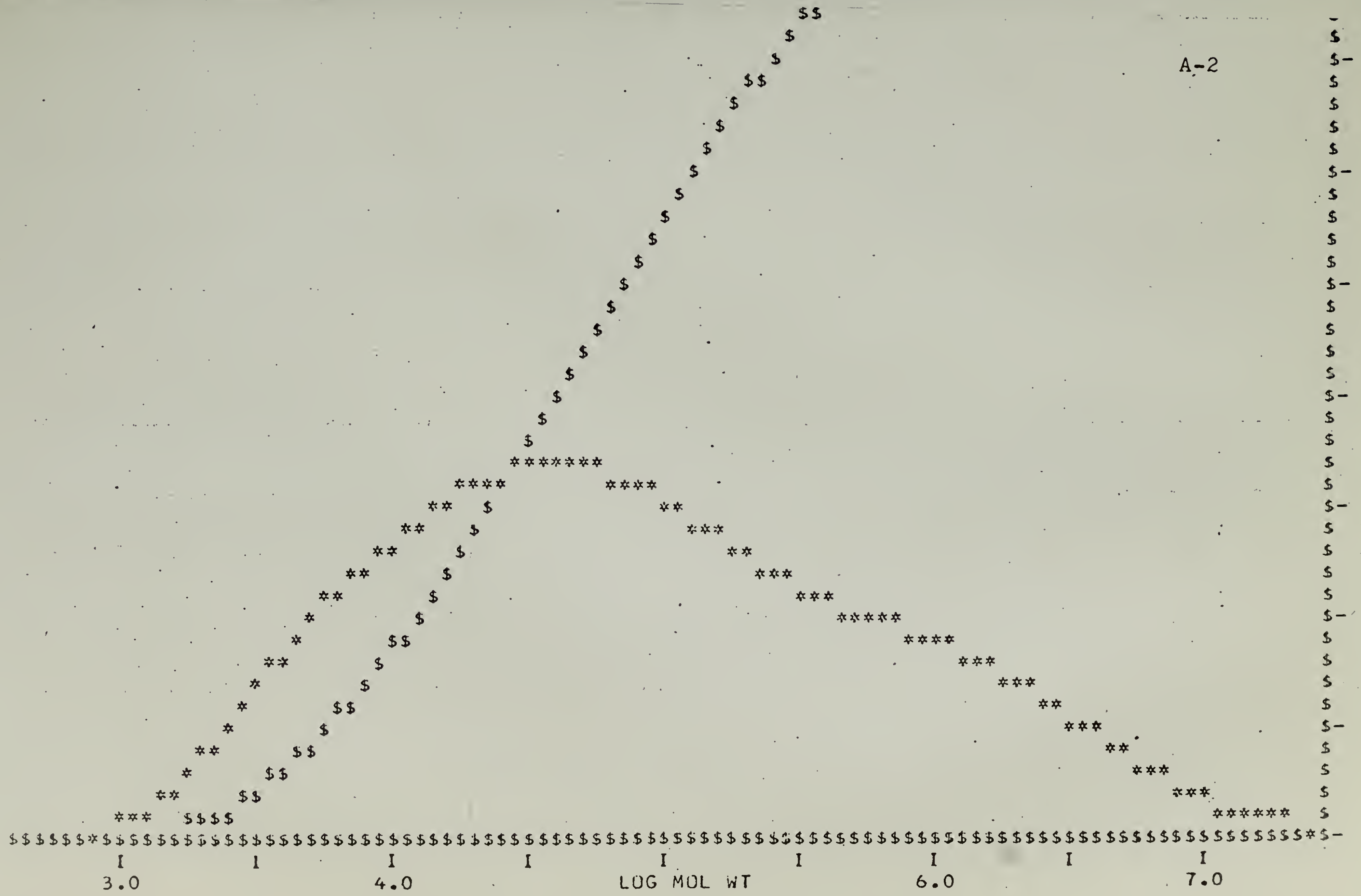

*---GRADE-0910 LOT AA1933 GPC NO.- 4664

CHAPTER IV

EXPERIMENTAL WORK AND DISCUSSION

Dynamic Mechanical Properties

Experiments.

Dynamic modulus E', loss modulus E" and tanδ were obtained as functions of temperature and frequency by using a Vibron DDV Type II (Toyo Measuring Company).

When the periodical (the sinusoidal) strain is applied to the viscoelastic specimen, the stress may also change periodically (sinusoidally) with a phase difference of δ with respect to the strain. The stress change, $\vec{\alpha}_1$, and strain change, $\vec{\alpha}_2$, are shown in Figure 14-A. Those quantities are adjusted electrically by using the resistances so that

$$\frac{|\vec{\alpha}_1|}{K_1} = \frac{|\vec{\alpha}_2|}{K_2} \tag{11}$$

as shown in Figure 14-B, where K_1 and K_2 are the readings of resistances. The amplitude of the complex modulus, $|E^*|$, is expressed by

$$|E^*| = \frac{|\vec{\alpha}_1|}{|\vec{\alpha}_2|} \tag{12}$$

and therefore is given by

$$|E^*| = \frac{K_1}{K_2} \tag{13}$$

and $\vec{\alpha}_1/K_1$ and $\vec{\alpha}_2/K_2$ are expressed by $\vec{a}_1$ and $\vec{a}_2$, that is,

$$\vec{a}_1 = \frac{\vec{\alpha}_1}{K_1} \tag{14-a}$$

$$\vec{a}_2 = \frac{\vec{\alpha}_2}{K_2} \tag{14-b}$$

On the other hand, when δ is small, $|\vec{a}_1 - \vec{a}_2|$ is given by

$$|\vec{a}_1 - \vec{a}_2| = 2\sin\delta/2 \cong \tan\delta \tag{15}$$

as shown in Figure 14-B. Therefore, $\tan\delta$ is given by

$$\tan\delta = |\vec{a}_1 - \vec{a}_2| = \left|\frac{\vec{\alpha}_1}{K_1} - \frac{\vec{\alpha}_2}{K_2}\right| \tag{16}$$

From $\tan\delta$ and $|E^*|$, dynamic modulus, E', and loss modulus, E'', are calculated by the equations

$$E' = |E^*| \cos\delta \tag{17}$$

$$E'' = |E^*| \sin\delta \tag{18}$$

The measurements were carried out in the temperature region between -55°C and 120°C for three different frequencies, 3.5, 11 and 110 Hz. at a heating rate of about 1°C/minute.

Results and Discussion.

Figures 15 - 20 show the temperature dispersion curves of E', E" and tanδ. For the H-series, four temperature regions were observed as shown in Figures 18 - 20. The first is the temperature region from -60 to -40°C, where the curve of E' showed a plateau with a very small slope, whose magnitude was about 9×10^9 dynes/cm^2 and where those of E" and tanδ were almost constant although they increased slightly because of the overlapping effect of the second temperature region. In this temperature region, the segmental motion of polymer chains might be frozen. The motion of small portions of polymer chains such as side groups, end groups, a crankshaft motion and a motion of crystal defects may be permitted, which may correspond to the γ-process observed as a peak in E" at about -120°C (44,45).

Second is the temperature region from -40 to 10°C where the magnitude of E' rapidly decreased from 8×10^9 to 3×10^9 dynes/cm^2 and where curves of E" and tanδ had a peak at about -15°C at a frequency of about 110 Hz. This peak is called the β-peak where the segmental motion of polymer chains in the amorphous region and the motion of branches may become possible. In the case of crystalline polymers, including polyethylene, such a drastic change in E' from the order of 10^9 to 10^6 dynes/cm^2 is not shown as is seen with non-crystalline polymers because of the restriction of crystallites on the motion of the amorphous part of chains and the direct contribution of crystals to the modulus. However, the absorption intensity in E" was much higher than those of single crystal mats and bulk-crystallized high density polyethylene (23,47).

Third is the α temperature region from 10 to 90°C, where curves of E' and E" showed a shoulder and those of tanδ showed a plateau region and another peak with a magnitude of 0.18 which may be related to the α-loss mechanism. The deformation mechanism in this region is rather complicated because mechanisms due to the mixing effect of amorphous and crystalline parts coming from inter-crystalline and intracrystalline regions may contribute. At least two peaks for bulk-crystallized high density polyethylene (11,17) and three or more peaks for the single crystal mat (23,47) were observed in the α region of the temperature dispersion curve of E". These are α_1 (or α by McCrum and Morris and α_c' by Takayanagi) α_2 (α_1 by McCrum and Morris and α_c by Takayanagi) and α_f (by Takayanagi). Takayanagi suggested that the α_f absorption is associated with structural change of the virgin crystal (73). The peak intensity of the α region as a whole was large for bulk-crystallized high density polyethylene, while that of the γ region was smaller, compared with the H-series.

Last is the temperature region over 90°C where the curves of E' and E" rapidly decreased and that of tanδ rapidly increased. This region may correspond to the melting of crystallites.

Any appreciable change in the curves of E' and E" due to the irradiation could not be recognized in the measured temperature region, as shown in Figures 18 - 20.

Figures 15 - 17 show the temperature dispersion curves of E', E" and tanδ for the Q-series. These curves also show four temperature regions as the H-series. As compared with the curves of E' and E" for the H-series, the third region, that is the so-called α region, was slightly different in that the shoulder of the curves was small but recognizable and was shifted to lower temperatures. The curve of tanδ for the Q-series showed a quite different shape from that of the H-series. The former showed apparently one peak and the latter consisted of, at least, two peaks. The magnitude of tanδ for the Q-series was 0.16, which was the intermediate value between the shoulder and peak of tanδ for the H-series. The tanδ peak for the Q-series may become one peak as a result of which the maximum of the α peak with relatively small intensity absorption might be shifted to lower temperature because the perfection of crystallites may be small due to the quenching process.

Irradiation may not relate so much to these mechanical quantities as compared with the thermal history as shown in Figures 15 - 20. The curve of the Q-I-10 samples shows extraordinary behavior which may be due to some different and unexpected thermal condition at the irradiation process or film preparation process as mentioned in a previous section.

All curves (Figures 15 - 20) are shifted to higher temperature with increasing frequency. Figures 21 - 26 show the frequency dependence of tanδ at several temperatures for the samples used in this

study. Figures 27 - 32 show the master curves of tanδ in the temperature region from 30° to 85°C which were obtained by only horizontal shift to the reference temperature of 50°C. The master curves of tanδ for the H and H-I-10 samples showed a maximum with a magnitude of about 0.18 at a frequency of 9.5 Hz. and the slope of the curve against frequency on the higher frequency side was much less than on the lower frequency side. That of the H-I-30 sample showed quite the same shape but the maximum point was shifted to lower frequency at about 0.1 Hz. Also, the magnitude of the maximum was a little bit smaller.

On the other hand, the master curves of Q and Q-I-30 increased with increasing frequency up to 10^3 Hz. and then decreased as predicted from the temperature dispersion curves of tanδ (Figures 15 - 17). The magnitude of the maximum was about 0.16. That of the Q-I-10 showed a slightly different behavior from that of the other Q-series, where the peak maximum shifted to lower frequency at about 10^2 Hz. This may be related to the anomalous spherulite size found for this sample.

Figures 32 - 37 show the plots of the logarithm of the shift factor, a_T, which was used in the superposition to the curve for the reference temperature against reciprocal absolute temperature. The activation energies, ΔH^{+}, were also noted in the figures corresponding to each slope of the straight line which was calculated by the equation

$$\Delta H^{+} = 2.303R \cdot \frac{d \log a_T}{d(\frac{1}{T})} \qquad (19)$$

where R is the gas constant (1.98 cal/mole^{-1} deg^{-1}). The activation energies obtained from tanδ curves for all samples are summarized in Table III, which may correspond to the α region.

TABLE III

Activation Energy Obtained from Tanδ Curve (kcal/mole)*

Sample	Low Temperature Part	High Temperature Part
Q	29.6	36.4
Q-I-10	25.0	31.8
Q-I-30	27.3	31.8
Average	27.3	33.3
H	31.8	38.7
H-I-10	27.3	38.7
H-I-30	23.6	36.4
Average	27.6	37.9

*Estimated error was less than 5 kcal/mole.

The activation energies were calculated from the two different slopes in the different temperature regions, as shown in Figures 32 - 37. Those for the low temperature parts were about 27 kcal/mole for both Q- and H-series, and those of the higher temperature part were about 33 kcal/mole for Q-series and about 38 kcal/mole for H-series. It seems that for the master curves of tanδ for the H-series the α peak might consist of not only the α peak itself but also a contribution from the β peak might be quite small and that the α_1 region shown as the plateau might consist of α, α_1 and α_2 contributions and that the α_2 region shown as another peak might consist of α_1, α_2 and melting peak, where the contribution of α_2 might be much higher.

On the other hand, there appears to be one peak for the Q-series, but it seems that this peak may also consist of at least three components coming from α_1, α_2 and β contributions. The contribution of the α_1 peak, predominantly associated with crystalline nature, might be very small because the Q-series samples showed a low crystallinity and small size of spherulites as measured by density and photographic light scattering. Thus, when these overlapping effects of two or more peaks were taken into account, the obtained values of the activation energy for the low temperature part, 27 kcal/mole for both Q- and H-series, and of the high temperature part, 33 kcal/mole for Q-series and 38 kcal/mole for H-series, were very comparable with 28 and 46 kcal/mole obtained by Nakayasu, Markovitz and Plazek for bulk crystallized high density polyethylene (11) and 25 and 46 kcal/mole for annealed single crystal mat by Takayanagi, et al. (23,47), 30 kcal/mole for low density polyethylene by Faucher (45) and 50-55 kcal/mole for a few different kinds of low density polyethylenes by Fukui (32). It may be due to a decreasing of contribution of the α_2 peak that activation energies of H-I-30 samples both in high and low temperature regions were small, indicating that the irradiation of H-samples may decrease the contribution of the α_2 mechanism.

It is interesting that the difference in thermal history brought the samples with two different mechanisms, α_1 and α_2, into the observable temperature region for rheo-optical studies.

Dynamic X-Ray Diffraction

Apparatus and Experimental Technique.

X-ray diffraction studies are one of the most useful means for determination of the orientation of particular crystal axes, as is well known. The dynamic x-ray diffraction technique was developed as a direct means of determining the time-dependent orientation of a particular crystal axis where the sample is vibrated sinusoidally and the diffraction counts are accumulated during specified intervals of the vibration period over many cycles (29-31). The apparatus and the method for determining the orientation function by this technique used in this study will be briefly discussed in the following section, although general discussions and techniques were reported by T. Ito, et al. (31).

Apparatus: The apparatus for dynamic x-ray diffraction used in this study was almost the same as the one reported by T. Ito, et al. (31) It was new for it was combined with a teletype connected with the computer, in which the time required up to the end of complete cycle next to a fixed time from the beginning and four different kinds of diffracted intensities accumulated during different specified intervals of the vibration period over many cycles were automatically stored on punch tape and typed on paper. Both in-phase and out-of-phase orientational compliances of particular crystal axes C_a', C_b', C_c', C_a'', C_b'' and C_c'' could be calculated by the University of Massachusetts computer system (48) from this punched tape input.

Also, the geiger counter of the original apparatus was replaced by a scintillation counter. This had the advantage of having a shorter "dead time" reducing coincidence errors and it also resulted in a reduction in background count because of the possibility for pulse height discrimination.

When the specimens sinusoidally deformed, the diffracted intensity may also change sinusoidally but with phase difference with respect to the strain phase. Such diffracted intensity is simultaneously accumulated over specified intervals of the strain phase ($0 - \pi$, $\pi/2 - 3\pi/2$, $3\pi/2 - 5\pi/2$ and $\pi - 2\pi$) by using photo-switches as a function of azimuthal angle ϕ at a fixed Bragg angle θ. From the values of these accumulated intensities, both the in-phase and out-of-phase orientational compliances of a particular crystal plane corresponding to the Bragg angle can be calculated as described later.

Figure 39 is a schematic diagram of the dynamic x-ray diffraction apparatus in an application of the transmission technique. A film specimen in a vertical plane is subjected to tensile sinusoidal deformation. A pinhole collimated x-ray beam falls on the specimen in the horizontal plane with an angle θ to the film normal and the diffracted x-ray beam is detected in the same horizontal plane by a scintillation counter tube at the same angle θ to the film normal. The film specimen can be rotated about its normal axis to give any desired azimuthal angle ϕ whose value is taken to be zero when the tensile stress direction of the film specimen is vertical. In practice,

the tensile stress is applied in the longitudinal direction of the film specimen which has a ribbon shape and it follows the ϕ rotation of the specimen.

While the specimen is sinusoidally deformed, the detected and preamplified x-ray signals are continuously fed to the four scalers. These scalers are activated repetitively only at particular strain phase intervals for each scaler by means of a gating circuit of eight sets of photoelectric switches. The necessary pulse signals for activating each scaler (to start and stop) are generated from each of two sets of photoelectric switches, which are controlled by a semicircular sector plate with four windows rotating in synchronism with the eccentric cam shaft so that the switches are energized at particular strain phases of the specimen.

The entrance slit was adjusted so that the cross-section area of the x-ray beam at the center position of the sample was 9.6 mm x 0.18 mm, which was checked by otaining a direct image of the x-ray beam. The receiver slit before the scintillation counter was 4 mm wide, for which the width of effective Bragg angle for the diffracted x-ray beam admitted to the scintillation counter was 1.06 degrees. This angular interval is intentionally broad so as to maximize the intensity and to minimize the effect of variation of the position of the diffraction peak due to sinusoidal variation of the crystal lattice spacings with strain.

Principle of the Method: When a sinusoidal strain was imposed on the specimen by two eccentric cams, the diffracted intensity of

x-rays varies sinusoidally with a dynamic amplitude, ΔI_{total}, and a phase difference, δ_x, with respect to the strain, as shown in Figure 41-B. These quantities at the Bragg angle, θ, and the azimuthal angle, ϕ, may be expressed by the equations

$$\varepsilon = \varepsilon_s^o + \Delta\varepsilon \sin\omega t \tag{20}$$

$$I_{total}(\theta,\phi) = I_{total}^o + \Delta I_{total} \sin(\omega t + \delta_x) \tag{21}$$

where I_{total}^o is the total diffracted intensity at the static strain ε_s^o. and ΔI_{total} and $\Delta\varepsilon$ are dynamic amplitudes of the diffracted intensity and strain, respectively. t is time and ω is the angular frequency. The frequency, ν, is expressed as

$$\nu = \frac{\omega}{2\pi} \tag{22}$$

The total diffracted intensity can also be described as a summation of

1. coherent scattering from crystalline phase and amorphous phase of the film, $I_{cr}(\theta,\phi)$ and $I_{am}(\theta,\phi)$,
2. incoherent scattering from the sample, $I_{incoh}(\theta,\phi)$, and,
3. background scattering, $I_{back}(\theta,\phi)$.

That is,

$$I_{total}(\theta,\phi) = I_{cr}(\theta,\phi) + I_{am}(\theta,\phi) + I_{incoh}(\theta,\phi) + I_{back}(\theta,\phi) \tag{23}$$

It is also assumed that

1. $I_{cr}(\theta,\phi)$ and $I_{am}(\theta,\phi)$ change sinusoidally. That is,

$$I_{cr}(\theta,\phi) = I^{o}_{cr}(\theta,\phi) + \Delta I_{cr} \sin(\omega t + \delta^{cr}_{x}) \tag{24}$$

$$I_{am}(\theta,\phi) = I^{o}_{am}(\theta,\phi) + \Delta I_{am} \sin(\omega t + \delta^{am}_{x}) \tag{25}$$

2. $I_{incoh}(\theta,\phi)$ and $I_{back}(\theta,\phi)$ are constant for the sinusoidal deformation. That is,

$$I_{incoh}(\theta,\phi) = I^{o}_{incoh}(\theta,\phi) \tag{26}$$

$$I_{back}(\theta,\phi) = I^{o}_{back}(\theta,\phi) \tag{27}$$

3. The thickness change for the dynamic strain is negligibly small. That is,

$$d = d_o$$

This assumption is reasonably good for the in-phase and out-of-phase orientational compliances if the thickness change is

is in phase with the strain because the error due to the thickness change is canceled out in the process of the calculation for orientational compliances.

In the polyethylene sample, there are three peaks in the region between 12° and 28° of Bragg angle, which are the amorphous peak, the 110 plane peak and the 200 plane peak. Each intensity of a crystalline plane or amorphous peak, I_i, may be described by the following equation after having made the correction of overlap effect from other peaks, which will be discussed later.

$$I_i(\theta,\phi) = I_i^o(\theta,\phi) + \Delta I_i \sin(\omega t + \delta_x^i) \tag{29}$$

By using the photoswitch shown in Figure 40, the four particular integrated values defined below, I_1^i, I_2^i, I_3^i and I_4^i may be obtained experimentally. I_1^i corresponds to the diffracted intensity accumulated during the interval between 0 and π of the strain phase over n cycles.

$$I_1^i \equiv I_{0-\pi} = \frac{n}{\tau} \int_0^{\pi/\omega} \{I_i^o(\theta,\phi) + \Delta I_i(\theta,\phi) \sin(\omega t + \delta_x^i)\} \, dt$$

where τ is a time required for n cycles.

$$\frac{\omega\tau}{n} = \pi \tag{31}$$

and therefore

$$I_1^i = I_i^o(\theta,\phi) + \frac{2}{\pi}\,\Delta I_i(\theta,\phi)\cos\delta_x^i \qquad (32)$$

In the same way, the other integrals are expressed as

$$I_2^i \equiv I_{\pi/2\sim 3\pi/2} = I_i^o(\theta,\phi) - \frac{2}{\pi}\,\Delta I_i(\theta,\phi)\sin\delta_x^i \qquad (33)$$

$$I_3^i \equiv I_{3\pi/2\sim 5\pi/2} = I_i^o(\theta,\phi) + \frac{2}{\pi}\,\Delta I_i(\theta,\phi)\sin\delta_x^i \qquad (34)$$

$$I_4^i \equiv I_{\pi\sim 2\pi} = I_i^o(\theta,\phi) - \frac{2}{\pi}\,\Delta I_i(\theta,\phi)\cos\delta_x^i \qquad (35)$$

On the other hand, the diffracted intensity described in Equation (29) could be rewritten as

$$I_i(\theta,\phi) = I_i^o(\theta,\phi) + \{\Delta I_i\cos\delta_x^i\}\sin\omega t + \{\Delta I_i\sin\delta_x^i\}\cos\omega t \qquad (36)$$

Comparing Equation (36) with Equation (20), the second term is the in-phase component of the diffracted intensity change and the third term is the out-of-phase component. That is,

$$\Delta I_i'(\theta,\phi) = \Delta I_i(\theta,\phi)\cos\delta_x^i \qquad (37)$$

$$\Delta I_i''(\theta,\phi) = \Delta I_i(\theta,\phi)\sin\delta_x^i \qquad (38)$$

By using Equations (32) - (35),

$$I_i^o(\theta,\phi) = \frac{I_1^i + I_4^i}{2} = \frac{I_2^i + I_3^i}{2} \tag{39}$$

$$\begin{aligned}\Delta I_i'(\theta,\phi) &\equiv \Delta I_i(\theta,\phi)\cos\delta_x^i \\ &= \frac{\pi}{4}(I_1^i - I_4^i)\end{aligned} \tag{40}$$

$$\begin{aligned}\Delta I_i''(\theta,\phi) &\equiv \Delta I_i(\theta,\phi)\sin\delta_x^i \\ &= \frac{\pi}{4}(I_3^i - I_2^i)\end{aligned} \tag{41}$$

Thus, experimentally, the static diffracted intensity, $I_i^o(\theta,\phi)$, the in-phase part of the diffracted intensity change, $\Delta I_i'(\theta,\phi)$ and the out-of-phase part of the diffracted intensity change, $\Delta I_i''(\theta,\phi)$ can be obtained as a function of azimuthal angle at a fixed Bragg angle, θ, corresponding to a particular crystal plane, i.

The Hermans type orientation function (49) is given by

$$f = \frac{3\,\langle\cos^2\eta_i\rangle - 1}{2} \tag{42}$$

where η_i is the angle between the stretching direction and the normal vector of the crystal plane, i. From the definition of ϕ, the mean square of $\cos\eta_i$, $\langle\cos^2\eta_i\rangle$, is expressed by

$$<\cos^2 \eta_i> = <\sin^2 \phi>$$

$$\frac{\int_0^{\pi/2} \cos\phi \ \sin^2\phi \ [I_i^o(\theta,\phi) + \Delta I_i \ \sin\ (\omega t + \delta_x^i)] \ d\phi}{\int_0^{\pi/2} \cos\phi \ [I_i^o(\theta,\phi) + \Delta I_i \ \sin\ (\omega t + \delta_x^i)] \ d\phi} \tag{43}$$

where $\cos\phi$ is a weighing factor. Equation (43) is rewritten as

$$<\cos^2 \eta_i> = \frac{I_{12} + I_{22} \sin\omega t + I_{32} \cos\omega t}{I_{11} + I_{21} \sin\omega t + I_{31} \cos\omega t} \tag{44}$$

where I_{11}, I_{12}, I_{21}, I_{22}, I_{31} and I_{32} are given by the following integrals:

$$I_{11} = \int_0^{\pi/2} I_i^o(\theta,\phi) \cos\phi \ d\phi \tag{45}$$

$$I_{12} = \int_0^{\pi/2} I_i^o(\theta,\phi) \sin^2\phi \cos\phi \ d\phi \tag{46}$$

$$I_{21} = \int_0^{\pi/2} \Delta I_i'(\theta,\phi) \cos\phi \ d\phi \tag{47}$$

$$I_{22} = \int_0^{\pi/2} \Delta I_i'(\theta,\phi) \sin^2\phi \cos\phi \ d\phi \tag{48}$$

$$I_{31} = \int_0^{\pi/2} \Delta I_i''(\theta,\phi) \cos\phi \ d\phi \tag{49}$$

$$I_{32} = \int_0^{\pi/2} \Delta I_i''(\theta,\phi) \sin^2\phi \cos\phi \ d\phi \tag{50}$$

These values can be numerically calculated from $I_i^o(\theta,\phi)$, $\Delta I_i'(\theta,\phi)$ and $\Delta I_i''(\theta,\phi)$ obtained as a function of ϕ at a fixed θ as shown in Equations (39), (40) and (41). Equation (44) may approximately equal the next equation.

$$<\cos^2 \eta_i> = \frac{I_{12}}{I_{11}} \left\{ 1 + \left(\frac{I_{22}}{I_{12}} - \frac{I_{21}}{I_{11}} \right) \sin\omega t + \left(\frac{I_{32}}{I_{12}} - \frac{I_{31}}{I_{11}} \right) \cos\omega t \right\} \tag{51}$$

By combining Equation (51) with Equation (42), we obtain

$$f = \frac{3 \frac{I_{12}}{I_{11}} - 1}{2} + \frac{3}{2} \frac{I_{12}}{I_{11}} \left(\frac{I_{22}}{I_{12}} - \frac{I_{21}}{I_{11}} \right) \sin\omega t + \frac{3}{2} \frac{I_{12}}{I_{11}} \left(\frac{I_{32}}{I_{12}} - \frac{I_{31}}{I_{11}} \right) \cos\omega t \tag{52}$$

Thus, the static orientation function, f_o, and in-phase and out-of-phase orientation functions, $\Delta f'$ and $\Delta f''$, can be obtained. These are expressed by the following equations:

$$f_o = \frac{3 \frac{I_{12}}{I_{11}} - 1}{2} \tag{53}$$

$$\Delta f' = \frac{3}{2} \frac{I_{12}}{I_{11}} \left(\frac{I_{22}}{I_{12}} - \frac{I_{21}}{I_{11}} \right) \tag{54}$$

$$\Delta f'' = \frac{3}{2}\frac{I_{12}}{I_{11}}\left(\frac{I_{32}}{I_{12}} - \frac{I_{31}}{I_{11}}\right) \tag{55}$$

Static and dynamic orientational compliances are defined by the equations:

$$C_o = f_o/\varepsilon_o \tag{56}$$

$$C' = \Delta f'/\Delta\varepsilon \tag{57}$$

$$C'' = \Delta f''/\Delta\varepsilon \tag{58}$$

where $\Delta\varepsilon$ is an amplitude of dynamic strain.

Corrections:

Correction for semi-circular sector plate: A photo-sector plate with four windows rotates in synchronism with sample vibration, but it is not always exactly in phase with the strain. To avoid this mechanical error in position of the sector plate, it was adjusted by replacing two wedge-shaped polyethylene specimens (as shown in Figure 42-B) by a sample. Two wedge-shaped polyethylene specimens move up and down sinusoidally by the eccentric cams without stretching. Therefore, the signal from such polyethylene specimens must be linear with the strain. If the-phase difference between sector plate and strain is δ_s, the difference between the diffracted

intensities from the wedge specimens accumulated in scaler #2 and scaler #3 after having made the correction for the sector constant discussed in the next section should be

$$I_2 - I_3 = 4L \sin\delta_s \qquad (59)$$

where L is a proportional constant. If $\delta_s = 0$,

$$I_2 - I_3 = 0 \qquad (60)$$

Therefore, the phase of the sector plate is adjusted so that $I_2 - I_3$ nearly equals zero. It was also examined by using an oscilloscope in which the strain signal obtained by the linear variable differential transformer fixed at jaws and the signal of the photoswitch are simultaneously recorded, as shown in Figure 41-A.

Sector constant: The opening range of each window cut in the sector plate itself is not exactly π but something like $\pi \pm \delta'$. Therefore, a sector constant corresponding to each window with a particular phase interval must be introduced so that each interval in which the diffracted intensity was actually accumulated is normalized. This was done by using a pulse signal of constant frequency as an input to the counters. Each sector constant corresponding to each window was defined by

$$S_1 = \frac{2\ I_4}{I_1 + I_4} \tag{61}$$

$$S_2 = \frac{2\ I_3}{I_2 + I_3} \tag{62}$$

$$S_3 = \frac{2\ I_2}{I_2 + I_3} \tag{63}$$

$$S_4 = \frac{2\ I_1}{I_1 + I_4} \tag{64}$$

where I_1, I_2, I_3 and I_4 are accumulating counts for particular intervals previously defined. These sector constants should be unity if sector plate is completely ideal. Deviations of the sector constants from unity were less than 0.3%, which is not a significant deviation for the measurement of the in-phase part of the orientational compliances.

Overlap effect: The variation of the diffracted x-ray intensity with Bragg angle for undeformed low density polyethylene shows three peaks in the region between 12° and 28° of Bragg angle, as shown in Figure 1. The peak at 19° corresponds to the amorphous peak, at 21.5° to the 110 plane of the crystal and at 23° to the 200 plane. These peaks may overlap each other and therefore the separation of the total intensity into the contribution from each peak is necessary. For this purpose, several assumptions were made:

1. The half width of each peak is constant, which was experimentally proven for the temperature region from 20° to 95°C.

2. The change in peak position with increasing temperature is negligibly small. This assumption is reasonably good because of the relatively wide slit (4 mm) used in this study.

3. The distribution function of the diffracted intensity for each peak obeys the Lorenzian function

$$I_i = \frac{I}{1 + \left(\frac{\theta - \theta_i}{\frac{A}{2}}\right)^2} \tag{65}$$

where I and I_i are the intensities at Bragg angle, θ and θ_i, and A is the half width.

4. The contribution of the diffracted intensity change of the amorphous peak, ΔI_{am}, introduced by a small dynamic strain to those of the 110 and 200 planes, ΔI_{110} and ΔI_{200}, is small. These contributions were estimated to be about 10% to C'_{110} and about 15% to C'_{200}. Although these are relatively large contributions, they are neglected by the reasons why the diffracted intensity change of the amorphous peak is independent of the frequency in the measured frequency region, as observed by T. Kawaguchi, et al. (74), and why this measurement is a very time-consuming process. This neglect may not affect the results qualitatively and may only cause the methodical error.

5. The degree of contribution of one peak to other peaks is the same both in dynamic and static measurements. This assumption is desirable because it is a very time-consuming process to separately determine the contribution of the dynamic diffracted intensity for one peak to those for other peaks.

From these assumptions, the peak separation could be made in the following way: the observed intensities of the amorphous, 110 plane and 200 peaks, I_{am}, I_{110} and I_{200} at a particular azimuthal angle, ϕ, are expressed by the following equations after the incoherent and background scattering intensities are subtracted:

$$I_{am}(\phi) = \alpha_{11} I^{o}_{am}(\phi) + \alpha_{12} I^{o}_{110}(\phi) + \alpha_{13} I^{o}_{200}(\phi) \qquad (66)$$

$$I_{110}(\phi) = \alpha_{21} I^{o}_{am}(\phi) + \alpha_{22} I^{o}_{110}(\phi) + \alpha_{23} I^{o}_{200}(\phi) \qquad (67)$$

$$I_{200}(\phi) = \alpha_{31} I^{o}_{am}(\phi) + \alpha_{32} I^{o}_{110}(\phi) + \alpha_{33} I^{o}_{200}(\phi) \qquad (68)$$

where I^{o}_{am}, I^{o}_{110} and I^{o}_{200} are the corrected intensities of the amorphous, 110 plane and 200 peaks after the peak separation has been made. α_{ij} is a coefficient for the contribution of the j-th peak to the i-th peak. These coefficients might be given by the following equations from the assumptions given before.

$$\alpha_{ij} = \frac{1}{1 + \left(\frac{\theta_i - \theta_j}{\frac{A_j}{2}}\right)^2} \qquad (69)$$

$$\alpha_{ij} = 1 \qquad \text{for } i = j \qquad (70)$$

where θ_i and θ_j are the Bragg angles corresponding to the i-th and j-th peaks, respectively, and A_j is the half width of the j-th peak. Each coefficient is determined from the half width and Bragg angle of the peak position of each peak. When the specimen is stretched with the strain $\Delta\varepsilon$, the intensity at each peak position is expressed by

$$I_{am} + \Delta I_{am} = \alpha_{11} (I^o_{am} + \Delta I^o_{am}) + \alpha_{12} (I^o_{110} + \Delta I^o_{110}) + \alpha_{13} (I^o_{200} + \Delta I^o_{200}) \qquad (71)$$

$$I_{110} + \Delta I_{110} = \alpha_{21} (I^o_{am} + \Delta I^o_{am}) + \alpha_{22} (I^o_{110} + \Delta I^o_{110}) + \alpha_{23} (I^o_{200} + \Delta I^o_{200}) \qquad (72)$$

$$I_{200} + \Delta I_{200} = \alpha_{31} (I^o_{am} + \Delta I^o_{am}) + \alpha_{32} (I^o_{110} + \Delta I^o_{110}) + \alpha_{33} (I^o_{200} + \Delta I^o_{200}) \qquad (73)$$

From assumptions,

$$\Delta I^{o}_{am} = 0 \tag{74}$$

By combining Equations (71) - (73) with Equations (66) - (68),

$$\Delta I_{110} = \Delta I^{o}_{110} + \alpha_{23} \Delta I^{o}_{200} \tag{75}$$

$$\Delta I_{200} = \alpha_{32} \Delta I^{o}_{110} + \Delta I^{o}_{200} \tag{76}$$

Therefore, ΔI^{o}_{110} and ΔI^{o}_{200} could be obtained from observed values, ΔI_{110} and ΔI_{200}, by solving simultaneous equations. That is

$$\Delta I^{o}_{110} = \frac{\Delta I_{110} - \alpha_{23} \Delta I_{200}}{1 - \alpha_{23} \alpha_{32}} \tag{77}$$

$$\Delta I^{o}_{200} = \frac{\Delta I_{200} - \alpha_{32} \Delta I_{110}}{1 - \alpha_{23} \alpha_{32}} \tag{78}$$

In this study, it is also assumed that the half width of each peak is constant with strain. This assumption may be reasonably good because the applied static strain was small (10%). Such a neglect may not cause a significant change, especially for the temperature and frequency dependencies of orientational compliances at a fixed static strain.

Computer Program: The program was written in Fortran language and is shown in Appendix B.

Results and Discussion.

Experimentally, there are mainly two difficulties in obtaining reasonably accurate results.

1. It is necessary to get enough diffracted intensity so that the relatively small change of the diffracted intensity due to the change of a small dynamic strain becomes large enough compared with the statistical error resulting from the fluctuations of the intensity of the x-ray source itself and of counting by the sector plate.

2. It is necessary to stretch the sample uniformly without causing the slacking and breaking of the specimen over many cycles of periodic strain for several hours.

The first difficulty can be avoided by accumulating the counts resulting from the diffracted intensity over many cycles or by using an x-ray source with high intensity which may have only small fluctuations. The second difficulty may be associated with the nature of the sample, but it can be avoided in some cases by applying a small enough dynamic amplitude of strain to the specimen, although the smaller dynamic amplitude of strain, the smaller change of the diffracted intensity. In some cases, such as that of high density polyethylene, it was not possible to carry out measurements with a small enough strain amplitude to avoid slacking. Therefore, by considering experimental difficulties, the following experimental condition was chosen in the strain region where the initial linear relationship between optical quantities and the strain may be kept.

The measurements were carried out with films at a static elongation of 10% and a dynamic strain amplitude of 2.5 - 3.0% at several frequencies between 0.05 and 2.0 Hz. in the temperature region between 30 and 90°C. Samples were vibrated for one hour or more prior to measurement to assure steady state conditions. Specimens with lengths of 4 cm, widths of 2 cm and thickness of 20 - 25 mil were used in this study.

Preliminary Checks:

(a) Figure 43 shows a check of the sinusoidal change of the diffracted intensity due to the sinusoidal change of strain, indicating the quite good agreement between the calculated sinusoidal curve and the observed points for the diffracted intensities.

(b) Figure 44 shows the dependence of the orientational compliances on the dynamic strain amplitude at a static strain of 10%. In the figure, the orientational compliances of three crystal axes were constant with the dynamic amplitude of the strain, indicating that the orientational compliances are linear in the range of dynamic strain amplitude of 1 - 5% at a static strain of 10%.

(c) The fluctuations of the x-ray source itself and the sector constant brought from the imperfection of the sector plate and counting system were estimated to be at most 0.1% and 0.02%, respectively, for the procedure which we used of accumulating a diffracted intensity of 800,000 counts for vibration of the sample at 1 Hz. The effect of fluctuations of the x-ray source itself becomes smaller when the accumulated diffracted intensity is larger, and

that of variation in the sector constant becomes smaller when the number of cycles of vibration are more. That is, the effect of this fluctuation becomes smaller at a higher frequency of sample vibration at the same number of counts of the diffracted intensity. However, at a diffracted intensity of 800,000 counts, there was not significant error even at the frequency of 0.05 Hz. On the other hand, the in-phase and out-of-phase parts of the diffracted intensity changes are approximately 1% and 0.25% of the total diffracted intensity, respectively. Therefore, the errors of in-phase and out-of-phase parts of the orientational compliances can be estimated to be 12% and 50%, respectively. Therefore, only in-phase parts of orientational compliances were extensively interpreted.

Results and Discussion: From the orientation functions of the (110) and (200) crystal planes of polyethylene, which are obtained from the dependence of the dynamic x-ray diffraction data from the (110) and (200) crystal planes upon the azimuthal angle as described in the last section, the orientation functions of the a, b and c crystal axes could be obtained by the following equations.

From the orthogonality of these axes (50),

$$f_a + f_b + f_c = 0 \tag{79}$$

and from the geometry of the polyethylene crystal (51),

$$f_b = 1.446\ f_{110} + 0.447\ f_{200} \tag{80}$$

$$f_a = f_{200} \tag{81}$$

It must follow that a similar restriction applies to the compliances,

$$C'_a + C'_b + C'_c = 0 \tag{82}$$

$$C'_b = 1.446\ C'_{110} + 0.447\ C'_{200} \tag{83}$$

$$C'_a = C'_{200} \tag{84}$$

and

$$C''_a + C''_b + C''_c = 0 \tag{85}$$

$$C''_b = 1.446\ C''_{110} + 0.447\ C''_{200} \tag{86}$$

$$C''_a = C''_{200} \tag{87}$$

Therefore, it is possible to characterize the dynamic orientational compliances of the three crystal axes by determination of dynamic orientational compliances for the (110) and (200) crystal planes which are independent.

Figure 45 shows the temperature dependence of static orientation functions of particular crystal axes for Q-samples. These "static" orientation functions are actually the average values of the orientation functions in the vibrational experiment and may differ from the static orientation functions that are directly measured during a static strain cycle. In the figure, the orientation function of the c axis, f^o_c, was positive and constant in the measured temperature region and those of the a and b axes were negative. The absolute value of f^o_a was larger than that of f^o_b, but these absolute values became closer to each other with increasing temperature, indicating that the orientation of the c axis due to static strain of 10% may be maintained in the measured temperature region from 30° to 90°C but that the a axis orientation with the direction perpendicular to the stretching direction may predominantly occur at low temperature. There seems to be no preferable orientation of either the a or b axes at high temperature.

Figures 46 - 51 show the temperature dependence of the in-phase orientational compliances at different frequencies for Q-samples. In these figures, orientational compliances of the a and b axes, C'_a and C'_b, showed the same value at the same frequency and same temperature. C'_c was positive and C'_a and C'_b were negative. This indicates that the c axis of crystallites predominantly orients parallel to the stretching direction without a particular orientational preference between the a and b axes for Q-samples. The deformation mechanism for Q-samples may be interpreted in terms of the floating

rod model by Kratky (52). C'_c shows a maximum at a temperature of about 40°C at the frequency of 2.0 Hz. This maximum shifted to lower temperature with decreasing frequency, and no maximum appeared at a smaller frequency than 0.5 Hz.

Figure 52 shows the temperature dependencies of static orientation functions for H-samples. In the figure, the orientation function of the b axis, f^o_b, was almost zero and that of the a axis, f^o_a, was negative and its magnitude was comparable to that of the c axis. This indicates that the a axis of the crystallites orients perpendicular but the c axis of crystallites orients parallel to the stretching direction at a static strain of 10%. The magnitude of these orientation functions decreased at high temperature, indicating that the irreversible slippage of chains which does not contribute to the orientation may occur.

Figures 53 - 58 show the temperature dependencies of in-phase orientational compliances at particular frequencies for H-samples. C'_a was negative in the measured temperature and frequency regions, but decreased with increasing temperature in the low temperature region and had a negative peak which shifted to higher temperature with increasing frequency. C'_b decreased with increasing temperature and it was positive at low temperature and negative at high temperature. The temperature at which C'_b was zero shifted toward higher values with increasing frequency. C'_c increased with increasing temperature in the low temperature region and had a positive peak at high temperature. The peak was recognized in curves at lower frequency than

0.2 Hz. In the curve at low frequency, C'_c was always positive, but in the curve at higher frequency than 0.2 Hz., C'_c showed negative values at low temperature.

These curves may be divided into three temperature regions:

1. C'_b is positive, C'_c is negative and C'_a is almost zero (low temperature region).

2. C'_b is positive, C'_a is negative and C'_c is almost zero (intermediate temperature region).

3. C'_a is negative, C'_b is zero and C'_c is positive (high temperature region).

The following deformation mechanisms are proposed:

a. Spherulite deformation. Spherulites deform from spheres to ellipsoids as a whole, as shown in Figure 73-A, which must cause b axis orientation parallel to the stretching direction. Such a deformation process was experimentally observed in interpretating light scattering patterns accompanying the rapid stretching by P. Erhardt, et al. (53) which occurred in relatively rapid times.

b. Tilting process. The chains tilt within the lamellae toward the stretching direction, as shown in Figure 73-B, in which process the orientation of the c axis must increase and those of the a and b axes must be constant.

c. Twisting process. The lamella at an equatorial part of the spherulite twists about the b axis, as shown in Figure 73-C, in which process the orientation of the b axis must be constant or

decrease a little and that of the a axis must decrease and that of the c axis must increase.

d. Uniaxial orientation of floating rod-like crystallites within the spherulites. The c axis of the crystallites orients parallel to the stretching direction and the a and b axes of crystallites orient by equal amounts perpendicular to the stretching direction.

The deformation mechanism in the first temperature region (low temperature region) may originate from both (a) and (b) processes, that is, the spherulite deformation from a sphere to an ellipsoid and tilting. That in the third temperature region (high temperature region) may mainly correspond to a (c) process occurring with (a), that is, twisting about the b axis. That in the second (intermediate) temperature region may correspond to the transition region from the first to the third temperature region. At low frequency and high temperature, Q-sample-like behavior was observed which may be interpreted by the floating rod model [(d) process].

Figures 59 - 62 show the temperature dependence of the static orientation functions for irradiated samples, Q-I-10, Q-I-30, H-I-10 and H-I-30. All curves showed orientation functions to be almost constant with temperature except in the high temperature region where the magnitude of the static orientation functions tended to decrease. For the Q-series, the magnitude of f^o_c increased with an increasing dose of irradiation. This indicates that the contribution of crystalline part to the total orientation may increase with an

increasing dose of irradiation. Irreversible processes like slippage of amorphous chains may decrease because the deformation of amorphous chains may be restricted by the crosslinking.

For H-series samples, the same tendency as that for the Q-series was recognized, but it was quite little, indicating that the deformation process for the H-series may include not only intercrystalline but also intracrystalline deformation mechanisms.

Figures 63 - 66 show the temperature dependence of the in-phase part of the orientational compliances for irradiated samples, Q-I-10, Q-I-30, H-I-10 and H-I-30. For Q-series samples this was very similar to that for the original Q-samples, that is, the orientational compliances of the a and b axes, C'_a and C'_b, were close to each other and C'_c had a peak maximum at 40 - 45°C. The effect of irradiation on the orientational compliances is that the magnitudes of C'_a, C'_b and C'_c increased with increasing the dose of irradiation.

For irradiated H-series samples, the orientational compliances showed an almost similar tendency to those of the original H-samples, but in this case it is not as simple as in the case of the Q-series. To understand this behavior, obtaining more systematic data is required. The irradiation appears to be more effective in modifying the properties of Q-samples rather than H-samples. In other words, it may affect the floating rod-like deformation mechanism very much.

Figures 67 and 68 show the master curves of orientational compliances of the 110 and 200 crystal planes obtained from the superposition by only a horizontal shift along the frequency axis to

the reference temperature (50°C for Q-samples). Figure 69 gives the master curves of the in-phase part of the orientational compliances, C'_a, C'_b and C'_c for Q-samples. The superposition of data was fairly good. The accuracy of the test was not great because of the quite small change of C'_{200} and C'_{110} against the frequency.

Figure 71 shows the plot of the logarithm of the shift factor c_T versus the reciprocal absolute temperature for the 110 and 200 crystal planes and also shows the activation energy calculated by the next equation from the slope of the curve in this plot.

$$H^{+} = 2.303R \frac{d(\log c_T)}{d(1/T)} \tag{88}$$

Activation energies for both the 110 and 200 crystal planes were 50 kcal/mole. The error for activation energy was estimated to be 5 kcal/mole for both crystal planes. For Q-samples, as shown in Figure 71, the following was observed:

1. The master curve of C'_c was positive and those of C'_b and C'_a were negative.
2. C'_b and C'_a were quite similar to each other.
3. The magnitude of all master curves monotonously increased with increasing frequency.

This may indicate the uniaxial orientation of the c axis to the stretching direction, which may be interpreted by the floating rod model. It seems that the crystalline part for Q-samples may be indistinguishable from the amorphous part in a point of view

for the deformation mechanism. This process had the activation energy of 50 kcal/mole, which may correspond to the α_2 loss mechanism.

Figure 72 shows the master curves of the 110 and 200 crystal planes and the b and c axes for H-samples. Figure 73 shows the plot of shift factors for orientational compliances of the 110 and 200 crystal planes, c_T, versus reciprocal absolute temperature. From the slope, one can estimate the activation energy to be 25 kcal/mole for both crystal planes. The error was estimated to be 10 kcal/mole for the 200 crystal plane and 5 kcal/mole for the 110 crystal plane. For the H-samples, as shown in Figure 72, the following were observed:

1. The master curve of C'_b was positive and that of C'_c negative and that of C'_a almost zero at the high frequency region.

2. The master curve of C'_b was almost zero and that of C'_a negative and that of C'_c positive at the low frequency region.

3. Transition region between two frequency regions was rather broad from 0.1 to 10 Hz. at the reference temperature of 50°C.

This may indicate that there might be at least two different deformation mechanisms in the measured region. Both deformation mechanisms have similar activation energies of 25 kcal/mole. It may be supposed that in the high frequency region, the predominant mechanisms are the combination of the spherulite deformation from a sphere to an ellipsoid together with tilting of lamella, which corresponds to the deformation mechanism in the high frequency region, but that twisting of lamella about the b axis corresponds to the deformation mechanism in the low frequency region. This may correspond to the α_1 process.

Dynamic Birefringence Properties

Apparatus and Experimental Technique.

The dynamic birefringence technique has been introduced and developed by Onogi, Keedy, Sasaguri and Stein (2,54), by LeGrand and Erhardt (5), Yamada (6,7,8), Read (55,56,57) and by Rudd (58). This technique permits the determination of the in-phase and out-of-phase strain optical coefficients, K' and K", which serves as an additional means of learning about molecular and structural mechanisms of response.

Apparatus: The apparatus used in this study has been described by R. S. Stein, et al. (1), and is designed to measure the dynamic birefringence, stress and strain of a sample subjected to forced tensile vibration. The sample is vibrated mechanically by a motor-transmission-cam assembly at relatively low frequencies (10^{-2} - 10 cycles/sec.). Birefringence is continuously measured by determining the transmission of light by the sample which vibrates between crossed polaroids. The diagram of the optics and measuring system is shown in Figure 74.

Principle: The transmission of light by a sample between 45° crossed polaroids, as shown in the diagram of Figure 74, is

$$T = A \sin^2(\delta/2) + T_s \qquad (89)$$

where δ is the retardation

$$\delta = (2\pi d/\lambda)\ \Delta \qquad (90)$$

where d is the sample thickness, λ is the wavelength of light in vacuum and Δ is the birefringence. A is an attenuation factor representing the reduction in intensity due to other factors than retardation which may be expressed as

$$A = e^{-(\kappa + \tau)d}\ (1 - r) \qquad (91)$$

where κ is the absorption coefficient, τ is the turbidity and r is the reflectivity. T_s is the transmission resulting locally oriented structures (such as spherulites) when the sample is placed between crossed polaroids. As shown in Figure 75, the function of $A \sin^2(\delta/2)$ is approximately proportional to δ in the vicinity of values of δ of $\pi/2$, $3\pi/2$, etc., so therefore

$$\sin^2(\delta/2) = c \cdot \delta \qquad (92)$$

where c is a constant. From Equations (89) and (92)

$$T = A'\delta + T_s \qquad (93)$$

where A' is another constant.

When a small amount of strain, ε, is applied,

$$\left(\frac{\partial T}{\partial \varepsilon}\right) = A' \left(\frac{\partial \delta}{\partial \varepsilon}\right) + \left(\frac{\partial T_s}{\partial \varepsilon}\right) \tag{94}$$

The term $\left(\frac{\partial T_s}{\partial \varepsilon}\right)$ may be neglected. On the other hand,

$$\delta = \delta_s + \delta_R \tag{95}$$

where δ_s is the retardation of the sample and δ_R is the retardation of retarding plates placed in the optical path.

Now, since δ_R is constant

$$\left(\frac{\partial \delta}{\partial \varepsilon}\right) = \left(\frac{\partial \delta_s}{\partial \varepsilon}\right)$$

$$= \frac{2\pi}{\lambda} \left[\Delta_s \left(\frac{\partial d}{\partial \varepsilon}\right) + d \left(\frac{\partial \Delta_s}{\partial \varepsilon}\right) \right] \tag{96}$$

The desired strain optical coefficient is

$$K = \left(\frac{\partial \Delta_s}{\partial \varepsilon}\right)$$

$$= \frac{\lambda}{2\pi d A'} \left(\frac{\partial T}{\partial \varepsilon}\right) - \Delta_s \left(\frac{\partial d}{\partial \varepsilon}\right) \frac{1}{d} \tag{97}$$

Assuming constant volume deformation,

$$\left(\frac{\partial d}{\partial \varepsilon}\right) = -d/2 \tag{98}$$

And so finally the next equation can be obtained

$$K = \frac{\lambda}{2\pi d A'}\left(\frac{\partial T}{\partial \varepsilon}\right) + \frac{1}{2}\Delta_s \tag{99}$$

$\left(\frac{\partial T}{\partial \varepsilon}\right)$ could be obtained from the slope of the Lissajous figure of the variation of transmitted intensity with strain during the vibration, as shown in Figure 76, and Δ_s can be obtained from the reading of a Babinet compensator.

The calculation was done as follows. First of all, a couple of retarding plates were placed in the optical path so that the retardation of light becomes in the vicinity of $\pi/2$ or $3\pi/2$ with respect to the strain phase, which corresponds to the portion with the maximum slope in the curve of $A' \sin^2(\delta/2)$. The standard retarding plate with a known small retardation was placed successively parallel and perpendicular to the stretching direction as a reference retardation. From two Lissajous figures from measurements obtained for these two orientations of the standard retarding plate, as shown in Figure 76, desired quantities could be calculated. That is, in the figure where the measurement is carried out by using the portion at the vicinity of $(2m\pi + \pi/2)$ (m - integer) of δ, the strain and transmitted intensity of light are expressed by the following equations

$$\varepsilon = \varepsilon_s^o + \Delta\varepsilon \sin\omega t \tag{100}$$

$$T = |T_0| \sin(\omega t + \delta_B) \tag{101}$$

where $|T_0|$ is the amplitude of transmitted intensity of light due to dynamic amplitude of strain, $\Delta\varepsilon$, and δ_B the phase difference (phase lag) with respect to the strain. The absolute value of $\sin\delta_B$, $|\sin\delta_B|$, must be calculated from the Lissajous figure.

$$|\sin\delta_B| = \frac{h_2}{h_1} \text{ or } \frac{h_2'}{h_1'} \tag{102}$$

The sign of $\sin\delta_B$ may be obtained by observing the rotating direction of the oscilloscope spot as it traces the Lissajous figure as follows:

1. In the vicinity of retardation, $(2m\pi + \pi/2)$ (m - integer)
   clockwise —— positive (phase lag)
   counterclockwise —— negative (phase lead)
2. In the vicinity of retardation, $[2(m + 1)\pi + \pi/2]$ (m - integer)
   clockwise —— negative (phase lead)
   counterclockwise —— positive (phase lag)

The difference of the retardation when the standard retardation plate is placed parallel and perpendicular to the stretching direction, δ_0, is

$$\delta_0 = \delta_0^{\parallel} + \delta_0^{\perp} \tag{103}$$

where $\delta_0^{\parallel}$ and $\delta_0^{\perp}$ are the retardations of the standard retardation plate in parallel and perpendicular orientations. Its value is known and corresponds to h_0 in Figure 76. The first term of Equation (99) may be expressed by

$$\begin{aligned} K_d &= \frac{\lambda}{2\pi dA'}\left(\frac{\partial T}{\partial \varepsilon}\right) \\ &= \frac{\lambda}{2\pi d}\ \frac{h_1}{h_0}\ \cdot\ \frac{\delta_0}{\varepsilon_0} \qquad \text{or} \\ &= \frac{\lambda}{2\pi d}\ \frac{h_1'}{h_0}\ \cdot\ \frac{\delta_0}{\varepsilon_0} \end{aligned} \tag{104}$$

Therefore, in-phase and out-of-phase parts of strain optical coefficients are expressed by the following equations.

$$K' = K_d \cos\delta_B + \frac{1}{2}\Delta_s \tag{105}$$

$$K'' = K_d \sin\delta_B \tag{106}$$

The Dependence of the Dynamic Amplitude of Strain Upon the Strain Optical Coefficient: The in-phase and out-of-phase parts of the strain optical coefficients, K' and K" and $\tan\delta_B$ were measured as a function of the dynamic amplitude of strain at the conditions of a static strain of 10%, a temperature of 30°C and a frequency of 1 Hz. The result is shown in Figure 77, indicating that K', K" and $\tan\delta_B$ were independent of the dynamic amplitude of strain for dynamic strains up to at least 4%, which may suggest to maintain the linearity in the measured region.

The Estimation of Crystalline and Amorphous Contributions to the Strain Optical Coefficient: It has been shown (59) that the birefringence of crystalline polymers consists of contributions from amorphous and crystalline parts and form birefringence as expressed by the equation:

$$\Delta = X_c \left[(n_a - n_c) f_a + (n_b - n_c) f_b\right] + (1 - x_c) f_{am} \Delta^o_{am} + \Delta_F \qquad (107)$$

where Δ is the birefringence; x_c is the volume fraction crystallinity; n_a, n_b and n_c are the refractive indeces along the a, b and c axes; f_{am} is the amorphous orientation function; Δ^o_{am} is the intrinsic birefringence of the amorphous part; and Δ_F is the form birefringence. The strain optical coefficient is then (60)

$$K = X_c \left[(n_a - n_c) \left(\frac{\partial f_a}{\partial \varepsilon} \right) + (n_b - n_c) \left(\frac{\partial f_b}{\partial \varepsilon} \right) \right]$$

$$+ (1 - X_c)\, \Delta^{o}_{am} \left(\frac{\partial f_{am}}{\partial \varepsilon} \right) + \left(\frac{\partial \Delta_F}{\partial \varepsilon} \right)$$

$$= K_{cr} + K_{am} + K_F \qquad (108)$$

where K_{cr}, K_{am} and K_F are the crystalline, amorphous and form birefringence contributions to the strain optical coefficient. By differentiating with respect to strain, one gets

$$K' = X_c \, [(n_a - n_c)\, C'_a + (n_b - n_c)\, C'_b]$$

$$+ (1 - X_c)\, \Delta^{o}_{am} \left(\frac{\partial f'_{am}}{\partial \varepsilon} \right) + \left(\frac{\partial \Delta'_F}{\partial \varepsilon} \right)$$

$$= K'_{cr} + K'_{am} + K'_F \qquad (109)$$

$$K'' = X_c \, [(n_a - n_c)\, C''_a + (n_b - n_c)\, C'_b]$$

$$+ (1 - X_c)\, \Delta^{o}_{am} \left(\frac{\partial f''_{am}}{\partial \varepsilon} \right) + \left(\frac{\partial \Delta''_F}{\partial \varepsilon} \right)$$

$$= K''_{cr} + K''_{am} + K''_F \qquad (110)$$

It is possible to calculate K'_{cr} from the dynamic x-ray data as has been shown by R. Stein, et al. (60) K'_{F} might be negligibly small, as has been shown by E. P. Chang, et al. (61) Therefore, the amorphous contribution to the strain optical coefficient, K'_{am}, could be estimated by combined use of dynamic x-ray and birefringence techniques. In this study, the volume fraction crystallinity was calculated by using the normalized weight fraction crystallinity obtained from the x-ray diffracted intensity method as described previously [Equation (6)].

However, if one uses the volume fraction crystallinity calculated from the DSC method, one will obtain different values of K'_{cr} and K'_{am}, especially for Q-samples, because absolute magnitude of K'_{cr} for Q-samples is larger than that for H-samples. K'_{cr} and K'_{am} were calculated for Q- and H-samples by using volume fraction crystallinity calculated from the DSC technique at a frequency of 1 Hz. as shown in Figures 80 and 86. In the figures, if one compares K'_{am} and K'_{cr} calculated by using the volume fraction crystallinity from the x-ray method with those calculated from the DSC method, the former underestimated K'_{cr} and overestimated K'_{am}, which is predicted from the crystallinity change with temperature as shown in Figure 2.

This indicates the specification of the proper degree of crystallinity is very important for the evaluation of the amorphous and crystalline contributions to total strain optical coefficient, K'_{am} and K'_{cr}.

Results and Discussion.

Measurements were carried out with films subjected to a static elongation of 10% and with a dynamic amplitude of strain of approximately 1%. As with the dynamic x-ray measurements, the samples were vibrated for one hour or more prior to measurement to assure steady-state conditions.

Figures 78 - 83 show the temperature dependencies of the in-phase strain optical coefficient, K' and $\tan\delta_B$, at particular frequencies for the Q-samples and also show the amorphous and crystalline contributions to the total in-phase strain optical coefficient, K'_{cr} and K'_{am}, at lower frequencies than 1.8 Hz. The following observations were made in the figures:

1. With increasing temperature, K' and K'_{cr} decreased and K'_{am} increased in the measured frequency region.

2. The contribution of the amorphous part to the in-phase strain optical coefficient was lower at low temperature than that of the crystalline part, but became larger at high temperature.

3. $\mathrm{Tan}\delta_B$ had two peaks at about 40 and 80°C at a frequency of 0.12 Hz. With increasing frequency, the lower temperature peak shifted to a higher temperature and its magnitude increased. Both the peak position and magnitude of the higher temperature peak may be almost independent of the frequency, although it became harder to resolve the higher temperature peak because of the overlap of the intense lower temperature peak with increasing frequency.

The decrease in K'_{cr} principally arises from the decrease of the crystallinity with increasing temperature, for which the contribution to the total decrease in K'_{cr} is estimated to be 60% at a frequency of 1 Hz. The rest of the contribution comes from the change in C' with temperature. The increase in K'_{am} also arises from the decrease of the crystallinity, that is, the increase of the volume fraction of amorphous part. The contribution of crystallinity change to the increase in K'_{am} is almost 100% or more at a frequency of 1 Hz. This means that the contribution of the amorphous chain itself may be constant or slightly decrease with temperature, which will be shown later (Figure 101). The lower temperature peak of $\tan\delta_B$ may be associated with the α_2 deformation mechanism discussed previously. On the other hand, the origin of the higher temperature peak of $\tan\delta_B$ is hard to understand because of a small amount of data. However, one can guess that this peak may be associated with the recrystallization or rearrangement of crystallites with a quite low perfectness. At a temperature of 80°C, the crystallinity change with temperature shows a plateau in Figure 2 and the (100) plane spacing change with temperature also had a different slope from that of the lower temperature part.

Figure 90 shows the temperature dependence of the total static birefringence Δ and the contributions of amorphous and crystalline parts to the static birefringence, Δ_{cr} and Δ_{am}. It was observed that Δ and Δ_{cr} decreased with increasing temperature and that Δ_{am}

was constant with temperature. The decrease of Δ with increasing temperature may originate from a mechanism such as the slippage of amorphous chains that do not contribute to the orientation or from the decrease of Δ^{o}_{cr} with temperature. Because f^{o}_{c} was constant with temperature, as shown in Figure 45, and the intrinsic birefringence of the amorphous part, Δ^{o}_{am}, is comparable with or larger than the intrinsic birefringence of the crystalline part, Δ^{o}_{cr}, which will be shown in Table IV and Equation (116), then the effect of the crystallinity change on Δ is very small or acts to increase Δ with increasing temperature.

For H-samples, on the other hand, the temperature dependencies of the in-phase part of the total strain optical coefficient, K', the crystalline and amorphous parts of the in-phase strain optical coefficients, K'_{cr} and K'_{am}, the static birefringence Δ, and the crystalline and amorphous parts of static birefringence Δ_{cr} and Δ_{am}, are shown in Figures 84 - 89 and 91. The following was observed in the figures.

1. K' was always positive and showed a maximum at a temperature of 55°C at 1.0 Hz., which shifted to higher temperature with increasing frequency.

2. $\tan\delta_{B}$ was positive and showed a maximum at about 70°C at 1.0 Hz. and also showed a minimum at the temperature where K' showed a maximum.

3. K'_{cr} was negative at low temperature and increased with increasing temperature and then became positive at high temperature after which it decreased with increasing temperature.

4. Δ, Δ_{cr} and Δ_{am} were positive and gradually decreased with increasing temperature. Δ_{cr} was larger than Δ_{am}.

Comparing the curves for the H-samples with those for the Q-samples, the contribution of K'_{am} to K' for H-samples was much larger, especially in the low temperature region, but was similar to those for the Q-samples at the higher temperature. K'_{cr} for H-samples was quite different from that for Q-samples, being negative at low temperatures. The contribution of K'_{cr} to K' was smaller than that of K'_{am} for H-samples even at the high temperature, as predicted from the dynamic x-ray data. This may be due to the nature of the superstructure of crystallites such as spherulites, in other words being due to the difference of the deformation mechanism between the Q- and H-samples. It obviously follows that for the dynamic deformation, the amorphous contribution to the strain optical coefficient for H-samples was larger than the crystalline contribution. The contribution of Δ_{am} to the total static birefringence, Δ, for H-samples was larger compared with that for Q-samples, although Δ_{am} was smaller than Δ_{cr}.

Figures 92 - 95 show the temperature dependence of the static birefringence, Δ, and the crystalline and amorphous contributions to the static birefringence, Δ_{cr} and Δ_{am}, for irradiated samples.

Figures 96 - 99 show the temperature dependence of the in-phase strain optical coefficient, K', and the crystalline and amorphous contributions to the in-phase strain optical coefficient, K'_{cr} and K'_{am}, at 1 Hz. for irradiated samples. The following was observed in the figures:

1. For the Q-series, Δ and Δ_{cr} increased with increasing the dose of irradiation. On the other hand, Δ_{am} decreased, as shown in Figures 90, 92, and 93. Δ_{am} for Q-I-30 samples was negative, but the magnitude was negligibly small. This indicates that the total static birefringence almost entirely originated from the crystalline part.

2. For the H-series, Δ and Δ_{cr} increased with increasing the dose of irradiation, but the change was rather small and Δ_{am} was almost constant with the dose of irradiation.

This may be due to the different nature of both amorphous and crystalline regions between Q- and H-samples. That is, the irradiation may be effective on the α_2 deformation mechanism very much, but slightly on the α_1 deformation mechanism. This may mean that the crosslinking by the β-ray irradiation may prevent local slippage of the amorphous chains. This process may not result to urge the orientation of crystallites for α_1 deformation mechanism but for α_2 deformation mechanism.

3. For Q-series samples, K' and K'_{cr} increased with increasing the dose of irradiation and K'_{am} was constant and the change of $\tan\delta_B$ with temperature decreased.

4. For H-series samples, K'_{cr} shows the tendency to increase with irradiation but the effect is small. $\tan\delta_B$ has no peak at all for irradiated H-samples.

Observations (3) and (4) may also be due to the same reason as the explanation in the static birefringence case as described in the last paragraph. Thus the irradiation is more effective in changing the strain optical coefficient for Q-samples than that for H-samples.

Figure 100 shows the frequency dependence of K' at several temperatures for Q-samples, which has an advantage in that it is not necessary to take into account the crystallinity change. This indicates that K' increases with increasing frequency, as predicted in the temperature dependence curves of K' at several frequencies. This tendency was larger at the lower temperature.

Figure 101 shows the master curve of K' for Q-samples obtained from the superposition by both vertical and horizontal shifts to the reference temperature of 50°C and also shows the master curves of K'_{cr} and K'_{am} for Q-samples in the same figure. The master curve of K'_{cr} was obtained from both master curves of C'_{110} and C'_{200} (Figures 67 and 68) and that of K'_{am} was obtained by subtraction of K'_{cr} from K'. In the figure, K', K'_{cr} and K'_{am} showed quite similar dependencies upon the frequency; that is, these increased with increasing frequency but these changes were very small at the low frequency. The contribution of K'_{cr} and K'_{am} to K' were almost the same. This fact may not contradict the explanation in terms of the floating rod-like model.

Figure 102 shows the logarithm of the horizontal shift factor, o_T, and the vertical shift value, P^*_T, which were necessary to get the smooth master curve of K' versus reciprocal absolute temperature. The activation energy is also shown in the same figure, which was calculated by the equation

$$H^+ = 2.303R\,\frac{d(\log o_T)}{d(1/T)} \qquad (111)$$

The calculated activation energies for Q-samples were 21 kcal/mole at the low temperature and 41 kcal/mole at the high temperature.

Figure 103 shows the frequency dependence of K' for H-samples at several temperatures. Figure 104 shows the master curve of K' for H-samples obtained from the superposition by both horizontal and vertical shifts and also shows those of K'_{cr} and K'_{am}. The master curve of K'_{cr} was obtained from the master curves of C'_{110} and C'_{200} for H-samples (Figure 70). In the figure, K' shows a maximum at about 0.5 Hz. and K'_{am} slightly increases with increasing frequency at lower frequency (10^{-3} Hz.) and more rapidly increases at intermediate frequency (in the vicinity of 5×10^{-2} Hz.) and reaches the equilibrium at 1 Hz. The value of K'_{cr} is negative in higher frequency regions and it increases with decreasing frequency and becomes positive in lower frequency regions than 1 Hz. at the reference temperature of 50°C. The contribution of K'_{am} to K' was much larger than that of K'_{cr}, especially at high frequencies. These

facts suggest that the deformation of the superstructure such as spherulites is an important mechanism as mentioned in a previous section.

Figure 105 shows the plots of the horizontal shift factor, o_T, and vertical shift value, P^*_T, versus the reciprocal absolute temperature, together with activation energies calculated by Equation (111). The activation energies obtained were 21 kcal/mole at lower temperatures and 34 kcal/mole at higher temperatures. These values at somewhat arbitrary because of the ambiguity of separating the vertical shift from the horizontal shift. Therefore, it seems that it is not proper to discuss here the activation energy obtained from the shift factors of the in-phase strain optical coefficient, but it is interesting that the values of activation energies were between 20 and 50 kcal/mole, which are the estimated activation energies for the α_1 and α_2 processes, and also that the activation energy for Q-samples was higher than that for H-samples at a higher temperature, indicating that the deformation of Q-samples may include more α_2 mechanisms than that for H-samples.

There have been a few discussions about the vertical shift by Nagamatsu, et al. (62,63), by Penn (22) and by Onogi, et al. (64) Nagamatsu, et al. (62,63), related the vertical shift factor of the stress relaxation data, b_T, to the degree of crystallinity, λ, by

$$\log b_T = \log \frac{\lambda}{1 - \lambda} \cdot \frac{1 - \lambda_o}{\lambda_o} \qquad (112)$$

where λ_o and λ are, respectively, the degree of crystallinity at the reference temperature, T_o, and arbitrary temperature, T. On the other hand, S. Onogi, et al. (64), related the vertical shift factor of relaxation modulus, b_T, to the mobility of molecular chains as determined by NMR technique M by

$$\log b_T = \log \frac{1 - M}{M} \cdot \frac{M_o}{1 - M_o} \tag{113}$$

where M_o and M are, respectively, the mobility of molecular chains at the reference temperature, T_o, and arbitrary temperature, T. Penn (22) explained the vertical shift factor of relaxation modulus as being due to premelting or softening of crystal boundaries. However, such irreversible deformation processes may not affect the in-phase strain optical coefficient in the linear region. It seems that the vertical shift for K' is due to the strain optical coefficient containing contributions from two or more different kinds of deformation mechanisms; contributions which may vary with temperature. This may be related to the degree of crystallinity and the mobility of molecular chains.

C' is related only to the degree of the average orientation of crystallites, and, on the other hand, K' is related to the degree of orientation of both amorphous and crystalline parts and also to the crystallinity. Therefore, in order to get the smooth master curve of K', it is necessary to make a vertical shift when Δ^o_{am} or Δ^o_{cr} depends

upon temperature, or the degree of crystallinity varies with temperature and K' contains contributions from both the amorphous and crystalline parts with different values of the intrinsic birefringence, even if Δ^{o}_{am} and Δ^{o}_{cr} are constant with temperature. Both may be the reason why a vertical shift is required for K' but not for C'.

K'_{am} is expressed as

$$K'_{am} = (1 - X_c)\, \Delta^{o}_{am}\, f'_{am} \qquad (114)$$

also Δ^{o}_{am} for polyethylene can be expressed by (65,66)

$$\Delta^{o}_{am} = \frac{2}{9}\, \frac{(n^2 + 2)^2}{n}\, N_{CH_2} \cdot (\alpha_{||} - \alpha_{\perp})_{CH_2} \qquad (115)$$

where n is the average refractive index (1.50), N_{CH_2} is the number of methylene units ($-CH_2-$) per unit volume (3.4×10^{22} cm^{-3}), and $(\alpha_{||} - \alpha_{\perp})_{CH_2}$ is the difference between polarizabilities of one methylene unit parallel and perpendicular to polymethylene chain, which has been estimated from the summation of bond polarizabilities by Bunn and Daubeny (67), Denbigh (68) and Vuks (69), as listed in Table IV. Table IV also lists the intrinsic birefringence calculated from those values.

TABLE IV

Intrinsic Birefringence of Amorphous Part

	$(\alpha_{\|\|} \quad \alpha_{\perp})_{CH_2}$	Δ^o_{am}
Case I by Bunn and Daubeny	1.5×10^{-25}	4.27×10^{-2}
Case II by Denbigh	7.2×10^{-25}	2.05×10^{-1}
Case III by Vuks	6.2×10^{-25}	1.76×10^{-1}

On the other hand, the intrinsic birefringence of crystalline part, Δ^o_{cr}, can be estimated from the data of refractive indices of n-paraffins (67). That is,

$$\Delta^o_{cr} = n_c - \frac{n_a + n_b}{2}$$

$$= 1.575 - \frac{1.514 + 1.519}{2}$$

$$= 0.0585 \qquad (116)$$

Using these Δ^o_{am} and Δ^o_{cr}, the ratio of the orientation function per unit strain of the crystalline part to that of the amorphous part, f'_{cr}/f'_{am}, is expressed by

$$\frac{f'_{cr}}{f'_{am}} = \frac{(1 - X_c)}{X_c} \frac{\Delta^o_{am}}{\Delta^o_{cr}} \cdot \frac{K'_{cr}}{K'_{am}}$$

Figure 106 shows the dependence of the values of f'_{cr}/f'_{am} for cases I, II and III upon the frequency for both Q- and H-samples. In the figure, f'_{cr}/f'_{am} for H-samples decreased with increasing frequency. f'_{cr}/f'_{am} for H-samples was smaller than for Q-samples, indicating that the contribution of the amorphous part to the in-phase orientation function is much higher for Q-samples than that for H-samples.

APPENDIX B

THE COMPUTER PROGRAM FOR THE CALCULATION OF ORIENTATIONAL COMPLIANCES FROM DATA OF DYNAMIC X-RAY DIFFRACTION

1. Name of Program: DXRAY

2. Input:

XLO: the length of a specimen

M: the number of measured azimuthal angles

S1: sector constant of scaler #1 ($0 - \pi$)

S2: sector constant of scaler #2 ($\pi/2 - 3\pi/2$)

S3: sector constant of scaler #3 ($3\pi/2 - 5\pi/2$)

S4: sector constant of scaler #5 ($\pi - 2\pi$)

AMR: the diffracted intensity of the amorphous peak which is the value after the background and incoherent scattering intensities are subtracted

BACK1: the contribution of the background and incoherent intensities to the diffracted intensity of the 110 plane

BACK2: the contribution of the background and incoherent intensities to the diffracted intensity of the 200 plane

AL12: the overlap coefficient, α_{12}

AL13: the overlap coefficient, α_{13}

AL23: the overlap coefficient, α_{23}

AL32: the overlap coefficient, α_{32}

I: the running index for the azimuthal angles

J: the running index for repeated measurements at fixed Bragg angle and azimuthal angle

IPHI(I): the azimuthal angle in degrees

N(I): the number of measurements repeated at a particular azimuthal angle

IT(I,J): the time required in seconds ($\times 10^2$)

N1(I,J): the diffracted intensity accumulated in scaler #1

N2(I,J): the diffracted intensity accumulated in scaler #2

N3(I,J): the diffracted intensity accumulated in scaler #3

N4(I,J): the diffracted intensity accumulated in scaler #4

The last five quantities would be given to the punch tape automatically by using the teletype system. Data of the quantities for the 110 plane should be supplied first and then those for the 200 plane.

3. Output (mainly):

CMPL10: static orientational compliance for the 110 plane, C^{o}_{110}

CMPL11: in-phase orientational compliance for the 110 plane, C'_{110}

CMPL12: out-of-phase orientational compliance for the 110 plane, C''_{110}

TANX1: $\tan\delta_x^{110}$

CMPL20: static orientational compliance for the 200 plane, C_{200}^{o}

CMPL21: in-phase orientational compliance for the 200 plane, $C_{200}^{'}$

CMPL22: out-of-phase orientational compliance for the 200 plane, $C_{200}^{''}$

TANX2: $\tan\delta_x^{200}$

CBO: static orientational compliance for the b axis

CB1: in-phase orientational compliance for the b axis, $C_b^{'}$

CB2: out-of-phase orientational compliance for the b axis, $C_b^{''}$

TANB: $\tan\delta_x^{b}$

CCO: static orientational compliance for the c axis, C_c^{o}

CC1: in-phase orientational compliance for the x axis, $C_c^{'}$

CC2: out-of-phase orientational compliance for the c axis, $C_c^{''}$

TANC: $\tan\delta_x^{c}$

GAMMA: the amplitude for the dynamic strain

The plots of the static diffracted intensity and in-phase and out-of-phase changes of the dynamic diffracted intensities against azimuthal angle for both the 110 and 200 planes and their values are supplied as a table.

COMPUTER PROGRAM.

```
010 PROGRAM DXRAY
015 DIMENSION II(30,5),N1(30,5),N2(30,5),N3(30,5),N4(30,5)
020 DIMENSION IPHI(30),T(30,5),C1(30,5),C2(30,5),C3(30,5),C4(30,
025 DIMENSION N(30)
030 DIMENSION Q0(30),Q1(30),Q2(30),P0(30),P1(30),P2(30)
035 DIMENSION PC0(30),PC1(30),PC2(30),PS0(30),PS1(30),PS2(30)
036 COMMON IPHI(30),A4Z,MIN
045 EQUIVALENCE (II,T)
050 EQUIVALENCE (N1,C1)
055 EQUIVALENCE (N2,C2)
060 EQUIVALENCE (N3,C3)
065 EQUIVALENCE (N4,C4)
070 PRINT 1500
100 READ,XLO,M
110 READ,S1,S2,S3,S4
120 READ,A4B,BACK1,BACK2
130 READ,AL12,AL13,AL23,AL32
140 K=2*M
150 DO 190 I=1,K
160 READ,IPHI(I),N(I)
170 DO 190 J=1,N(I)
180 READ 1300,II(I,J),N1(I,J),N2(I,J),N3(I,J),N4(I,J)
190 CONTINUE
200 DO 410 I=1,K
210 D1=0.0
220 D2=0.0
230 D3=0.0
240 D4=0.0
250 DO 360 J=1,N(I)
260 T(I,J)=II(I,J)/200
270 C1(I,J)=N1(I,J)
280 C2(I,J)=N2(I,J)
290 C3(I,J)=N3(I,J)
300 C4(I,J)=N4(I,J)
310 NJ=J
320 D1=(D1*(NJ-1)+C1(I,J)/T(I,J))/NJ
330 D2=(D2*(NJ-1)+C2(I,J)/T(I,J))/NJ
340 D3=(D3*(NJ-1)+C3(I,J)/T(I,J))/NJ
350 D4=(D4*(NJ-1)+C4(I,J)/T(I,J))/NJ
360 CONTINUE
370 RPHI(I)=FLOAT(IPHI(I))*3.14/180.
380 Q0(I)=(D1*S1+D4*S4)/2.
390 Q1(I)=(D4*S4-D1*S1)*3.14/4.
395 Q1(I)=-Q1(I)
400 Q2(I)=(D3*S3-D2*S2)*3.14/4.
410 CONTINUE
```

```
420 DO 530 I=1,M
430 L=I+M
440 Q0(I)=Q0(I)-BACK1-AM1*AL12
450 Q0(L)=Q0(L)-BACK2-AM2*AL13
460 S=1.-AL23*AL32
470 P0(I)=(Q0(I)-AL23*Q0(L))/S
480 P0(L)=(Q0(L)-AL32*Q0(I))/S
490 P1(I)=(Q1(I)-AL23*Q1(L))/S
500 P1(L)=(Q1(L)-AL32*Q1(I))/S
510 P2(I)=(Q2(I)-AL23*Q2(L))/S
520 P2(L)=(Q2(L)-AL32*Q2(I))/S
530 CONTINUE
540 DO 610 I=1,K
550 PC0(I)=COSF(RPHI(I))*P0(I)
560 PC1(I)=COSF(RPHI(I))*P1(I)
570 PC2(I)=COSF(RPHI(I))*P2(I)
580 PS0(I)=PC0(I)*SINF(RPHI(I))**2
590 PS1(I)=PC1(I)*SINF(RPHI(I))**2
600 PS2(I)=PC2(I)*SINF(RPHI(I))**2
610 CONTINUE
620 X1=0.0
630 X2=0.0
640 X3=0.0
650 X4=0.0
660 X5=0.0
670 X6=0.0
680 Y1=0.0
690 Y2=0.0
700 Y3=0.0
710 Y4=0.0
720 Y5=0.0
730 Y6=0.0
740 DO 820 I=1,M-1
750 RK=RPHI(I+1)-RPHI(I)
760 X1=X1+RK*(PC0(I)+PC0(I+1))/2.
770 X2=X2+RK*(PS0(I)+PS0(I+1))/2.
780 X3=X3+RK*(PC1(I)+PC1(I+1))/2.
790 X4=X4+RK*(PS1(I)+PS1(I+1))/2.
800 X5=X5+RK*(PC2(I)+PC2(I+1))/2.
810 X6=X6+RK*(PS2(I)+PS2(I+1))/2.
820 CONTINUE
830 DO 910 I=M+1,K-1
840 RK=RPHI(I+1)-RPHI(I)
850 Y1=Y1+RK*(PC0(I)+PC0(I+1))/2.
860 Y2=Y2+RK*(PS0(I)+PS0(I+1))/2.
870 Y3=Y3+RK*(PC1(I)+PC1(I+1))/2.
880 Y4=Y4+RK*(PS1(I)+PS1(I+1))/2.
890 Y5=Y5+RK*(PC2(I)+PC2(I+1))/2.
900 Y6=Y6+RK*(PS2(I)+PS2(I+1))/2.
910 CONTINUE
```

```
920 GAMMA=0.04/XL0
930 CMPL10=(3.*X2/X1-1.)/2./GAMMA
940 CMPL11=1.5*X2/X1*(X4/X2-X3/X1)/GAMMA
950 CMPL12=1.5*X2/X1*(X6/X2-X5/X1)/GAMMA
960 TANX1=CMPL12/CMPL11
970 CMPL20=(3.*Y2/Y1-1.)/2./GAMMA
980 CMPL21=1.5*Y2/Y1*(Y4/Y2-Y3/Y1)/GAMMA
990 CMPL22=1.5*Y2/Y1*(Y6/Y2-Y5/Y1)/GAMMA
1000 TANX2=CMPL22/CMPL21
1001 CB0=1.447*CMPL10-0.446*CMPL20
1002 CB1=1.447*CMPL11-0.446*CMPL21
1003 CB2=1.447*CMPL12-0.446*CMPL22
1004 CC0=-CB0-CMPL20
1005 CC1=-CB1-CMPL21
1006 CC2=-CB2-CMPL22
1007 TANB=CB2/CB1
1008 TANC=CC2/CC1
1009 PRINT 1012,CMPL10,CMPL11,CMPL12,TANX1,CMPL20,CMPL21,CMPL22,
1010XTANX2,CB0,CB1,CB2,TANB,CC0,CC1,CC2,TANC
1012 FORMAT(16X,*S.O.C.*,4X,*I.P.O.C.*,4X,*O.P.O.C.*,6X,
1013X*TAN X*,/,1X,*110 PLANE*,4(E11.3,2X),/,
1014X1X,*200 PLANE*,4(E11.3,2X),/,4X,*B AXIS*,4(E11.3,2X),/,
1015X4X,*C AXIS*,4(E11.3,2X))
1020 PRINT 1505,GAMMA
1030 PRINT 1510
1040 PRINT 1515,CMPL10,CMPL11,CMPL12,TANX1
1050 PRINT 1520
1060 PRINT 1525,X1,X2,X3,X4,X5,X6
1070 PRINT 1400
1080 DO 1130 I=1,M
1090 PRINT 1535,IPHI(I)
1100 PRINT 1540,Q0(I),P0(I),PC0(I),PS0(I)
1110 PRINT 1540,Q1(I),P1(I),PC1(I),PS1(I)
1120 PRINT 1540,Q2(I),P2(I),PC2(I),PS2(I)
1130 CONTINUE
1135 PRINT 1545
1137 PRINT 1510
1140 PRINT 1515,CMPL20,CMPL21,CMPL22,TANX2
1150 PRINT 1520
1160 PRINT 1525,Y1,Y2,Y3,Y4,Y5,Y6
1170 PRINT 1400
1180 DO 1230 I=M+1,K
1190 PRINT 1535,IPHI(I)
1200 PRINT 1540,Q0(I),P0(I),PC0(I),PS0(I)
1210 PRINT 1540,Q1(I),P1(I),PC1(I),PS1(I)
1220 PRINT 1540,Q2(I),P2(I),PC2(I),PS2(I)
1230 CONTINUE
1235 PRINT 1236
1236 FORMAT(/,1X,*110PLANE*,/,3X,*IPHI.VS.P0*)
```

```
1238 MIN=1
1239 MAX=M
1240 CALL GRAPH(IPHI,P0)
1241 PRINT 1242
1242 FORMAT(/,3X,*IPHI.VS.P1*)
1243 CALL GRAPH(IPHI,P1)
1244 PRINT 1245
1245 FORMAT(/,3X,*IPHI.VS.P2*)
1246 CALL GRAPH(IPHI,P2)
1266 PRINT 1267
1267 FORMAT(/,1X,*200PLANE*,/,3X,*IPHI.VS.P0*)
1268 MIN=M+1
1269 MAX=K
1270 CALL GRAPH(IPHI,P0)
1271 PRINT 1242
1273 CALL GRAPH(IPHI,P1)
1274 PRINT 1245
1276 CALL GRAPH(IPHI,P2)
1300 FORMAT(2(I6,2X),I6)
1400 FORMAT(3X,*00*,9X,*P0*,9X,*PC0*,9X,*PS0*,/,
1401X3X,*01*,9X,*P1*,9X,*PC1*,9X,*PS1*,/,
1402X3X,*02*,9X,*P2*,9X,*PC2*,9X,*PS2*)
1446 FORMAT(7IA1)
1500 FORMAT(1X,*RESULT OF DYNAMIC X RAY*)
1505 FORMAT(1X,*GAMMA=*,F4.2,/,3X,*110PLANE*)
1510 FORMAT(11X,*CMPL0*,8X,*CMPL1*,8X,*CMPL2*,8X,*TANX1*)
1515 FORMAT(3X,4(F11.3,2X))
1520 FORMAT(14X,*X1*,11X,*X2*,11X,*X3*,/,14X,*X4*,11X,*X5*,
1521X11X,*X6*)
1525 FORMAT(3X,3(E11.3,2X),/,3X,3(E11.3,2X))
1535 FORMAT(3X,I3)
1540 FORMAT(3X,4(E11.3,2X))
1545 FORMAT(3X,*200PLANE*)
1550 END
1590 SUBROUTINE GRAPH(IX,F)
1592 DIMENSION F(30),NBUFF(72)
1593 DIMENSION IX(30)
1594 COMMON IPHI(30),MAX,MIN
1604 FMAX=F(MIN)
1605 FMIN=F(MIN)
1606 DO 1612 I=MIN,MAX
1607 IF(FMAX.GT.F(I))GO TO 1610
1608 FMAX=F(I)
1609
1610 IF(FMIN.LT.F(I))GO TO 1612
1611 FMIN=F(I)
1612 CONTINUE
```

```
1613 PRINT 1647,FMIN,(FMIN+FMAX)/2.,FMAX
1614 DO 1615 I=1,5
1615 NBUFF(I)=2020202020202020B
1616 DO 1617 I=6,66
1617 NBUFF(I)=1H.
1618 NBUFF(6)=NBUFF(36)=NBUFF(66)=1H+
1619 PRINT 1652,(NBUFF(J),J=1,66)
1620 ILINE=0
1621 DO 1645 I=MIN,MAX
1622 IF(IX(I).NE.ILINE)GO TO 1635
1623 NCOL=(F(I)-FMIN)/(FMAX-FMIN)*60.+6.5
1624 DO 1625 J=1,70
1625 NBUFF(J)=2020202020202020B
1626 IF(ILINE.NE.(ILINE/30)*30)GO TO 1631
1627 NBUFF(6)=1H+
1628 NBUFF(NCOL)=1H*
1629 PRINT 1651,IX(I),(NBUFF(J),J=5,66)
1630 GO TO 1645
1631 NBUFF(6)=1H.
1632 NBUFF(NCOL)=1H*
1633 PRINT 1652,(NBUFF(J),J=1,NCOL)
1634 GO TO 1645
1635 PRINT 1650
1636 ILINE=ILINE+5
1637 GO TO 1622
1645 ILINE=ILINE+5
1646 CONTINUE
1647 FORMAT(5X,E11.3,17X,E11.3,17X,E11.3)
1650 FORMAT(/)
1651 FORMAT(I4,66A1)
1652 FORMAT(72A1)
1680 RETURN
1685 END
1690 ENDPROG
```

CHAPTER V

CONCLUSION AND FUTURE PROBLEM

Conclusion

The observation of the change in the in-phase orientational compliances of particular crystal axes by the dynamic x-ray measurements with temperature and frequency clarified the nature of the deformation mechanism of the crystalline part in the low density polyethylene sample. By combining the dynamic x-ray measurements with the dynamic birefringence measurements, one obtained useful information about the contributions of both the amorphous and crystalline parts to the deformation process in the measured temperature region, which may correspond to the α loss mechanism as observed in the mechanical dynamic modulus, E', the loss modulus, E", and the loss tangent, tanδ.

In the measured temperature region between 30 and 90°C, Q-samples showed quite different behavior from H-samples in the master curves of tanδ, K', C'_a, C'_b and C'_c, in spite of the fact that no appreciable difference was found in the degree of crystallinity as determined by the x-ray method and by density. Also, both samples show spherulitic structure as observed by photographic light scattering patterns. The differences might arise from the size and perfectness of the superstructure such as the spherulite and also from the nature of the amorphous chains.

For Q-samples, the activation energies obtained from mechanical, dynamic x-ray and birefringence data were 36.4, 50 and 41 kcal/mole in the high temperature region and for H-samples, the activation energies are 31.8, 25 and 21 kcal/mole in the low temperature region. These values may correspond to the activation energies of the α_2 loss mechanism for Q-samples and the α_1 loss mechanism for H-samples. Thus, in Q-samples, the α_1 loss mechanism did not appear clearly. This may suggest that the α_1 loss mechanism may be associated with the nature of the superstructure.

The α_2 loss mechanism appears to be associated with the uniaxial orientation of the c axis of crystallites to the stretching direction with no preferable axis orientation between the a and b axes, which is interpreted in terms of the floating rod-type model by Kratky (52).

The α_1 loss deformation mechanism may be interpreted by the combination of a few deformation mechanisms, that is, the deformation of the spherulite from a sphere to an ellipsoid, the tilting process of the c axis in the lamella and the twisting process of the lamella about the b axis. The contributions of the first and second deformation processes were large in the low temperature region and that of the last deformation process was large at the high temperature region.

The contribution of the amorphous part to the strain optical coefficient was larger for H-samples than for Q-samples, that is, larger for the α_1 loss mechanism than for the α_2 loss mechanism, which does not contradict the speculation of the deformation processes for the α_1 and α_2 loss mechanisms.

The results for irradiated samples were quite complicated, but one can conclude that the crosslinking brought from the β-ray irradiation may be more effective for Q-samples than for H-samples, that is, more effective in modifying the α_2 loss mechanism than the α_1 loss mechanism.

Future Problems

a. Rheo-optical quantities must be measured with the well-characterized films which were prepared under well-controlled conditions because rheo-optical properties are quite sensitive to the nature of morphology, especially in the α loss temperature region.

b. In order to get the data for the out-of-phase orientational compliance, C", with reasonably good accuracy, which is helpful to clarify the deformation mechanism in detail, it is necessary to use the x-ray source with high intensity and to accumulate the diffracted intensity for long times so that the statistical fluctuation of the x-ray source itself becomes negligibly small compared with the diffracted intensity change due to C". For this purpose, the construction of a new dynamic x-ray apparatus, equipped with a high intensity x-ray source and an automatical operation, is desired.

c. At the present stage, the contribution of the amorphous peak ($2\theta = 19.0$) to the orientational compliances of the 110 and 200 crystal planes is neglected, but at the higher temperature, this contribution becomes large and was observed to bring the error of about 15% for C'_{200}. Therefore, if more accurate data can be obtained by improvement of the apparatus, the contribution of the amorphous

peak to the orientational compliances of the 110 and 200 crystal planes must be considered, especially for the out-of-phase orientational compliances.

d. The two-phase model consisting of the amorphous and crystalline phases is now used in the evaluation of the amorphous and crystalline contribution to the strain optical coefficient. In the future, however, if more accurate data are accumulated, it might be necessary to consider the other term (like a cross-term) which cannot be represented by a simple addition of the quantities due to the amorphous and crystalline parts. Then, it is desirable to directly observe the motion of the amorphous chain simultaneously for the clarification of the deformation mechanism. This may be provided by the infrared dichroism of a particular band characteristic of the amorphous chain, the visible dichroism of the dye stuff which may attach itself to the amorphous chain, and the fluorescence polarization method.

e. To investigate the relationship between the degree of crystallinity and the α loss deformation mechanism, it is very helpful to use samples such as polyethyleneterephthalate in which one can easily control the degree of crystallinity.

f. The phenomenological approach by the model calculation must be helpful to clarify the deformation mechanism and to get the suggestion of additional experiments. These have been proposed by R. S. Stein, et al. (1,71), and by S. Iwayanagi (12,70). From this

standpoint, the observation of $\tan\delta_x$, that is, the accurate measurement of C" is desired.

g. The measurement of the time dependence of the crystal plane spacing will be interesting, as proposed by H. Kawai, et al. (31)

h. Rheo-optical work will provide the helpful information about the deformation mechanism of the copolymer and blend systems because the deformation of each component can be separately observed.

BIBLIOGRAPHY

1. R. S. Stein, S. Onogi and D. A. Keedy, J. Polymer Sci. 57, 801 (1962).
2. R. S. Stein, S. Onogi, K. Sasaguri and D. A. Keedy, J. Appl. Phys. 34, 80 (1963).
3. K. Sasaguri and R. S. Stein, J. Polymer Sci. C5, 139 (1964).
4. B. E. Read, Polymer 3, 143 (1962).
5. D. G. LeGrand and P. F. Erhardt, Trans. Soc. Rheology 6, 301 (1962).
6. R. Yamada, J. Polymer Chem. (Japan) 20, 97 (1963).
7. R. Yamada, C. Hayashi and S. Onogi, J. Soc. Materials Sci., Japan 12, 812 (1963).
8. R. Yamada, C. Hayashi and S. Onogi, J. Soc. Materials Sci., Japan 13, 117 (1964).
9. D. G. LeGrand and P. F. Erhardt, J. Appl. Phys. 34, 68 (1963).
10. R. S. Stein, J. Polymer Sci. 62, S2 (1962).
11. H. Nakayasu, H. Markovitz and D. J. Plazek, Trans. Soc. Rheology 5, 261 (1961).
12. S. Iwayanagi in SOLID STATE PHYSICS, Vol. 14, F. Seitz and E. Turnbull, Eds., Academic Press, New York, 1963, p. 458.
13. M. Takayanagi, PROC. INTERN. CONGRESS RHEOLOGY, 4TH PROVIDENCE, 1963, Interscience Publishers, New York, Part 1, 1965.
14. M. Takayanagi, T. Aramaki, M. Yoshino and K. Hoashi, J. Polymer Sci. 46, 531 (1960).

15. T. Aramaki, S. Minami. F. Nagatoshi and M. Takayanagi, Report Progress Polymer Physics in Japan 7, 237 (1964).

16. T. Hideshima, Report Progress Polymer Physics in Japan 9, 279 (1966).

17. N. G. McCrum and E. L. Morris, Proc. Royal Soc. (London) A292, 506 (1966).

18. K. H. Illers, Rheologica Acta 3, 202 (1964).

19. K. M. Sinnott, J. Appl. Phys. 37, 3385 (1966); J. Polymer Sci. C, 14, 141 (1966).

20. J. D. Hoffman, G. Williams and E. Passaglia, J. Polymer Sci. C, 14, 173 (1966).

21. C. Nakafuku, K. Minato and T. Takemura, Report Progress Polymer Physics in Japan 11, 297 (1968).

22. R. W. Penn, J. Polymer Sci. A2, 4, 545 (1966).

23. M. Takayanagi and T. Matsuo, J. Macromol. Sci.-Phys. B1(3), 407 (1967).

24. S. Iwayanagi and H. Nakane, Abstr. Int. Cong. Rheol., Kyoto, 1968, p. 40.

25. K. Iohara, K. Imada and M. Takayanagi, "Thermal Expansion of Lattice Constant of Polyethylene Crystal," in press.

26. P. Geil, POLYMER SINGLE CRYSTALS, Interscience Publishers, New York, 1963.

27. M. G. Gubler and A. J. Kovacs, J. Polymer Sci. 34, 551 (1959).

28. R. Chiang and J. Flory, J. Am. Chem. Soc. 83, 2857 (1961).

29. H. Kawai, T. Ito, D. A. Keedy and R. S. Stein, J. Polymer Sci. B, 2, 1075 (1964).

30. T. Ito, T. Oda and H. Kawai, Report Progress Polymer Physics in Japan 11, 191 (1968).

31. T. Ito, T. Oda, H. Kawai, T. Kawaguchi, D. A. Keedy and R. S. Stein, Rev. Sci. Inst. 39, No. 12, 1847 (1968).

32. Y. Fukui, Master's Thesis, Kyoto University, 1967.

33. C. W. Bunn, Trans. Faraday Soc. 35, 482 (1939).

34. J. L. Mathews, H. S. Peiser and R. B. Richards, Acta. Cryst. 2, 85 (1949).

35. P. H. Hermans and A. Weidinger, J. Polymer Sci. 4, 709 (1949).

36. M. Kakudo and R. Ullman, J. Polymer Sci. 45, 91 (1960).

37. E. S. Watson, M. J. O'Neill, J. Justin and N. Brenner, Anal. Chem. 3, 1238 (1964).

38. M. Motegi, T. Oda, M. Moritani and H. Kawai, Polymer J. Japan 1, 209 (1970).

39. R. S. Stein and W. Chu, J. Polymer Sci. A2, 8, 1137 (1970).

40. T. Hashimoto, Ph.D. Thesis, University of Massachusetts, Amherst, 1970.

41. R. S. Stein and M. B. Rhodes, J. Appl. Phys. 31, 1873 (1960).

42. R. S. Stein and C. Picot, J. Polymer Sci., in preparation.

43. C. Picot and R. S. Stein, J. Polymer Sci., in preparation.

44. M. Takayanagi, Pure and Appl. Chem. 15, 555 (1967).

45. J. A. Faucher, Trans. Soc. Rheology 3, 81 (1959).

46. R. S. Stein and P. R. Wilson, ONR Technical Report No. 35, Project: NR 056-378, Contract: Nonr 3357(01), Polymer Research Institute, University of Massachusetts, Amherst, 1960.

47. A. Manabe, A. Sakoda, A. Katada and M. Takayanagi, Mem. Fac. Eng. Kyushu Univ. 28, 279 (1969); J. Macromol. Sci.-Phys. B4(1), 161 (1970).

48. USER'S MANUAL, Research Computing Center, University of Massachusetts, Amherst.

49. J. J. Hermans, P. Hermans, D. Vermaas and A. Weidinger, Rec. Trav. Chim. 65, 427 (1946).

50. C. W. Bunn, Trans. Faraday Soc. 35, 317 (1945).

51. POLYMER HANDBOOK, J. Brandrup and E. H. Immergut, Eds., Interscience Publishers, New York, 1965, p. VI-48.

52. O. Kratky, Kolloid-Z. 64, 213 (1933).

53. P. Erhardt, K. Sasaguri and R. S. Stein, J. Polymer Sci. C5, 179 (1964).

54. S. Onogi, D. A. Keedy and R. S. Stein, J. Polymer Sci. 50, 153 (1961).

55. B. E. Read, Techniques of Polymer Sci., S.C.I. Monograph No. 17 (Society of the Chemical Industry, London), 1963, p. 198.

56. B. E. Read, J. Polymer Sci. C5, 87 (1964).

57. B. E. Read, Polymer 5, 1 (1964).

58. J. F. Rudd, J. Polymer Sci., B, 3, 345 (1956).

59. R. S. Stein, J. Polymer Sci. 31, 327 (1958).

60. R. S. Stein, T. Kawaguchi, I. Kimura and A. Takeuchi, J. Polymer Sci. B, 5, 339 (1967).

61. E. P. Chang, Ph.D. Thesis, University of Massachusetts, Amherst, 1970.

62. K. Nagamatsu, T. Takemura, T. Yoshitomi and T. Takemoto, J. Polymer Sci. 33, 515 (1958).

63. K. Nagamatsu, Kolloid-Z. 172, 141 (1960).

64. S. Onogi, T. Sato, T. Asada and Y. Fukui, J. Polymer Sci., in press.

65. R. S. Stein and F. H. Norris, J. Polymer Sci. 21, 381 (1956).

66. T. Oda, Ph.D. Thesis, Kyoto University, 1969.

67. C. W. Bunn and Rde P. Dandeny, Trans. Faraday Soc. 50, 1173 (1954).

68. K. G. Denbigh, Trans. Faraday Soc. 36, 936 (1940).

69. M. F. Vuks, Optikai Spekroskopiya 2, 494 (1957).

70. S. Iwayanagi and H. Nakane, "Role of the Lamellar Boundary in the Relaxation of Crystalline Polymer," in preparation.

71. I. Kimura, A. Tanaka, E. P. Chang, B. Delf and R. S. Stein, "Rheo-Optical Studies of the Nature of the Alpha Mechanical Loss Mechanism of Polyethylene," in preparation.

72. M. B. Rhodes and R. S. Stein, J. Appl. Phys. 32, 2344 (1961).

73. M. Takayanagi and T. Matsuo, Abstr. Int. Symp. Macromol. (IUPAC), Kyoto, 1966, p. VIII-76.

74. T. Kawaguchi, T. Ito, H. Kawai, D. A. Keedy and R. S. Stein, Macromolecules 1, 126 (1968).

75. M. Dole, W. P. Hettinger, Jr., N. R. Larson and J. A. Wethington, Jr. J. Chem. Phys. 20, 781 (1952).

76. P. H. Hermans and A. Weidinger, Makro. Chem. 44-46, 24 (1961).
77. S. Krimm and A. V. Tobolsky, J. Polymer Sci. 7, 57 (1951).
78. S. L. Aggarwal and G. P. Tilley, J. Polymer Sci. 18, 17 (1955).
79. Bryant, Tordella, Pierce, Jr., paper on the 118th National Meeting of the ACS, Chicago, September, 1950.
80. W. Ruland, Acta. Cryst. 14, 1180 (1961).

CAPTIONS FOR FIGURES

1. The variation of the x-ray diffracted intensity with Bragg angle at 32°C for H-samples.
2. The variation of the degree of crystallinity (weight percent) with temperature for unirradiated samples.
3. The variation of the degree of crystallinity (weight percent) with temperature for Q-series.
4. The variation of the degree of crystallinity (weight percent) with temperature for H-series.
5. The variation of the (100) crystal plane spacing with temperature for unirradiated samples.
6. The variation of the (100) crystal plane spacing with temperature for Q-series.
7. The variation of the (100) crystal plane spacing with temperature for H-series.
8. The variation of the heat capacity in the heating and cooling processes with temperature for unirradiated samples.
9. The variation of the heat capacity in the heating and cooling processes with temperature for Q-series.
10. The variation of the heat capacity in the heating and cooling processes with temperature for H-series.
11. Schematic diagram of the apparatus for photographic light scattering.
12. H_v scattering patterns of unirradiated and irradiated samples at the undeformed state.

26. The variation of tanδ with frequency at several temperatures for H-I-30 samples.

27. The variation of tanδ with reduced frequency for Q-samples. The reference temperature is 50°C.

28. The variation of tanδ with reduced frequency for Q-I-10 samples. The reference temperature is 50°C.

29. The variation of tanδ with reduced frequency for Q-I-30 samples. The reference temperature is 50°C.

30. The variation of tanδ with reduced frequency for H-samples. The reference temperature is 50°C.

31. The variation of tanδ with reduced frequency for H-I-10 samples. The reference temperature is 50°C.

32. The variation of tanδ with reduced frequency for H-I-30 samples. The reference temperature is 50°C.

33. The variation of log a_T with (1/T) for tanδ for Q-samples. The reference temperature is 50°C.

34. The variation of log a_T with (1/T) for tanδ for Q-I-10 samples. The reference temperature is 50°C.

35. The variation of log a_T with (1/T) for tanδ for Q-I-30 samples. The reference temperature is 50°C.

36. The variation of log a_T with (1/T) for tanδ for H-samples. The reference temperature is 50°C.

37. The variation of log a_T with (1/T) for tanδ for H-I-10 samples. The reference temperature is 50°C.

105. The variation of o_T and P^*_T with (1/T) for K' for H-samples. The reference temperature is 50°C.

106. The variation of f'_{cr}/f'_{am} with reduced frequency for Q- and H-samples for different values of Δ^o_{am}. The reference temperature is 50°C.

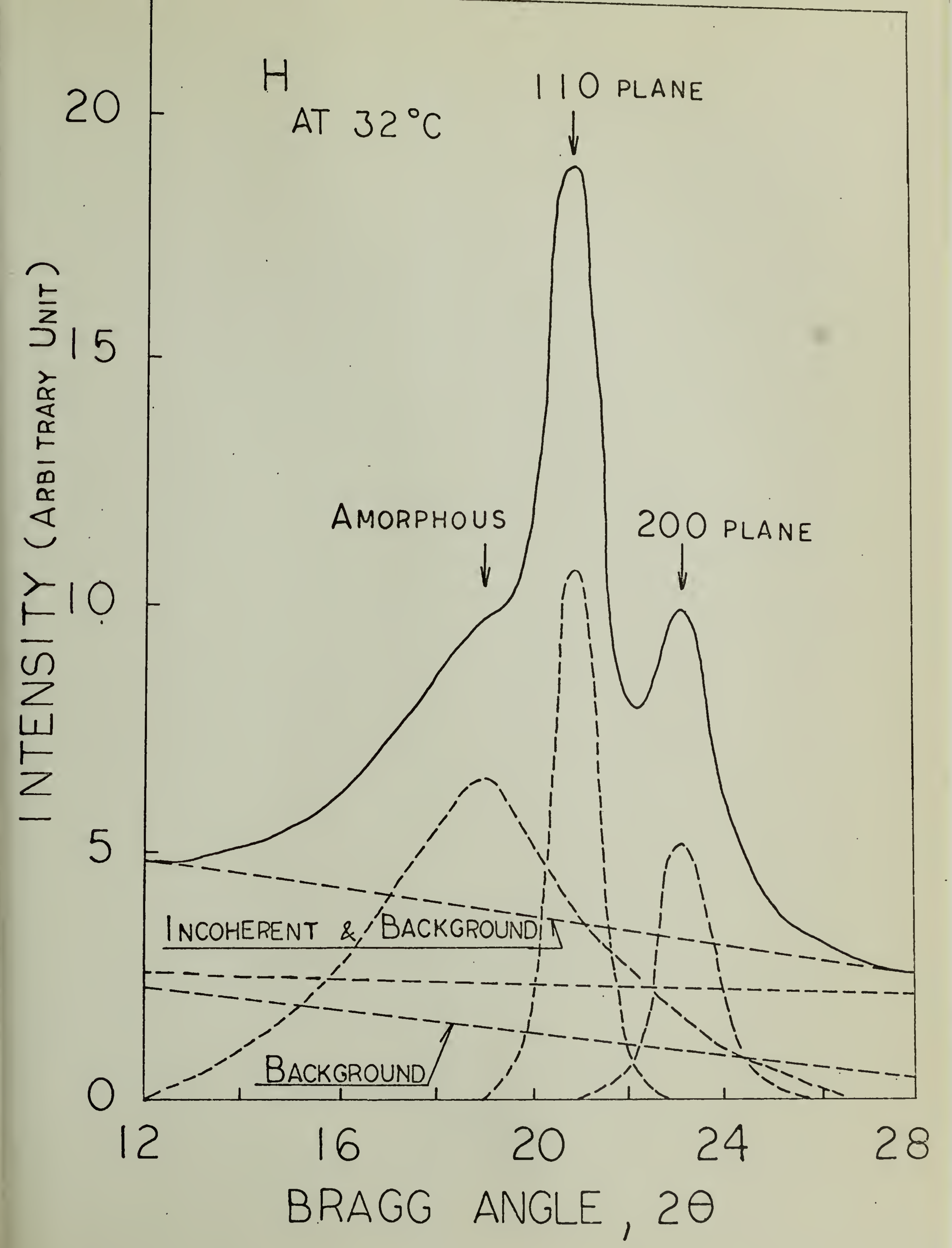
H
AT 32°C
110 PLANE
AMORPHOUS
200 PLANE
INCOHERENT & BACKGROUND
BACKGROUND
INTENSITY (ARBITRARY UNIT)
0
5
10
15
20
12
16
20
24
28
BRAGG ANGLE, 2θ

FIG 1

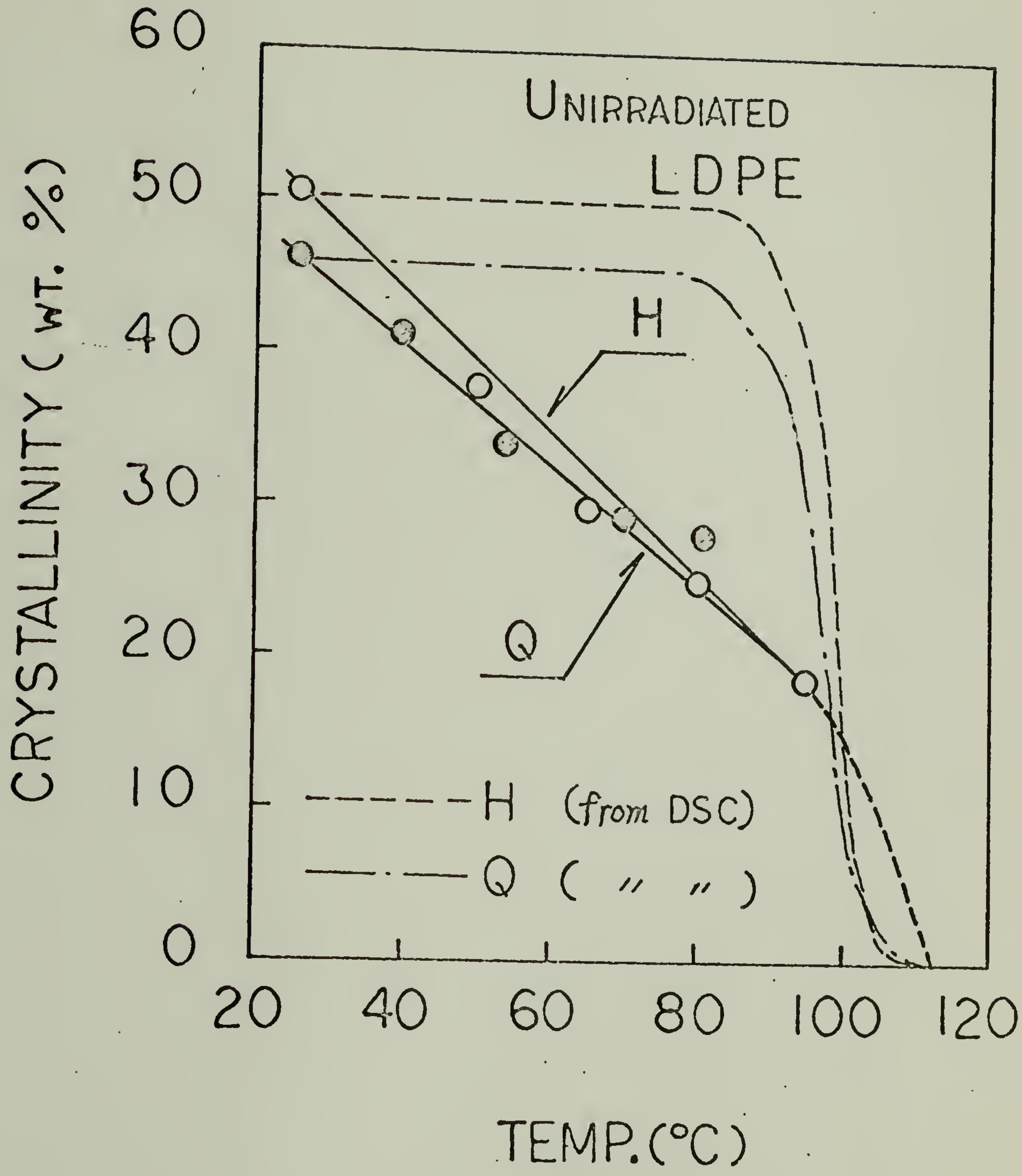
UNIRRADIATED
LDPE
H
Q
------H (from DSC)
—·—Q (" ")
CRYSTALLINITY (WT. %)
0
10
20
30
40
50
60
20
40
60
80
100
120
TEMP. (°C)

FIG. 2

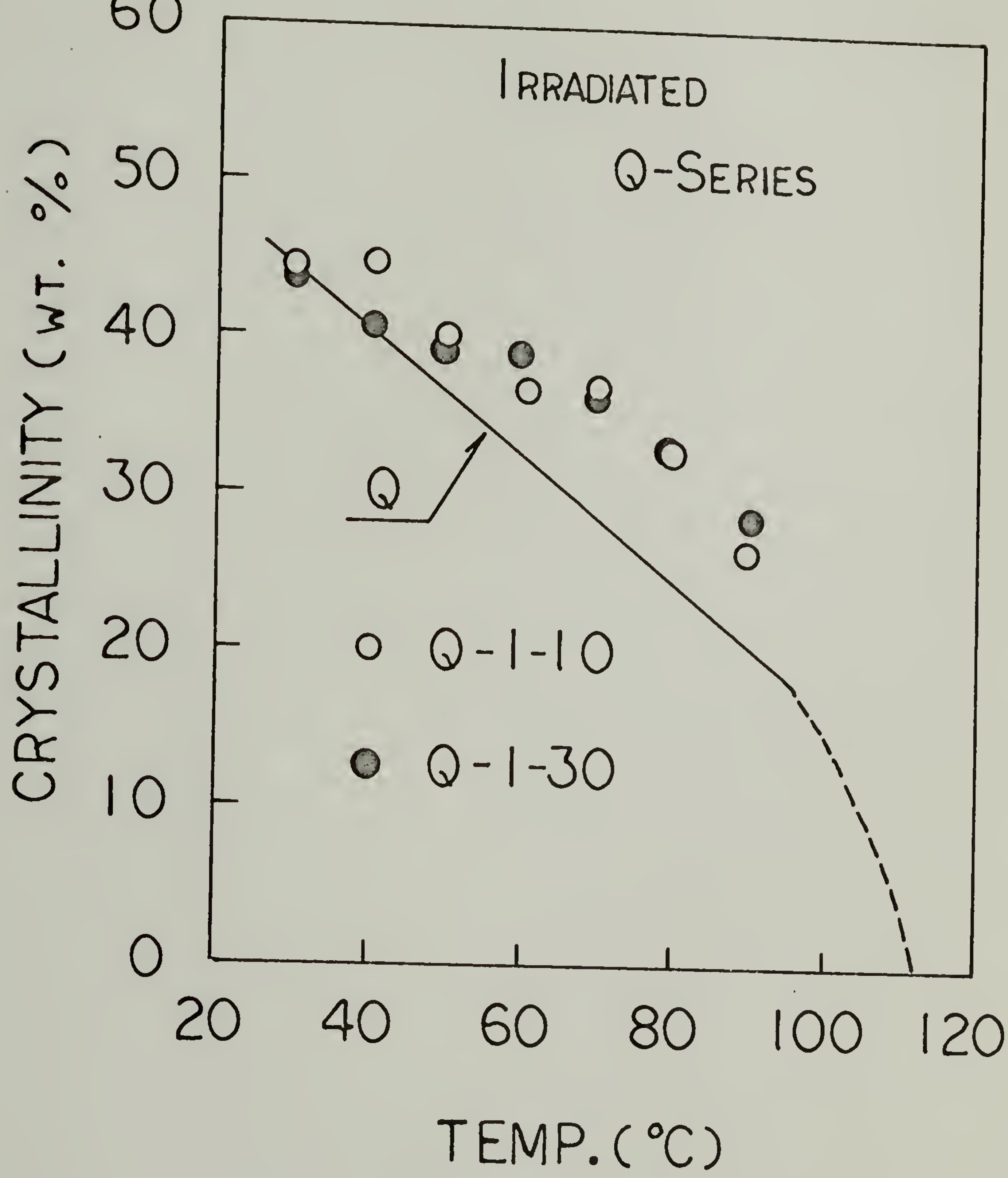
IRRADIATED
Q-SERIES
Q
○ Q-1-10
● Q-1-30
CRYSTALLINITY (WT. %)
0
10
20
30
40
50
60
20
40
60
80
100
120
TEMP. (°C)

FIG. 3

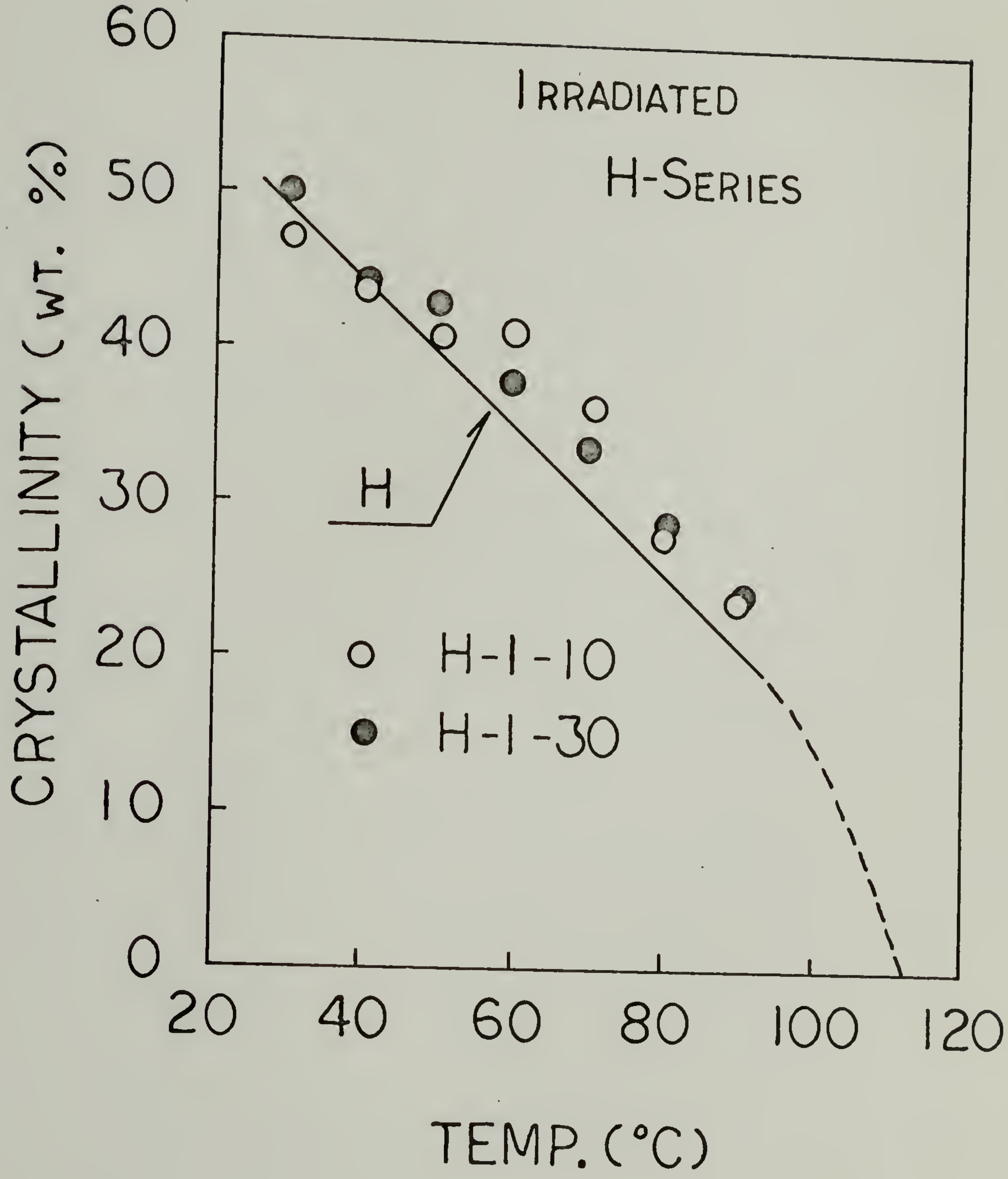
IRRADIATED
H-SERIES
H
○ H-1-10
● H-1-30
CRYSTALLINITY (WT. %)
60
50
40
30
20
10
0
20
40
60
80
100
120
TEMP. (°C)

FIG. 4

UNIRRADIATED
LDPE

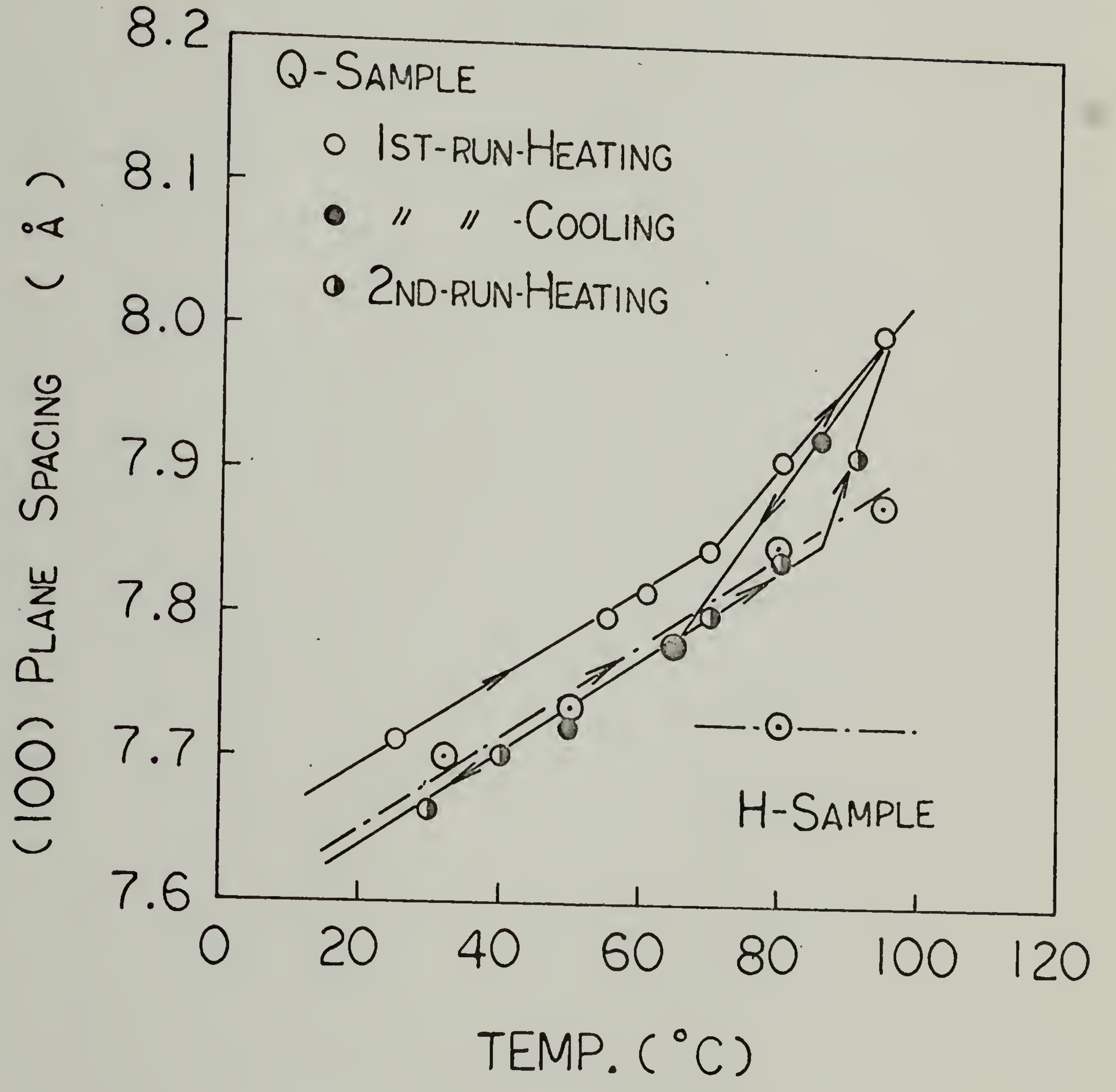

FIG. 5

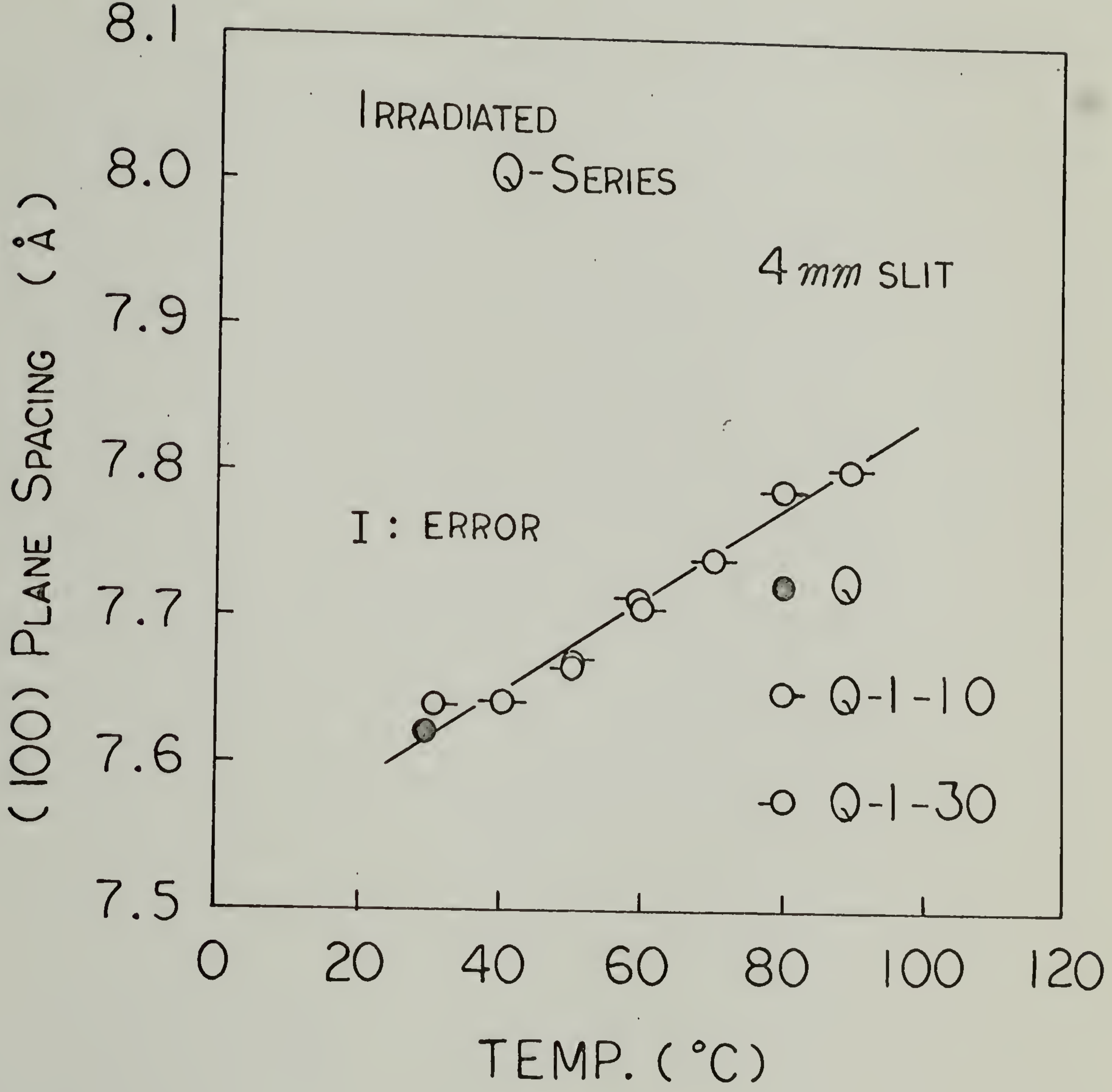
IRRADIATED
Q-SERIES
4 mm SLIT
I : ERROR
● Q
-○- Q-1-10
-○ Q-1-30
(100) PLANE SPACING (Å)
8.1
8.0
7.9
7.8
7.7
7.6
7.5
0
20
40
60
80
100
120
TEMP. (°C)

FIG. 6

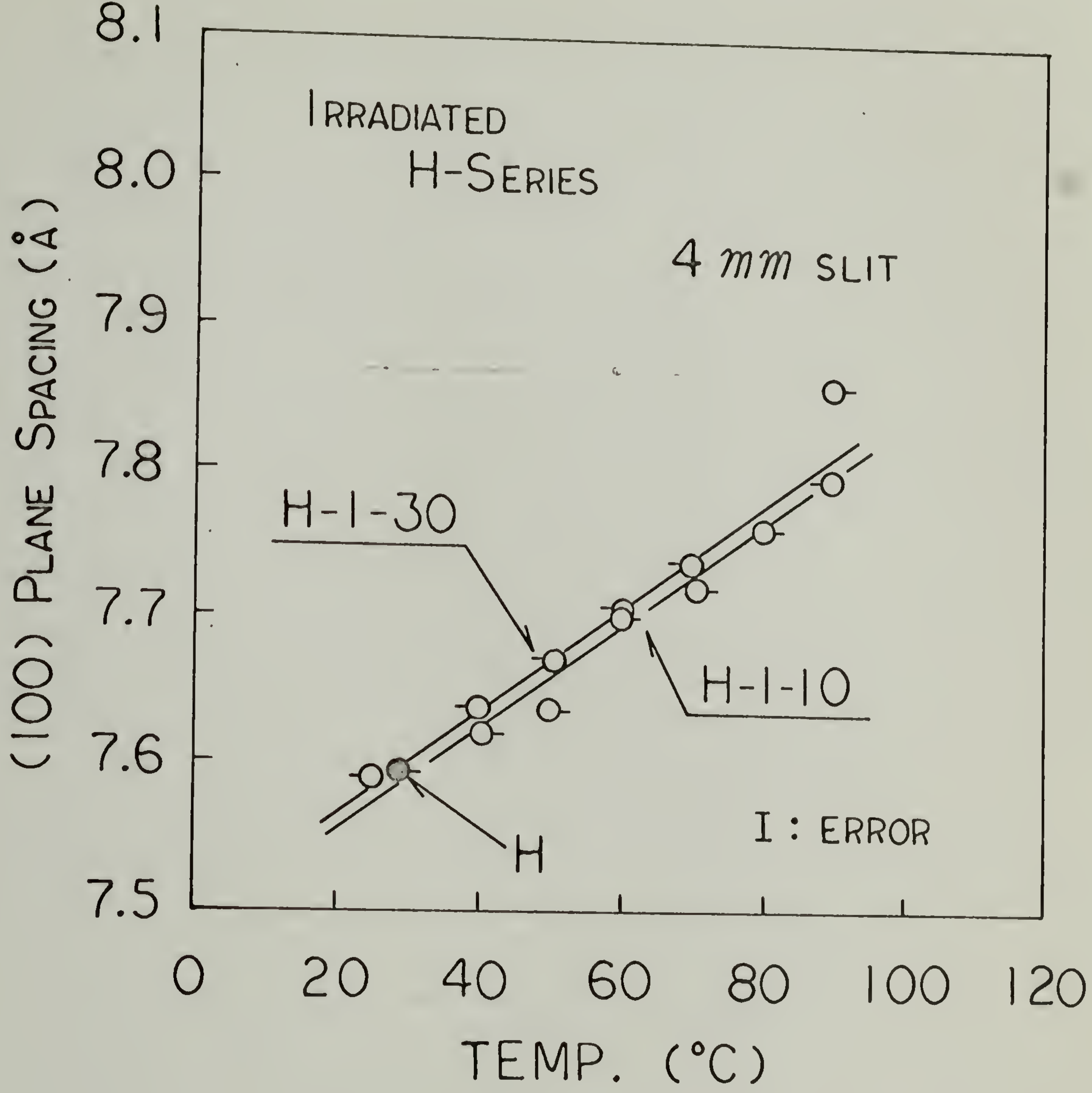
8.1
8.0
7.9
7.8
7.7
7.6
7.5
(100) Plane Spacing (Å)
0
20
40
60
80
100
120
TEMP. (°C)
Irradiated
H-Series
4 mm slit
H-1-30
H-1-10
H
I : ERROR

FIG. 7

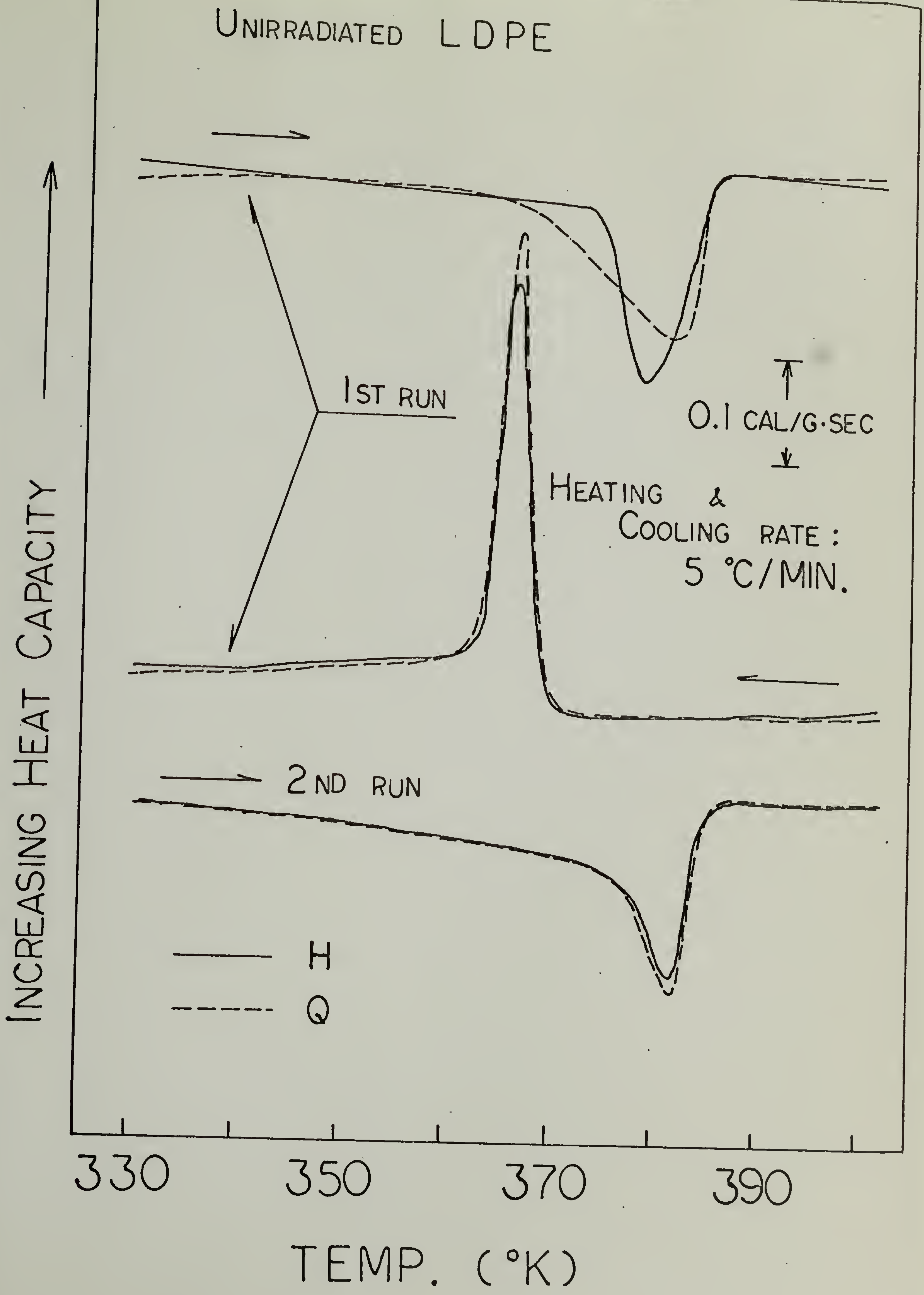
UNIRRADIATED LDPE
1ST RUN
2ND RUN
0.1 CAL/G·SEC
HEATING & COOLING RATE: 5 °C/MIN.
H
Q
INCREASING HEAT CAPACITY
330
350
370
390
TEMP. (°K)

FIG. 8

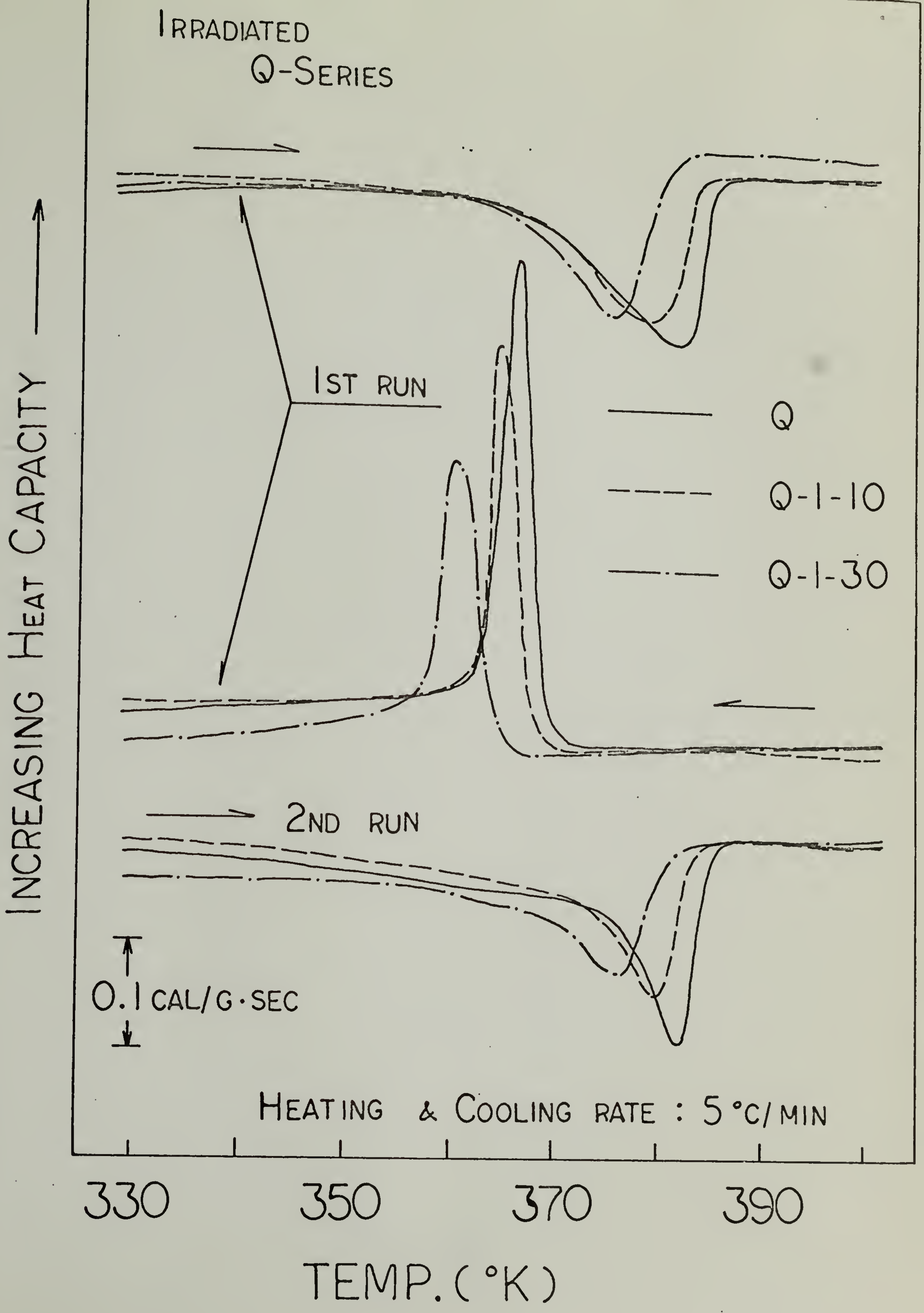
IRRADIATED
Q-SERIES
INCREASING HEAT CAPACITY
1ST RUN
2ND RUN
Q
Q-1-10
Q-1-30
0.1 CAL/G·SEC
HEATING & COOLING RATE : 5 °C/MIN
330
350
370
390
TEMP. (°K)

FIG. 9

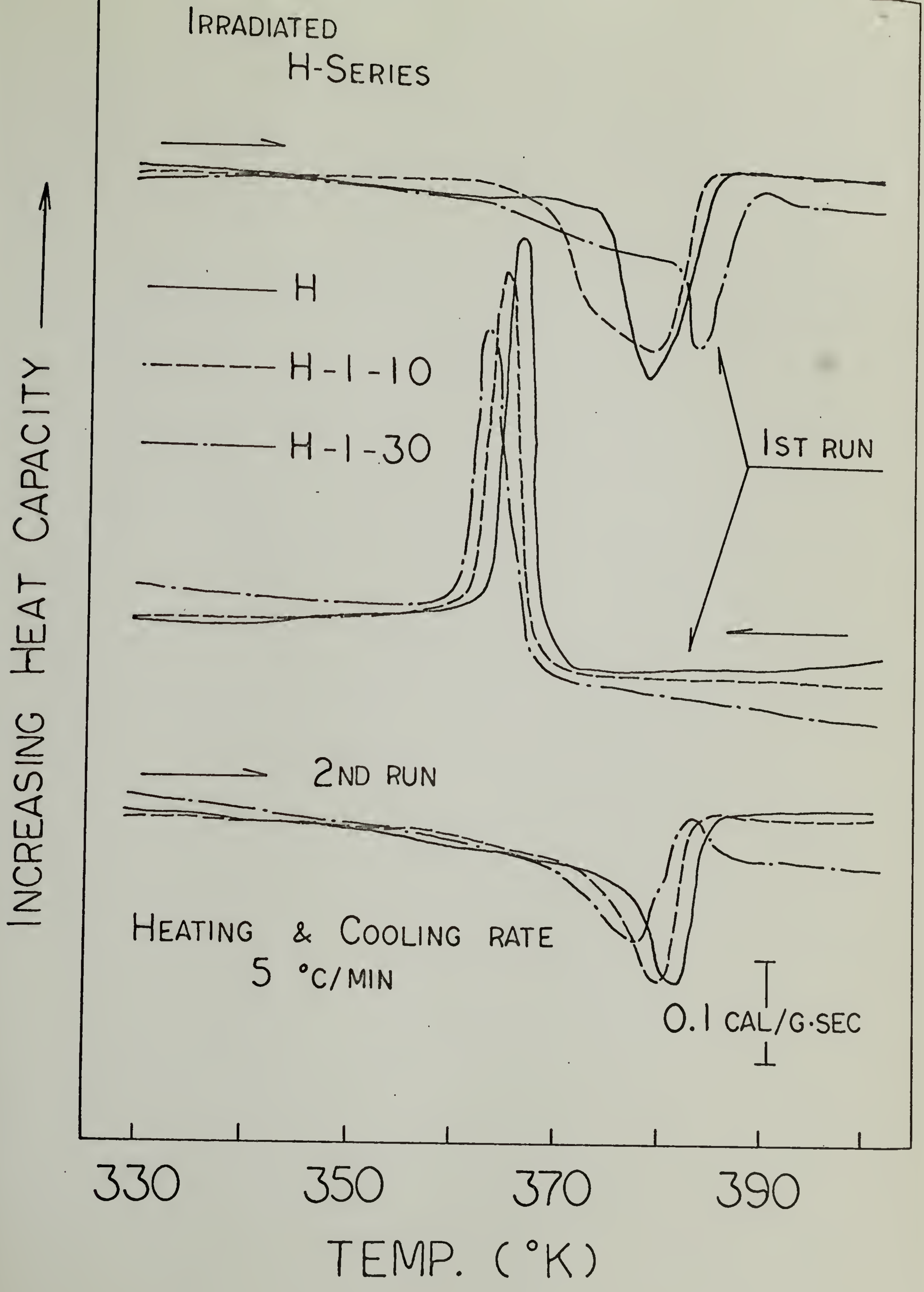
IRRADIATED
H-SERIES
H
H-1-10
H-1-30
1ST RUN
2ND RUN
HEATING & COOLING RATE
5 °C/MIN
0.1 CAL/G·SEC
INCREASING HEAT CAPACITY
330
350
370
390
TEMP. (°K)

FIG. 10

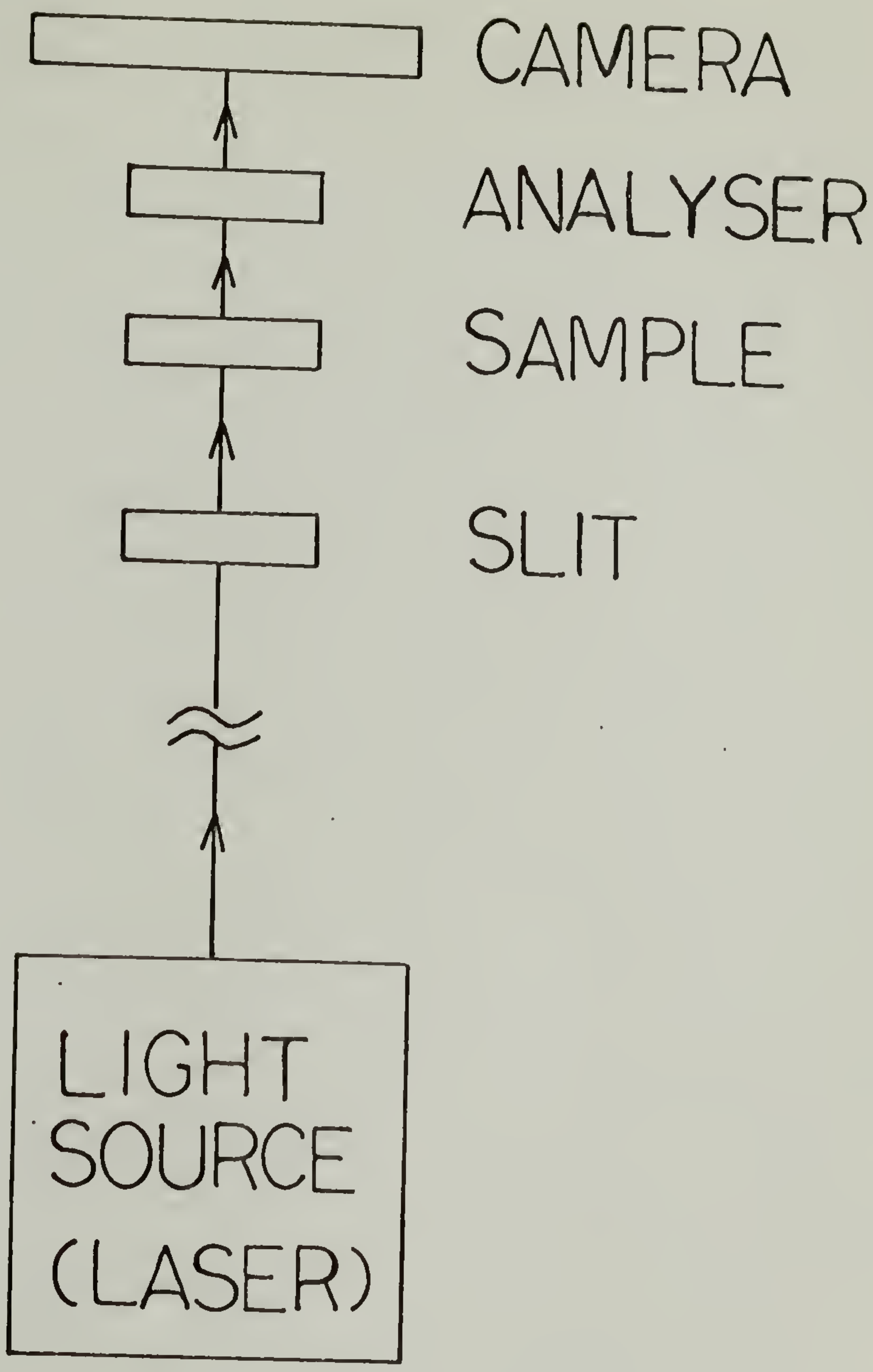

APPARATUS FOR PHOTOGRAPHIC LIGHT SCATTERING

FIG. 11

Hv Patterns Of Undeformed Samples

Q (20.2 *mil*)

H (20.1 *mil*)

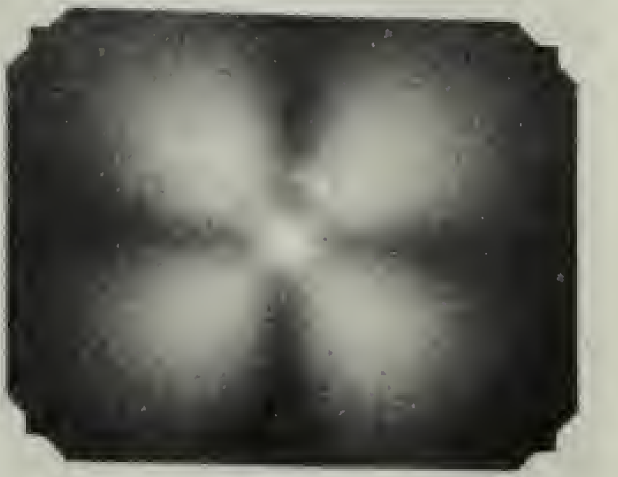

Q-1-10 (21.1 *mil*)

H-1-10 (20.2 *mil*)

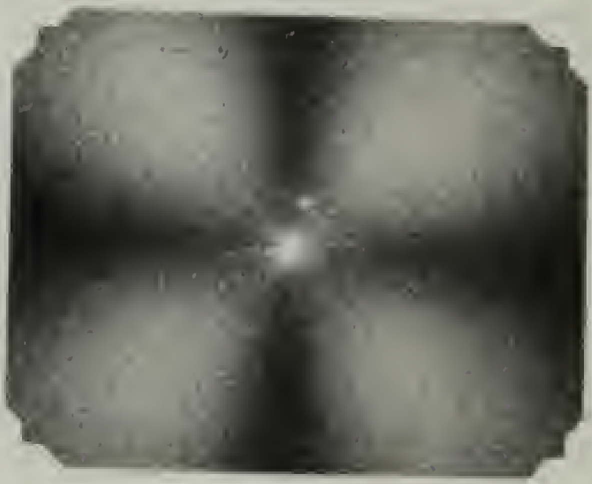

Q-1-30 (20.7 *mil*)

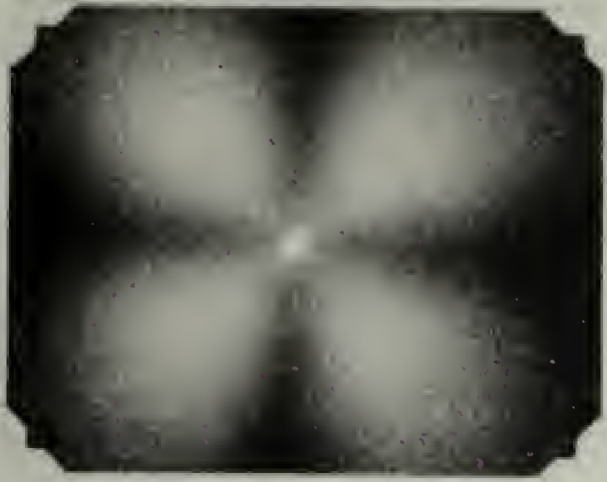

H-1-30 (22.4 *mil*)

FIG. 12

Hv PATTERNS OF STRETCHED SAMPLES

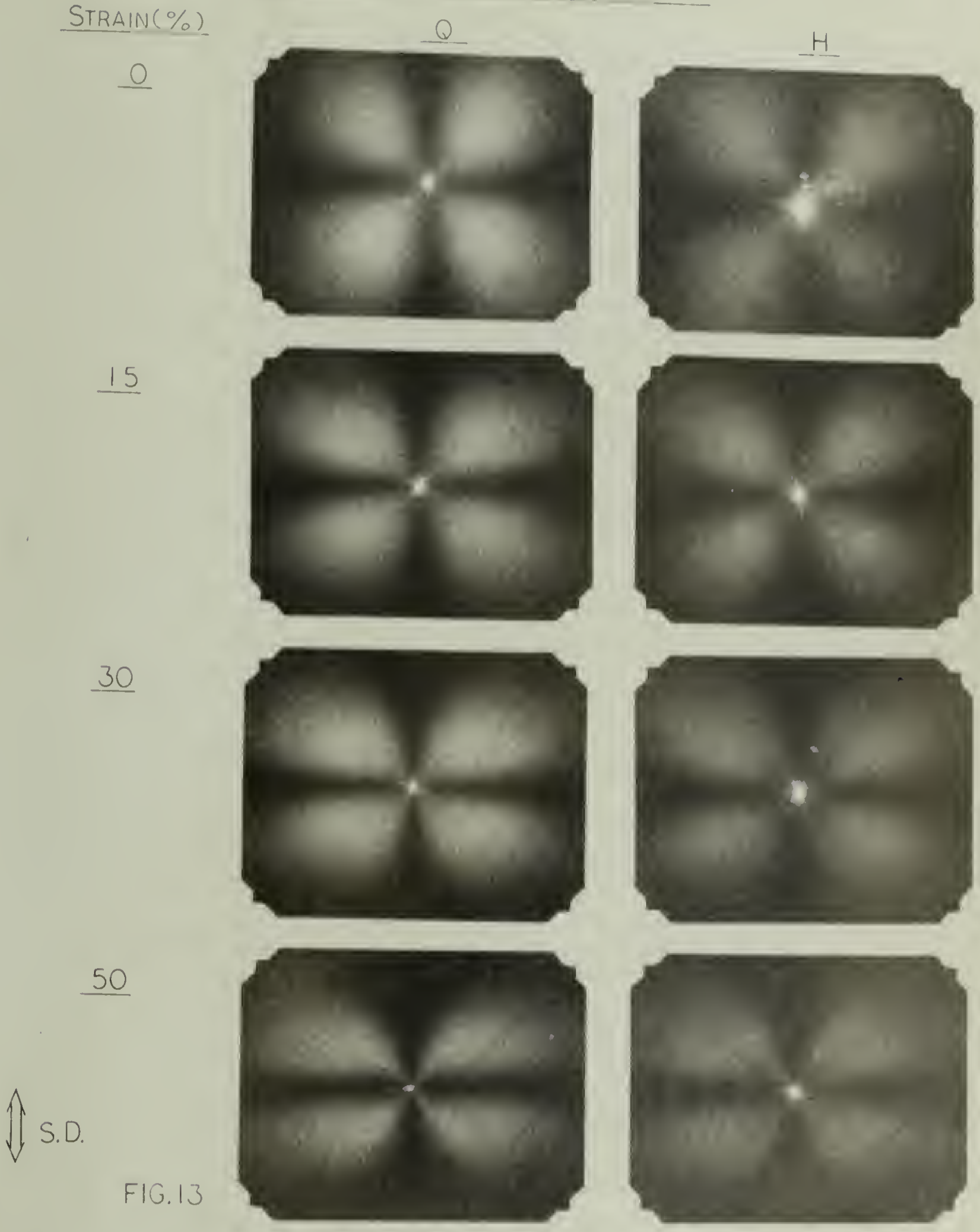

FIG. 13

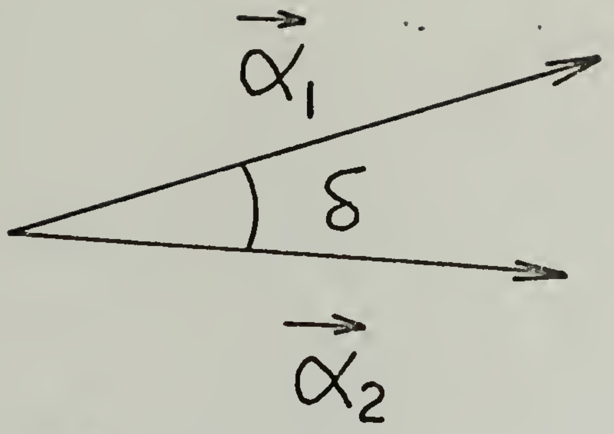

$\vec{\alpha}_1$: STRESS

$\vec{\alpha}_2$: STRAIN

FIG. 14A

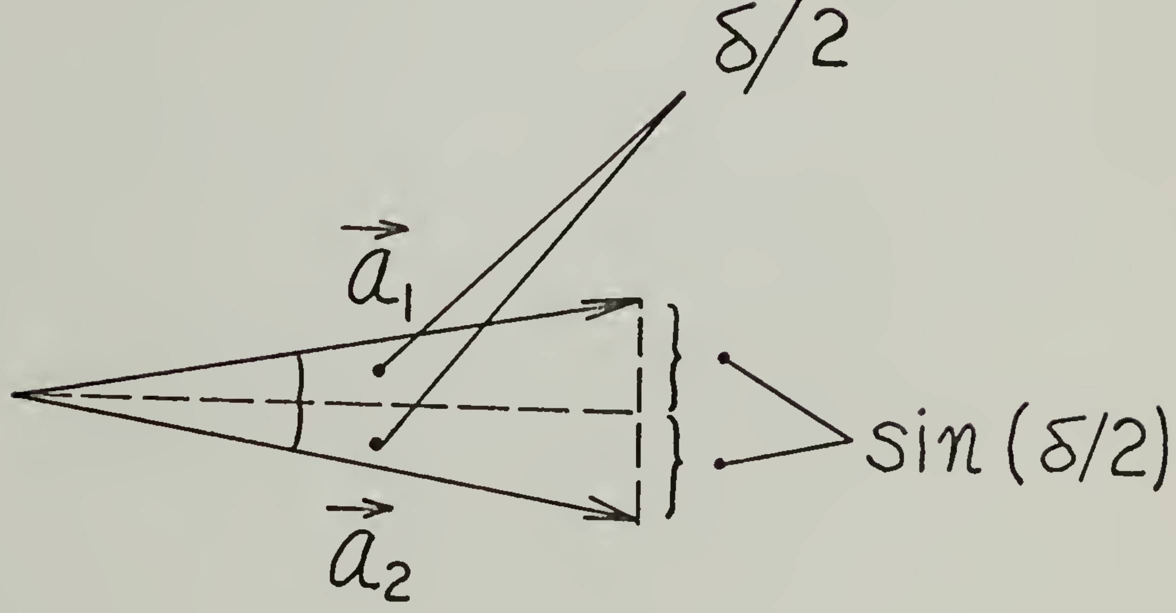

$$\vec{a}_1 = \frac{\vec{\alpha}_1}{K_1} \qquad \vec{a}_2 = \frac{\vec{\alpha}_2}{K_2}$$

FIG. 14B

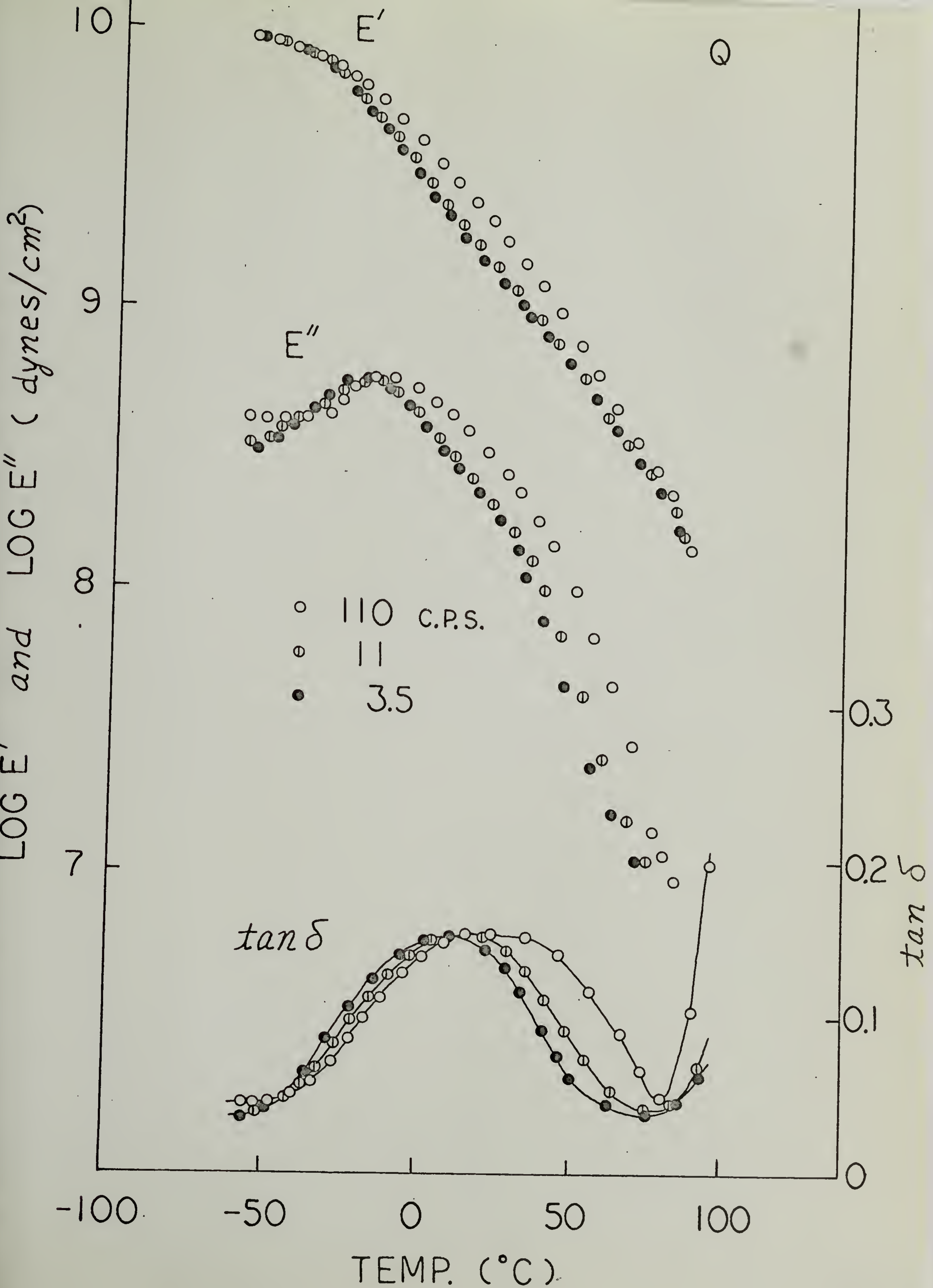

E′
Q
E″
○ 110 C.P.S.
⦶ 11
● 3.5
tan δ
LOG E′ and LOG E″ (dynes/cm²)
10
9
8
7
tan δ
0.3
0.2
0.1
0
-100
-50
0
50
100
TEMP. (°C)

FIG.15

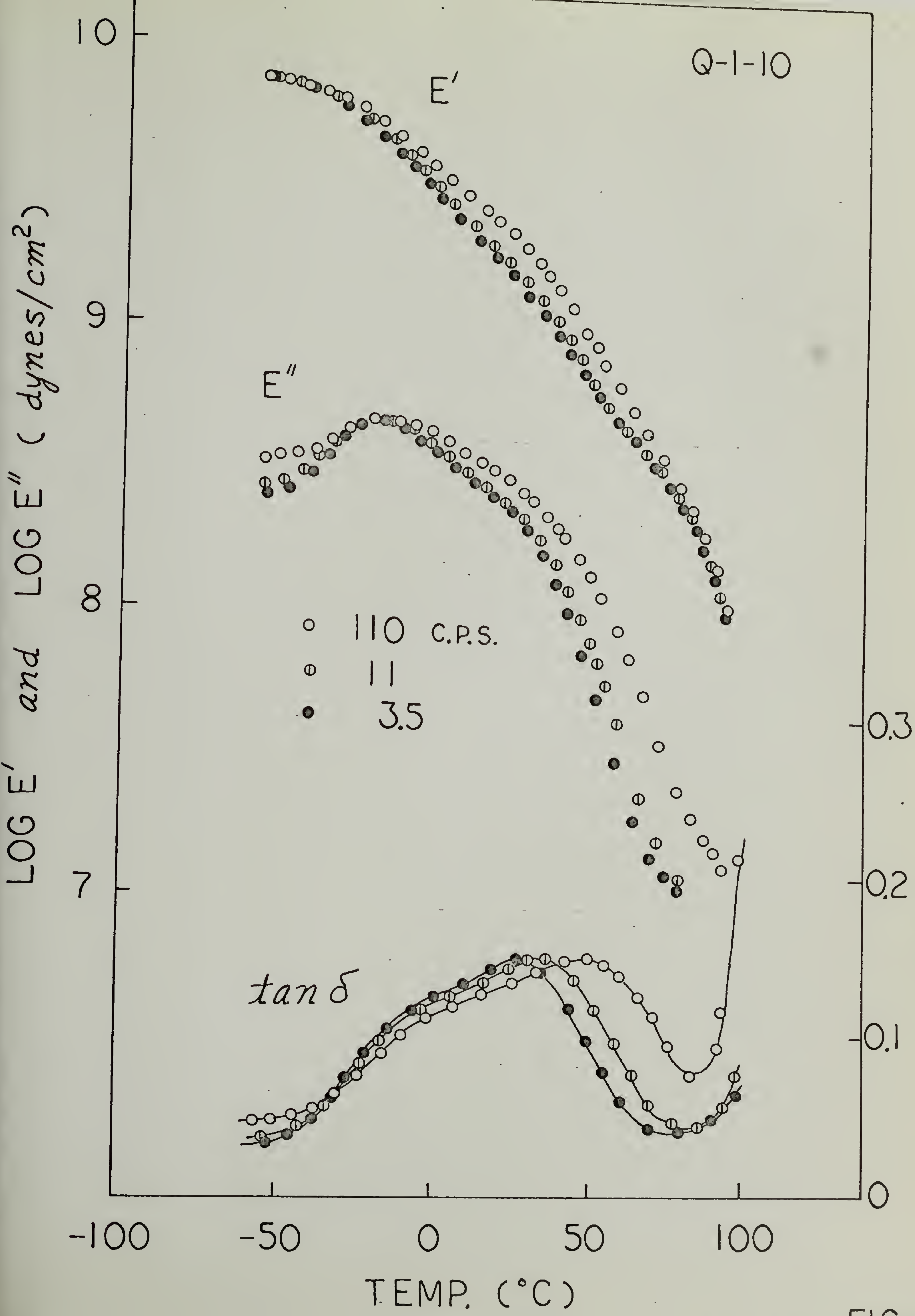
Q-1-10
E'
E''
tan δ
○ 110 C.P.S.
⦶ 11
● 3.5
LOG E' and LOG E'' (dynes/cm^2)
10
9
8
7
0.3
0.2
0.1
0
tan δ
-100
-50
0
50
100
TEMP. (°C)

FIG.16

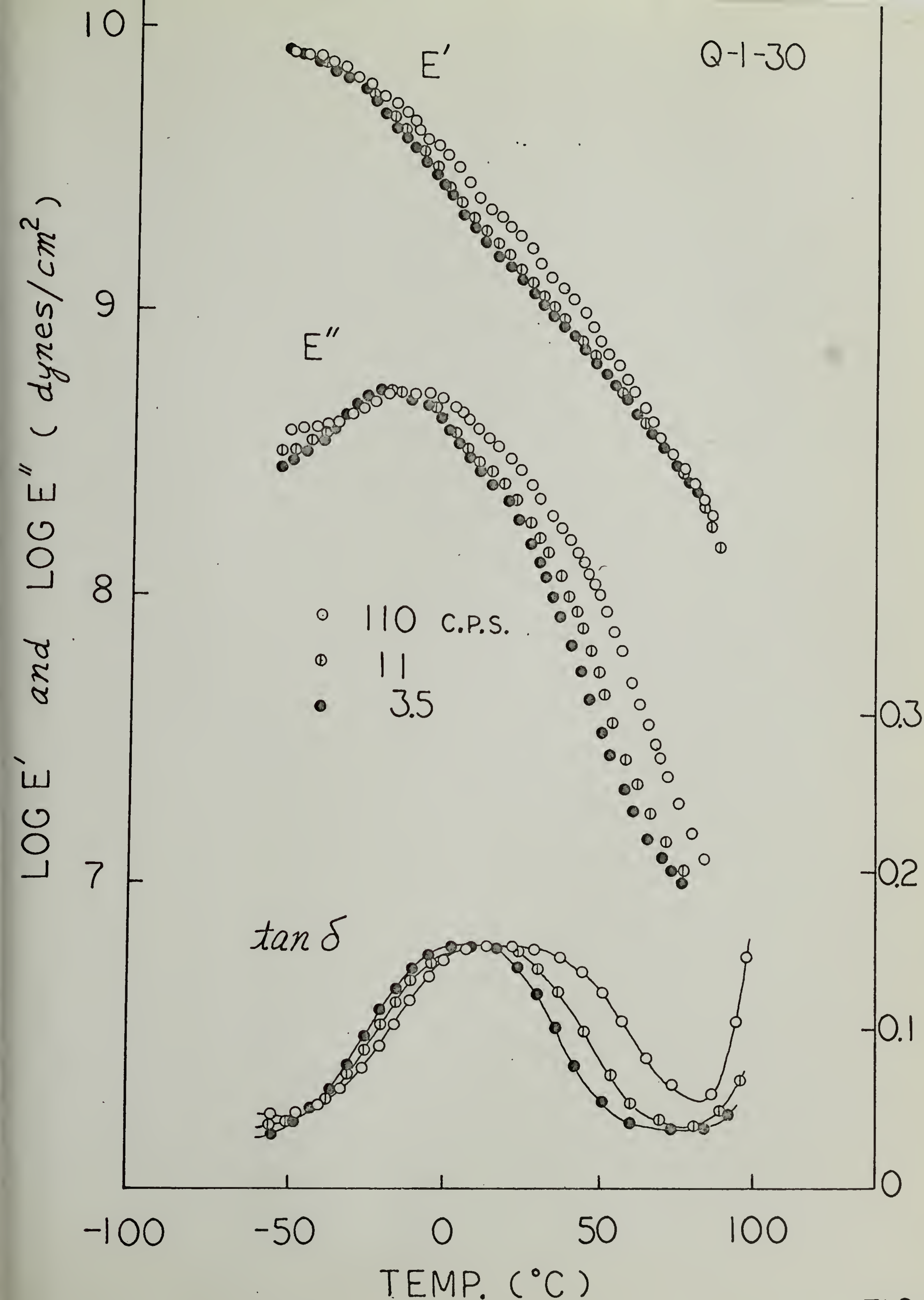
Q-1-30
E′
E″
tan δ
○ 110 c.p.s.
⦶ 11
● 3.5
LOG E′ and LOG E″ (dynes/cm^2)
10
9
8
7
tan δ
0.3
0.2
0.1
0
-100
-50
0
50
100
TEMP. (°C)

FIG.17

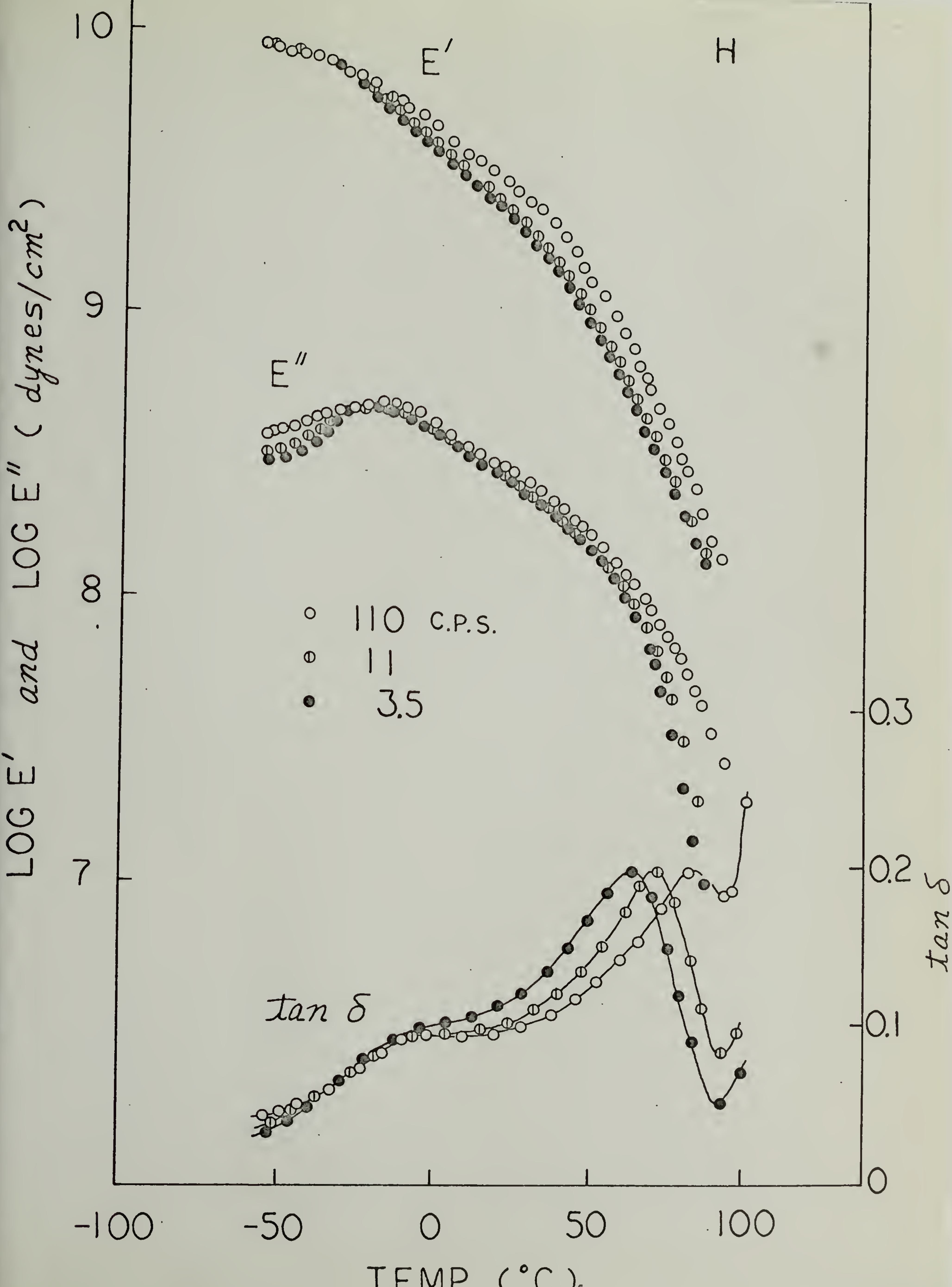
10
9
8
7
LOG E' and LOG E'' (dynes/cm^2)
E'
E''
H
○ 110 c.p.s.
⦶ 11
● 3.5
tan δ
0.3
0.2
0.1
0
tan δ
-100
-50
0
50
100
TEMP. (°C)

FIG. 18

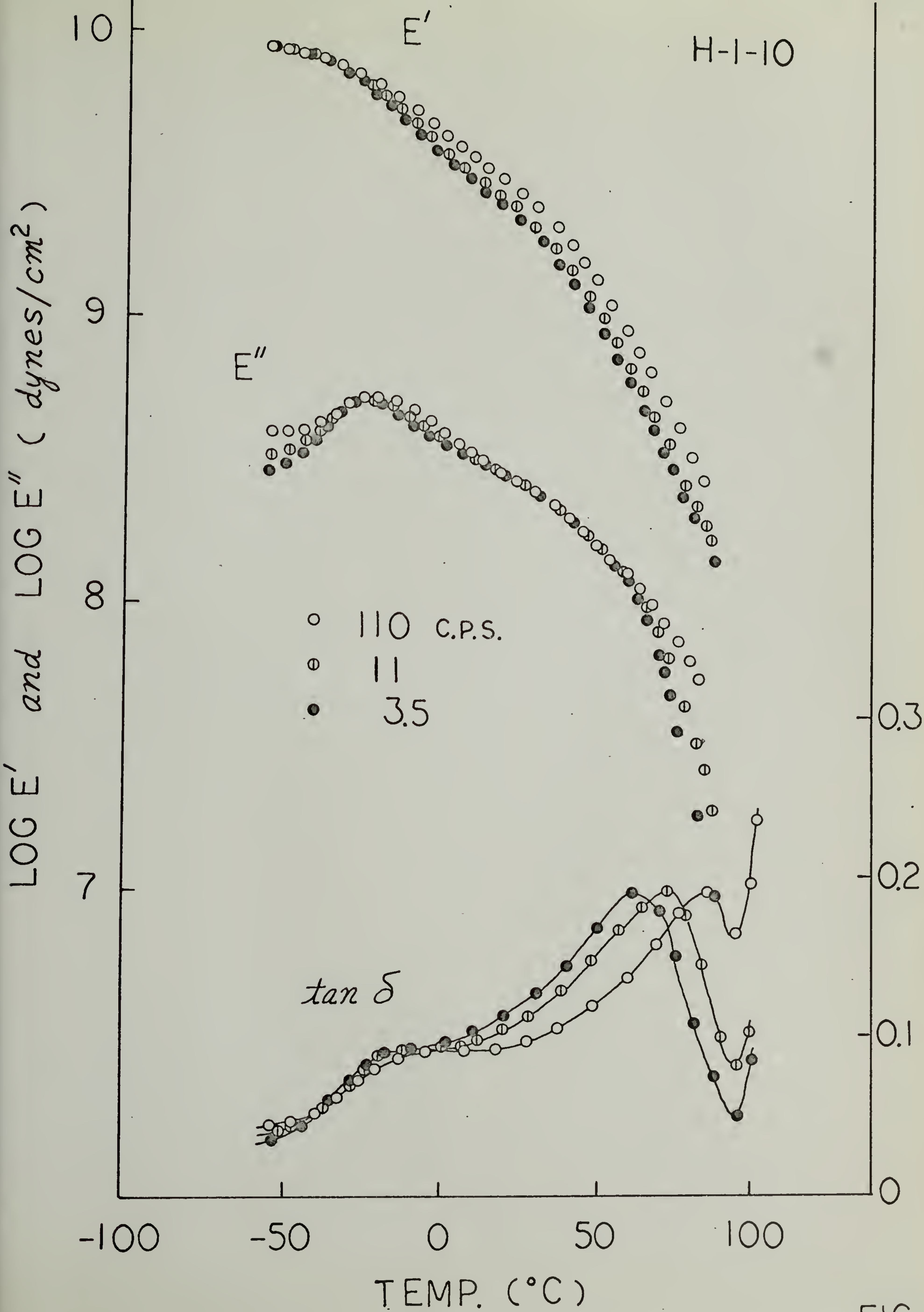

H-1-10
E'
E''
tan δ
○ 110 C.P.S.
⦶ 11
● 3.5
LOG E' and LOG E'' (dynes/cm^2)
10
9
8
7
tan δ
0.3
0.2
0.1
0
-100
-50
0
50
100
TEMP. (°C)

FIG.19

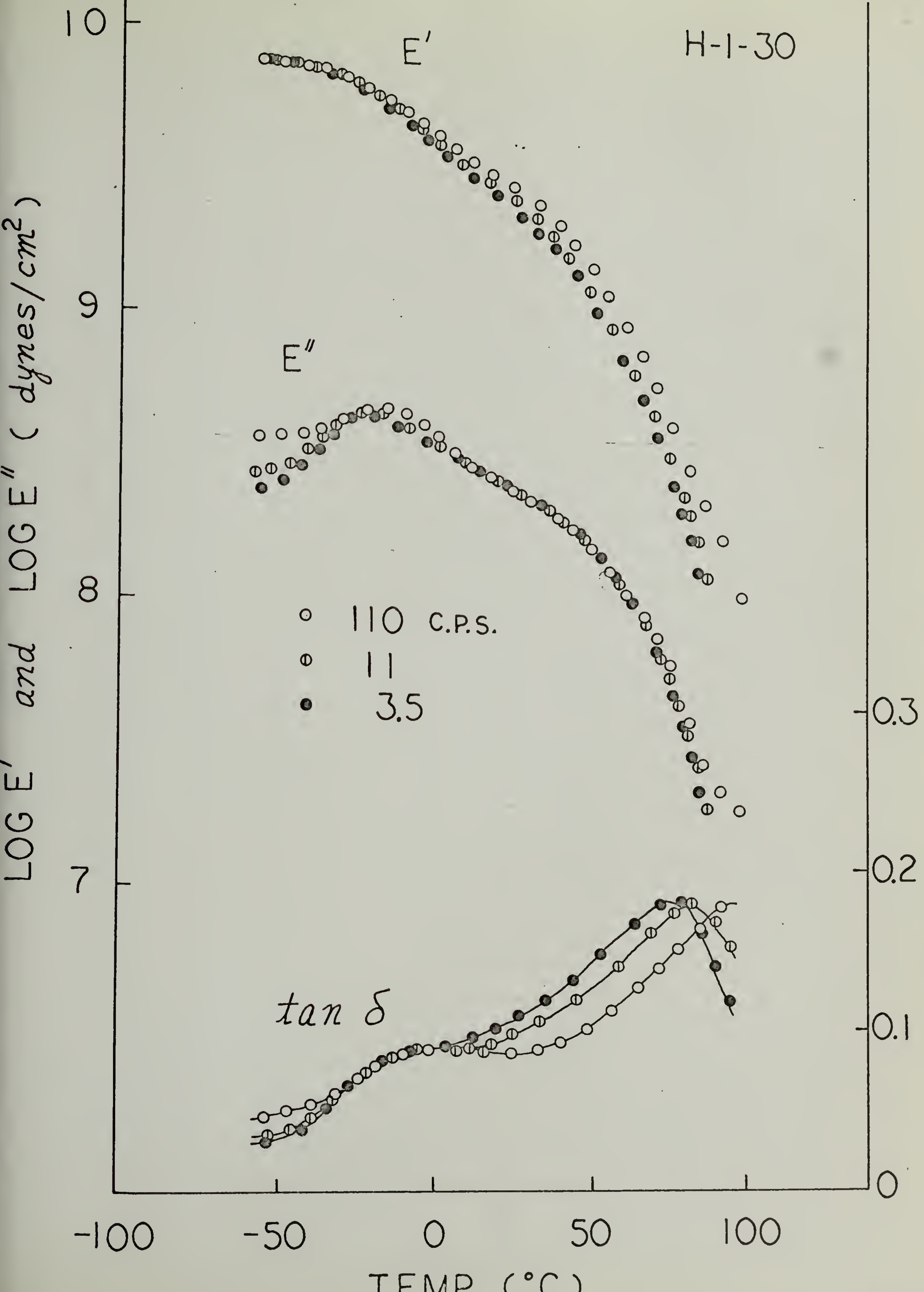
E'
H-1-30
E''
○ 110 C.P.S.
⦶ 11
● 3.5
tan δ
LOG E' and LOG E'' (dynes/cm^2)
10
9
8
7
0.3
0.2
0.1
0
tan δ
-100
-50
0
50
100
TEMP. (°C)

FIG. 20

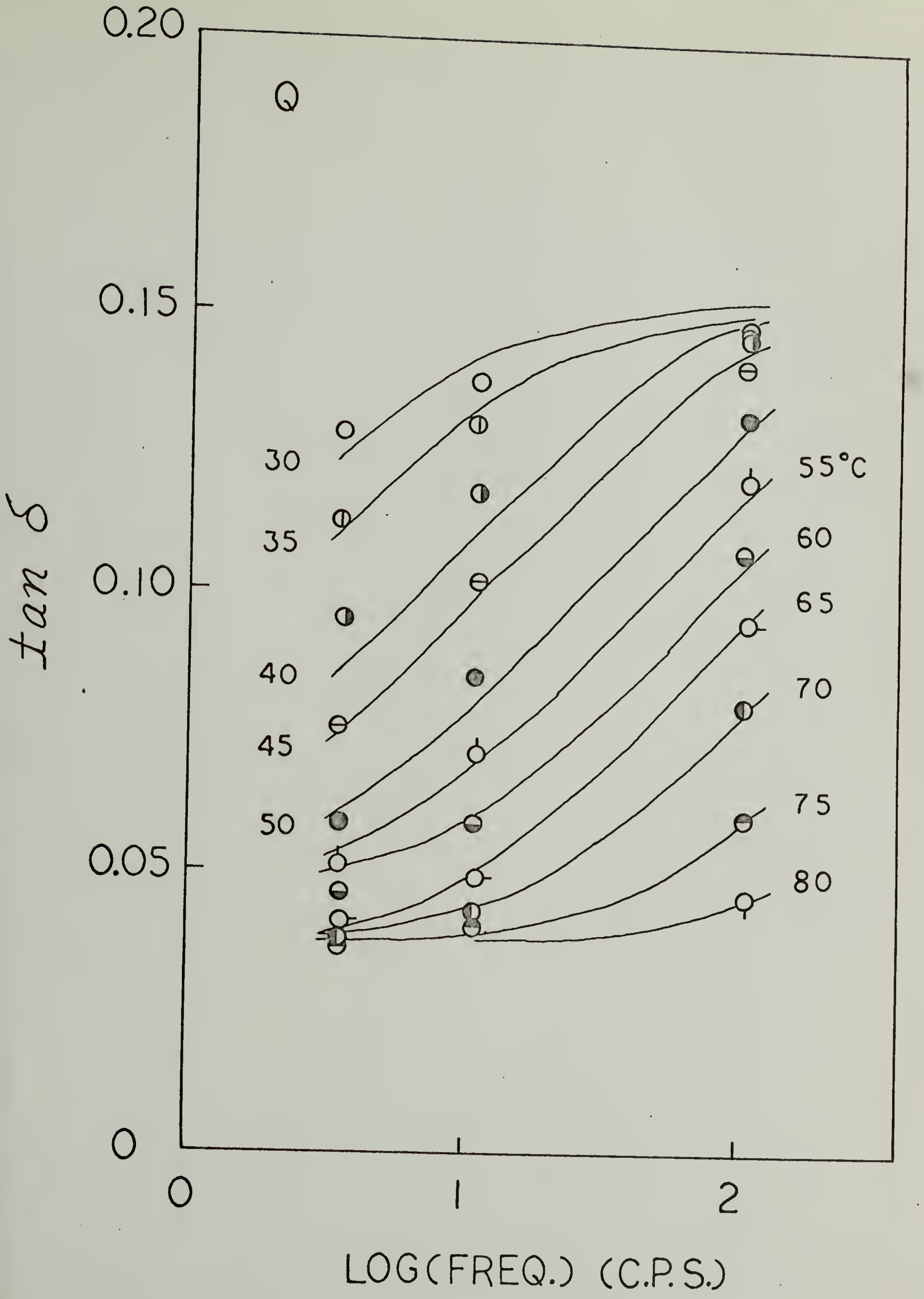
Q
tan δ
0.20
0.15
0.10
0.05
0
0
1
2
LOG(FREQ.) (C.P.S.)
30
35
40
45
50
55°C
60
65
70
75
80

FIG.21

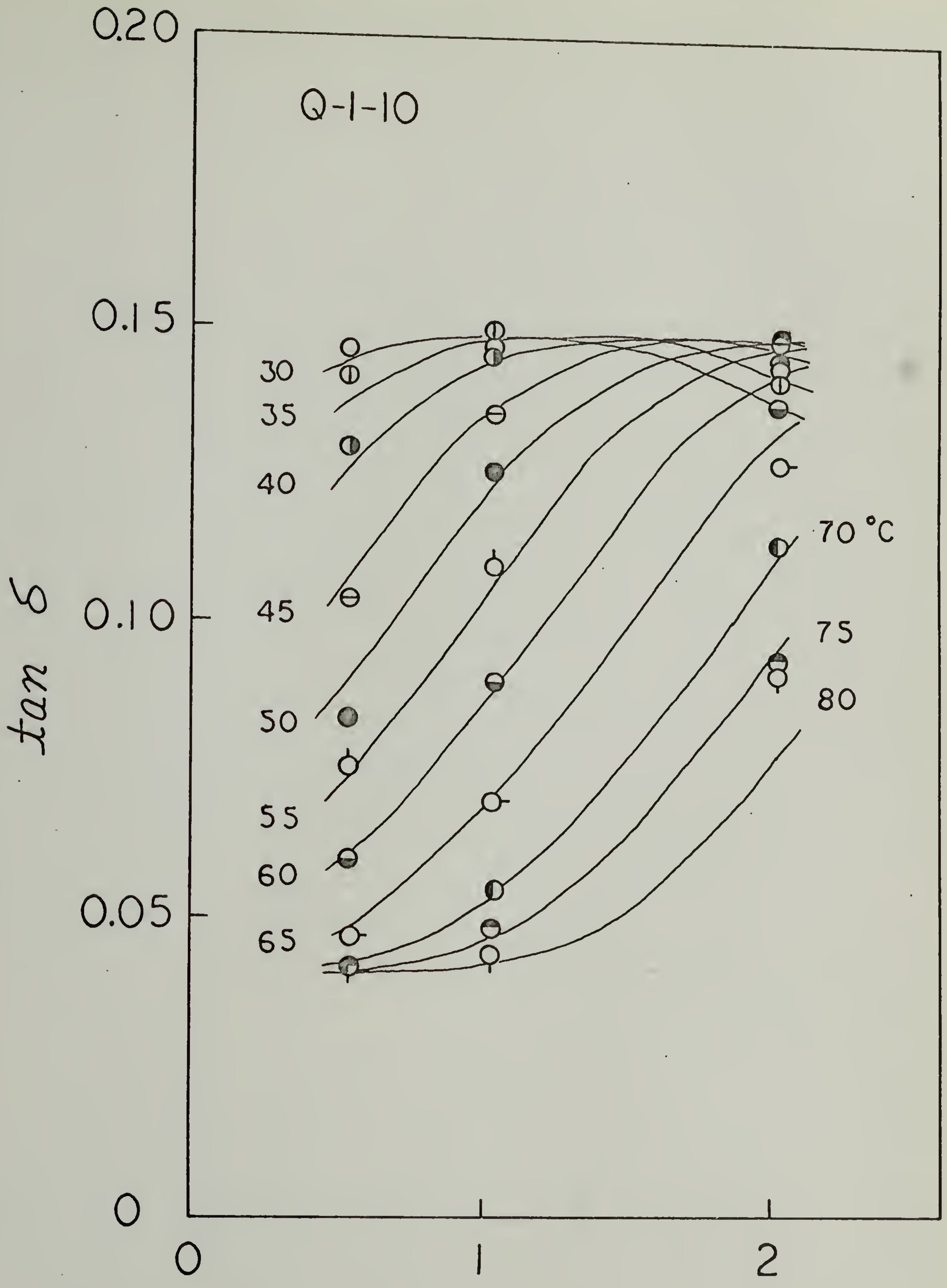
Q-1-10
0.20
0.15
0.10
0.05
0
tan δ
0
1
2
LOG (FREQ.) (C.P.S.)
30
35
40
45
50
55
60
65
70 °C
75
80

FIG. 22

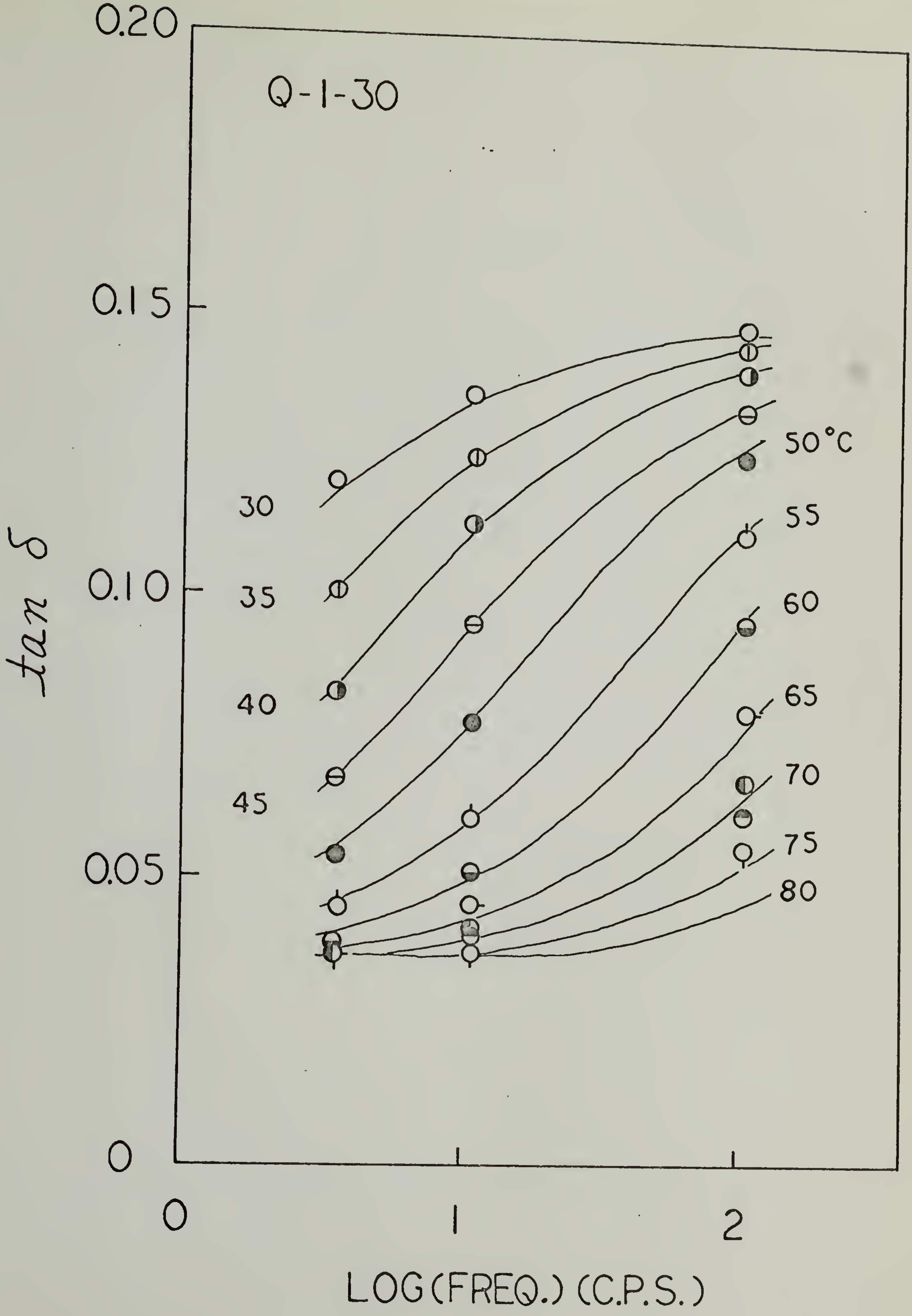
0.20
Q-1-30
0.15
0.10
0.05
0
tan δ
30
35
40
45
50°C
55
60
65
70
75
80
0
1
2
LOG(FREQ.) (C.P.S.)

FIG.23

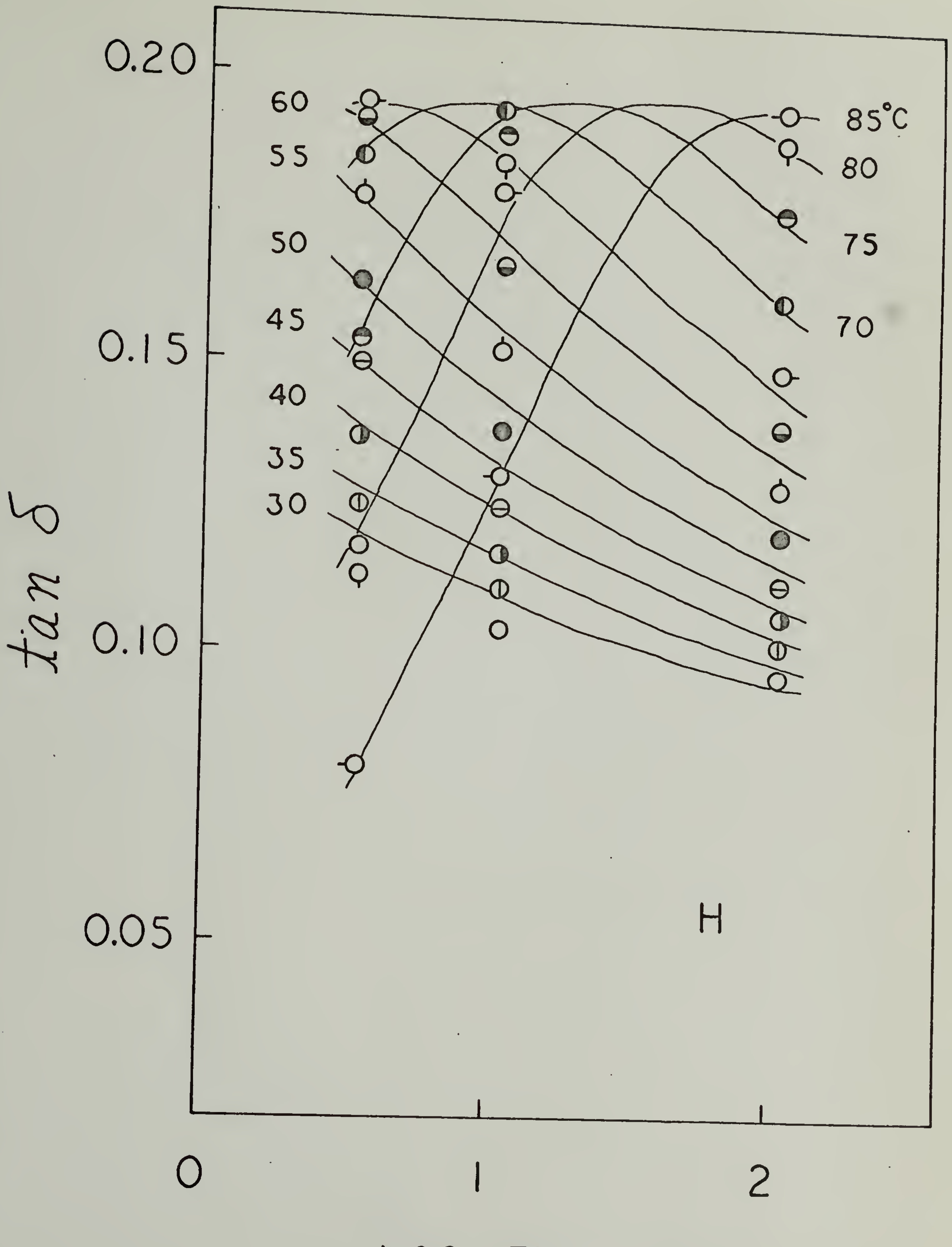
0.20
0.15
0.10
0.05
tan δ
60
55
50
45
40
35
30
85°C
80
75
70
H
0
1
2
LOG (FREQ.) (C.P.S.)

FIG. 24

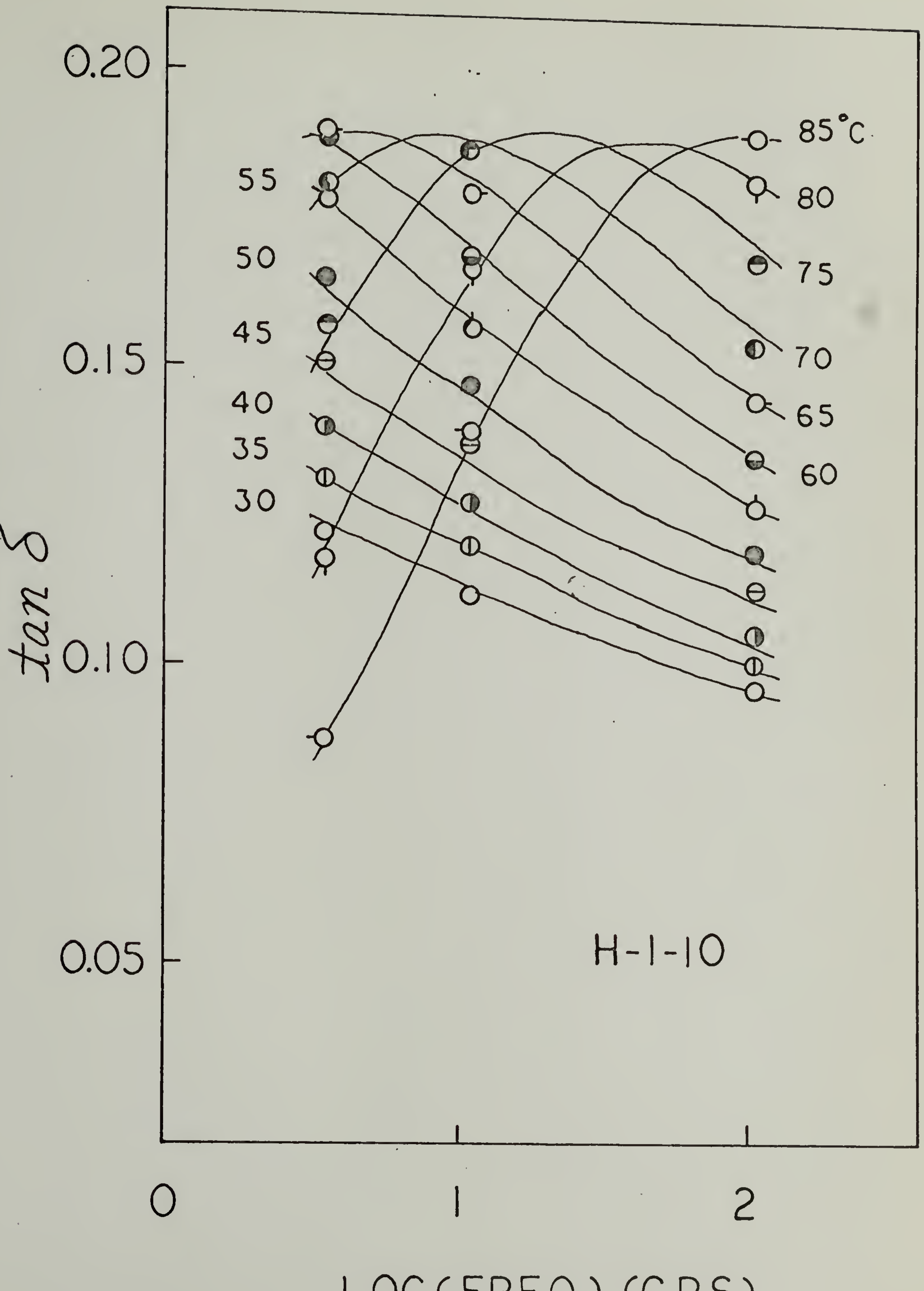
0.20
0.15
0.10
0.05
tan δ
0
1
2
LOG (FREQ.) (C.P.S.)
55
50
45
40
35
30
85°C
80
75
70
65
60
H-1-10

FIG. 25

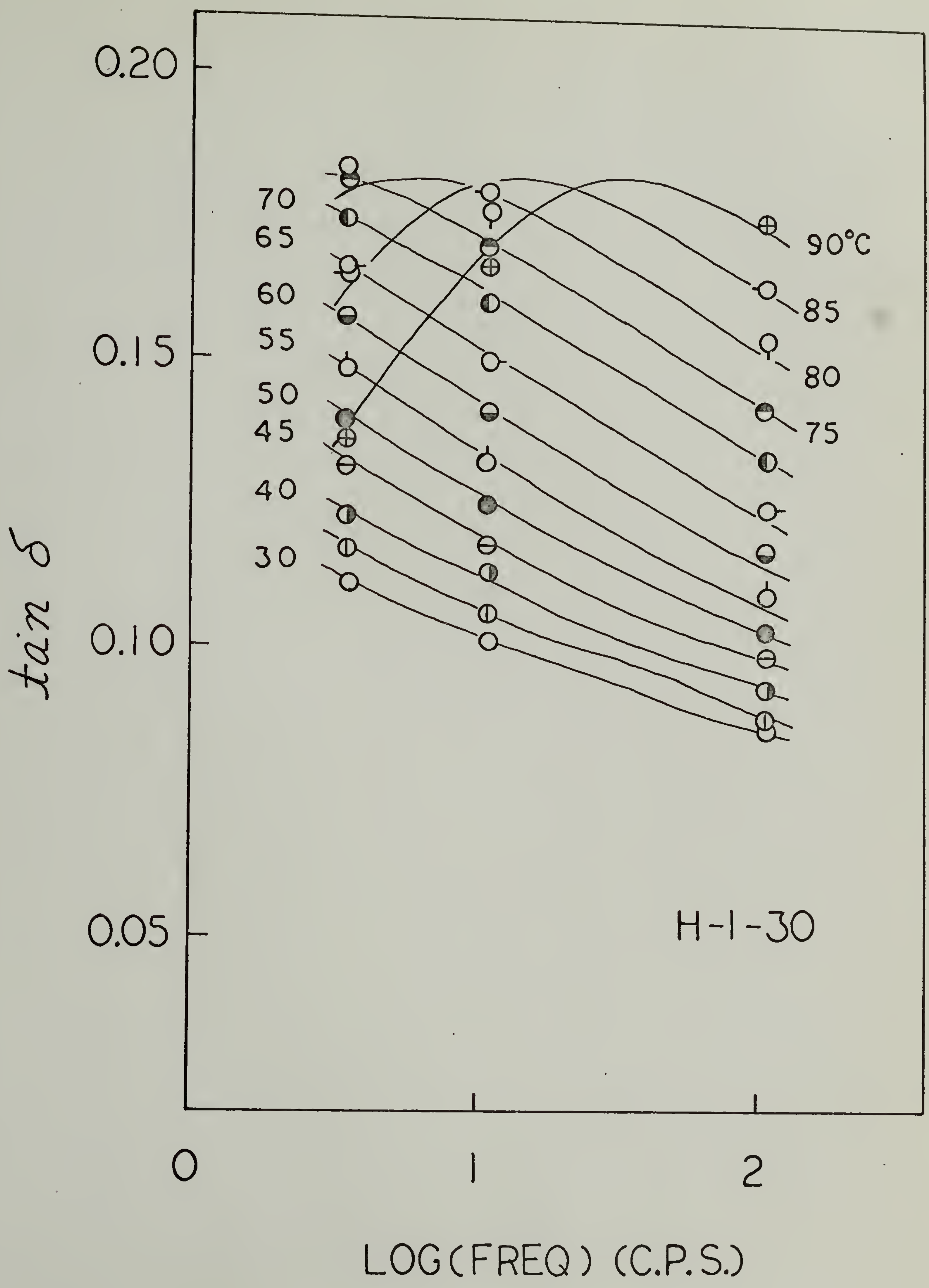

0.20
0.15
0.10
0.05
tan δ
70
65
60
55
50
45
40
30
90°C
85
80
75
H-1-30
0
1
2
LOG(FREQ) (C.P.S.)

FIG. 26

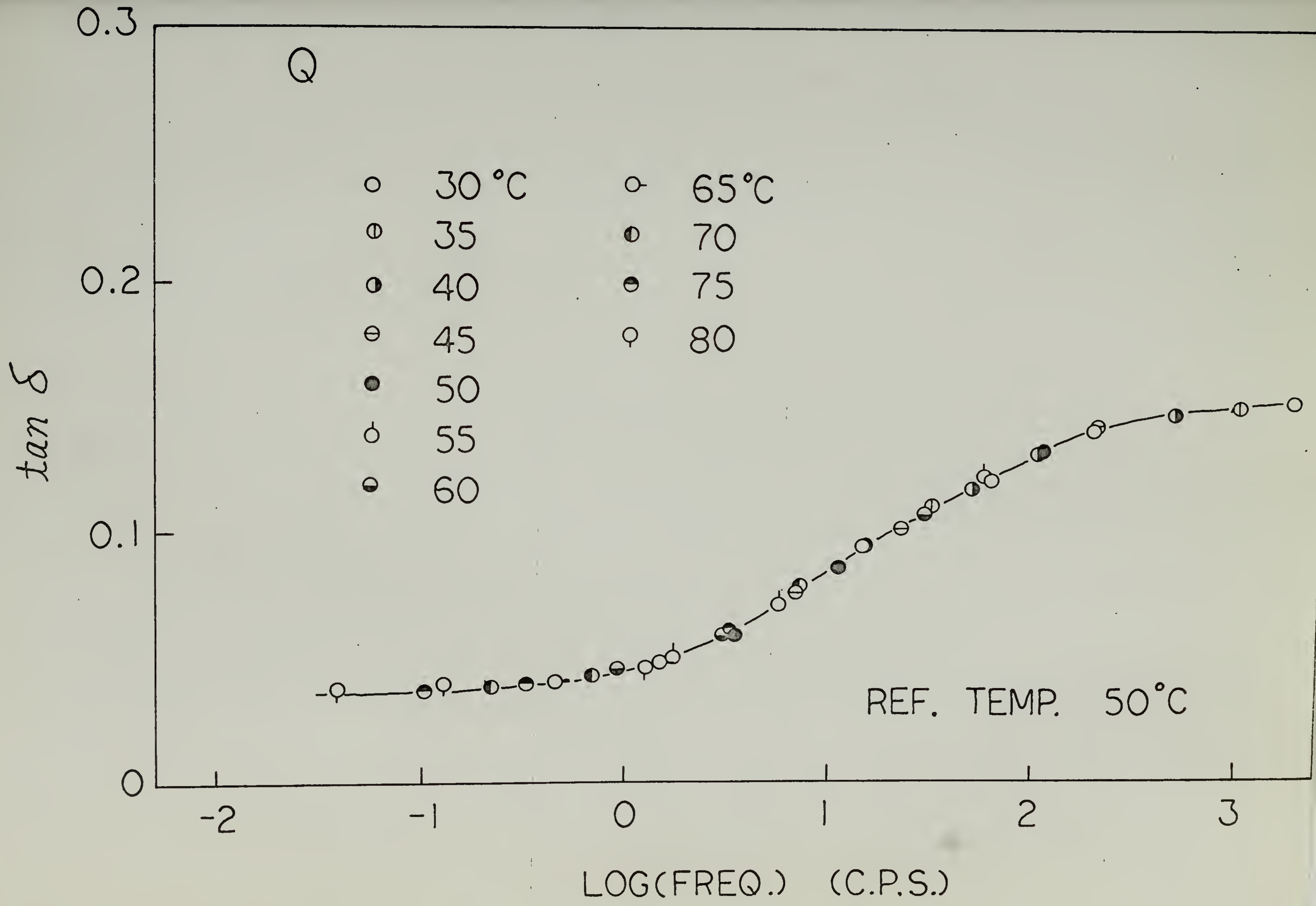
Q
tan δ
0.3
0.2
0.1
0
○ 30 °C
◐ 35
◑ 40
⊖ 45
● 50
○ 55
◒ 60
○ 65°C
◐ 70
◓ 75
○ 80
REF. TEMP. 50°C
-2
-1
0
1
2
3
LOG(FREQ.) (C.P.S.)

FIG. 27

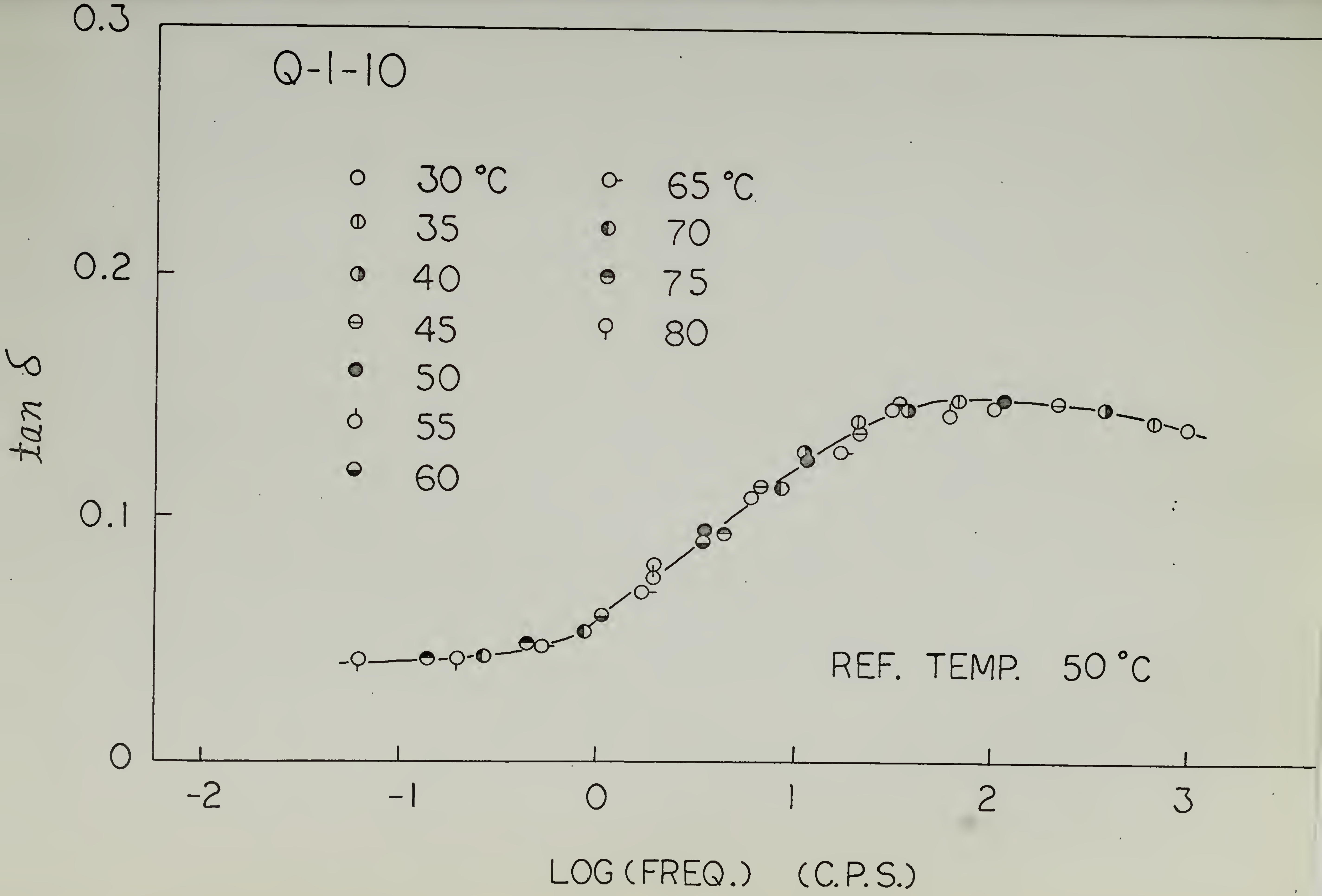
0.3
0.2
0.1
0
tan δ
Q-1-10
30 °C
35
40
45
50
55
60
65 °C
70
75
80
REF. TEMP. 50 °C
-2
-1
0
1
2
3
LOG (FREQ.) (C.P.S.)

FIG 28

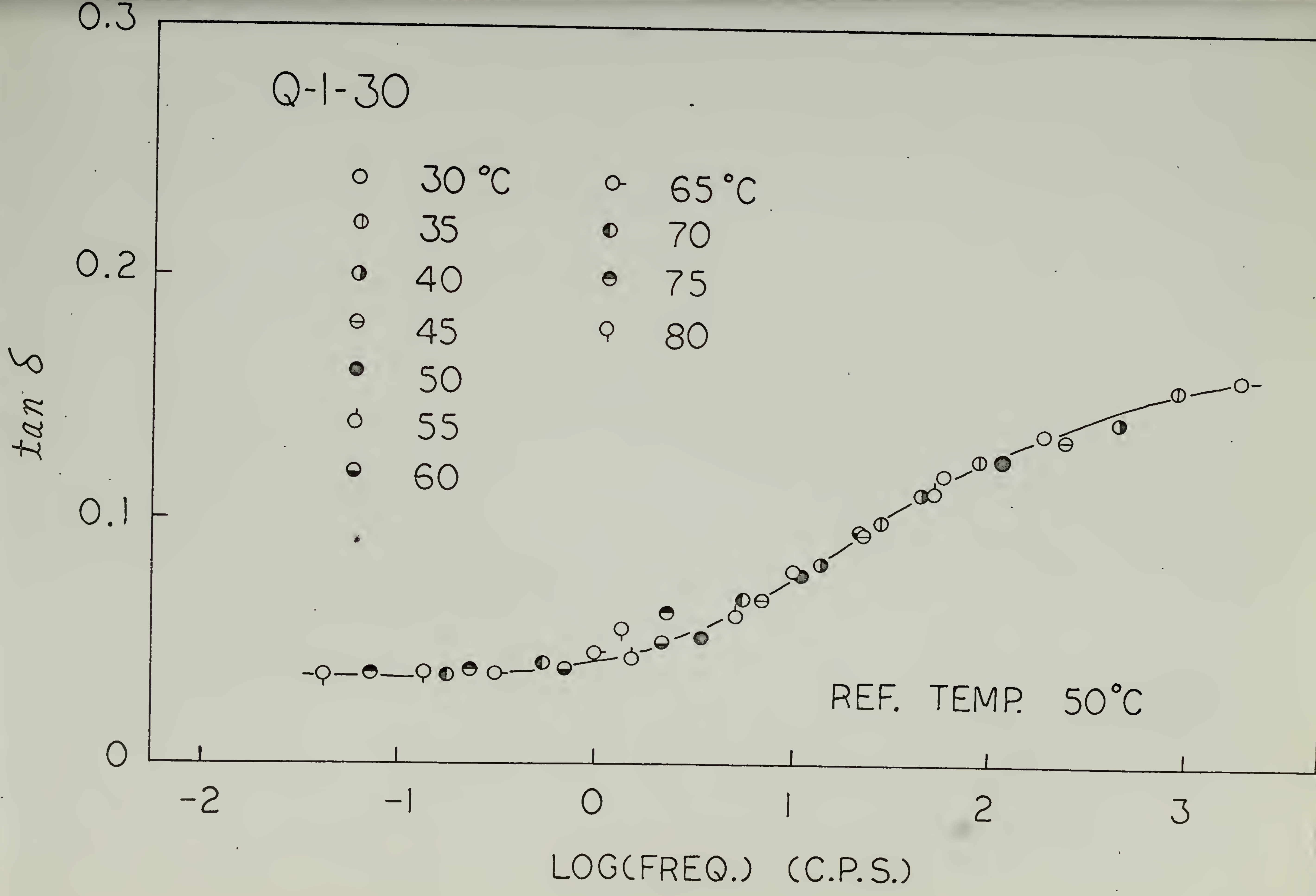
Q-1-30
○ 30 °C
⊖ 35
◐ 40
⊖ 45
● 50
○ 55
◒ 60
○ 65 °C
◐ 70
◒ 75
○ 80
REF. TEMP. 50°C
tan δ
0.3
0.2
0.1
0
-2
-1
0
1
2
3
LOG(FREQ.) (C.P.S.)

FIG. 29

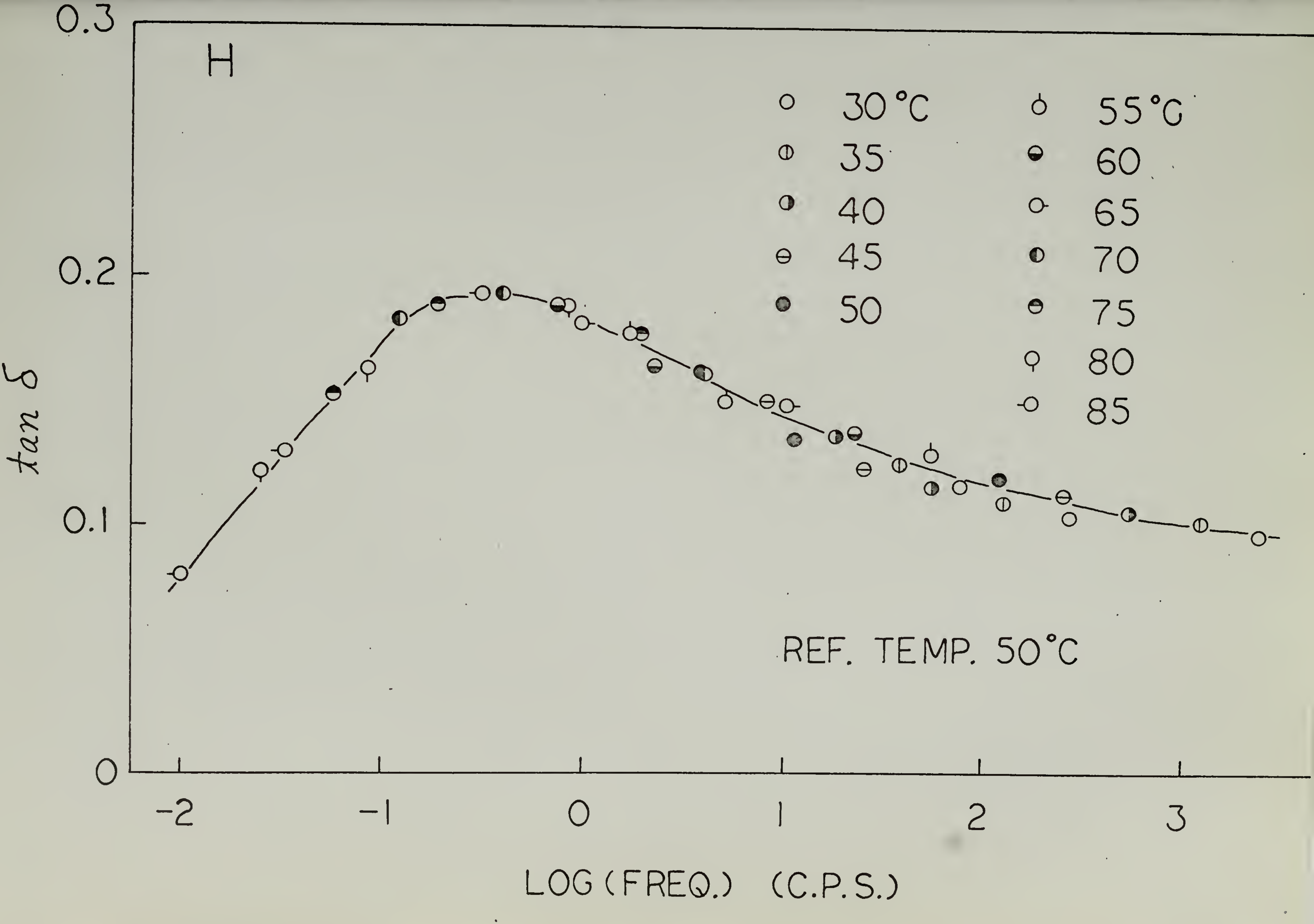
0.3
0.2
0.1
0
tan δ
H
○ 30 °C
⦶ 35
◐ 40
⊖ 45
● 50
○ 55 °C
◒ 60
○ 65
◐ 70
◒ 75
○ 80
○ 85
REF. TEMP. 50 °C
-2
-1
0
1
2
3
LOG (FREQ.) (C.P.S.)

FIG. 30

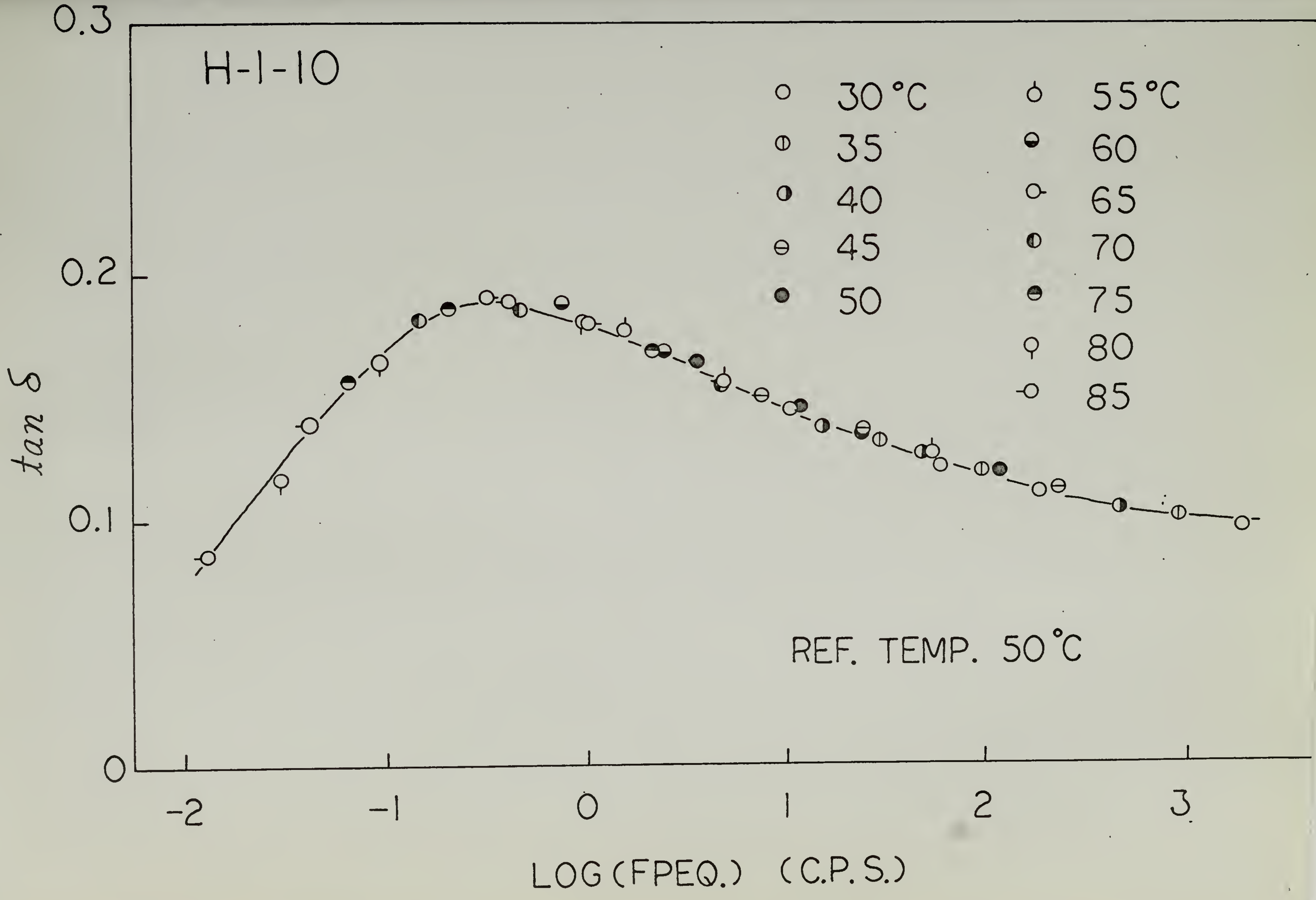
0.3
0.2
0.1
0
tan δ
H-1-10
○ 30°C
⦶ 35
◐ 40
⊖ 45
● 50
55°C
60
65
70
75
80
85
REF. TEMP. 50°C
-2
-1
0
1
2
3
LOG(FPEQ.) (C.P.S.)

FIG.31

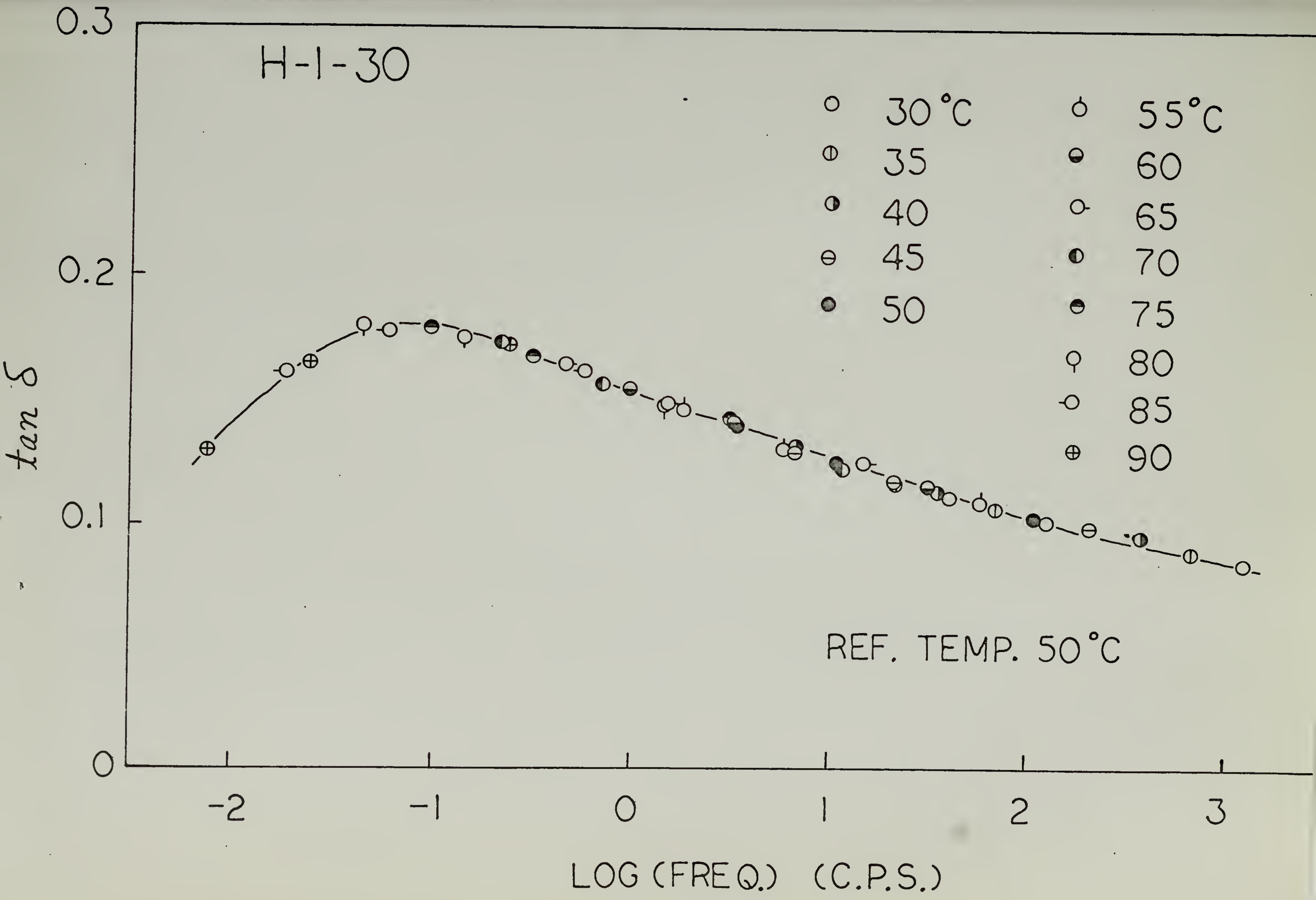
H-1-30
○ 30°C
⦶ 35
◑ 40
⊖ 45
● 50
55°C
60
65
70
75
80
85
⊕ 90
REF. TEMP. 50°C
tan δ
0.3
0.2
0.1
0
-2
-1
0
1
2
3
LOG (FREQ.) (C.P.S.)

FIG. 32

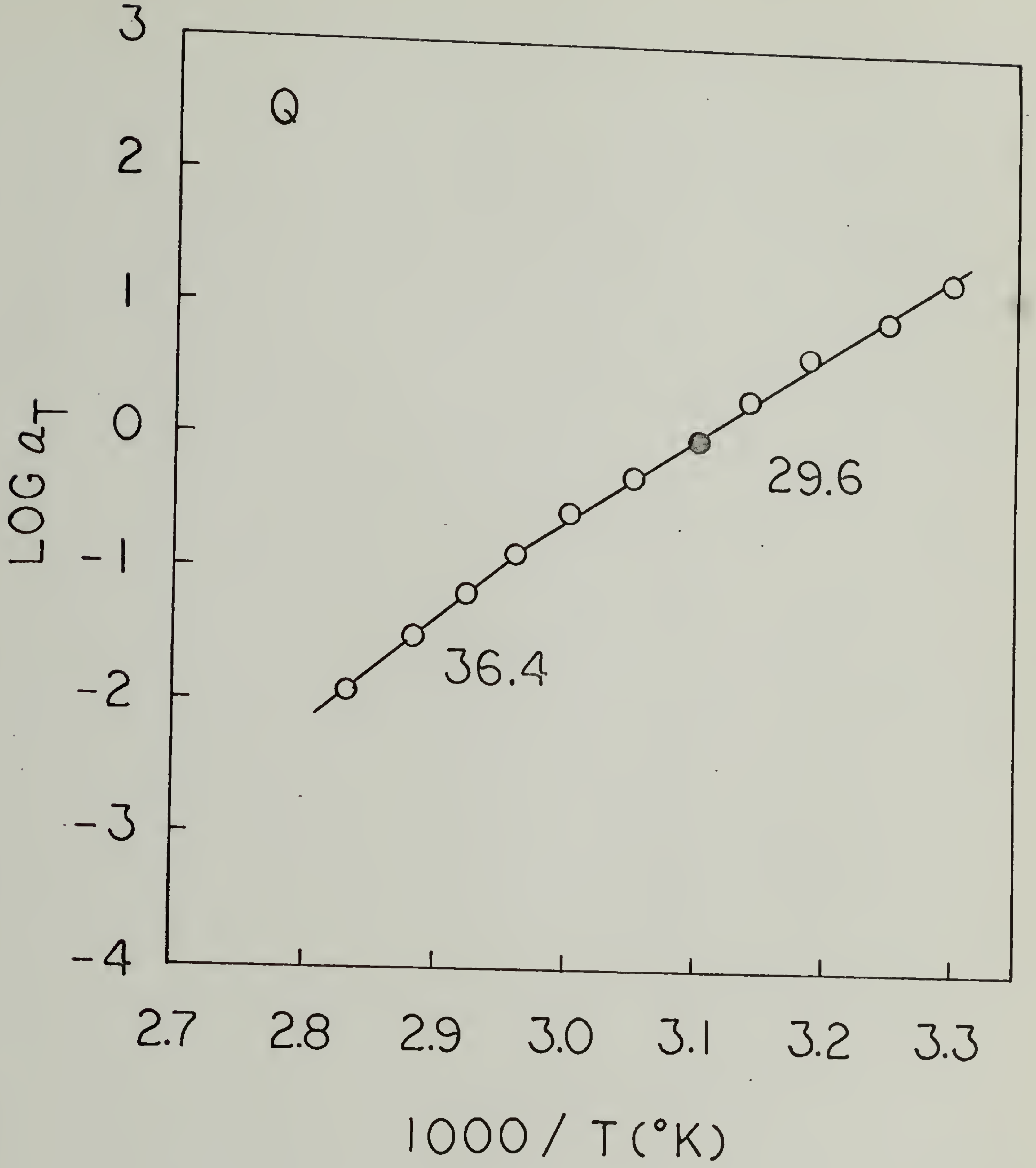

FIG. 33

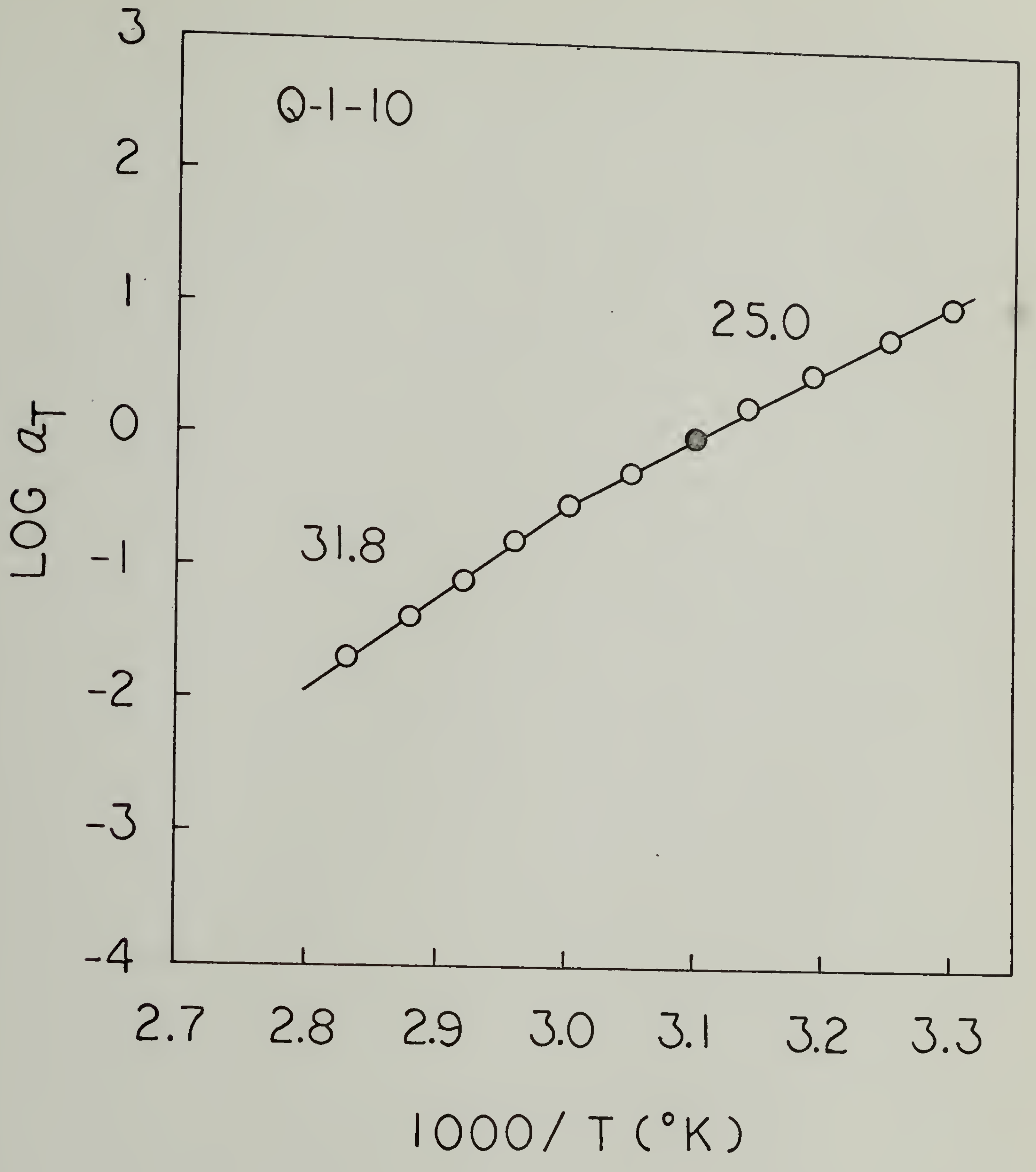

FIG. 34

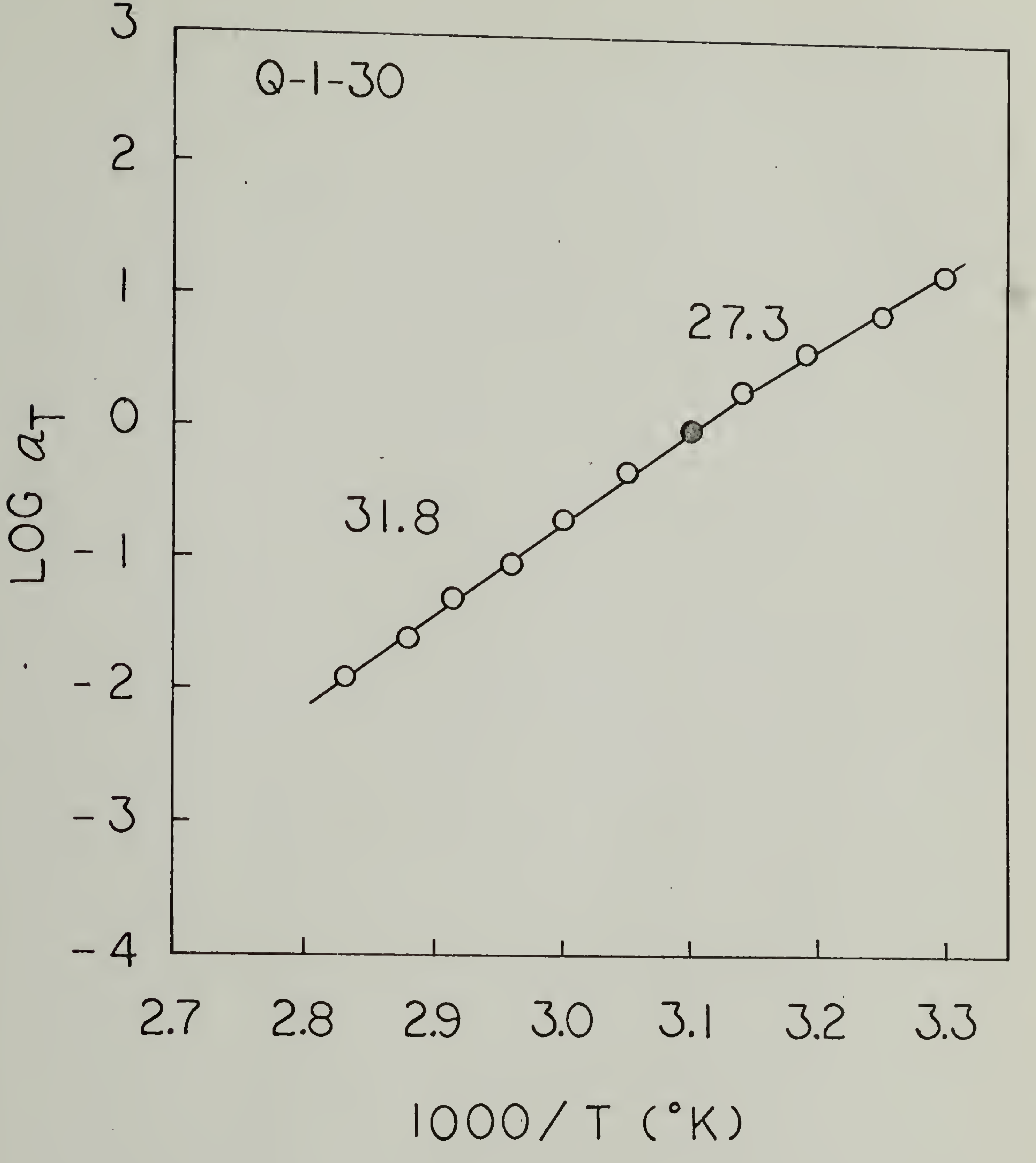

FIG. 35

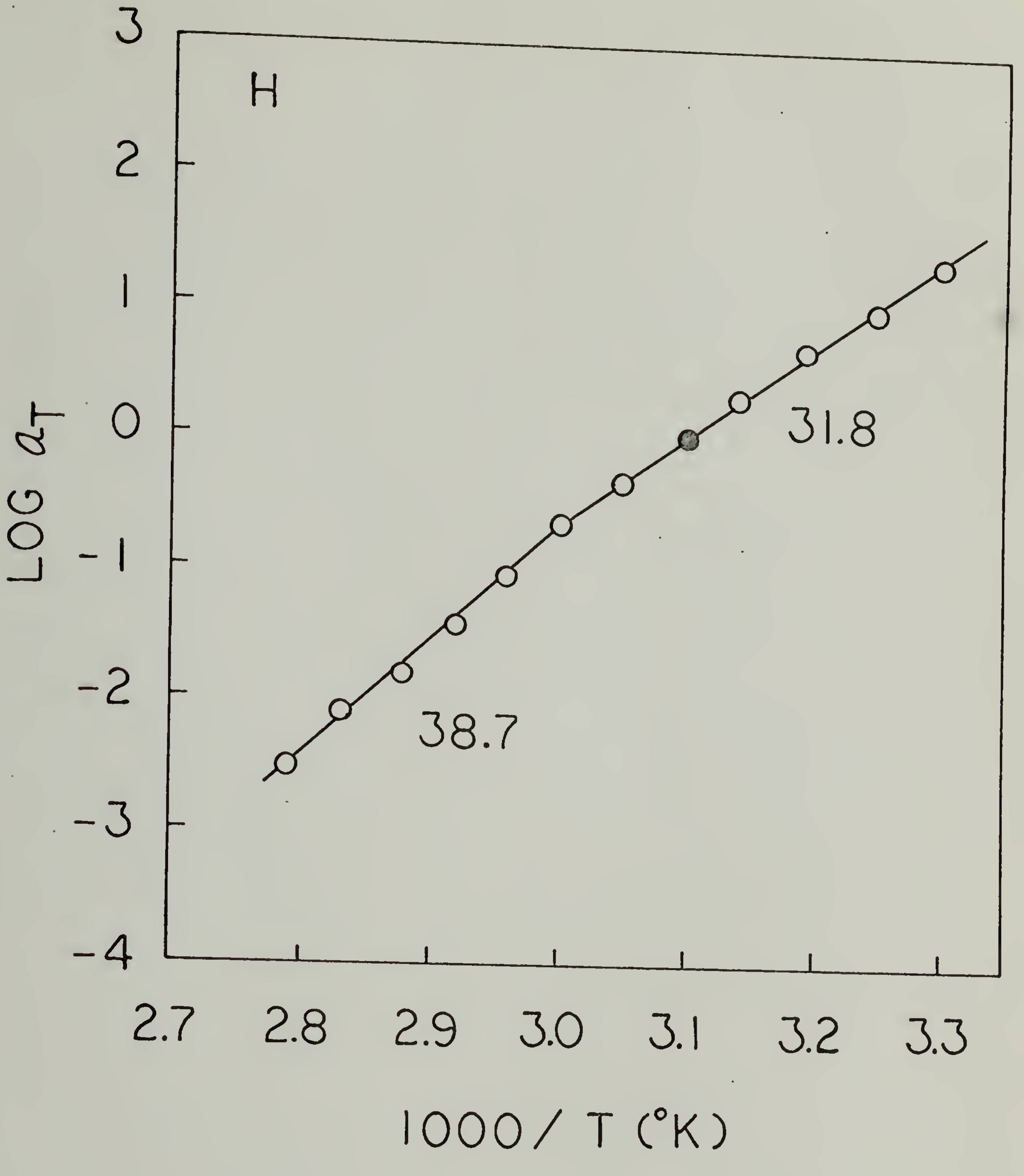

FIG. 36

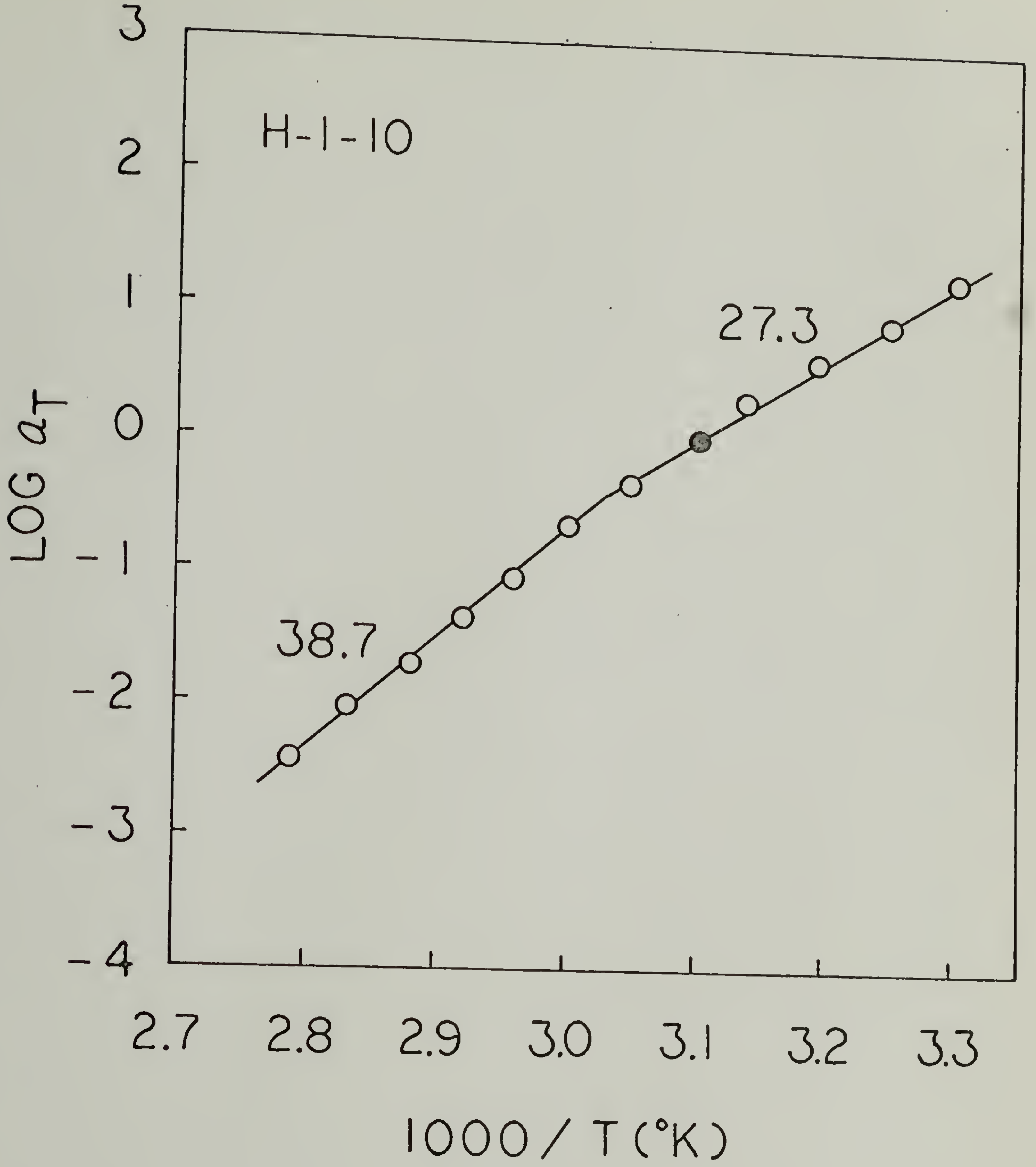

FIG. 37

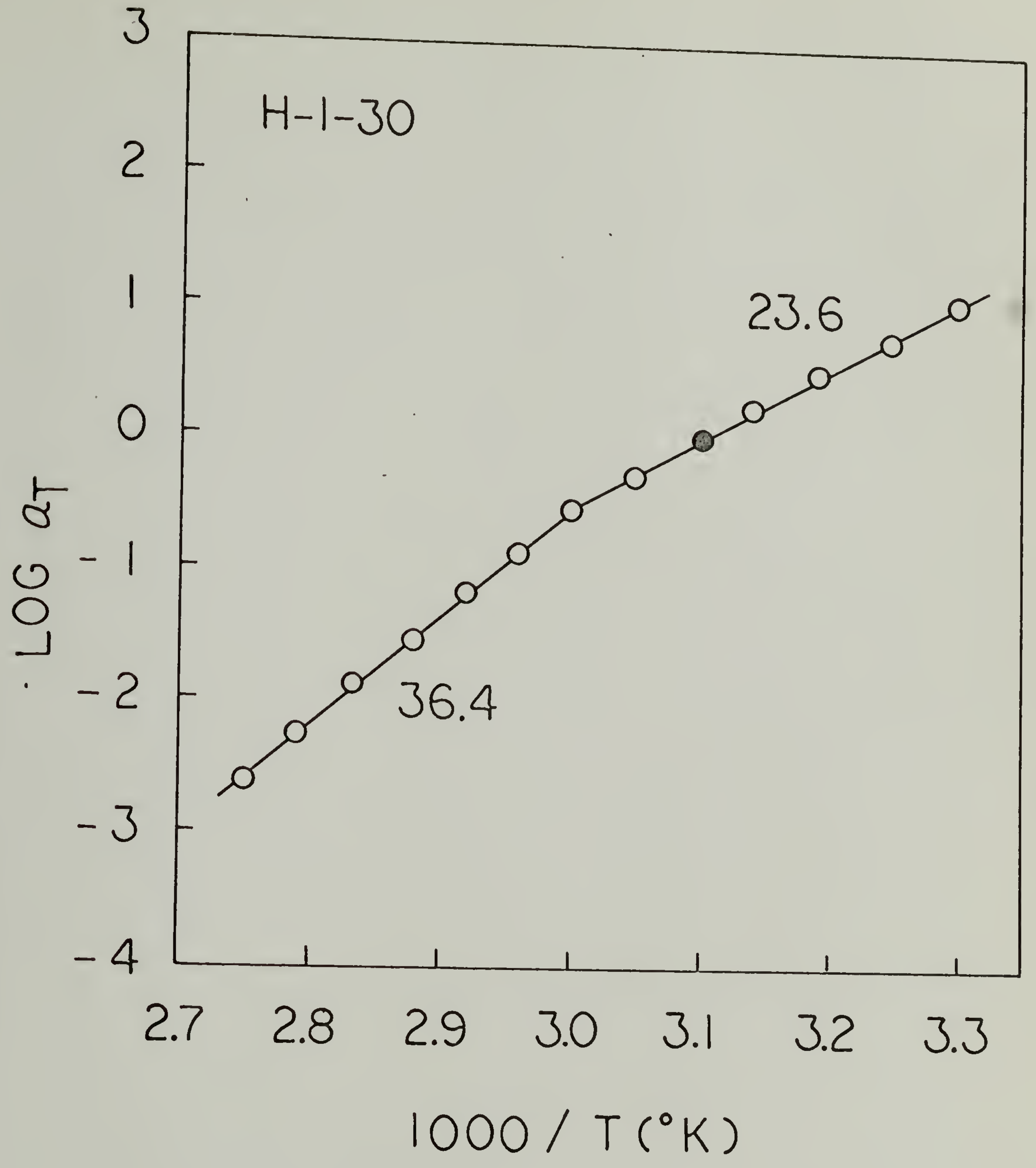

FIG. 38

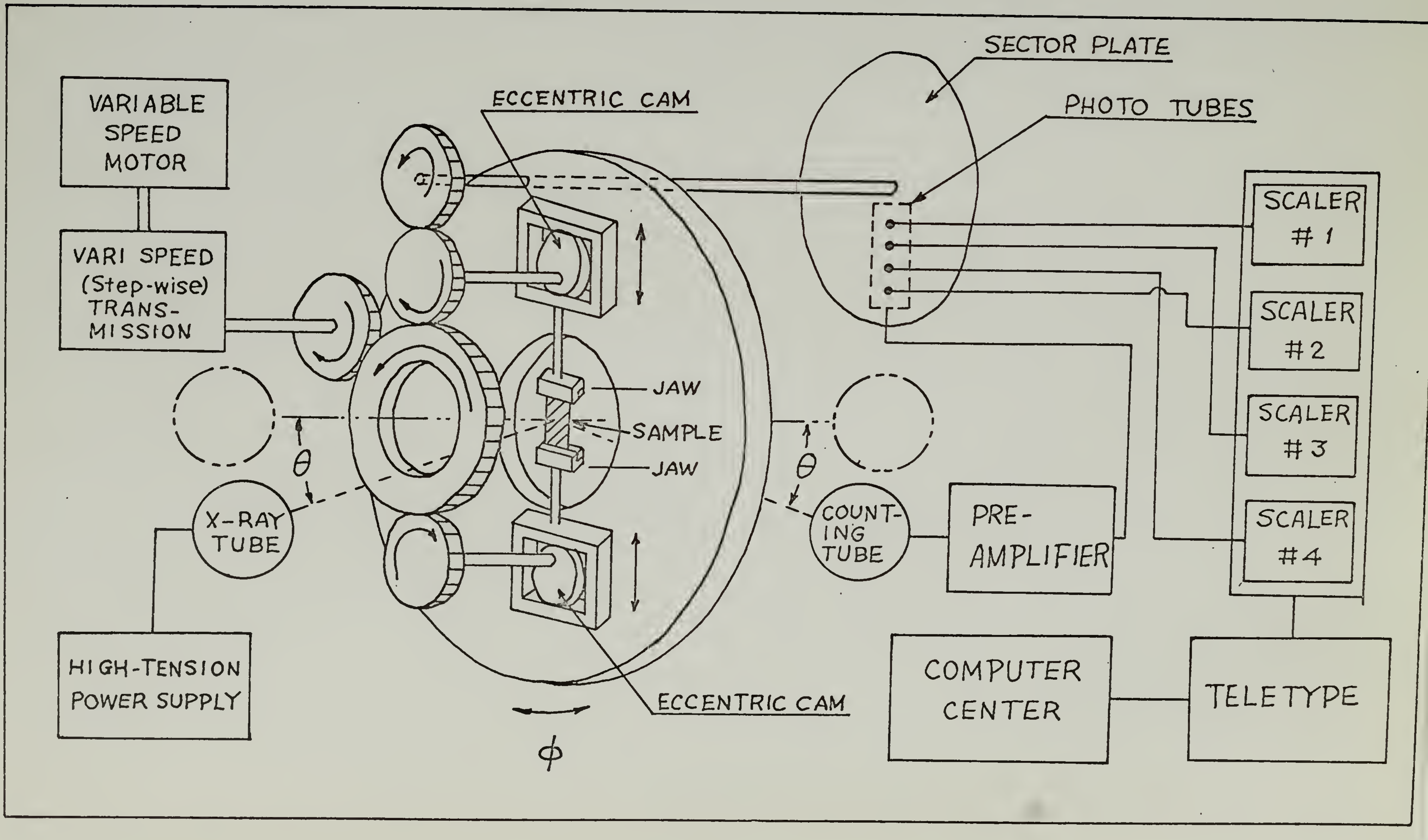
VARIABLE SPEED MOTOR
VARI SPEED (Step-wise) TRANS-MISSION
HIGH-TENSION POWER SUPPLY
X-RAY TUBE
θ
ECCENTRIC CAM
JAW
SAMPLE
JAW
ECCENTRIC CAM
φ
θ
COUNT-ING TUBE
PRE-AMPLIFIER
SECTOR PLATE
PHOTO TUBES
SCALER #1
SCALER #2
SCALER #3
SCALER #4
COMPUTER CENTER
TELETYPE

FIG.39

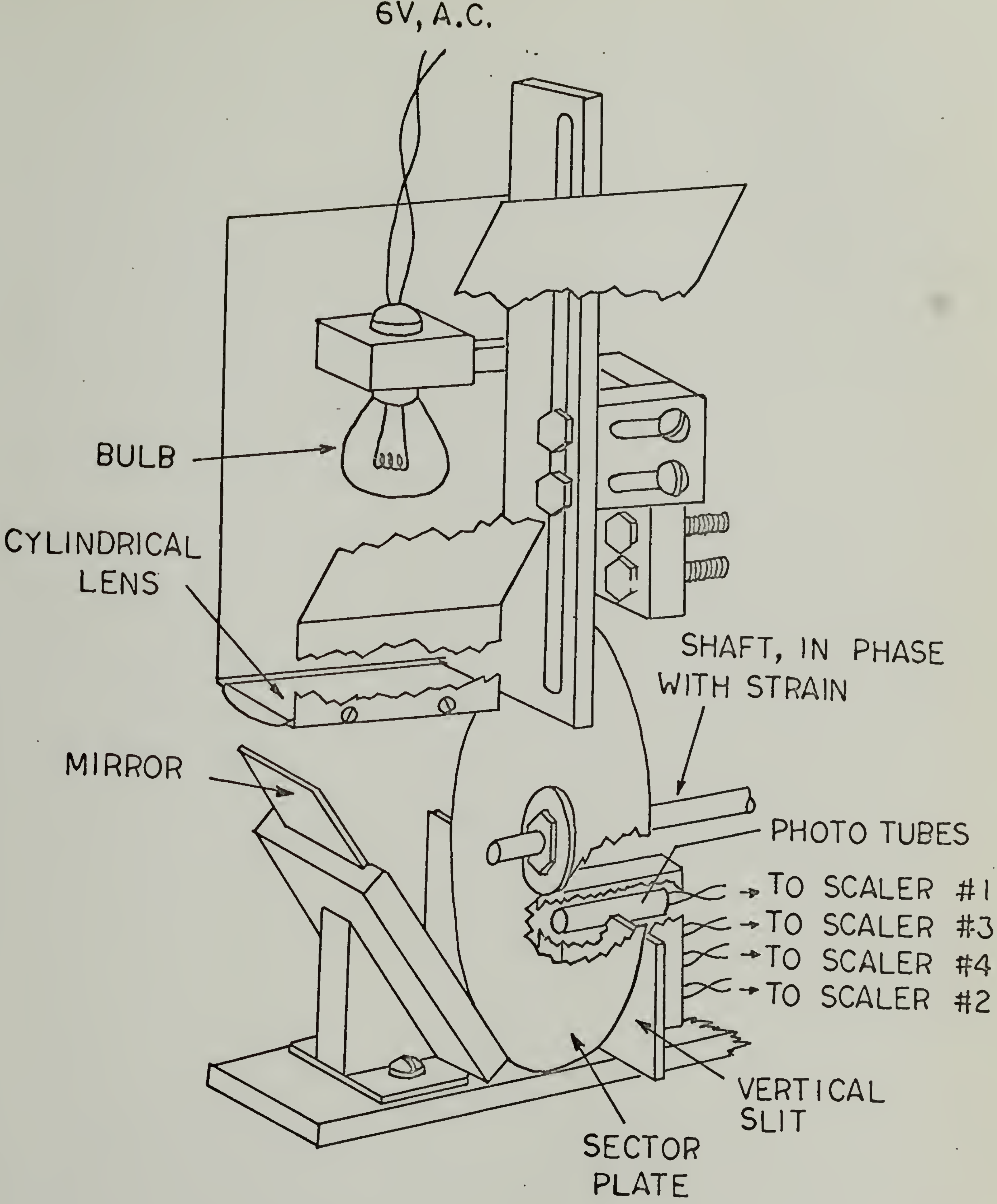
6V, A.C.
BULB
CYLINDRICAL LENS
MIRROR
SHAFT, IN PHASE WITH STRAIN
PHOTO TUBES
TO SCALER #1
TO SCALER #3
TO SCALER #4
TO SCALER #2
VERTICAL SLIT
SECTOR PLATE

FIG. 40

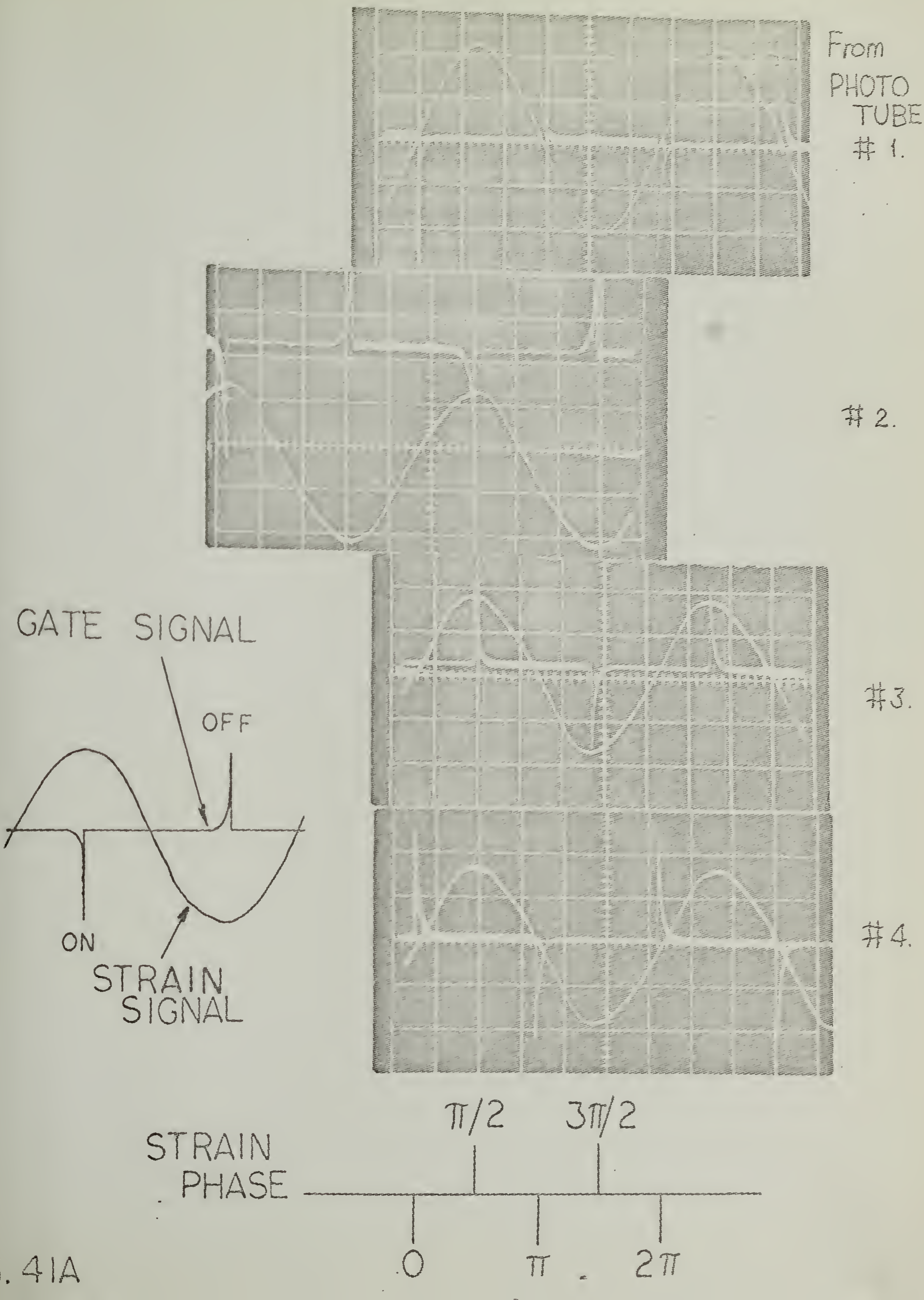
From PHOTO TUBE #1.
#2.
#3.
#4.
GATE SIGNAL
OFF
ON
STRAIN SIGNAL
STRAIN PHASE
π/2
3π/2
0
π
2π

FIG. 41A

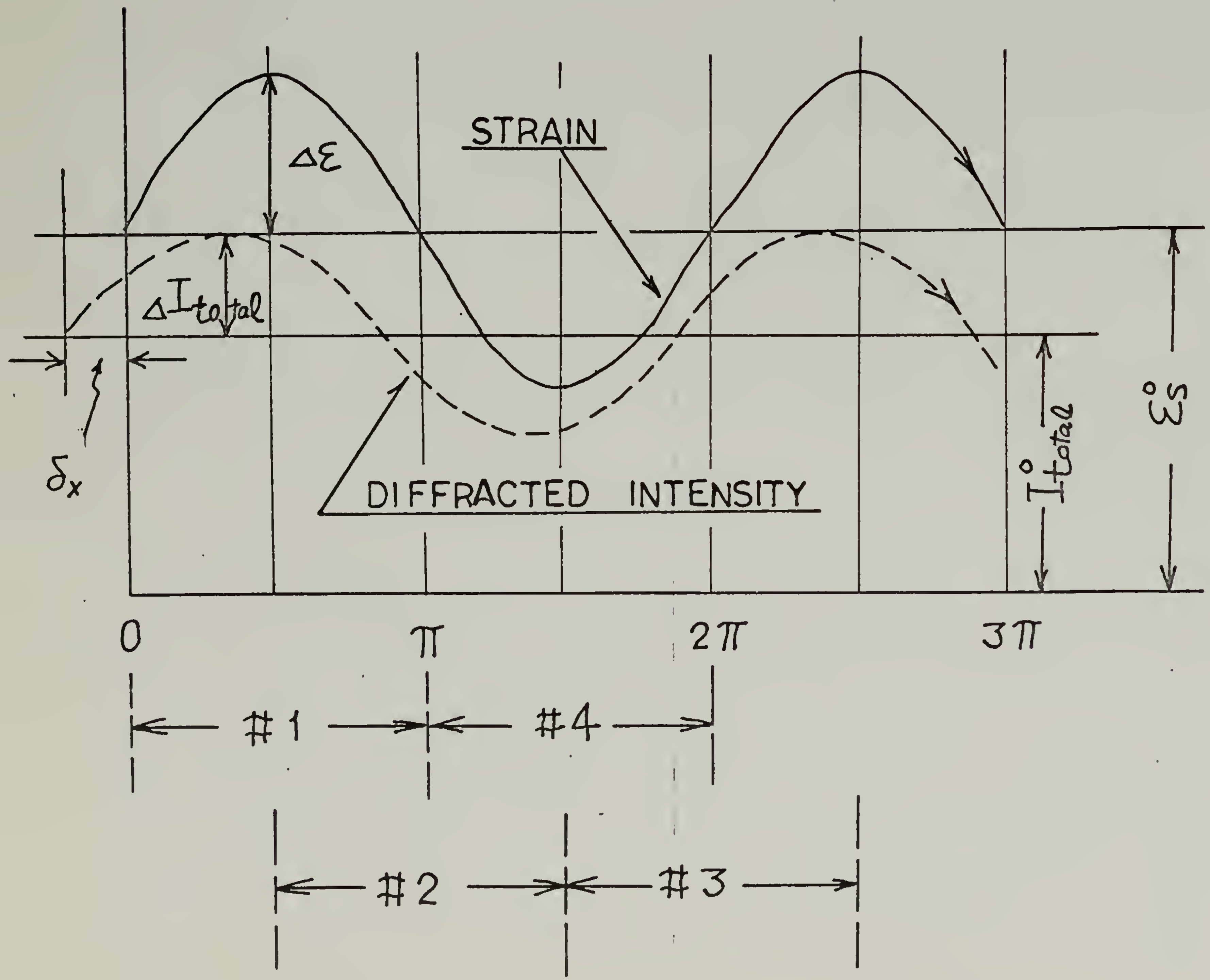

FIG.41B

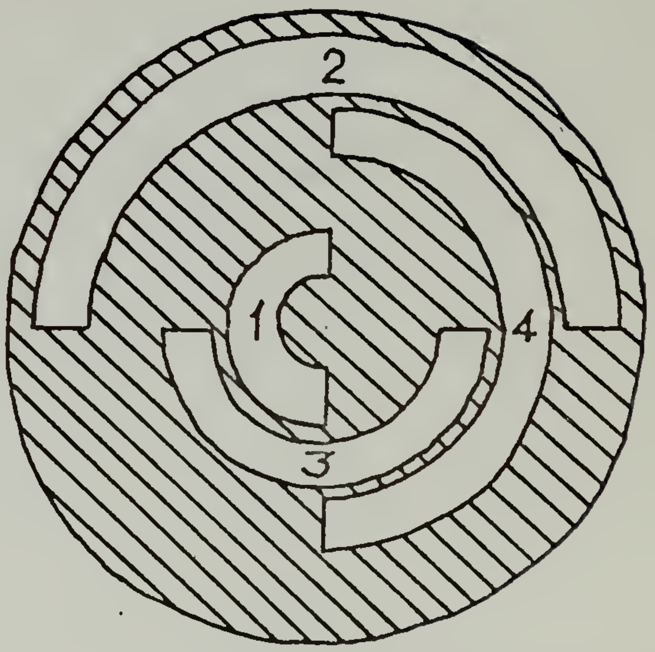

FIG.42A

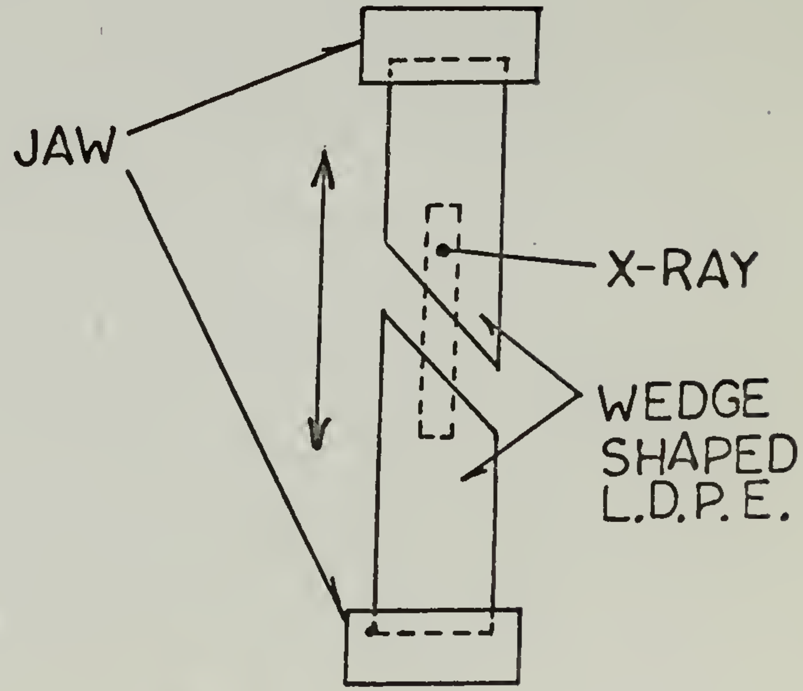

FIG.42B

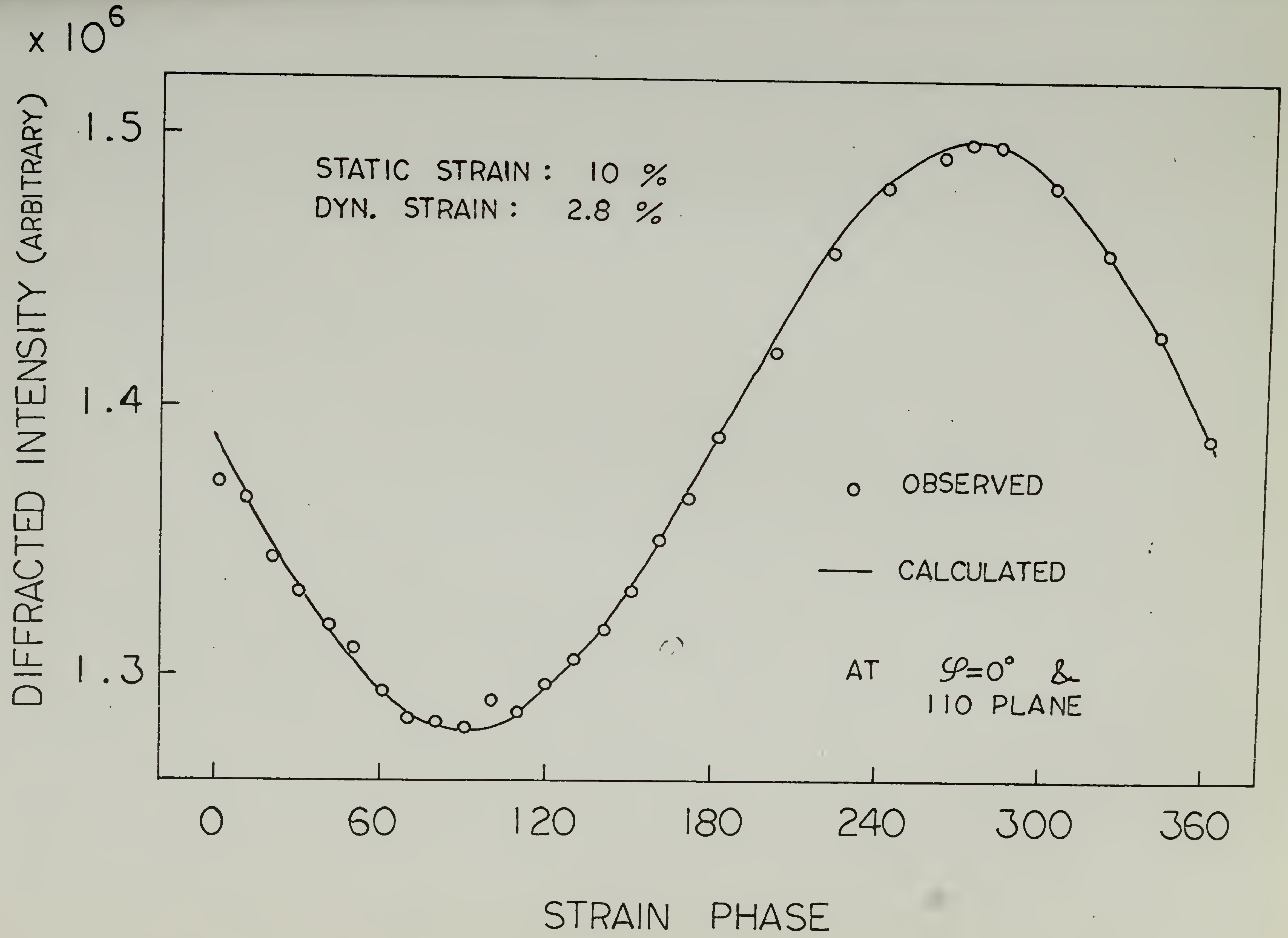
x 10^6
DIFFRACTED INTENSITY (ARBITRARY)
1.5
1.4
1.3
STATIC STRAIN : 10 %
DYN. STRAIN : 2.8 %
○ OBSERVED
— CALCULATED
AT φ=0° &
110 PLANE
0
60
120
180
240
300
360
STRAIN PHASE

FIG.43

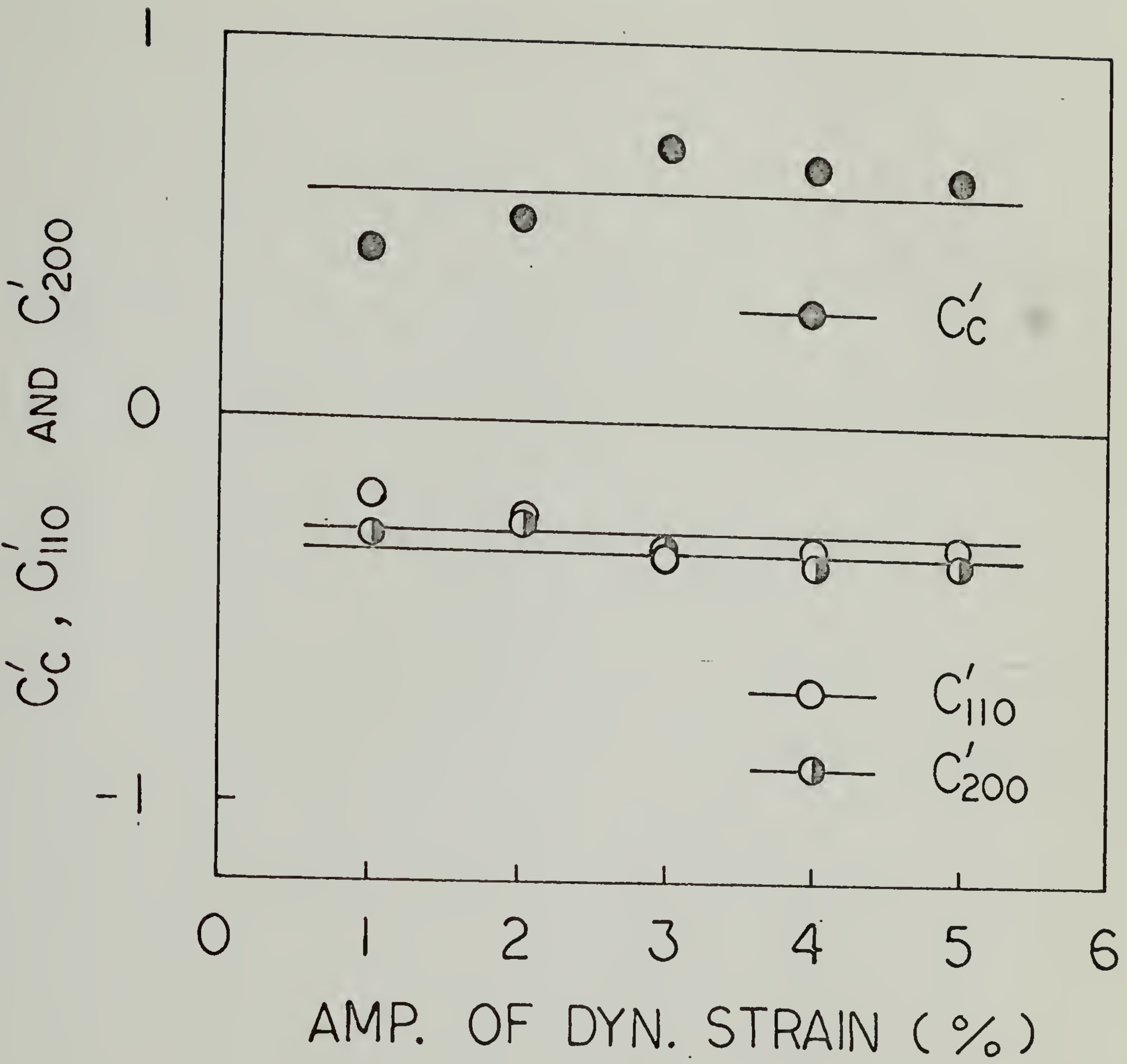

SAMPLE Q
FREQ. 1.0 C.P.S.
TEMP. 30 °C
STATIC STRAIN 10 %

FIG. 44

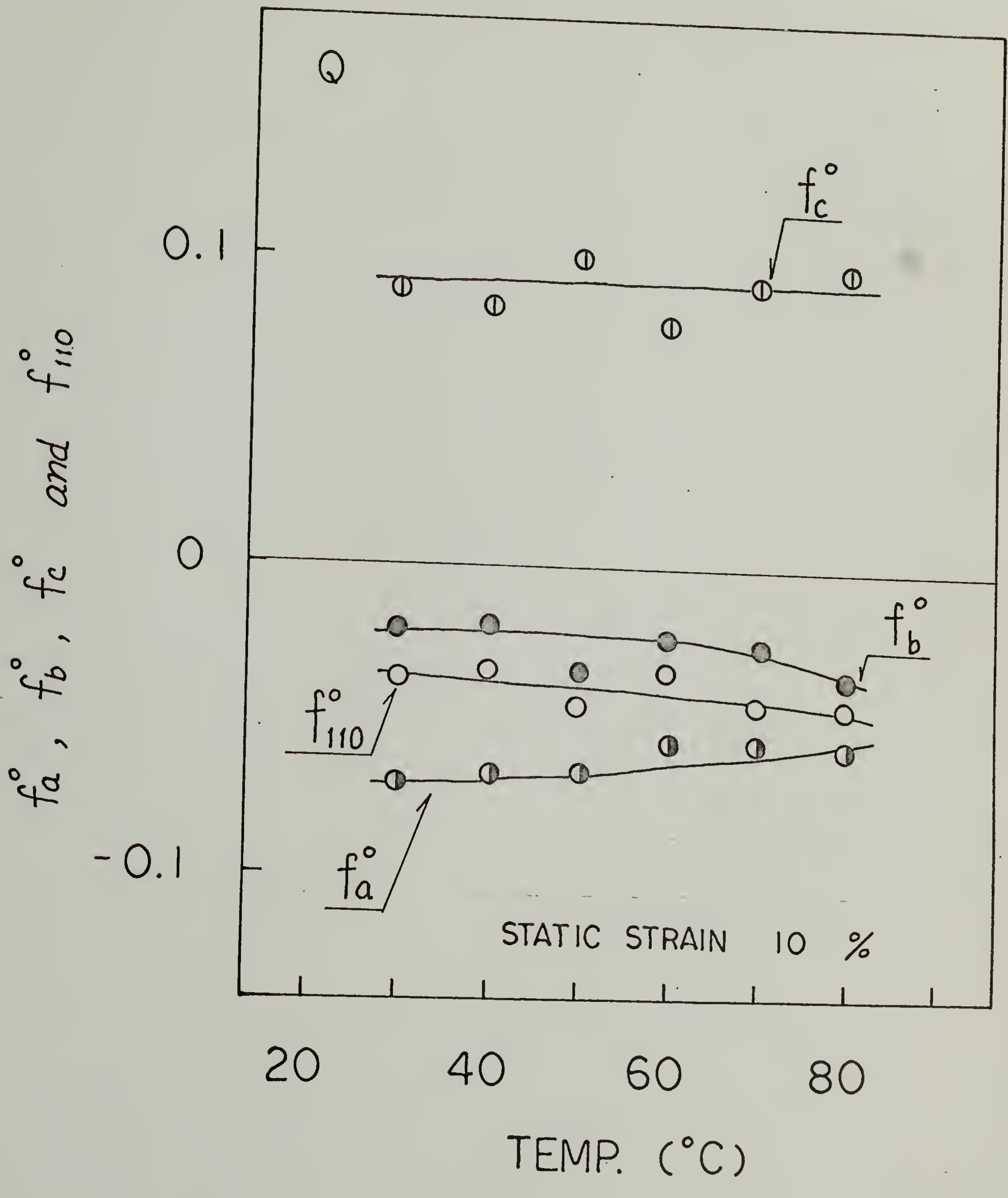
Q
f_c°
f_b°
f_{110}°
f_a°
0.1
0
-0.1
f_a°, f_b°, f_c° and $f_{11.0}^\circ$
STATIC STRAIN 10 %
20
40
60
80
TEMP. (°C)

FIG.45

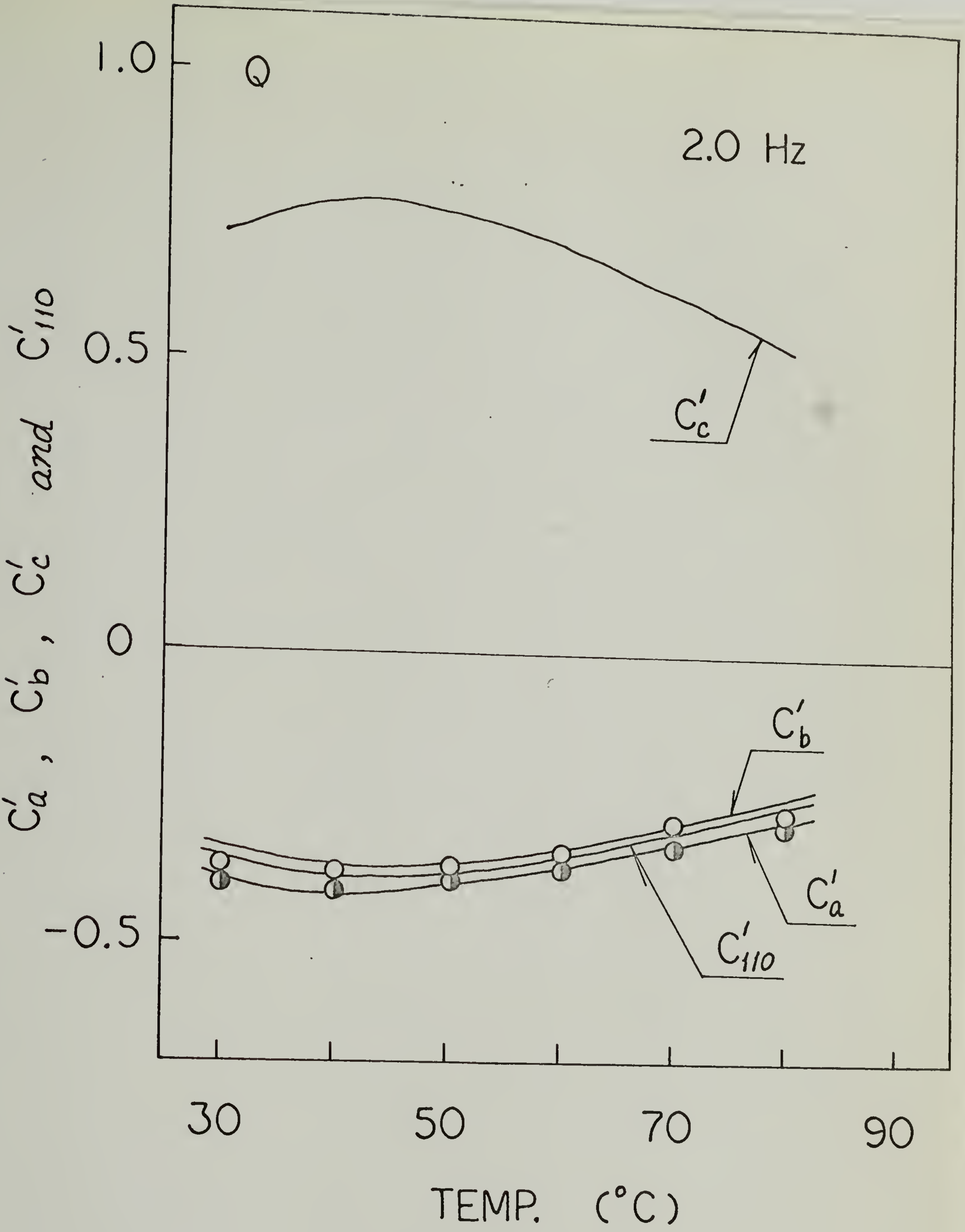

FIG.46

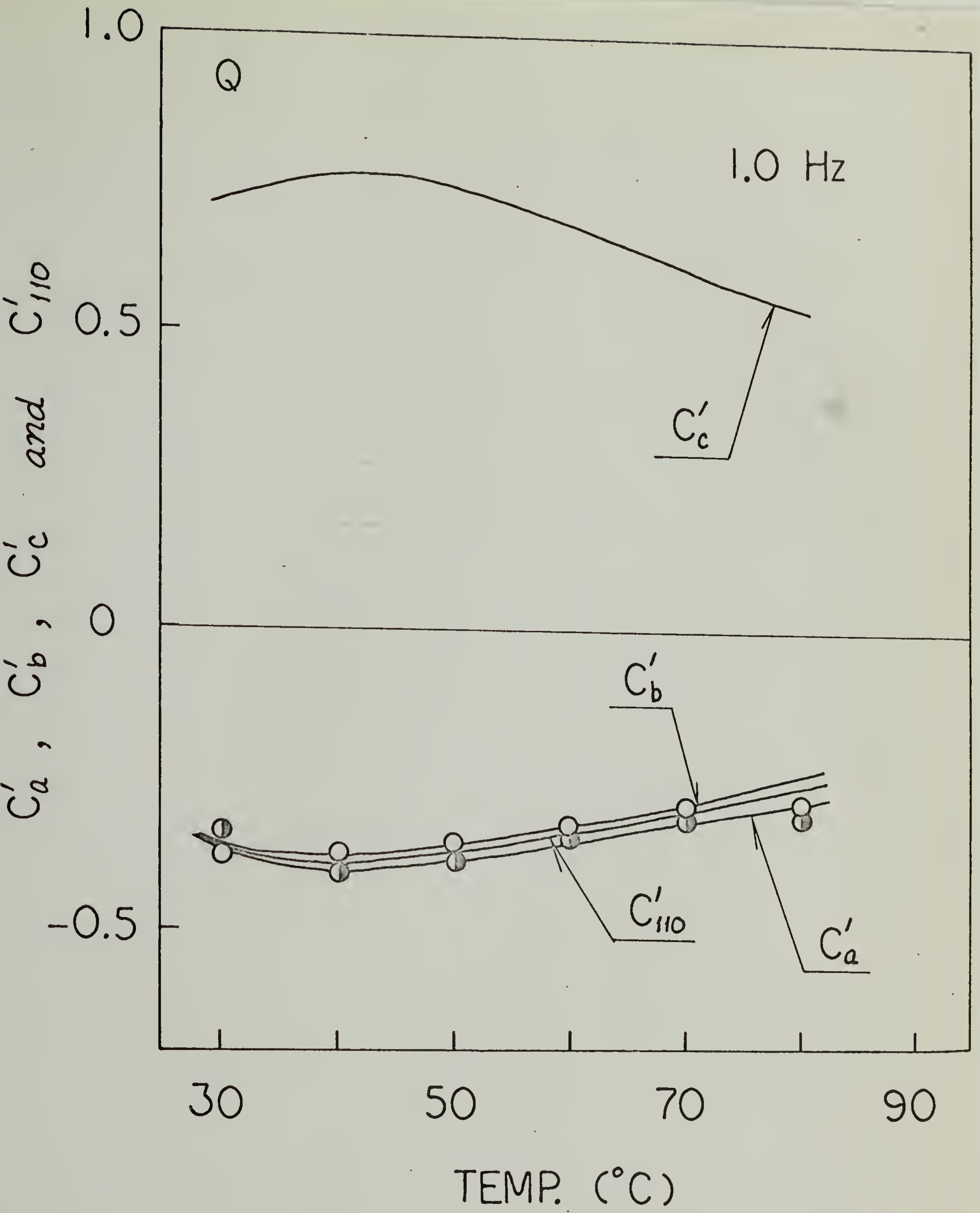

FIG.47

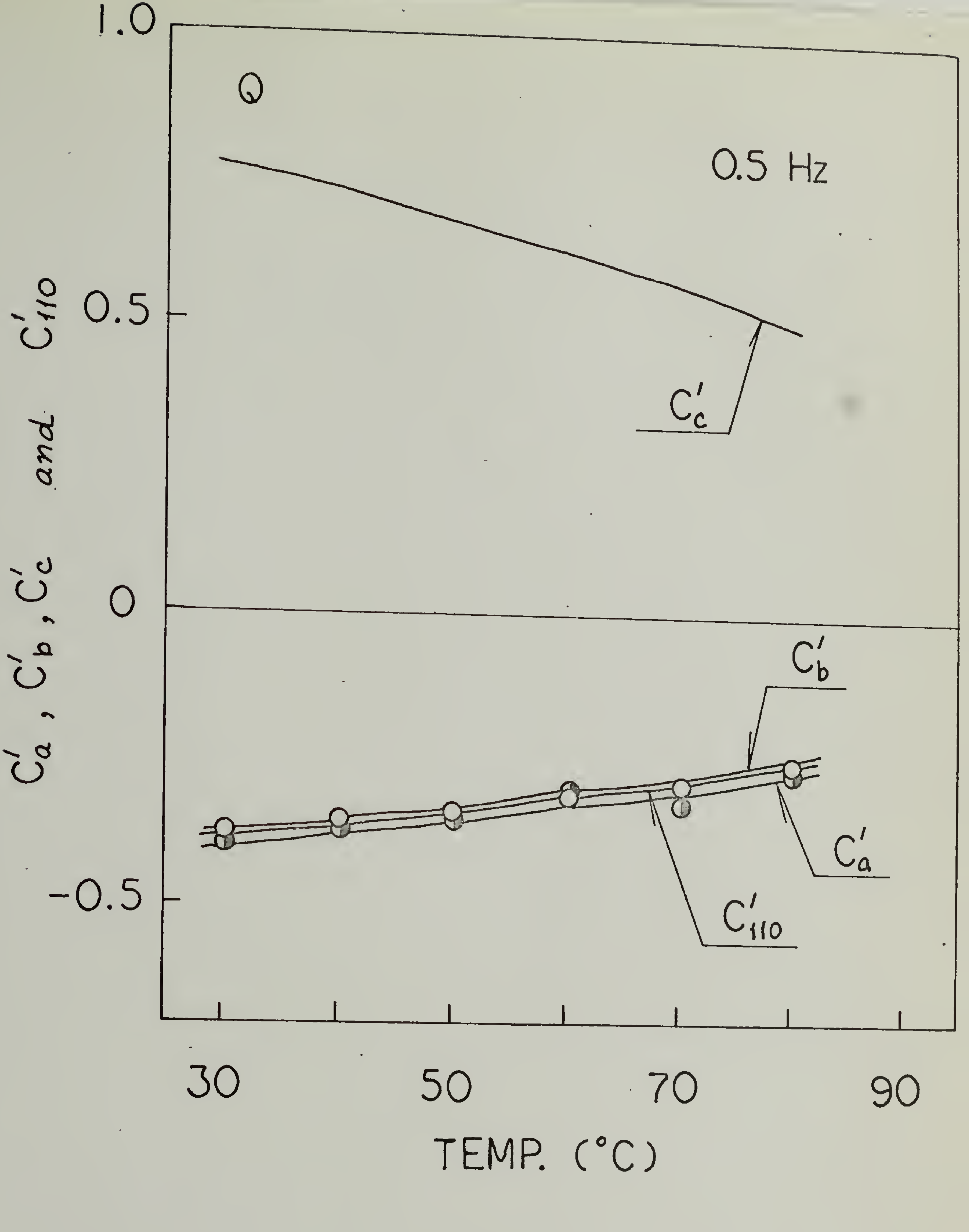

FIG.48

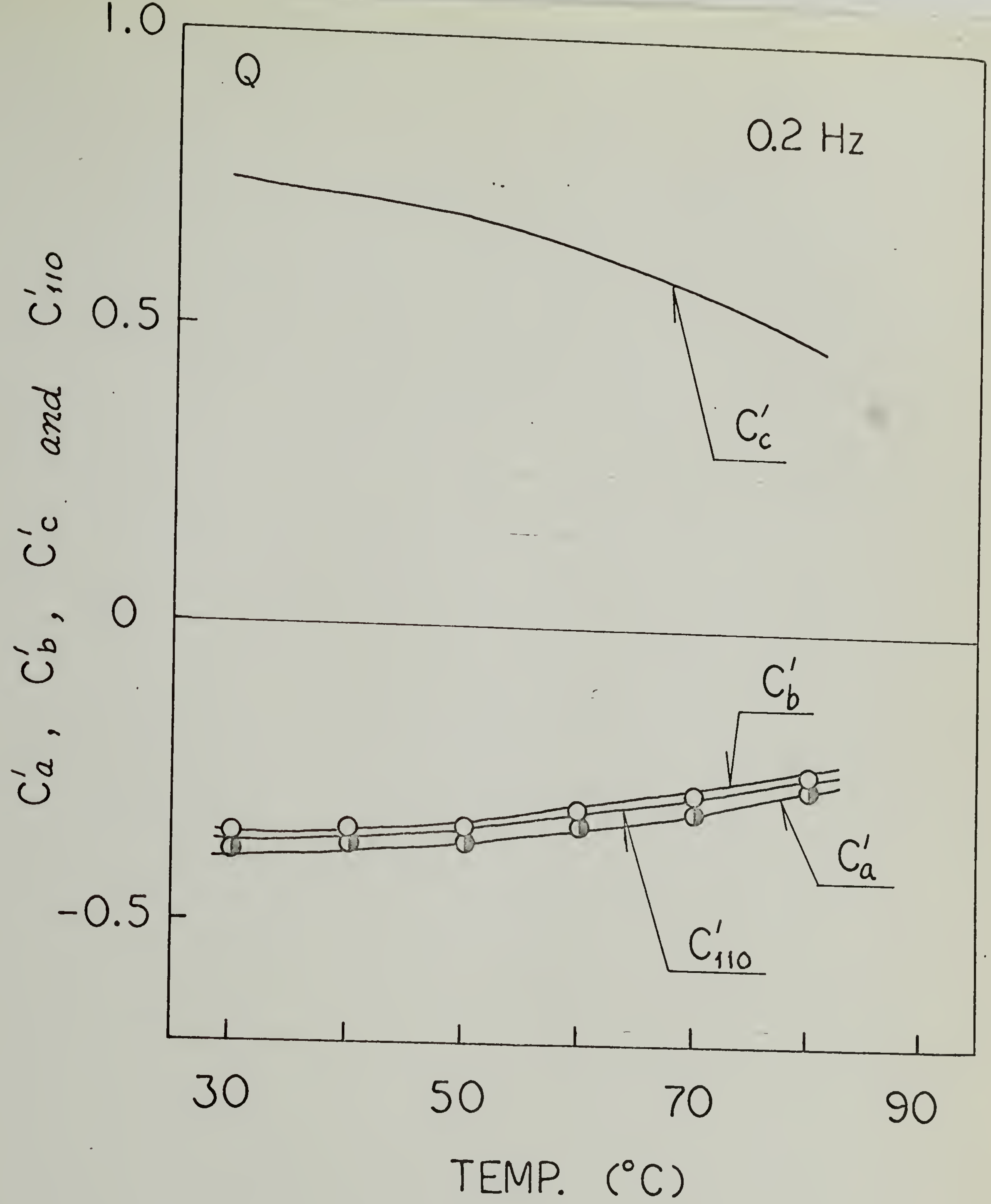

FIG.49

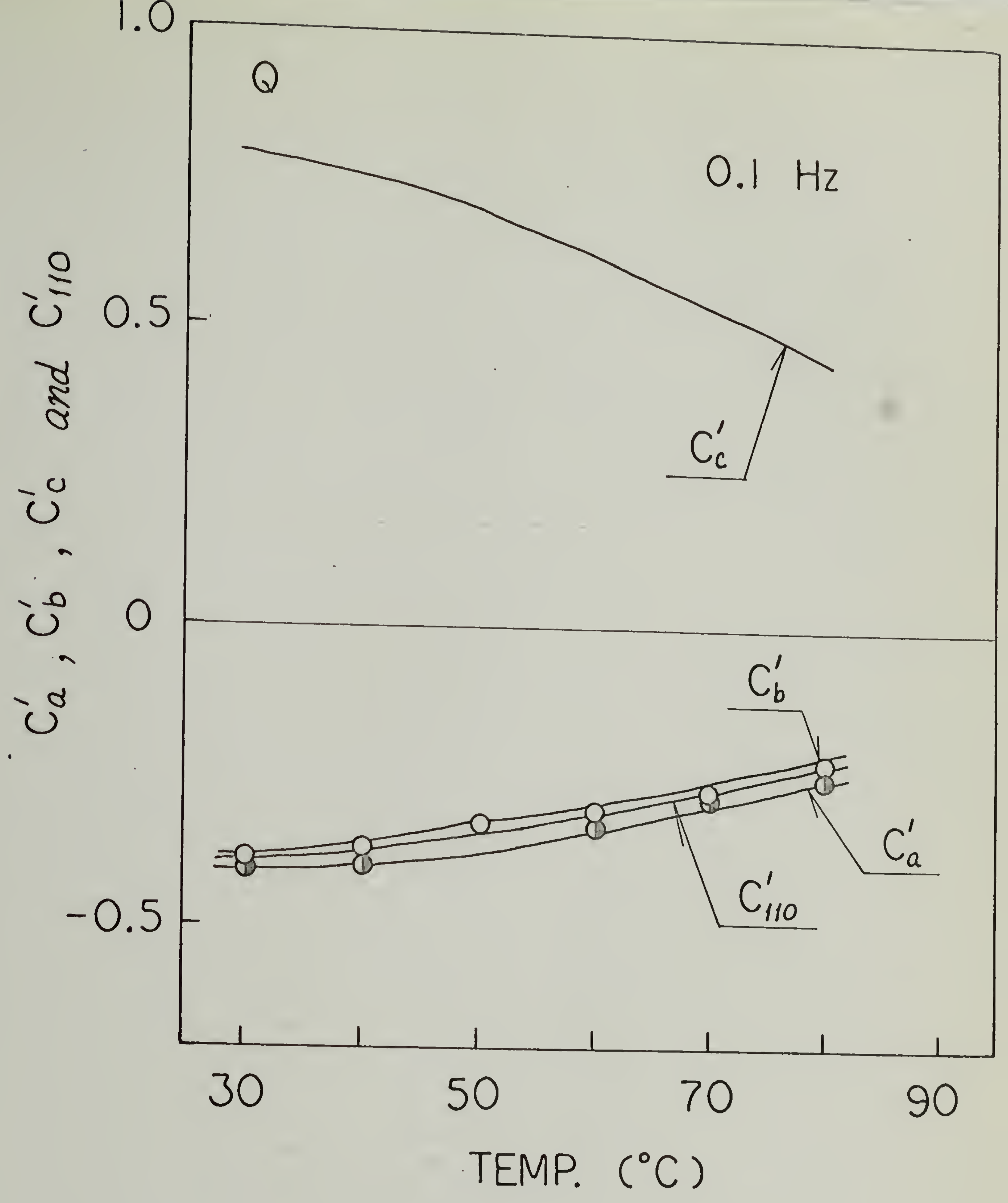

FIG. 50

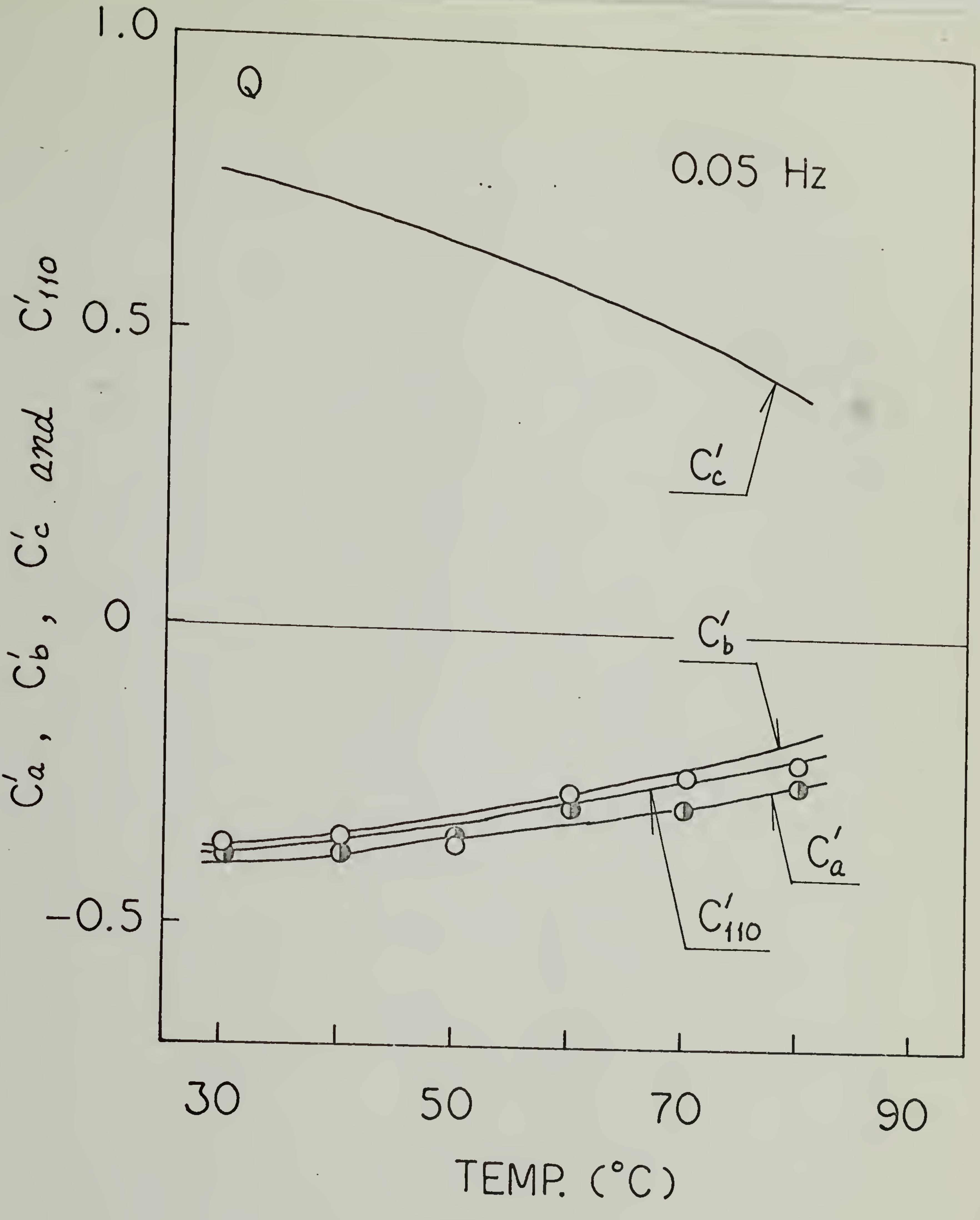

FIG. 51

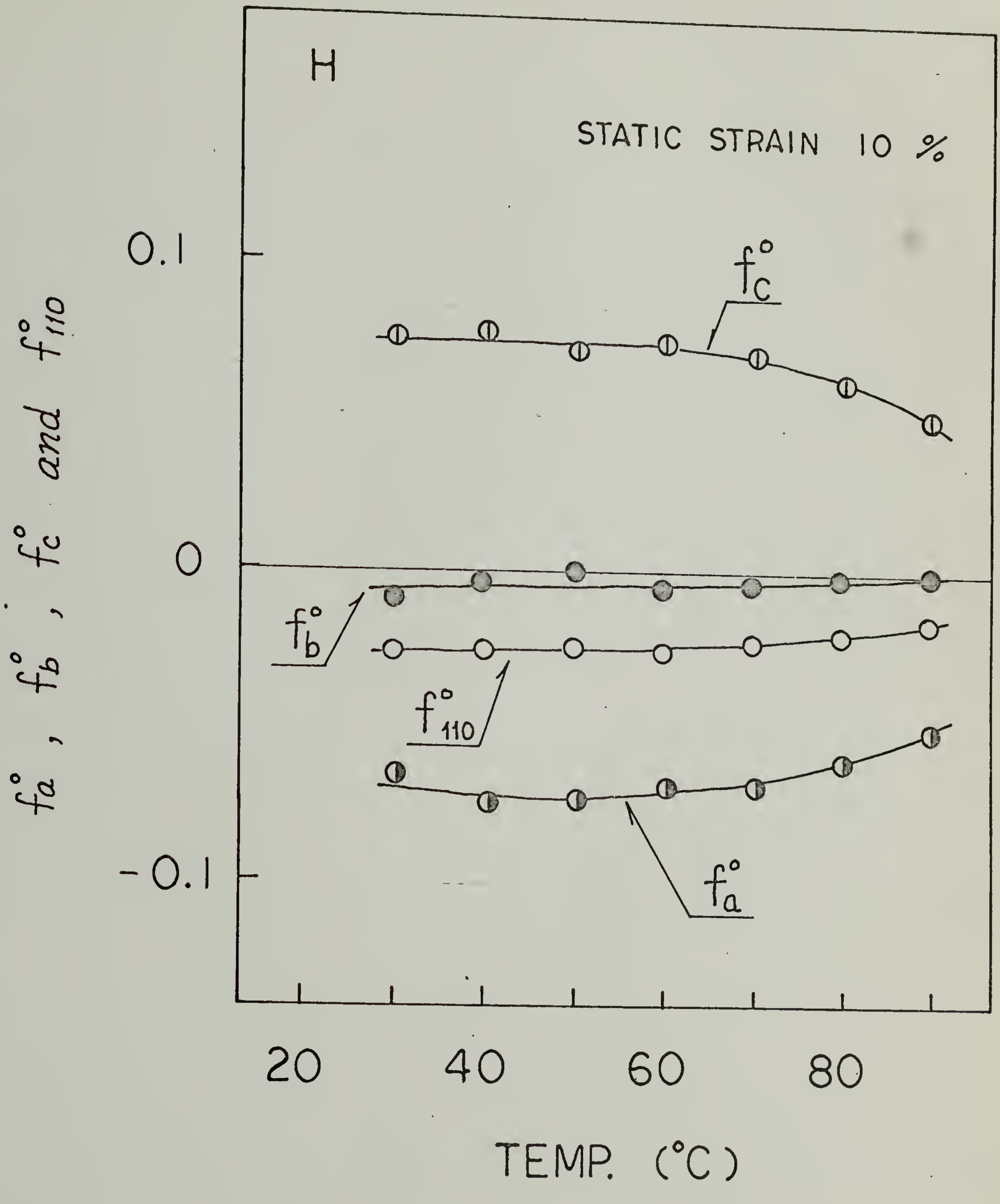
H
STATIC STRAIN 10 %
0.1
0
-0.1
f_c°
f_b°
f_{110}°
f_a°
f_a° , f_b° , f_c° and f_{110}°
20
40
60
80
TEMP. (°C)

FIG.52

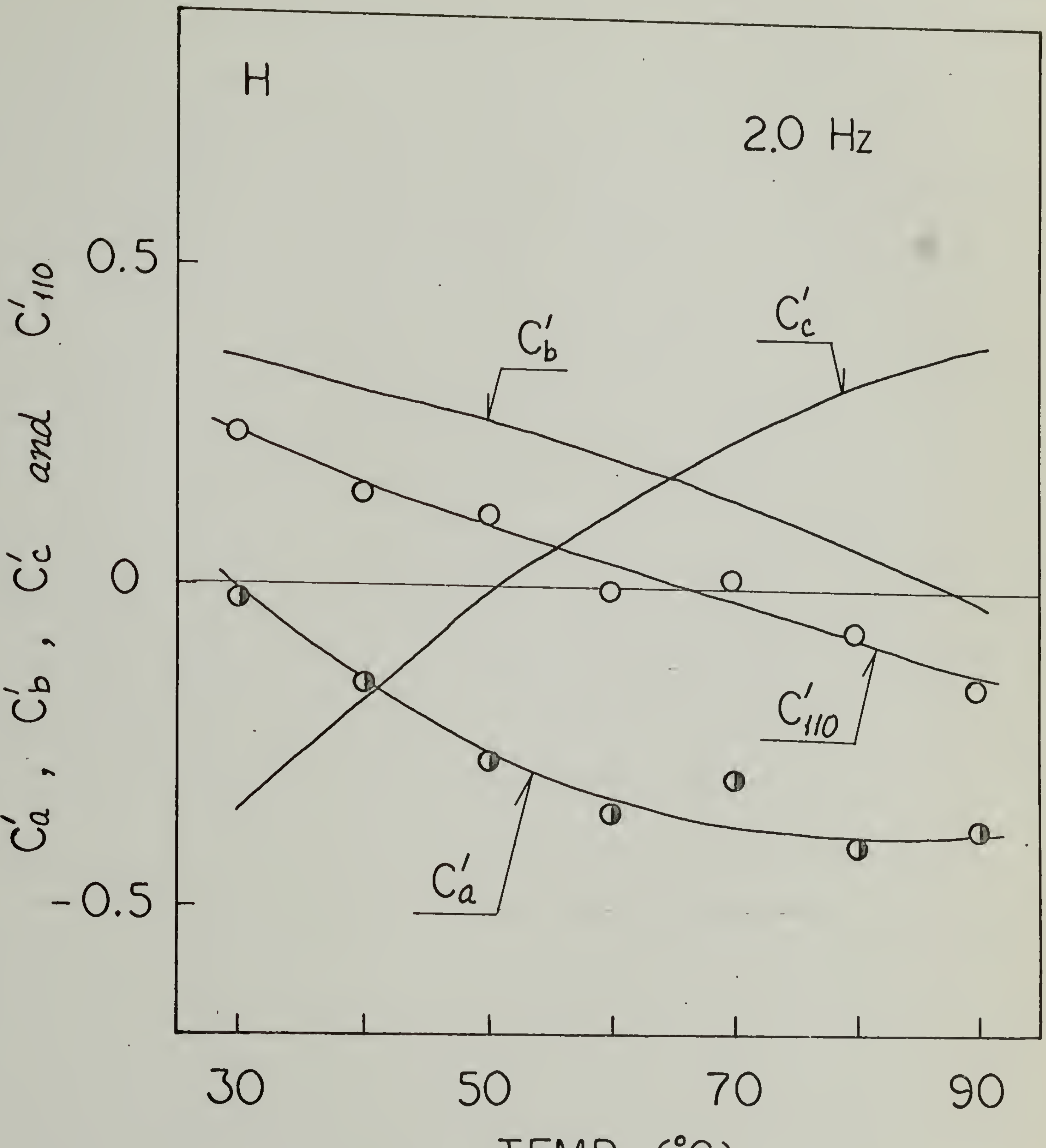

FIG. 53

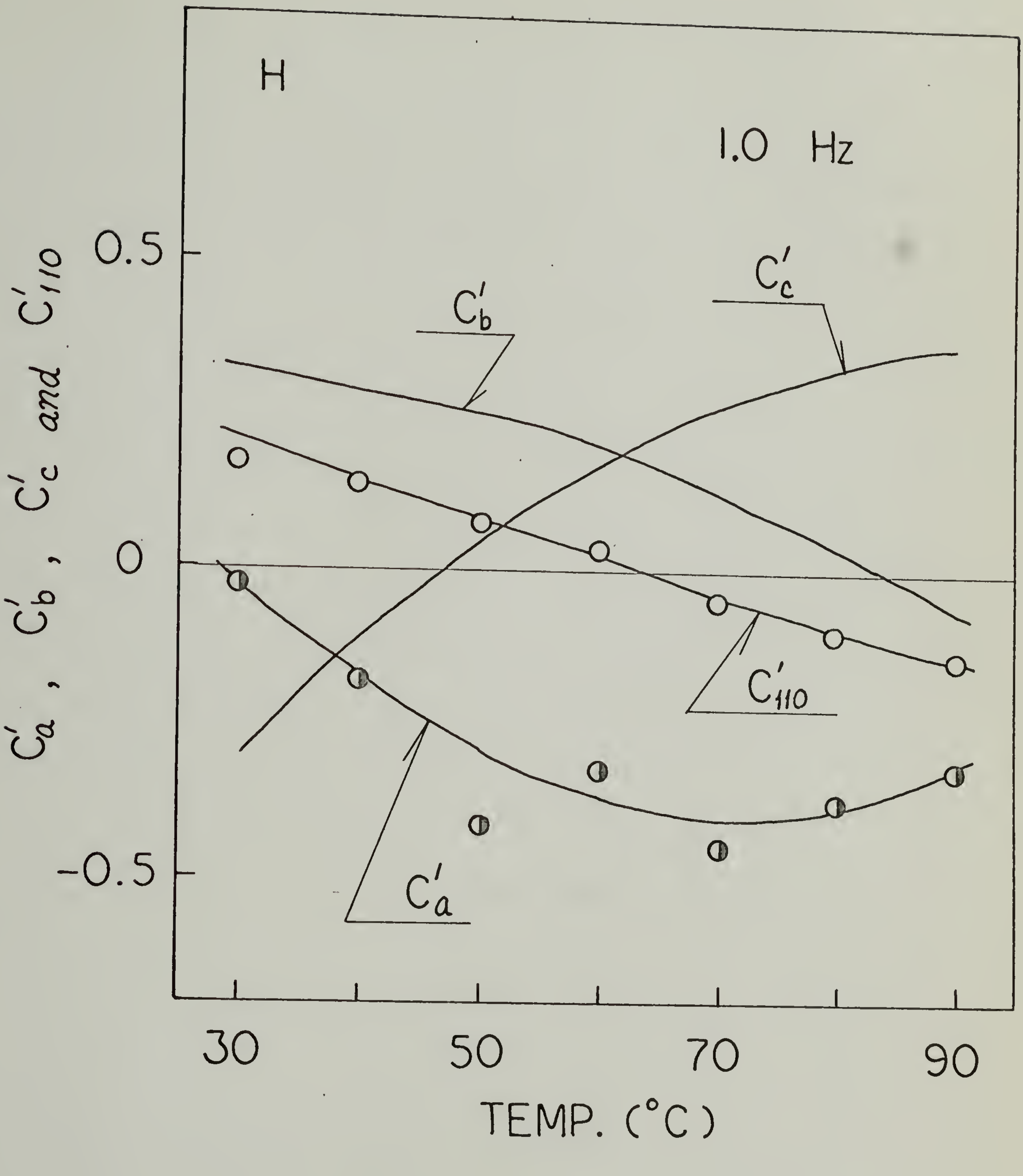

FIG. 54

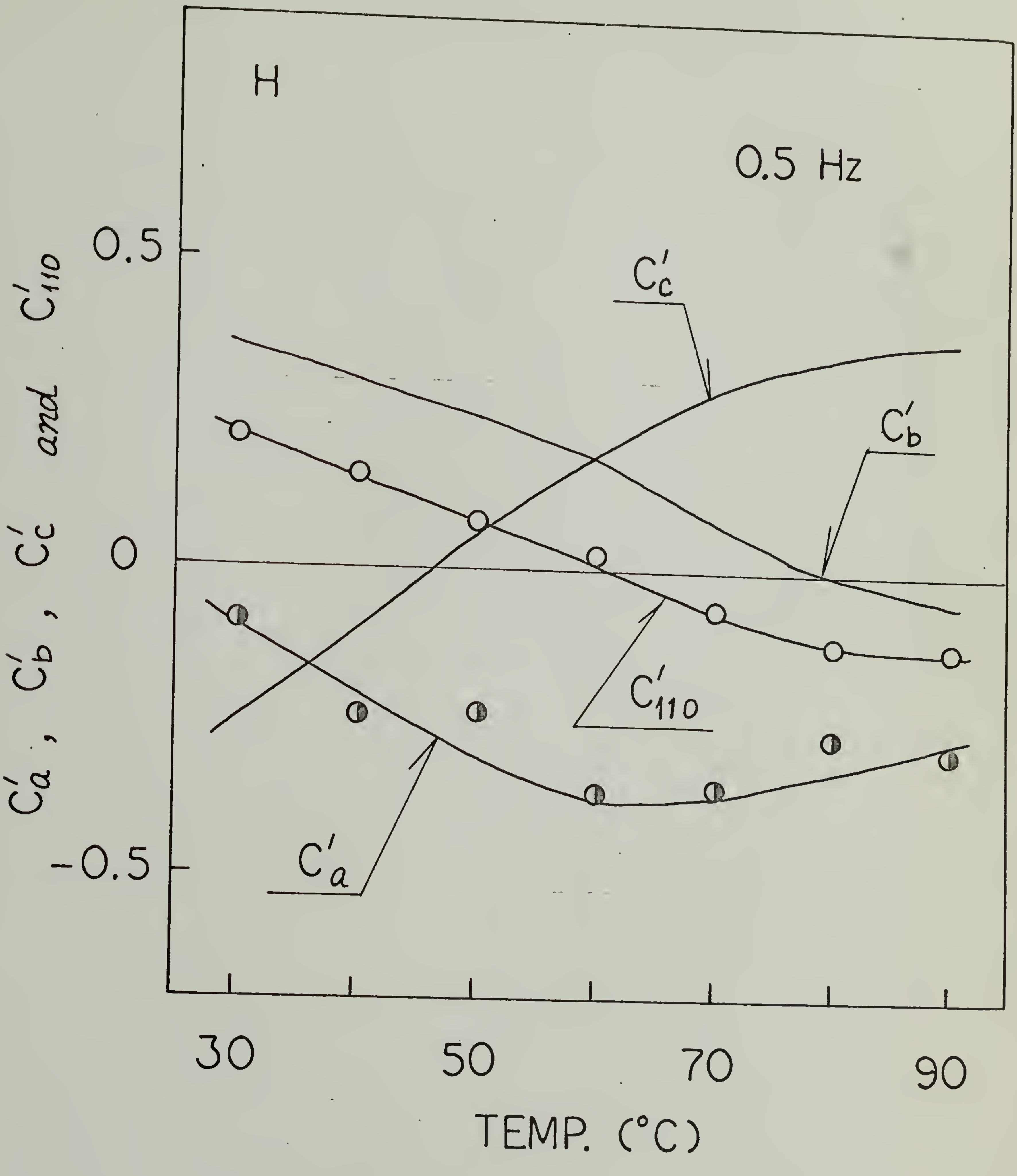

FIG. 55

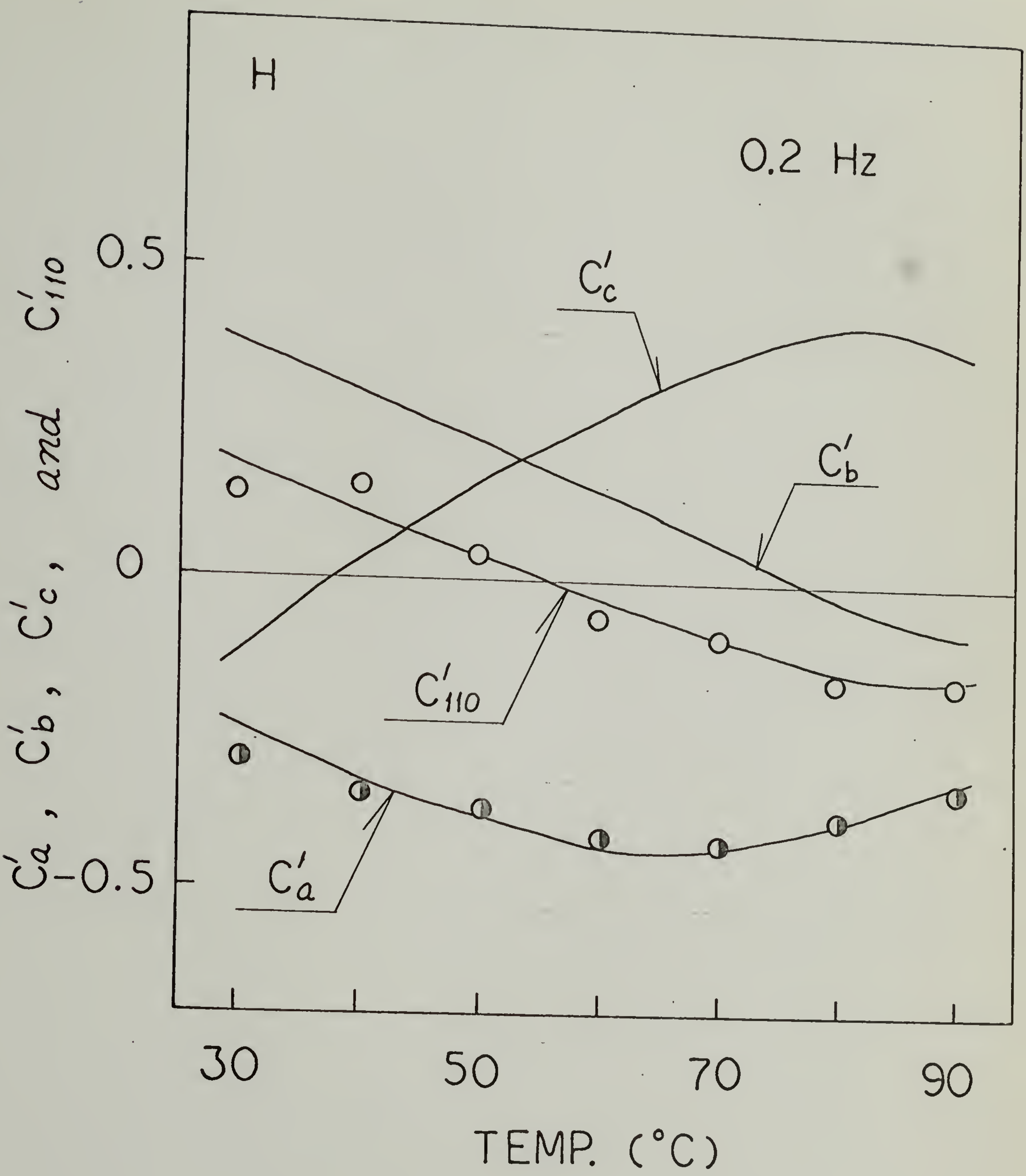

FIG. 56

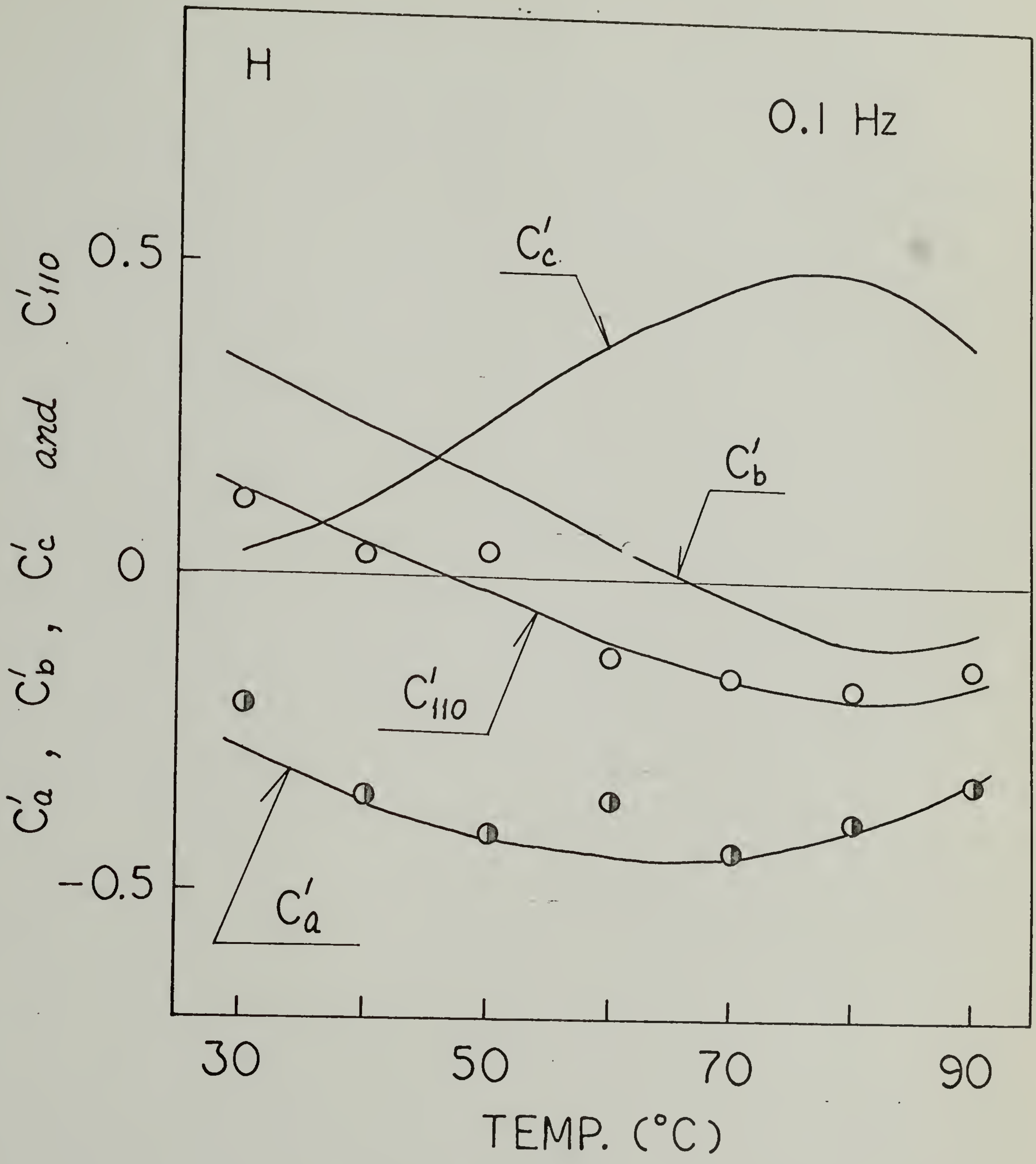

FIG. 57

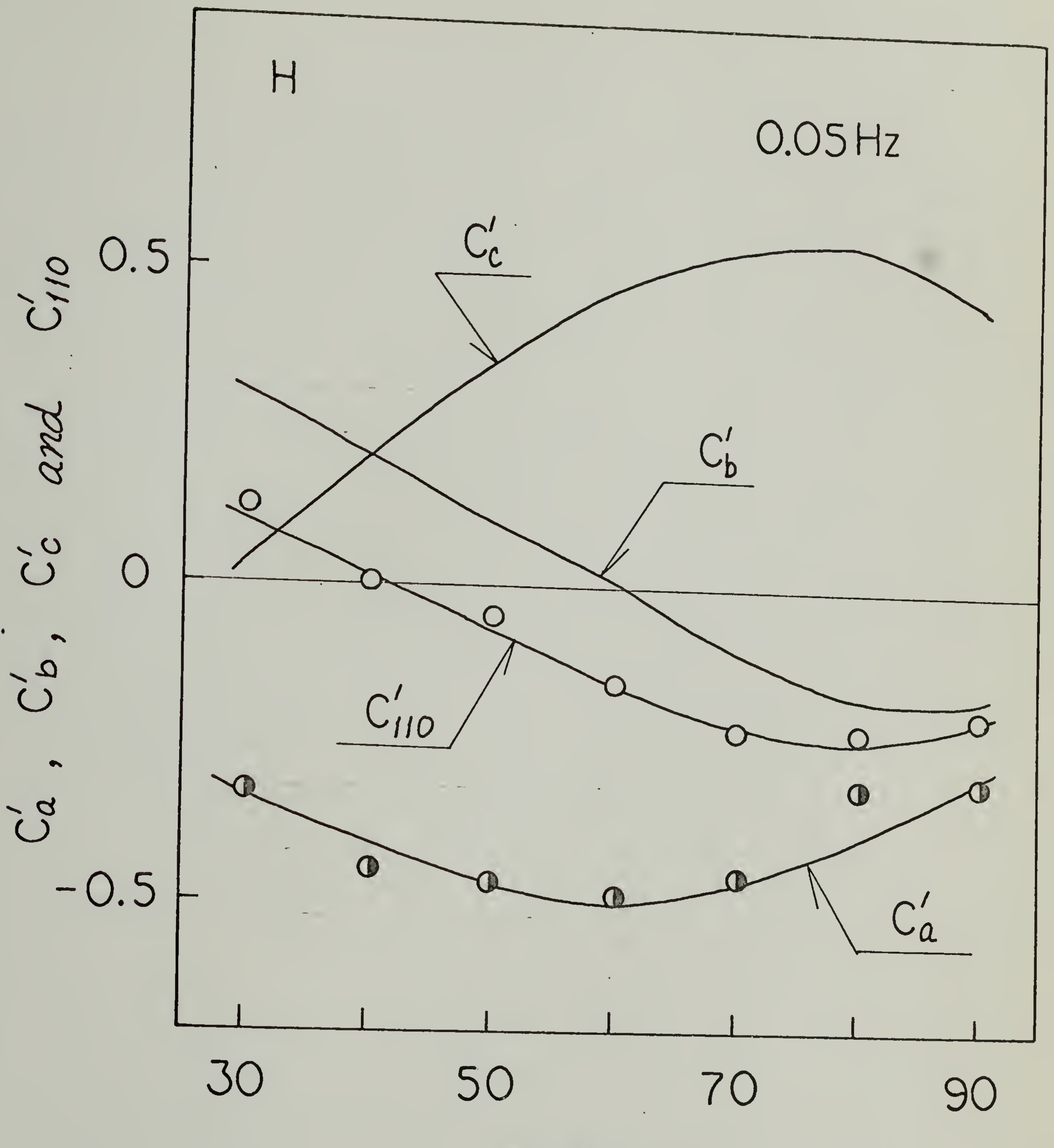

FIG. 58

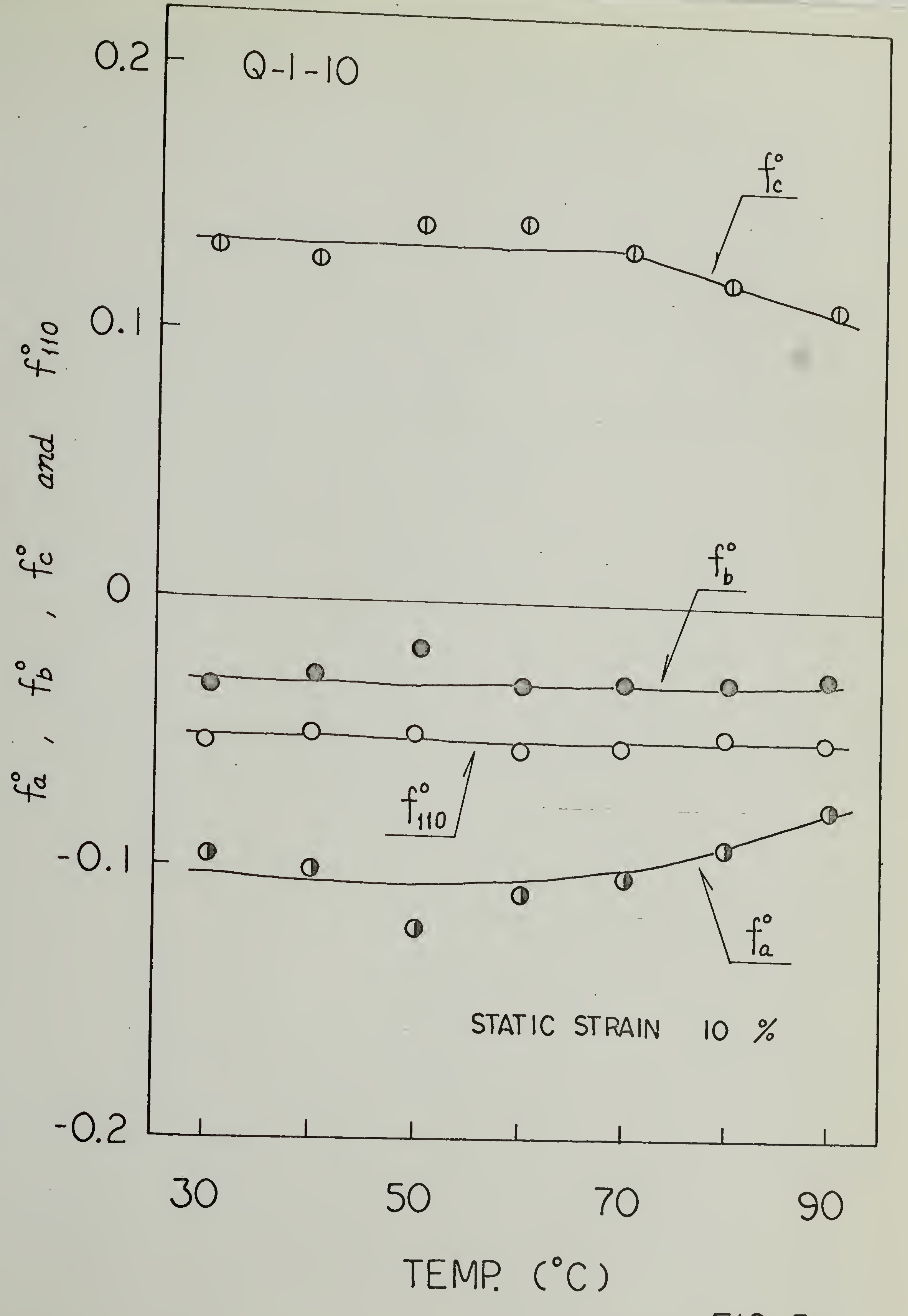
Q-1-10
0.2
0.1
0
-0.1
-0.2
f_a° , f_b° , f_c° and f_{110}°
f_c°
f_b°
f_{110}°
f_a°
STATIC STRAIN 10 %
30
50
70
90
TEMP. (°C)

FIG. 59

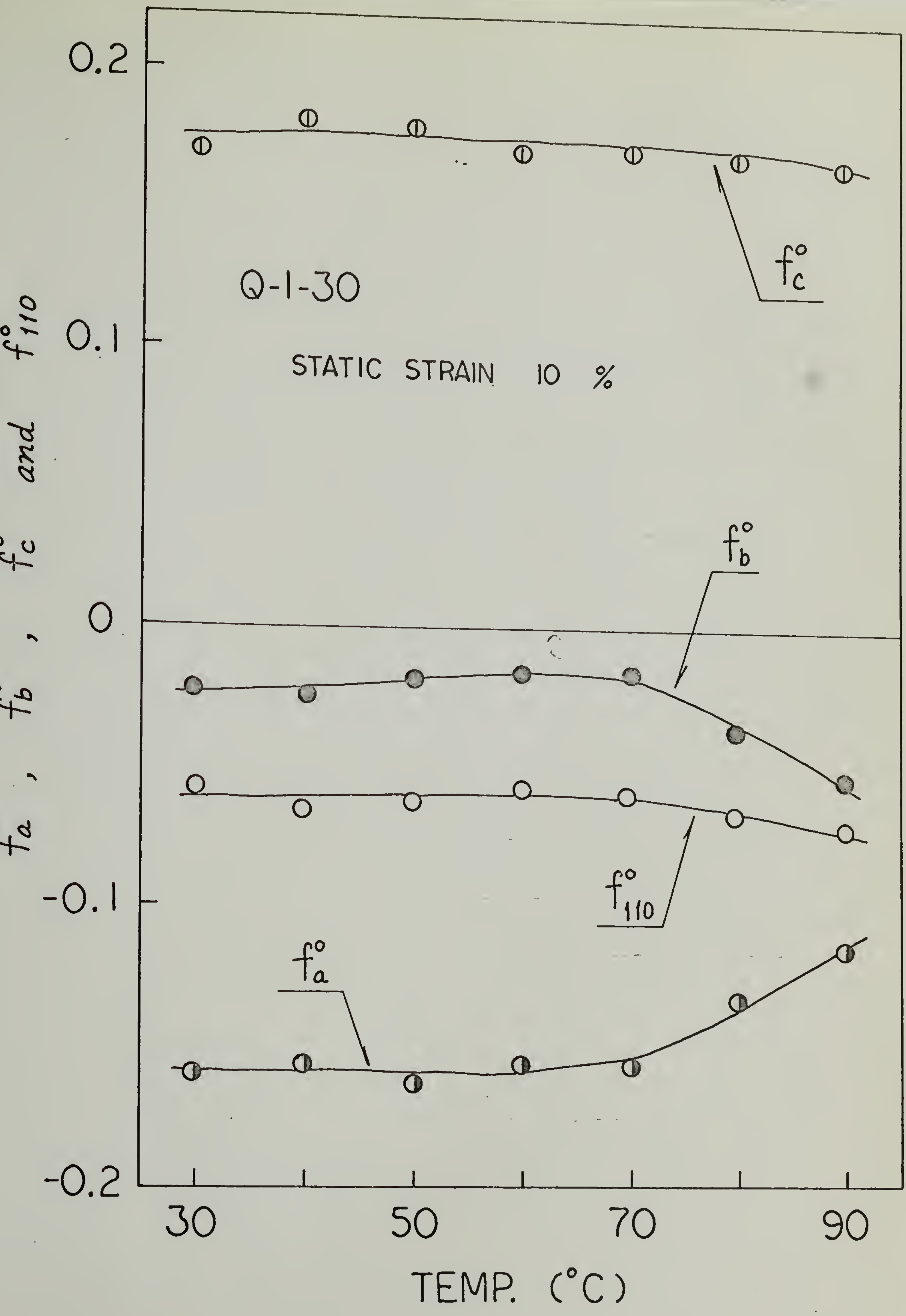
0.2
0.1
0
-0.1
-0.2
f_a° , f_b° , f_c° and f_{110}°
Q-1-30
STATIC STRAIN 10 %
f_c°
f_b°
f_{110}°
f_a°
30
50
70
90
TEMP. (°C)

FIG. 60

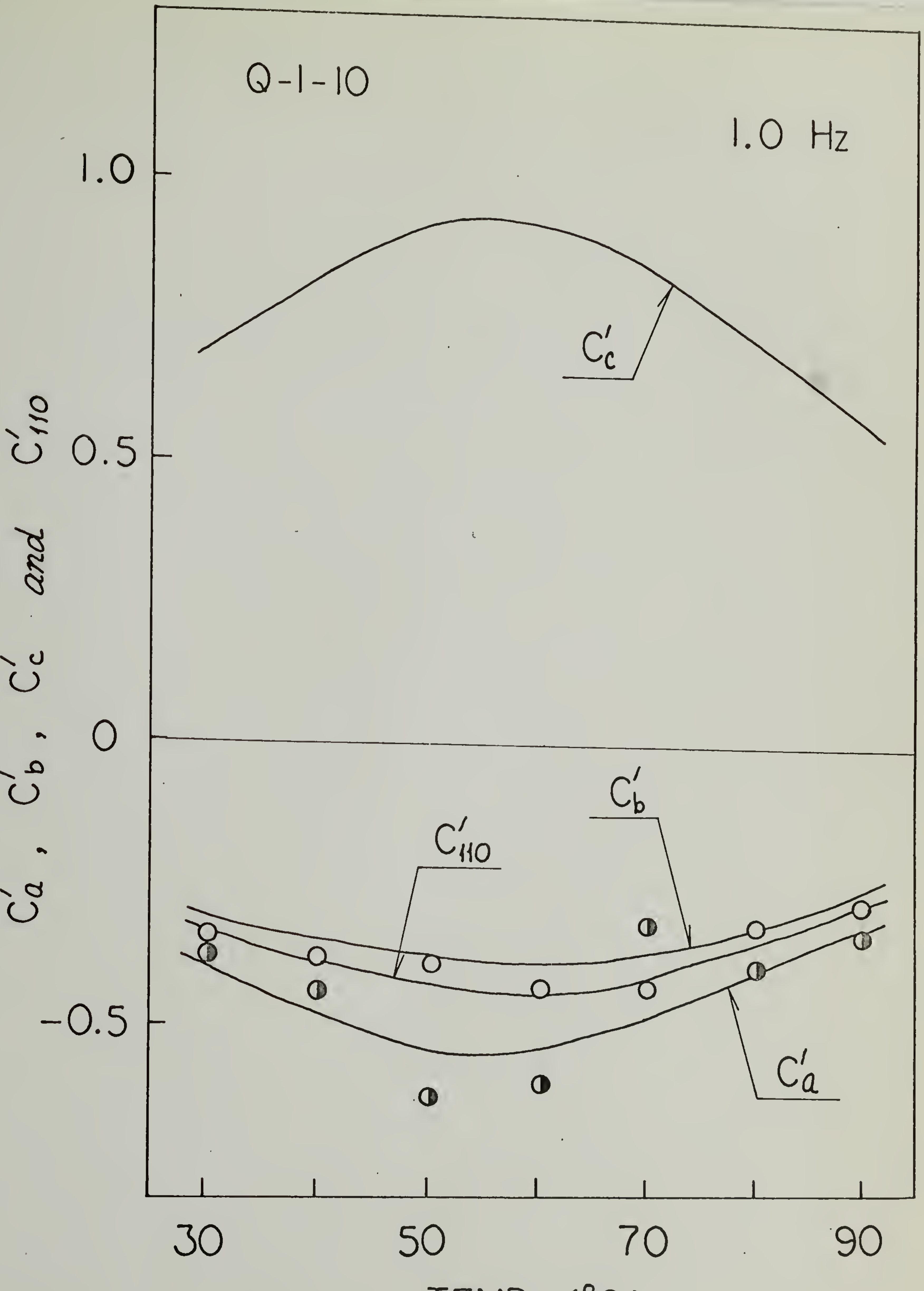
Q-1-10
1.0 Hz
1.0
0.5
0
-0.5
C'a , C'b , C'c and C'110
C'c
C'b
C'110
C'a
30
50
70
90
TEMP. (°C)

FIG. 61

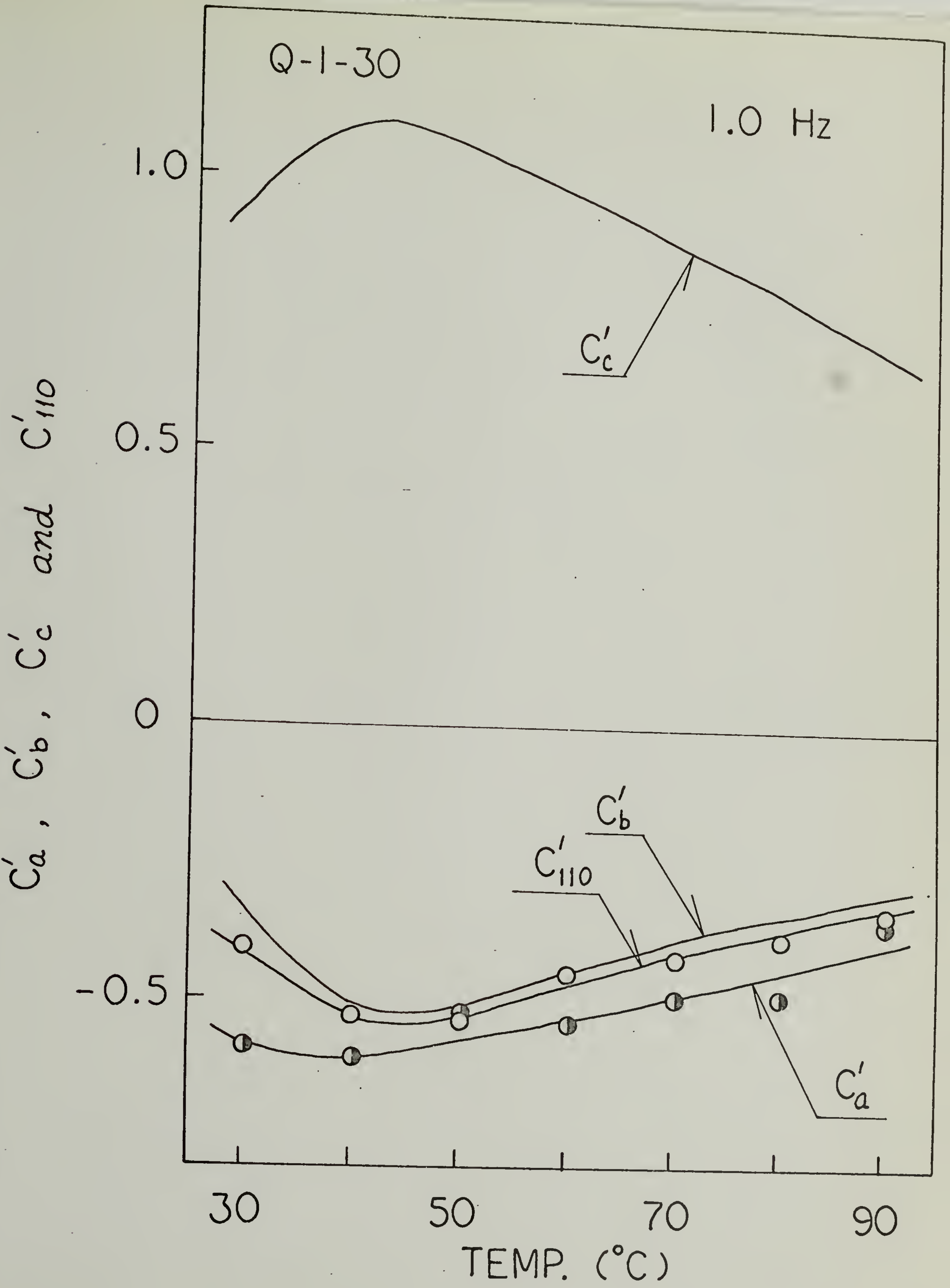
Q-1-30
1.0 Hz
C'_a, C'_b, C'_c and C'_{110}
1.0
0.5
0
-0.5
C'_c
C'_b
C'_{110}
C'_a
30
50
70
90
TEMP. (°C)

FIG. 62

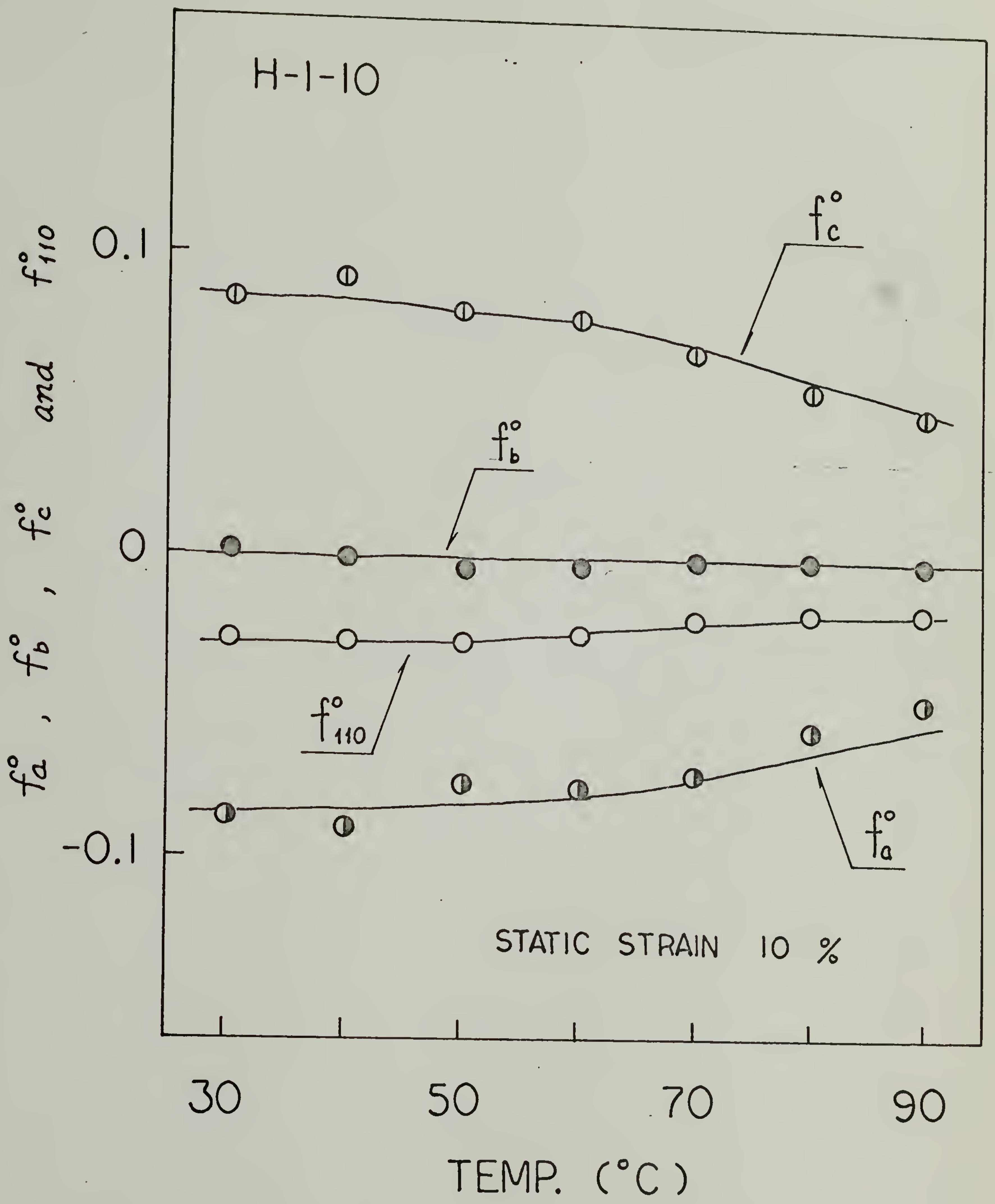
H-1-10
f_a° , f_b° , f_c° and f_{110}°
0.1
0
-0.1
f_c°
f_b°
f_{110}°
f_a°
STATIC STRAIN 10 %
30
50
70
90
TEMP. (°C)

FIG. 63

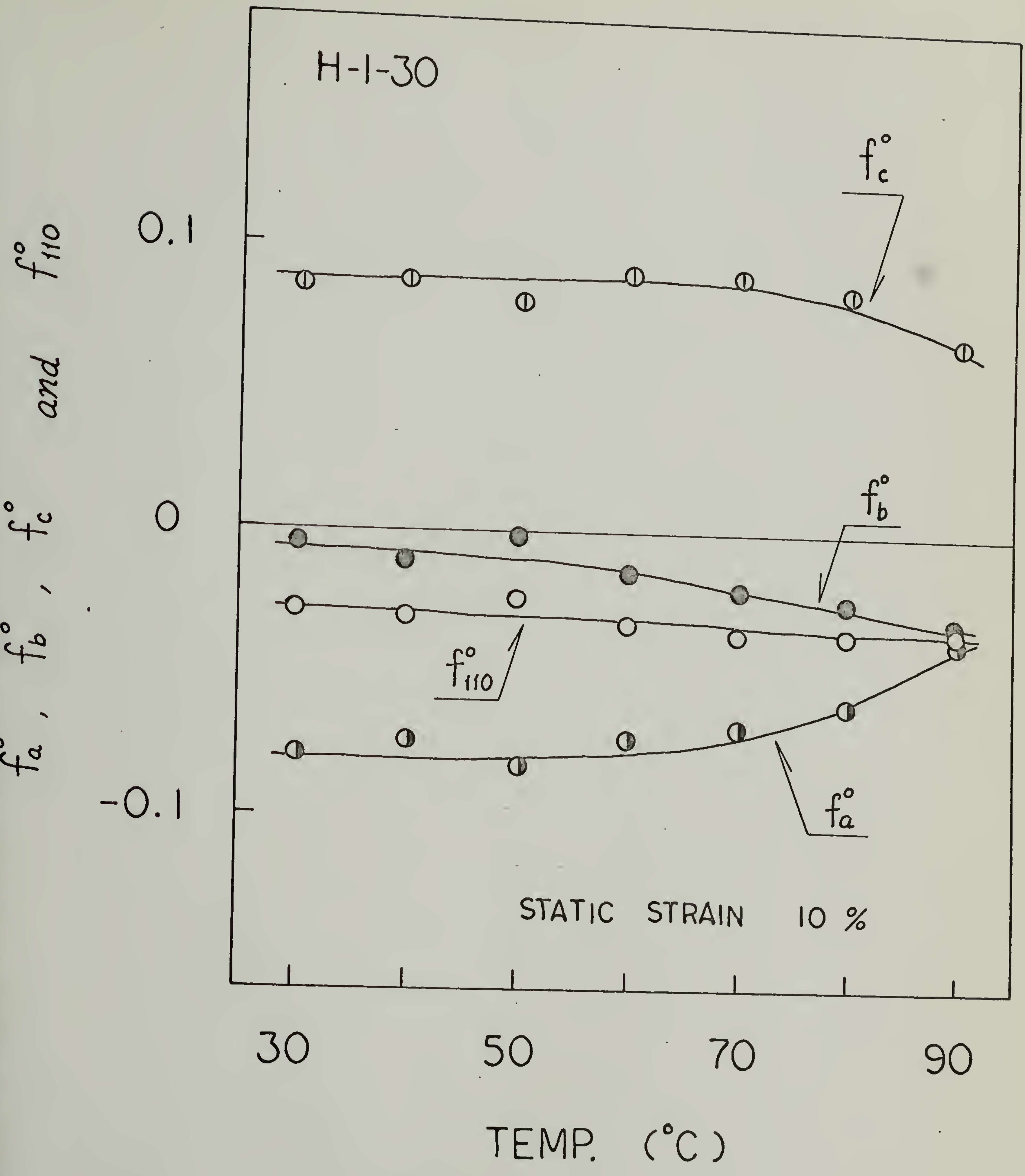
H-1-30
f_c°
f_b°
f_{110}°
f_a°
0.1
0
-0.1
f_a° , f_b° , f_c° and f_{110}°
STATIC STRAIN 10 %
30
50
70
90
TEMP. (°C)

FIG. 64

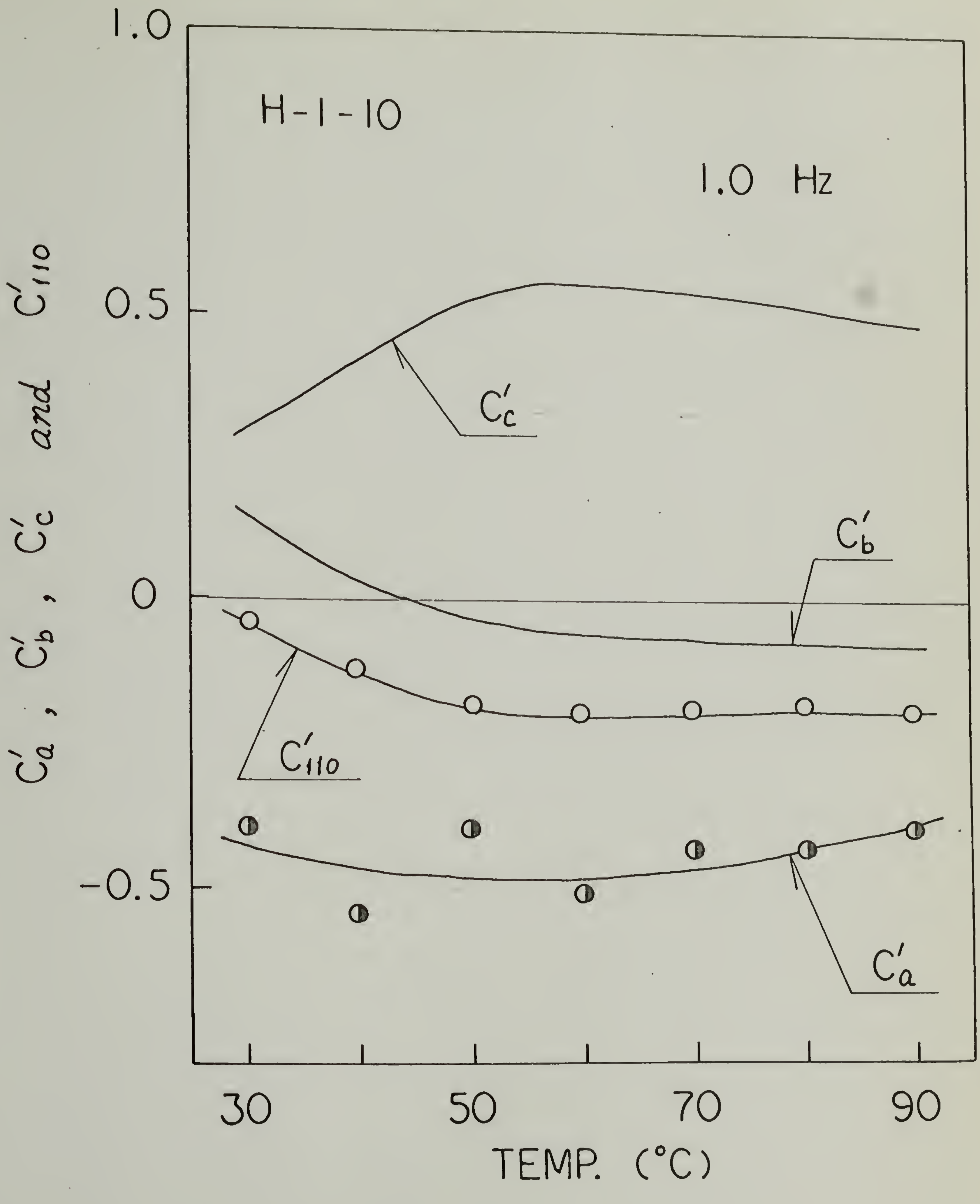
1.0
0.5
0
-0.5
H-1-10
1.0 Hz
C'_c
C'_b
C'_{110}
C'_a
30
50
70
90
TEMP. (°C)
C'_a , C'_b , C'_c and C'_{110}

FIG. 65

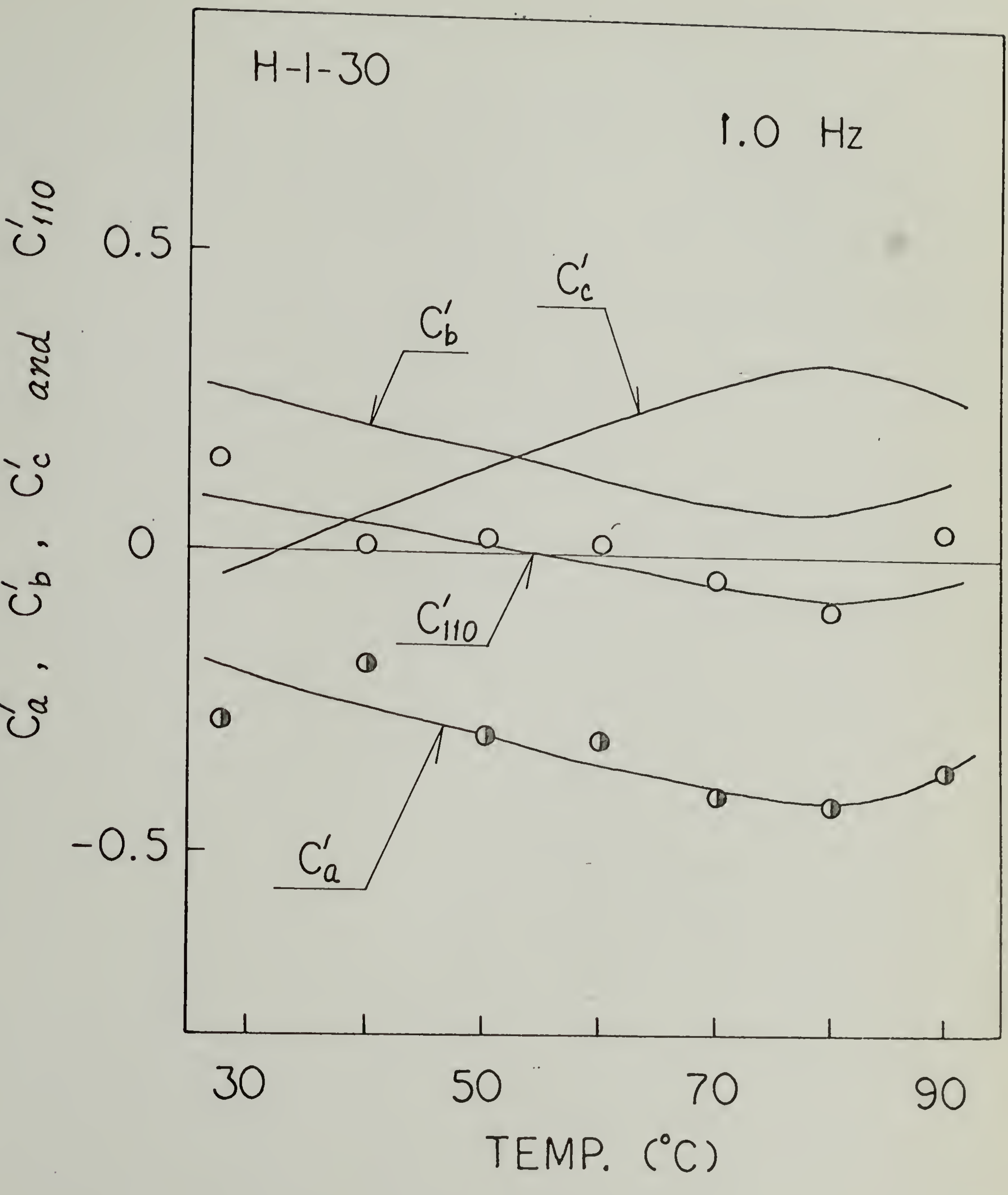

FIG.66

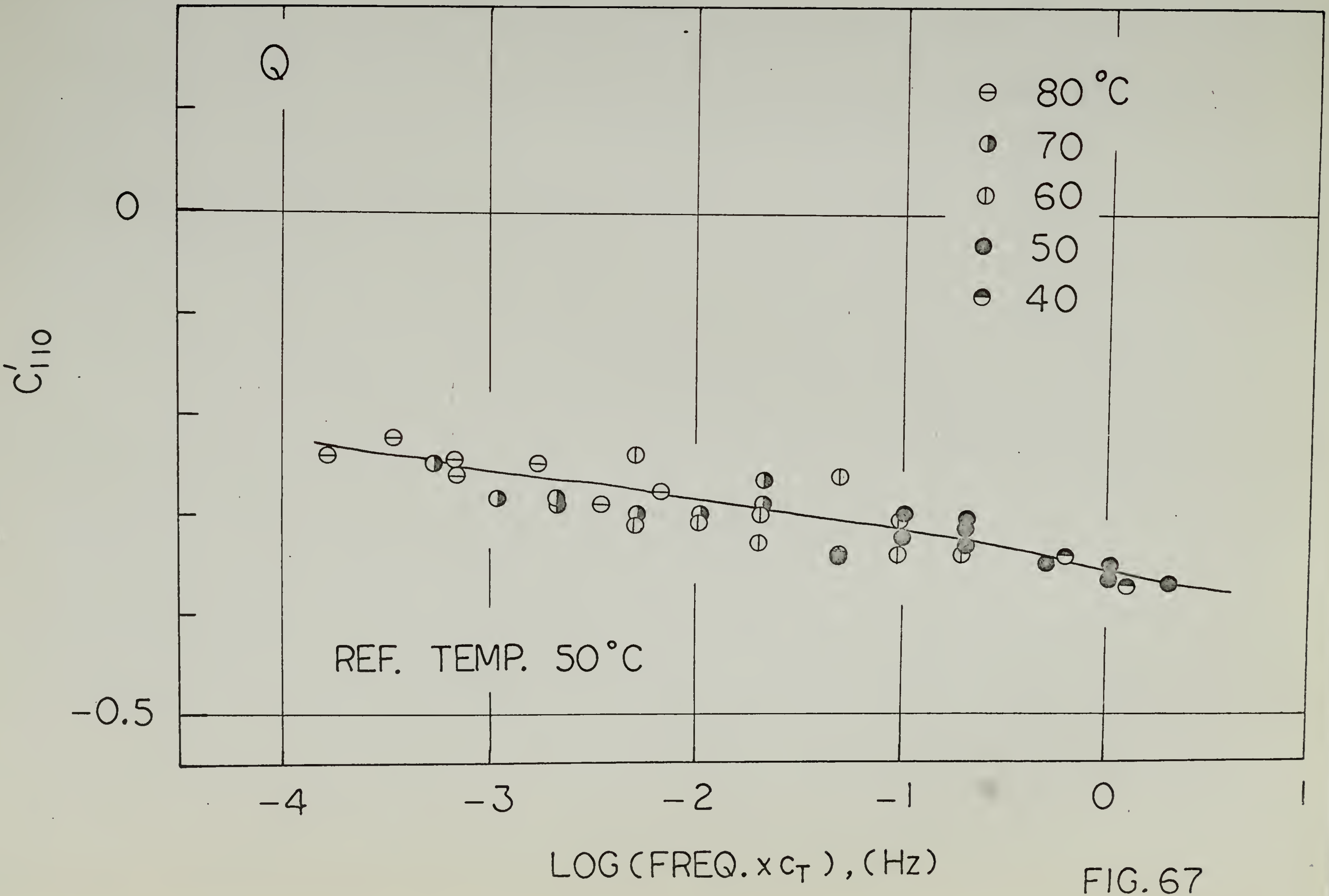

FIG. 67

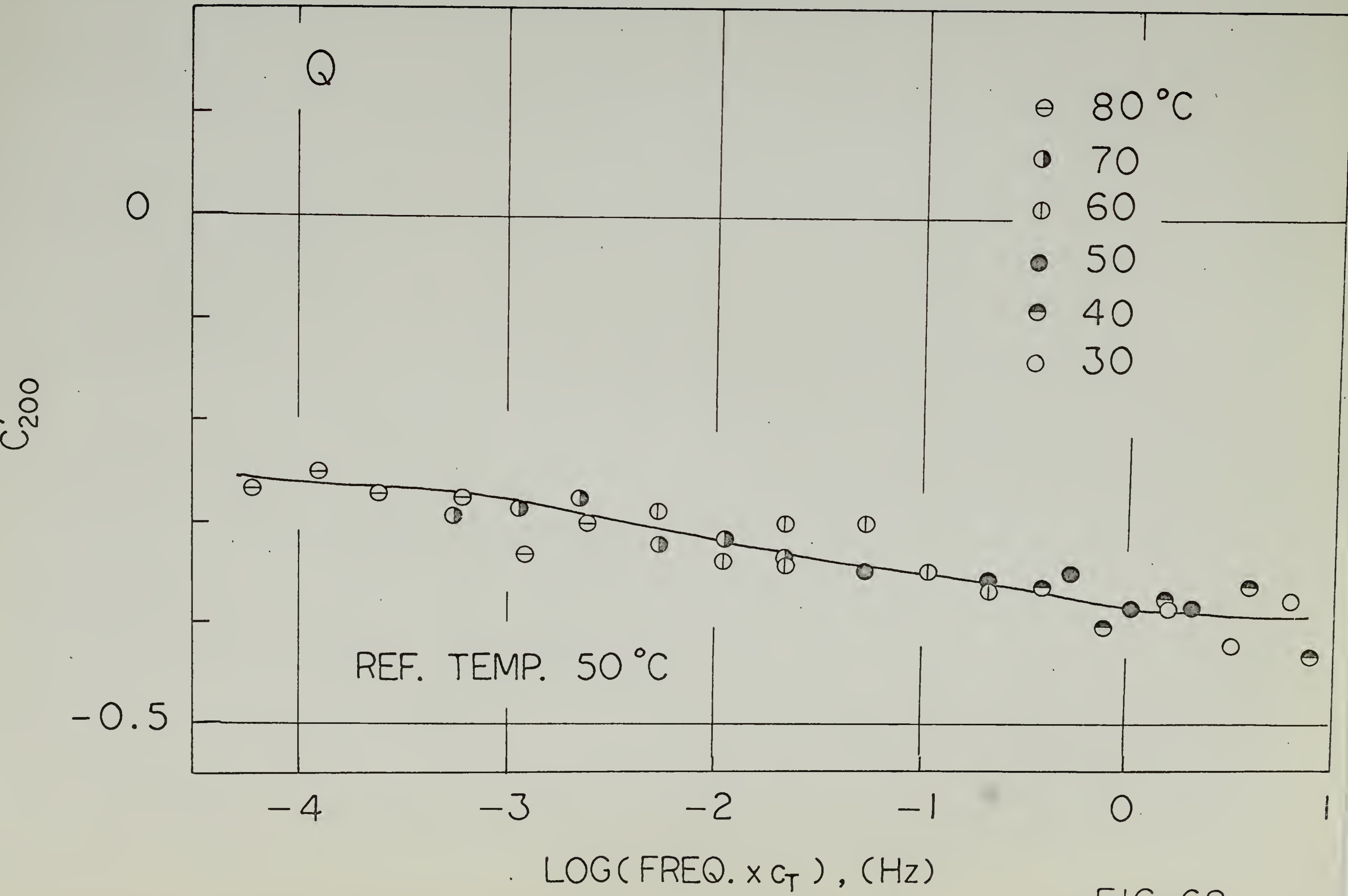

FIG. 68

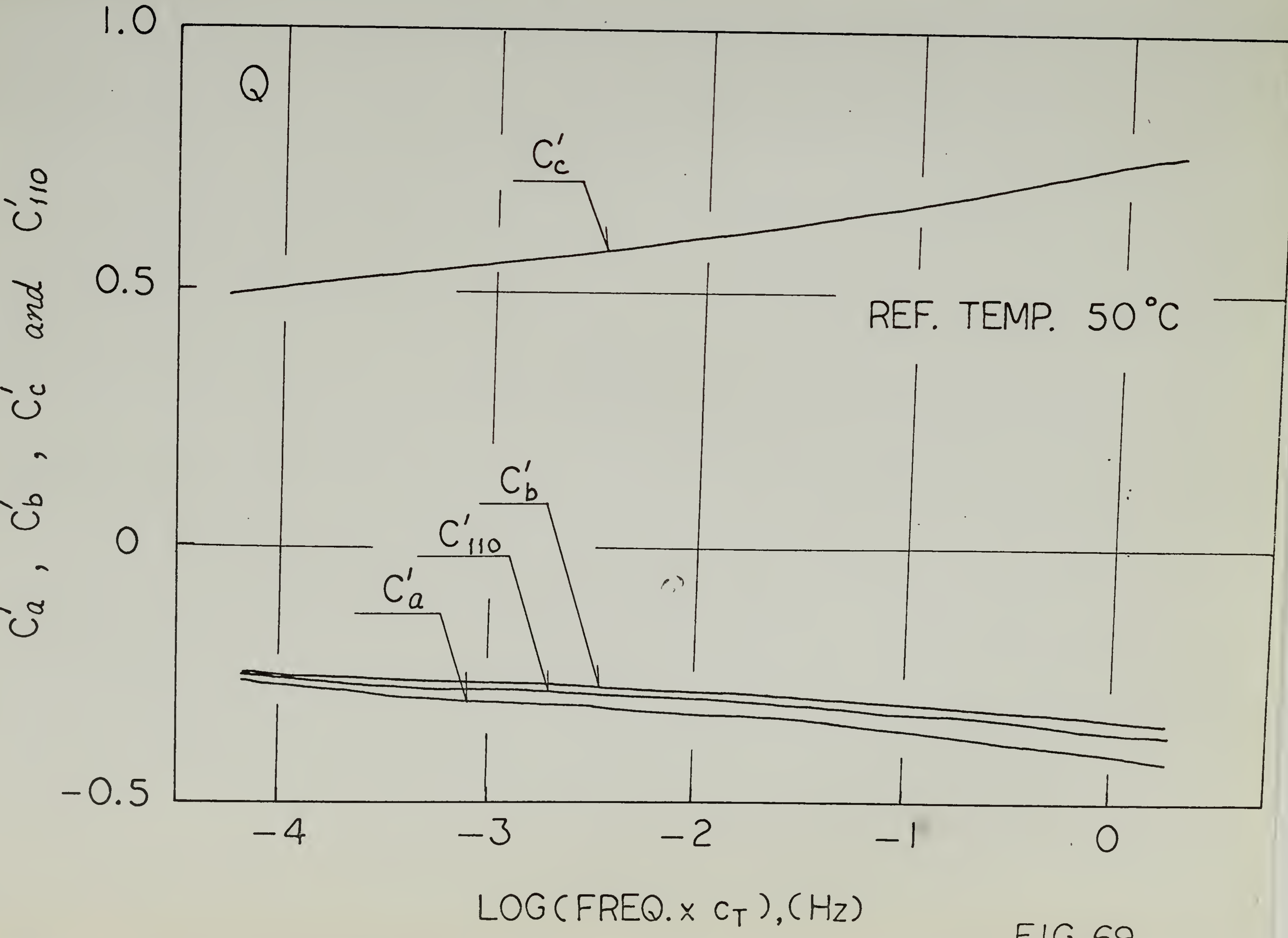
Q
C'_c
REF. TEMP. 50°C
C'_b
C'_{110}
C'_a
1.0
0.5
0
-0.5
-4
-3
-2
-1
0
C'_a , C'_b , C'_c and C'_{110}
LOG(FREQ. x c_T),(Hz)

FIG. 69

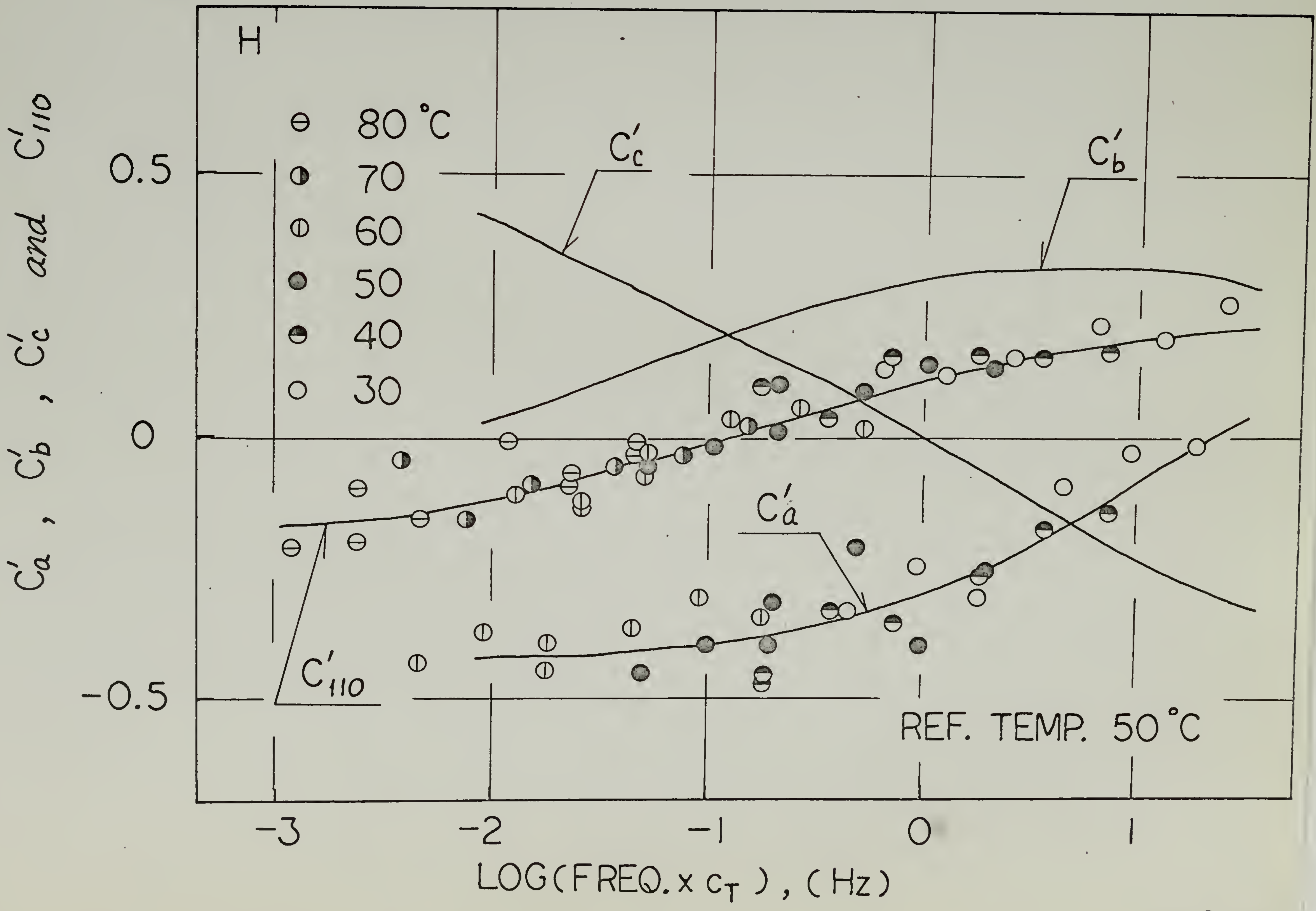

H
⊖ 80 °C
◑ 70
⦶ 60
● 50
◒ 40
○ 30
C'_c
C'_b
C'_a
C'_{110}
REF. TEMP. 50 °C
0.5
0
−0.5
C'_a , C'_b , C'_c and C'_{110}
−3
−2
−1
0
1
LOG(FREQ. x c_T), (Hz)

FIG. 70

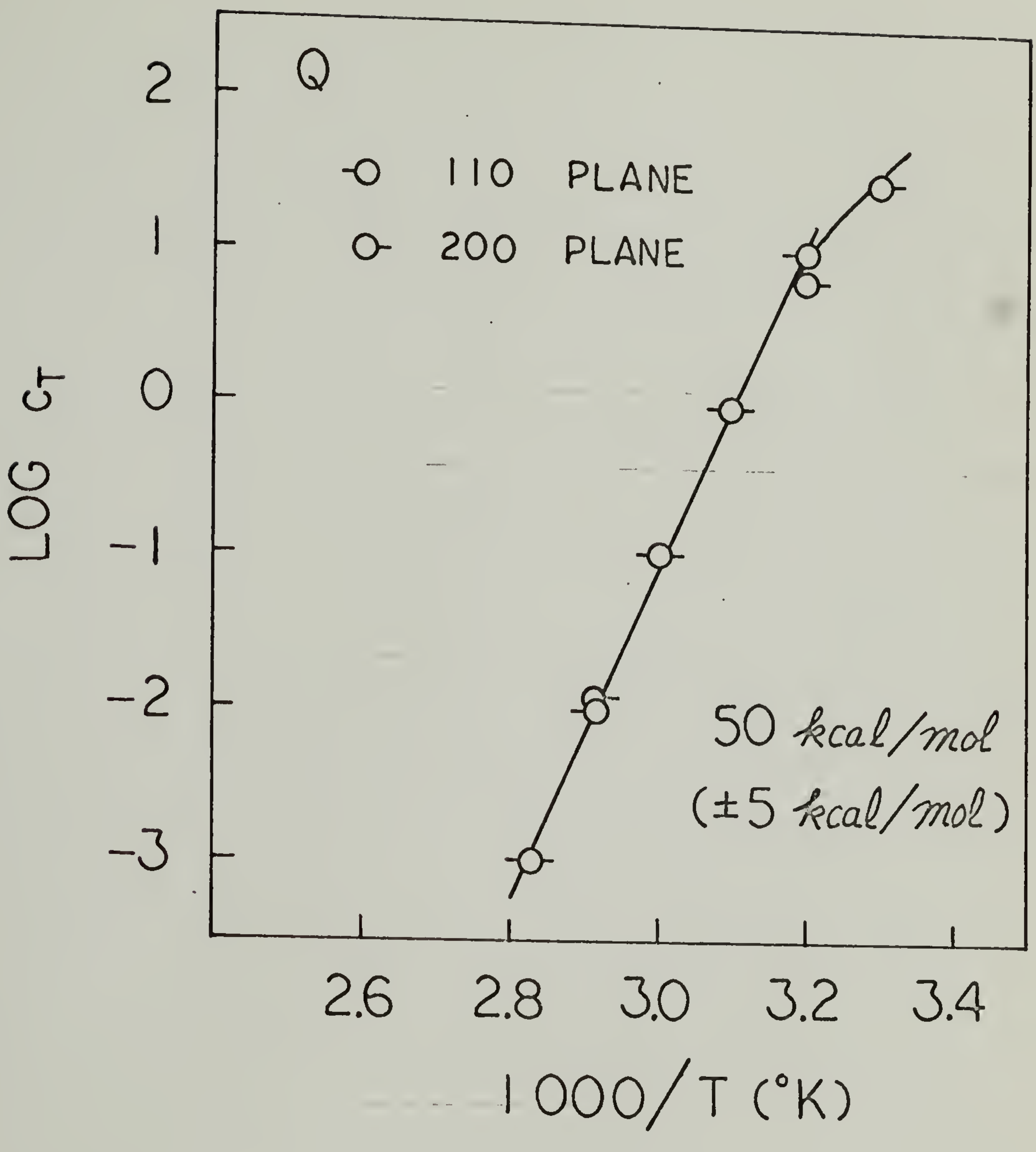
Q
-O 110 PLANE
O- 200 PLANE
LOG c_T
2
1
0
-1
-2
-3
50 kcal/mol
(±5 kcal/mol)
2.6
2.8
3.0
3.2
3.4
1000/T (°K)

FIG. 71

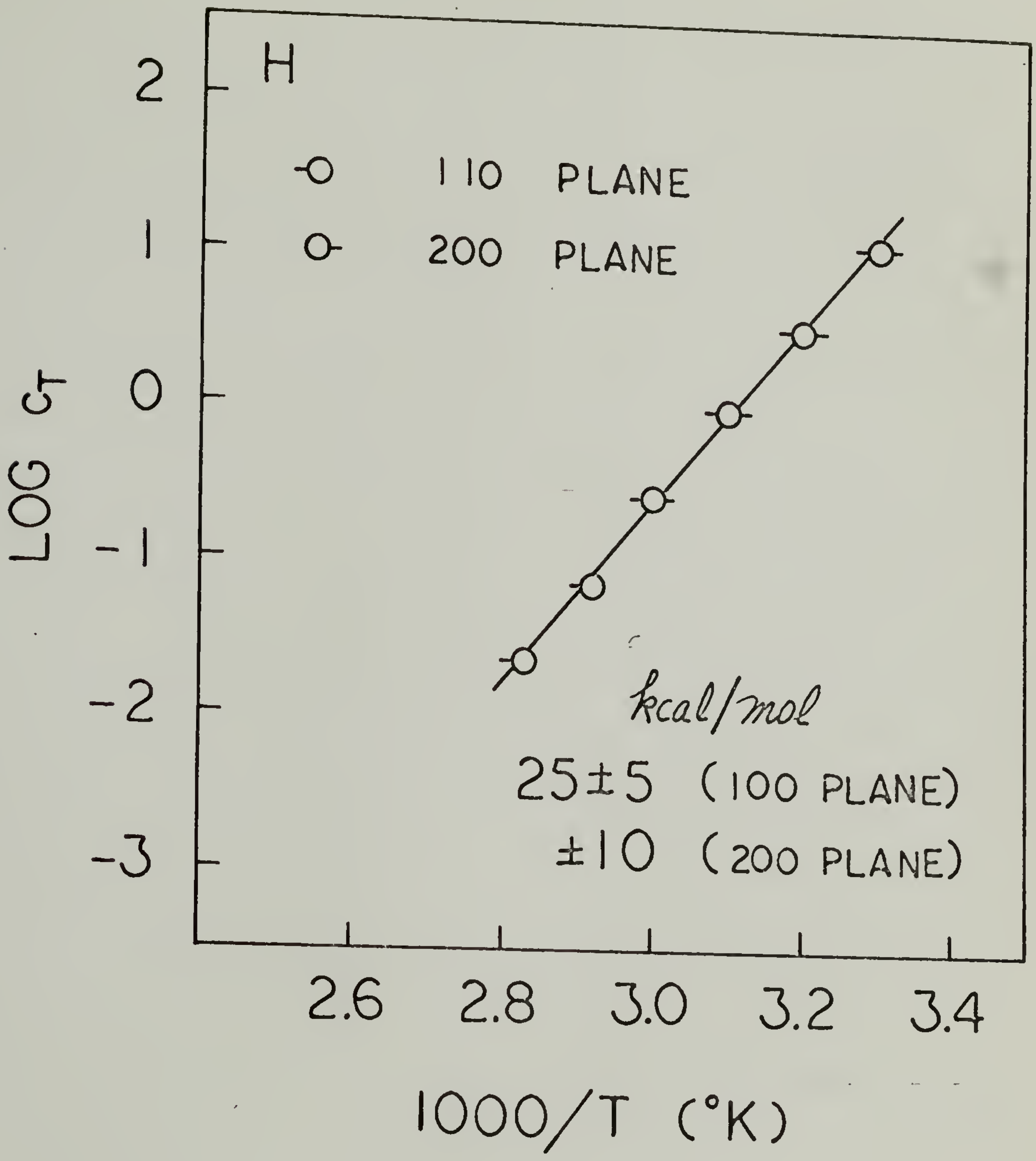
H
-O 110 PLANE
O- 200 PLANE
kcal/mol
25±5 (100 PLANE)
±10 (200 PLANE)
LOG c_T
2
1
0
-1
-2
-3
2.6
2.8
3.0
3.2
3.4
1000/T (°K)

FIG. 72

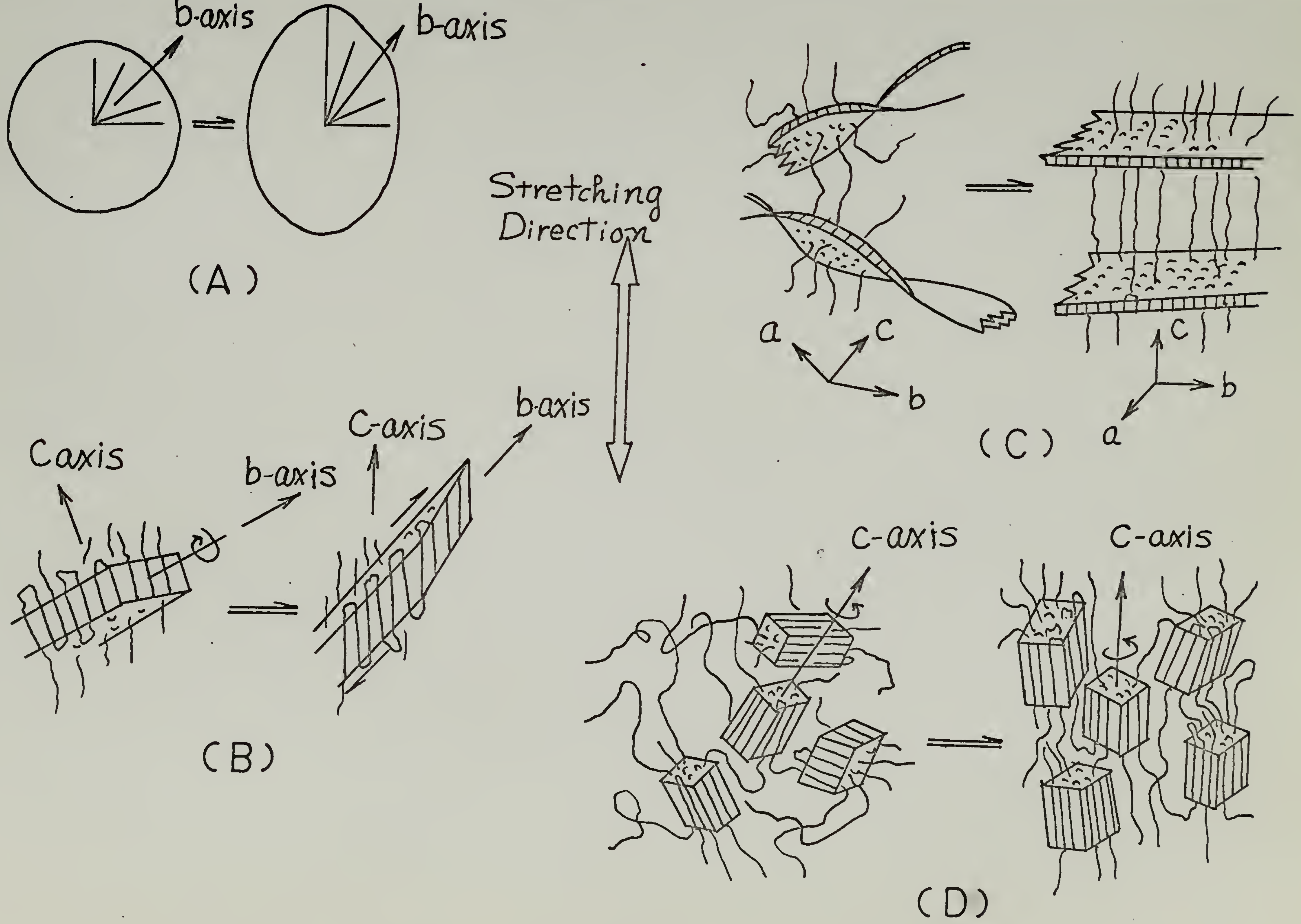
b-axis
b-axis
(A)
Stretching Direction
a
c
b
c
b
a
(C)
Caxis
b-axis
C-axis
b-axis
(B)
C-axis
C-axis
(D)

FIG. 73

FIG.74

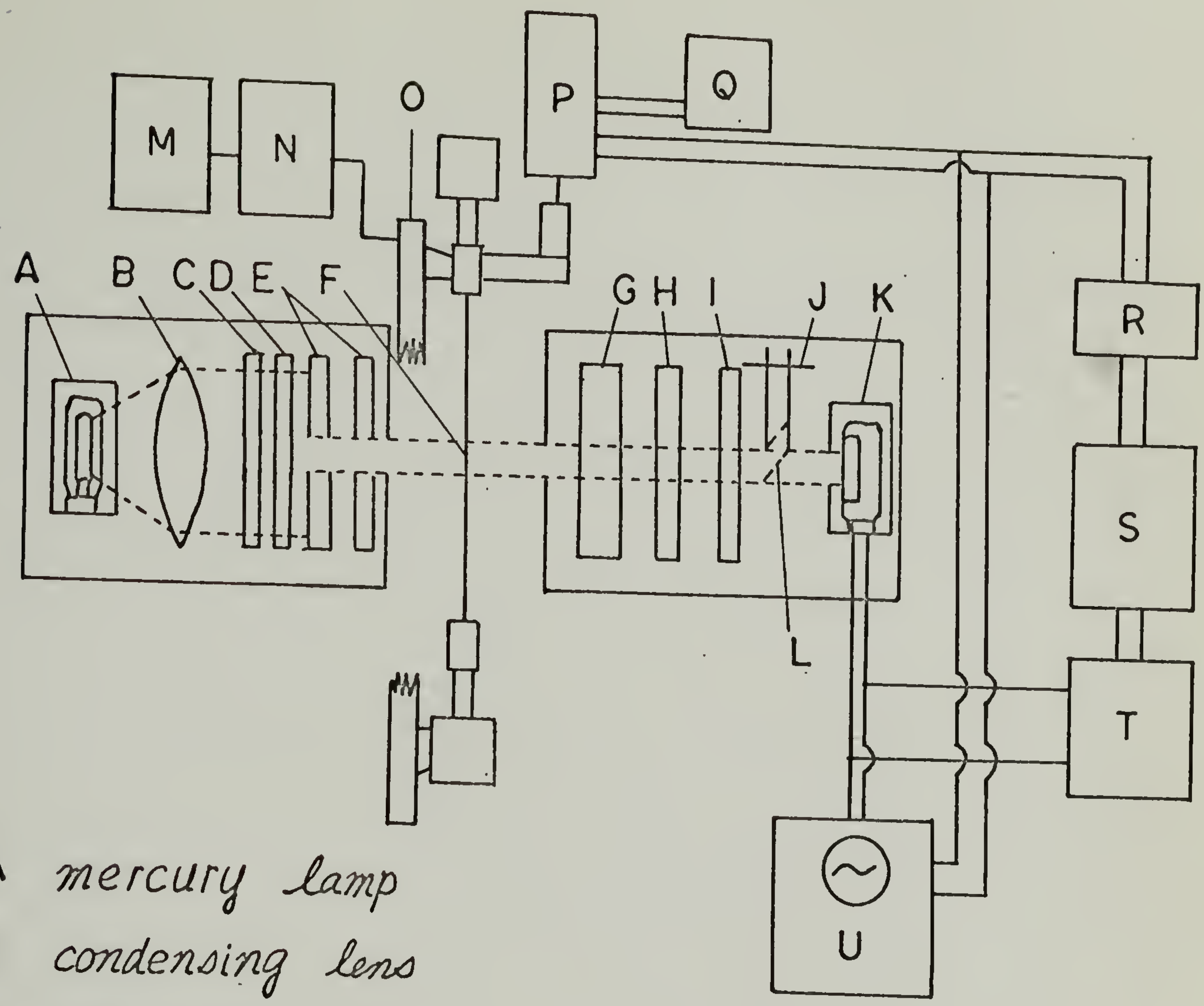

A	mercury lamp		
B	condensing lens		
C	filter (5461 Å)		
D	polariser	M	transmission system
E	slits	N	worm gear reducer
F	sample	O	arm of mechanical vibrator
G	retadation plate	P	linear variable differential transformer
H	analyser	Q	oscillator
I	neutral density filter	R	rectifier
J	Babinet compensator	S	preamplifier
K	photomultiplier tube	T	D-C amplifier
L	mirror	U	oscilloscope

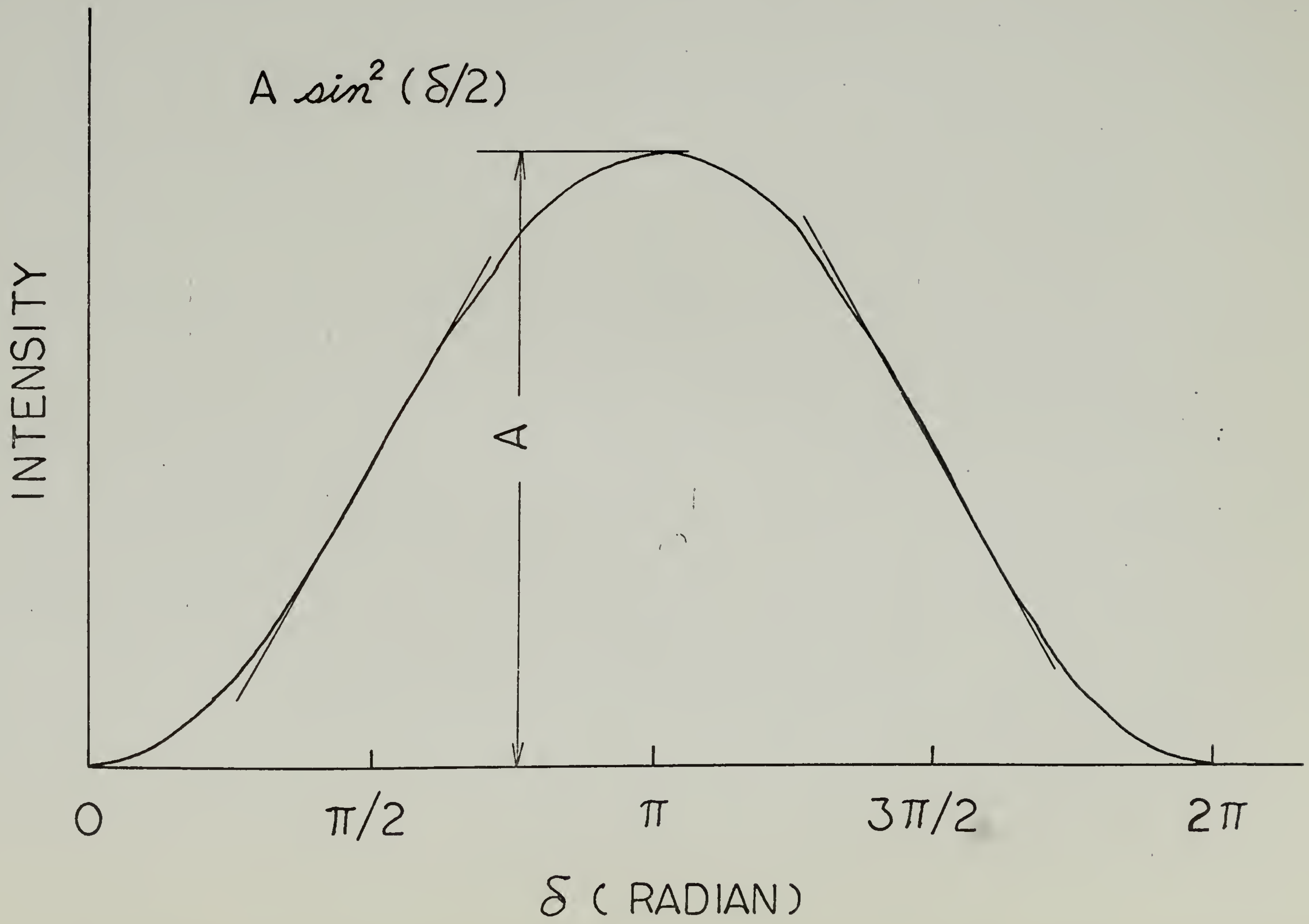

FIG. 75

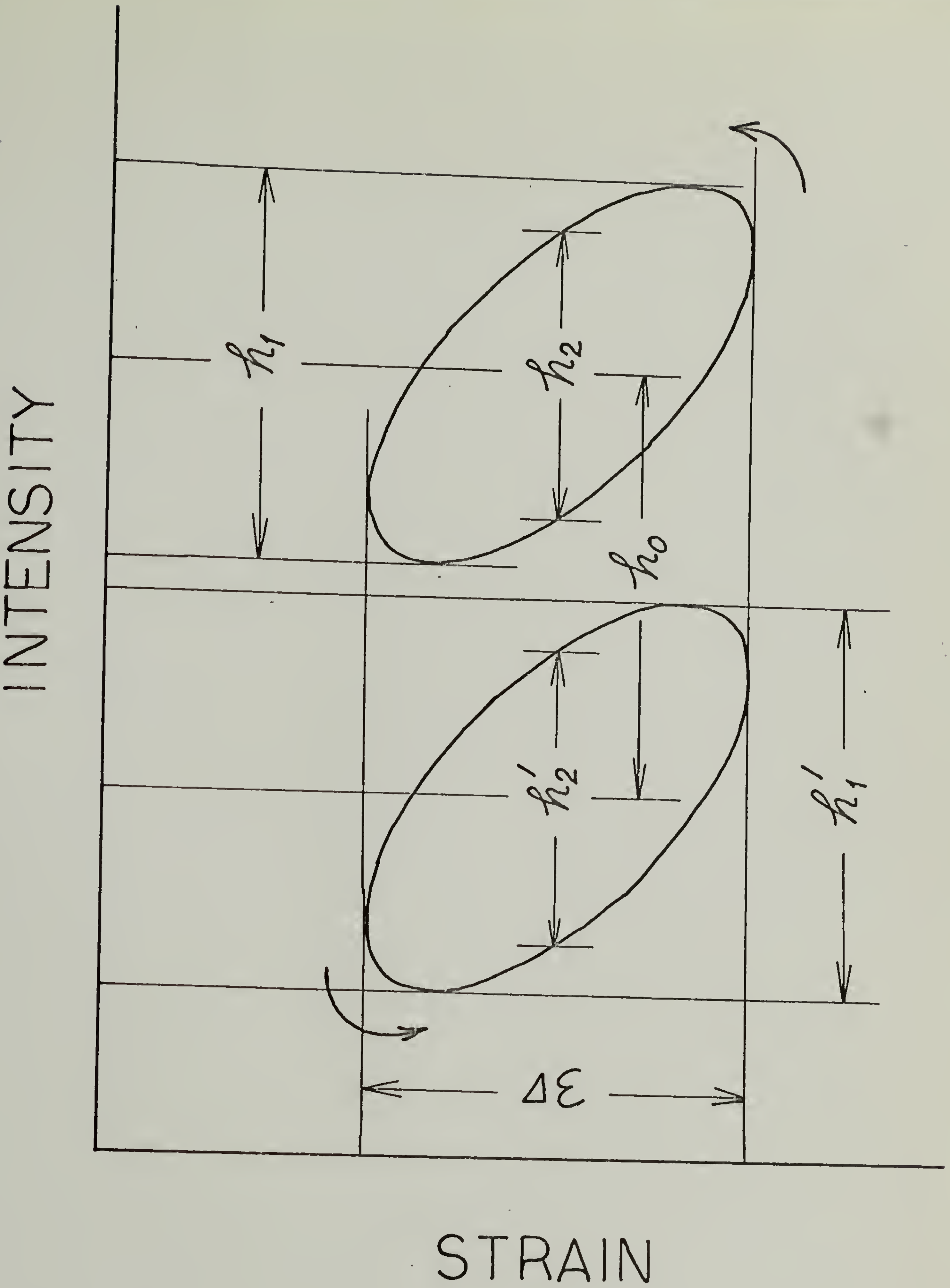

FIG. 76

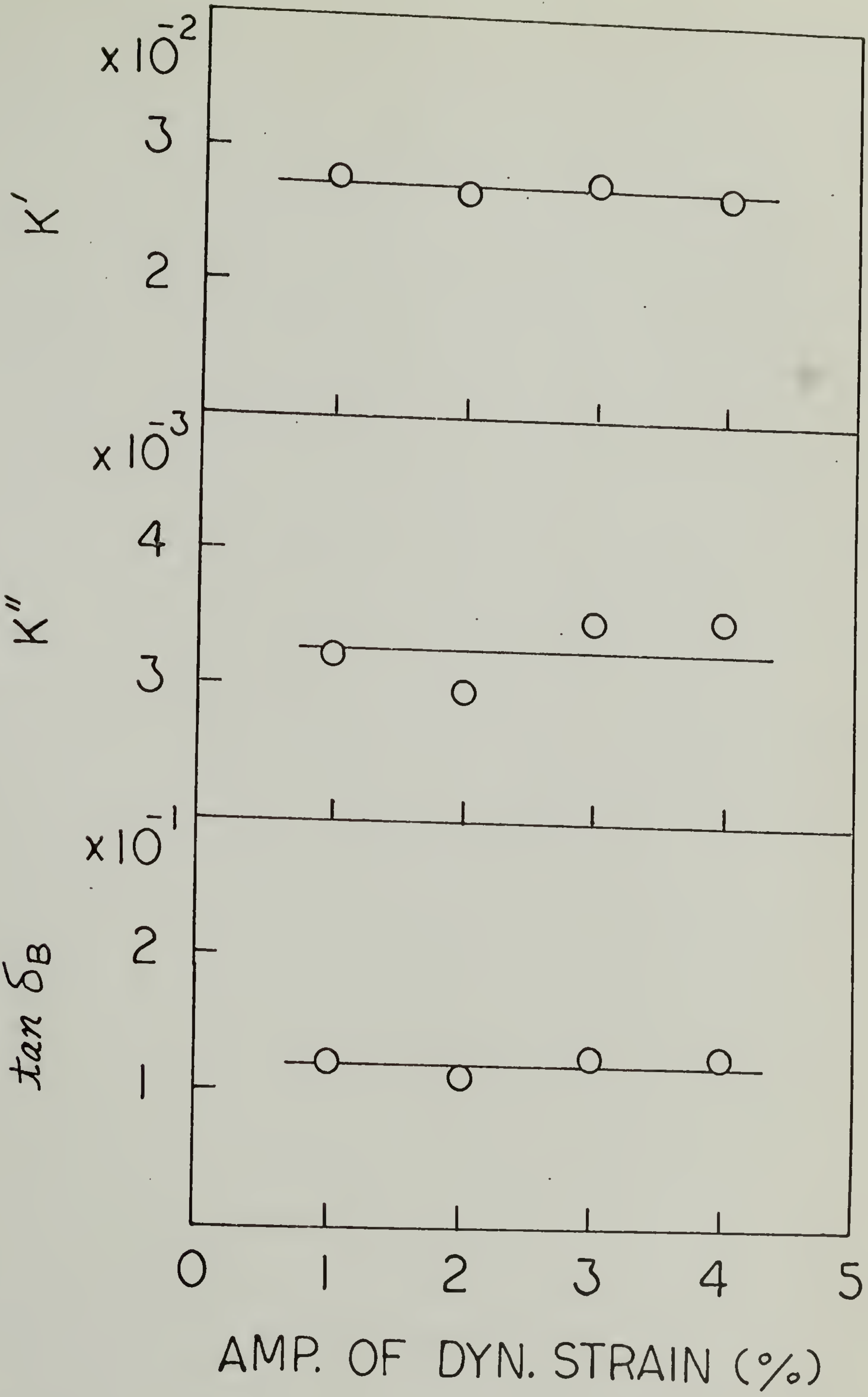

SAMPLE Q
TEMP. 30°C
FREQ. 1 Hz

STATIC STRAIN 10 %

FIG. 77

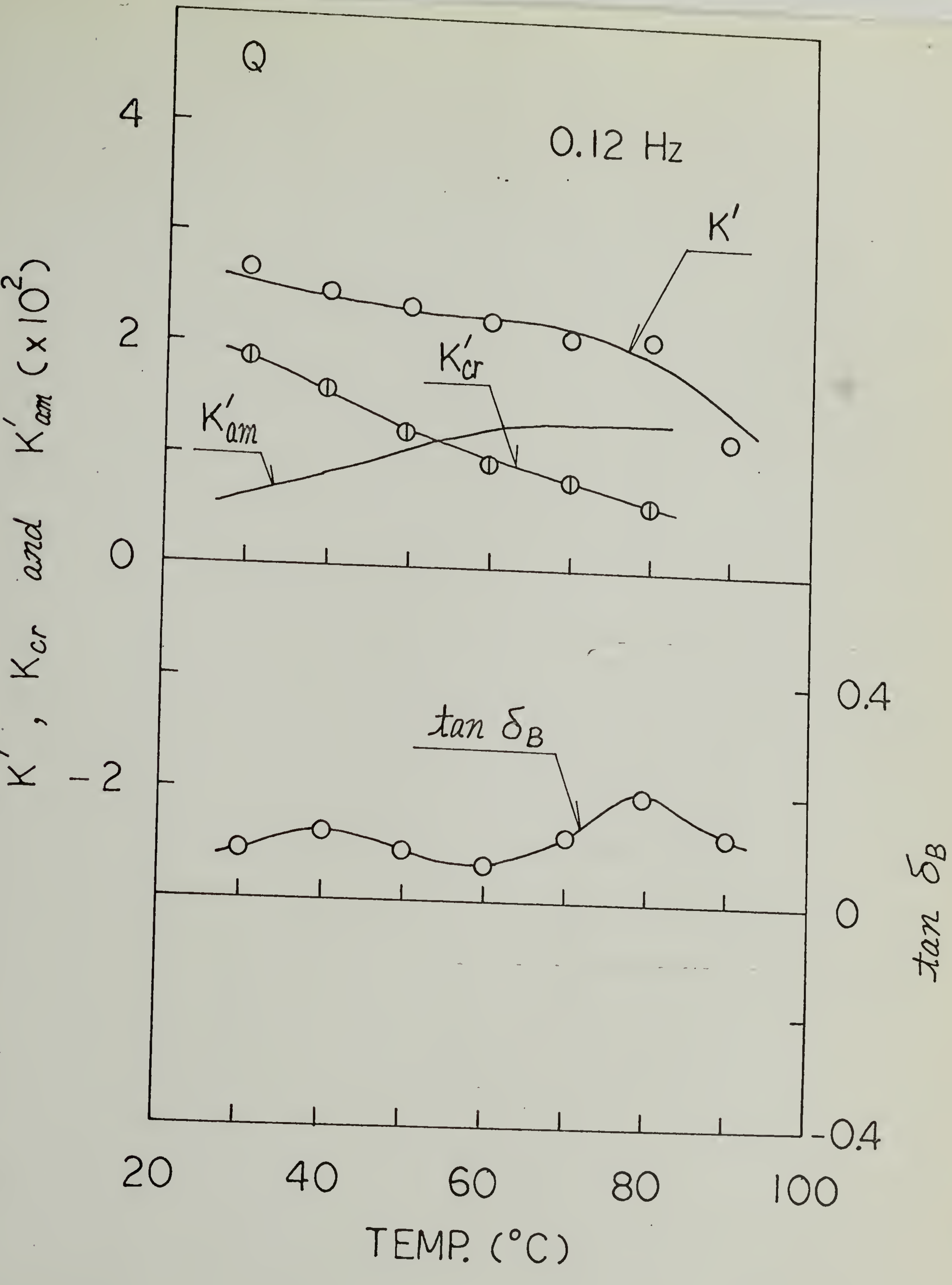
Q
0.12 Hz
K'
K'_{cr}
K'_{am}
tan δ_B
K', K_{cr} and K'_{am} (x 10^2)
4
2
0
-2
0.4
0
-0.4
tan δ_B
20
40
60
80
100
TEMP. (°C)

FIG. 78

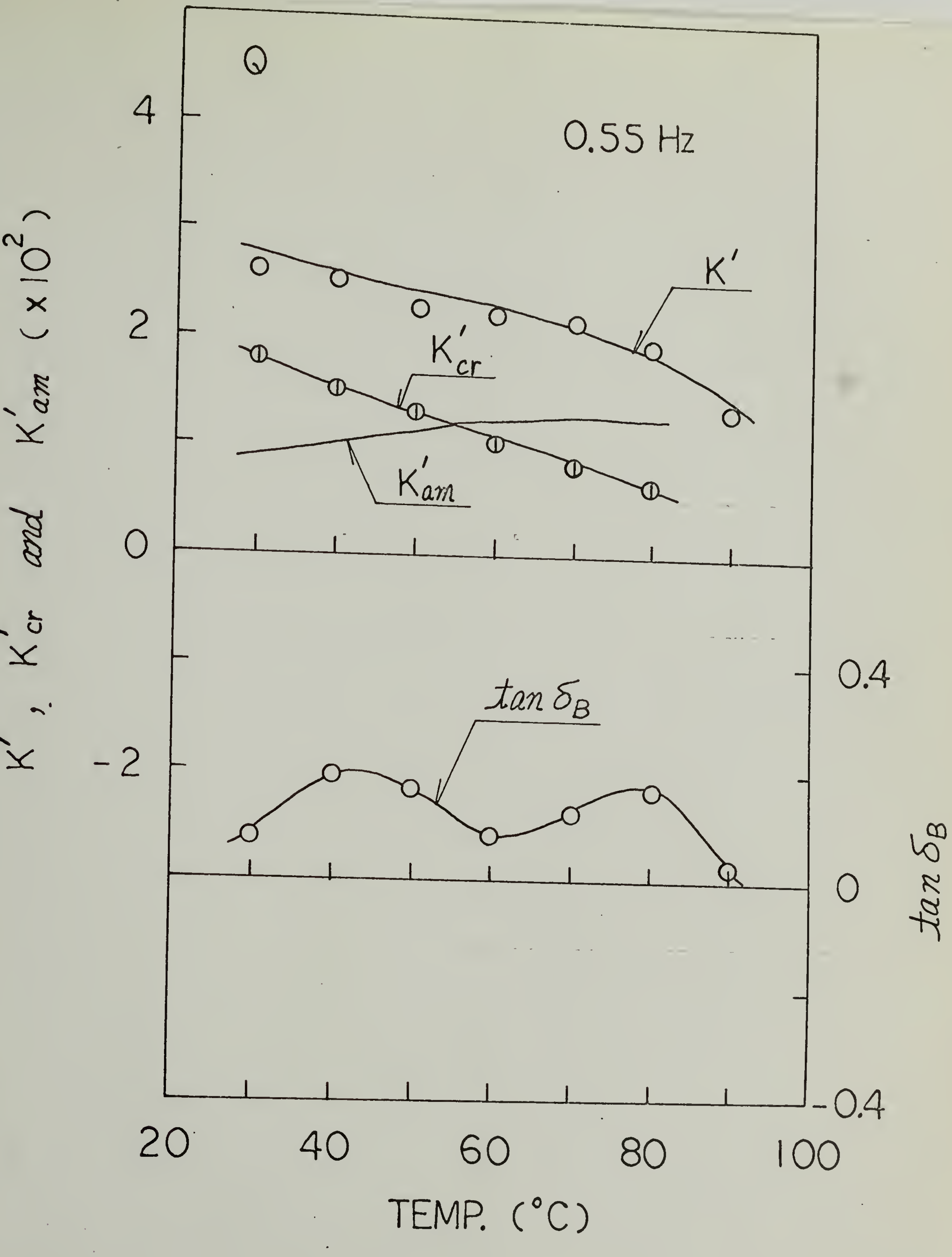
Q
0.55 Hz
K′
K′cr
K′am
tan δB
K′ , K′cr and K′am (x 10²)
tan δB
4
2
0
-2
0.4
0
-0.4
20
40
60
80
100
TEMP. (°C)

FIG. 79

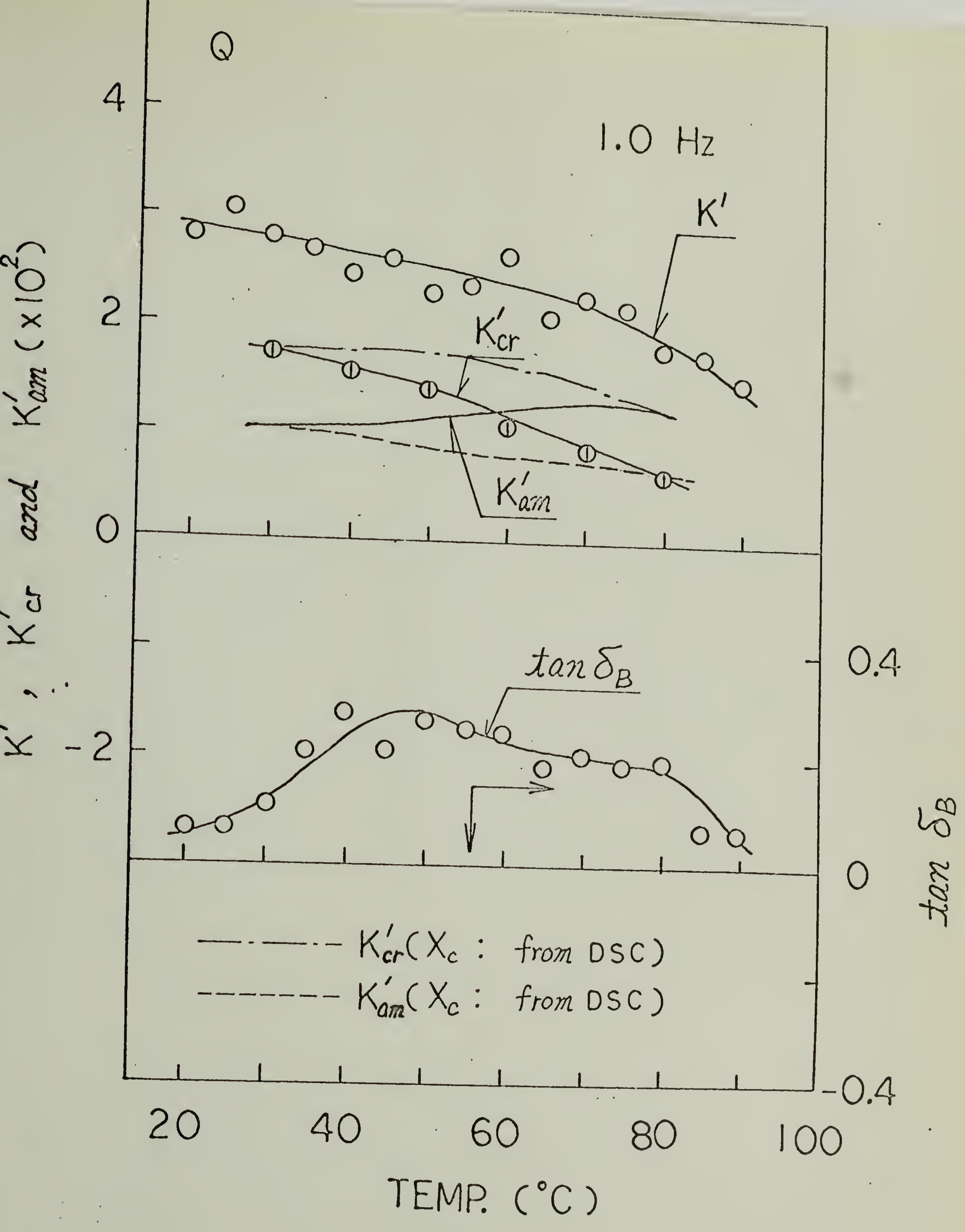
Q
1.0 Hz
K'
K'_cr
K'_am
tan δ_B
K'_cr (X_c : from DSC)
K'_am (X_c : from DSC)
K', K'_cr and K'_am (×10²)
4
2
0
-2
0.4
0
-0.4
tan δ_B
20
40
60
80
100
TEMP. (°C)

FIG. 80

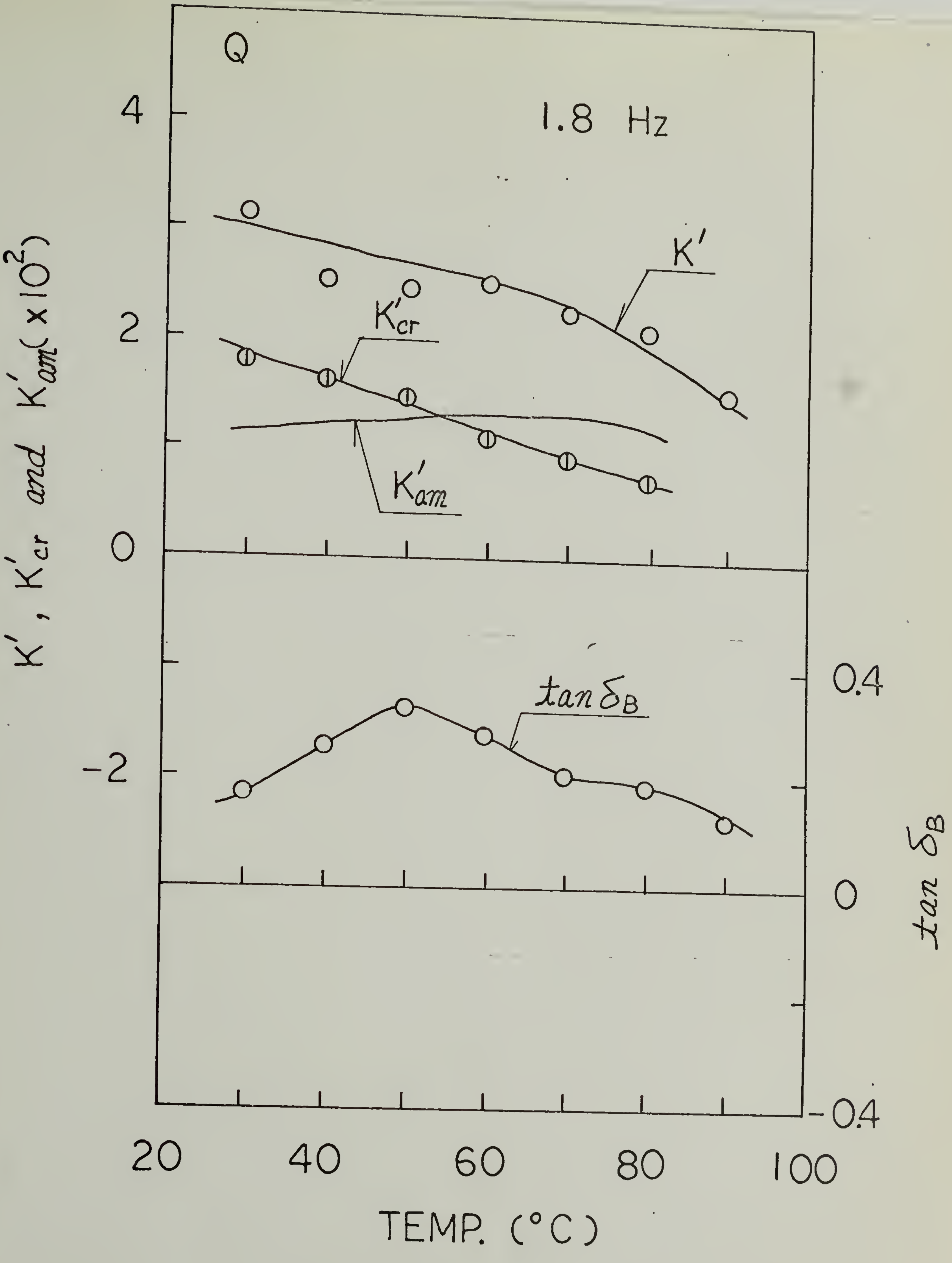
Q
1.8 Hz
K′
K′cr
K′am
tan δB
K′, K′cr and K′am (x10²)
4
2
0
−2
tan δB
0.4
0
−0.4
20
40
60
80
100
TEMP. (°C)

FIG. 81

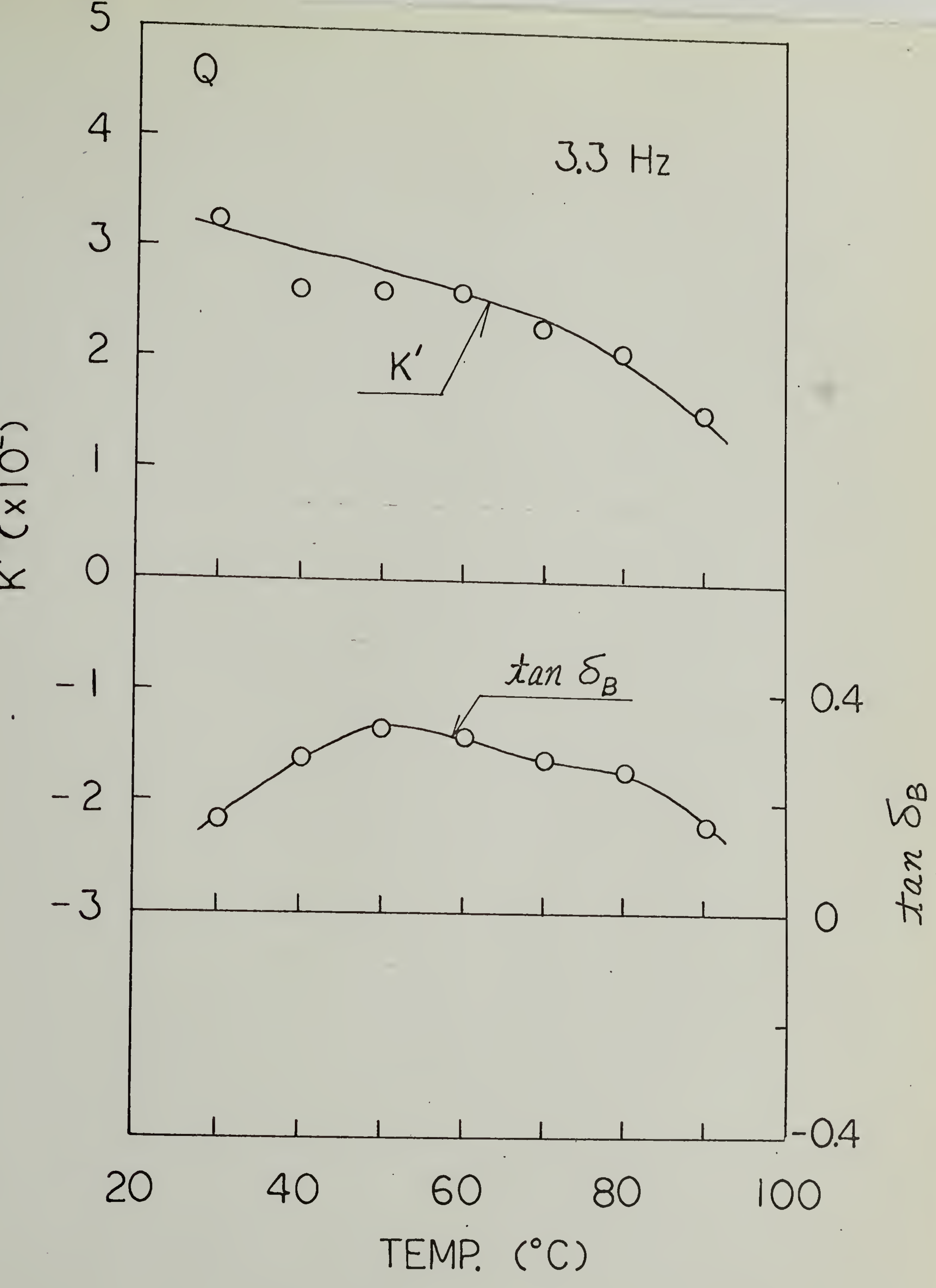

Q
3.3 Hz
K'
tan δ_B
K' (x10²)
5
4
3
2
1
0
-1
-2
-3
0.4
0
-0.4
tan δ_B
20
40
60
80
100
TEMP. (°C)

FIG. 82

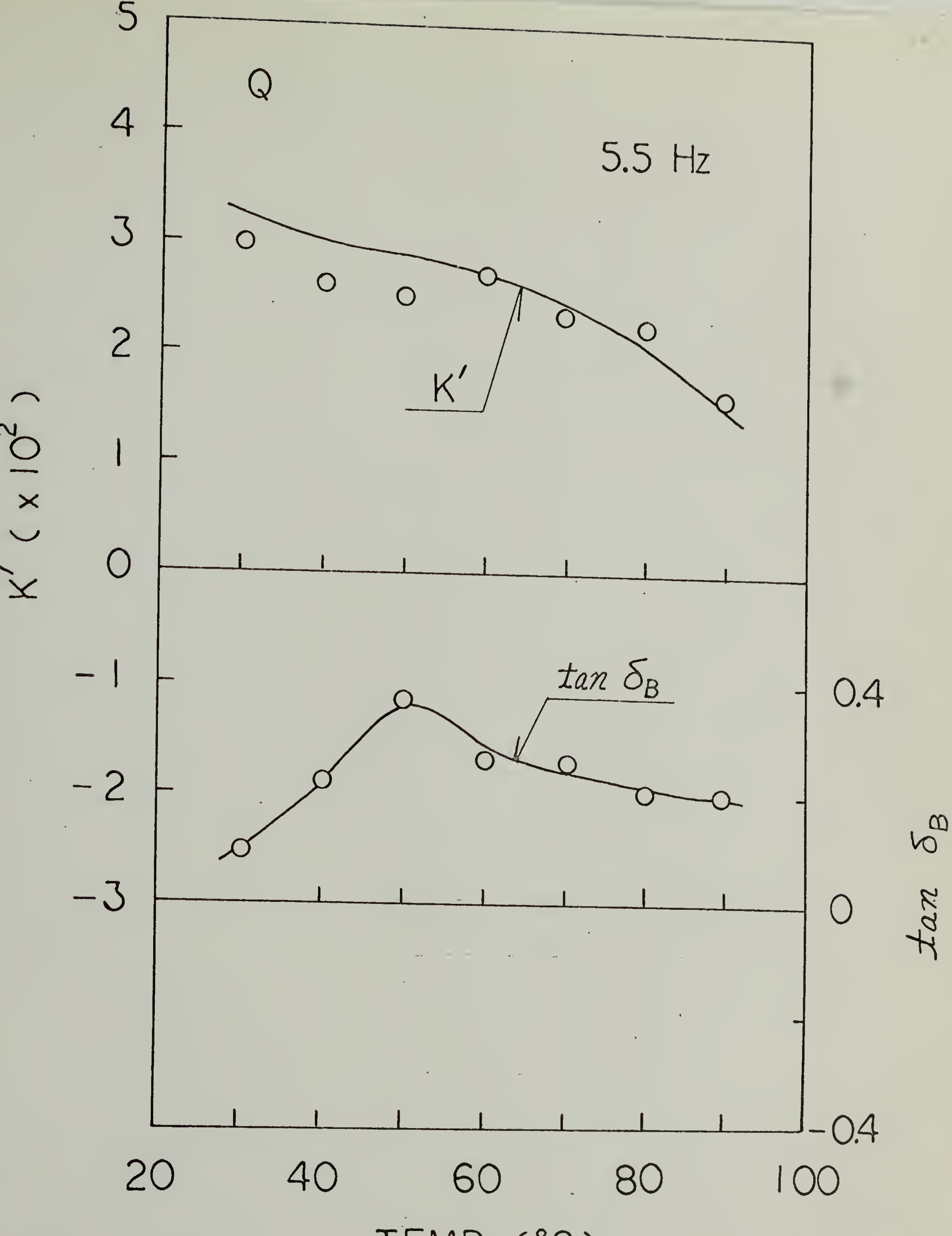

Q
5.5 Hz
K′
tan δ_B
K′ (x 10^2)
5
4
3
2
1
0
-1
-2
-3
0.4
0
-0.4
tan δ_B
20
40
60
80
100
TEMP. (°C)

FIG. 83

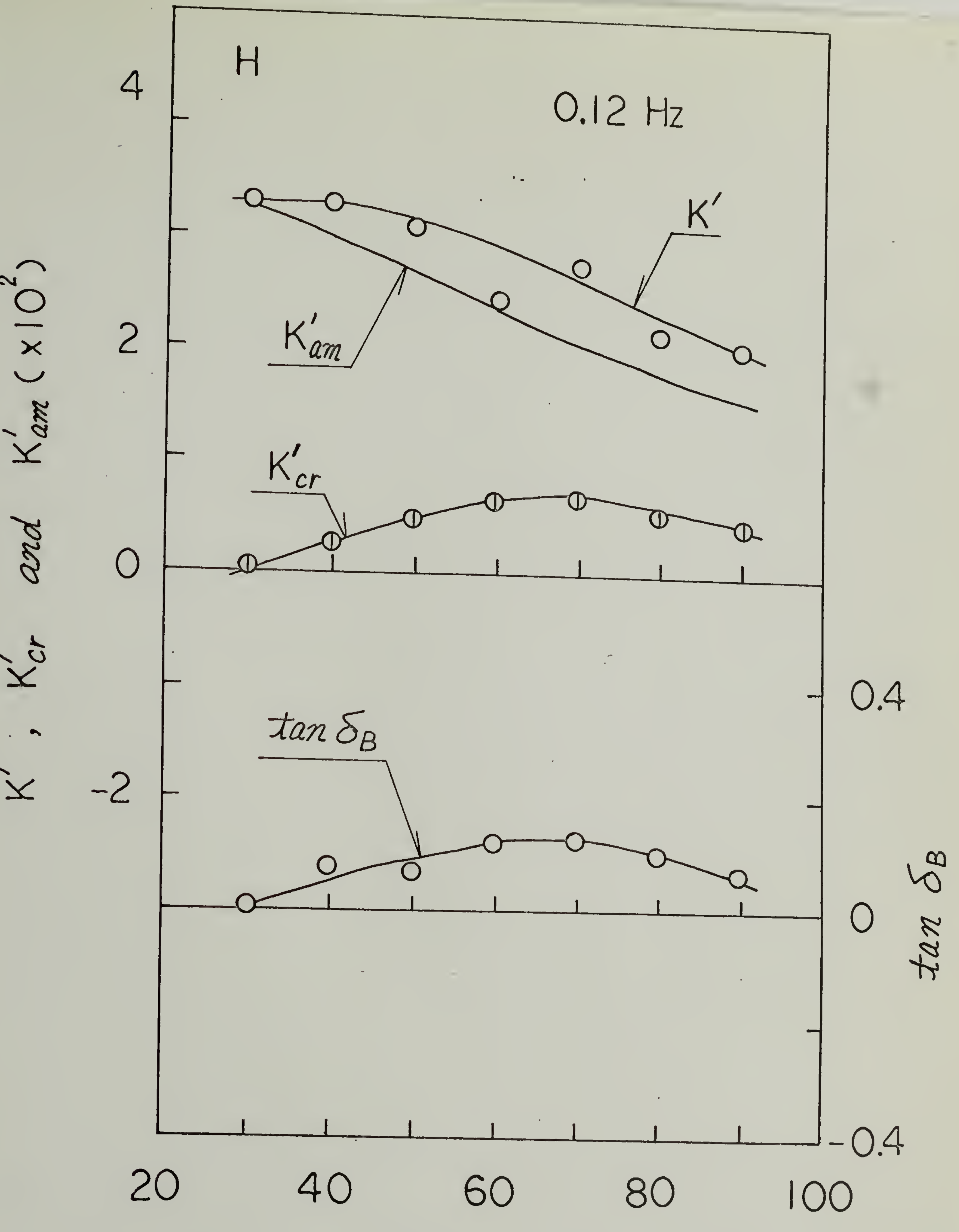
H
0.12 Hz
K'
K'_am
K'_cr
tan δ_B
K' , K'_cr and K'_am (x10^2)
4
2
0
-2
0.4
0
-0.4
tan δ_B
20
40
60
80
100
TEMP. (°C)

FIG. 84

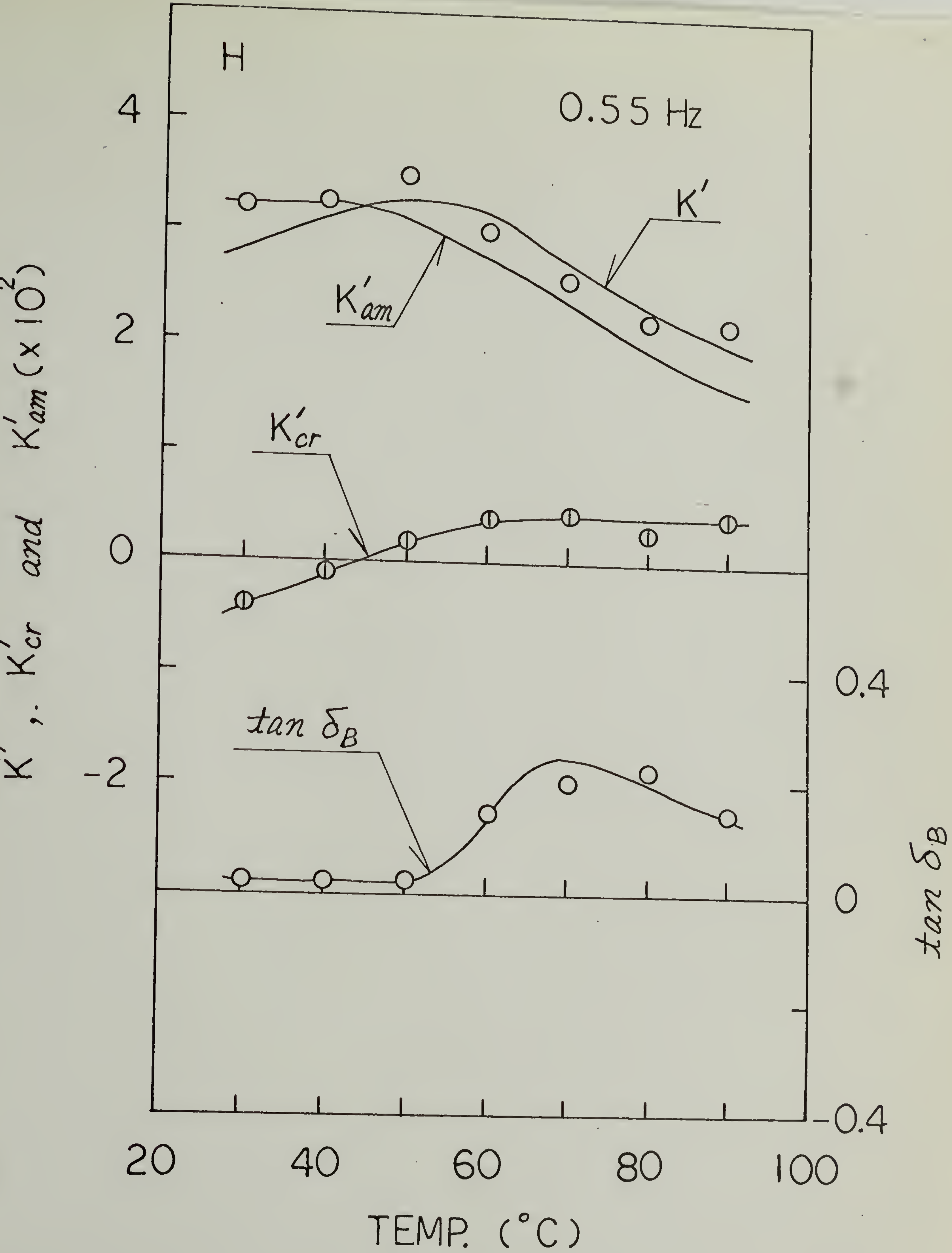
H
0.55 Hz
K'
K'_{am}
K'_{cr}
$\tan \delta_B$
K' , K'_{cr} and K'_{am} ($\times 10^2$)
4
2
0
-2
0.4
0
-0.4
$\tan \delta_B$
20
40
60
80
100
TEMP. (°C)

FIG. 85

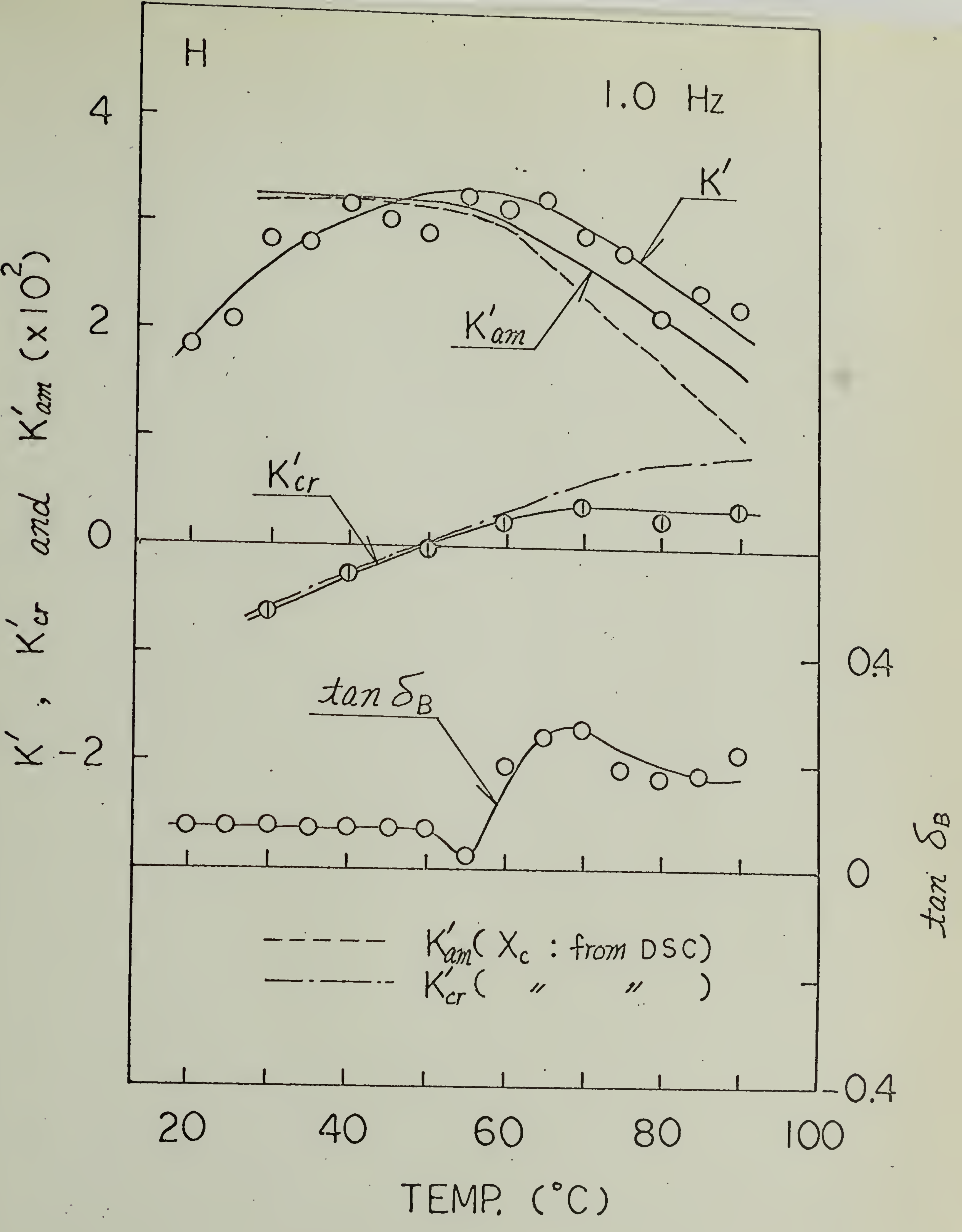
H
1.0 Hz
K'
K'_am
K'_cr
tan δ_B
K'_am(X_c : from DSC)
K'_cr(〃 〃)
K', K'_cr and K'_am (x10^2)
4
2
0
-2
tan δ_B
0.4
0
-0.4
20
40
60
80
100
TEMP. (°C)

FIG. 86

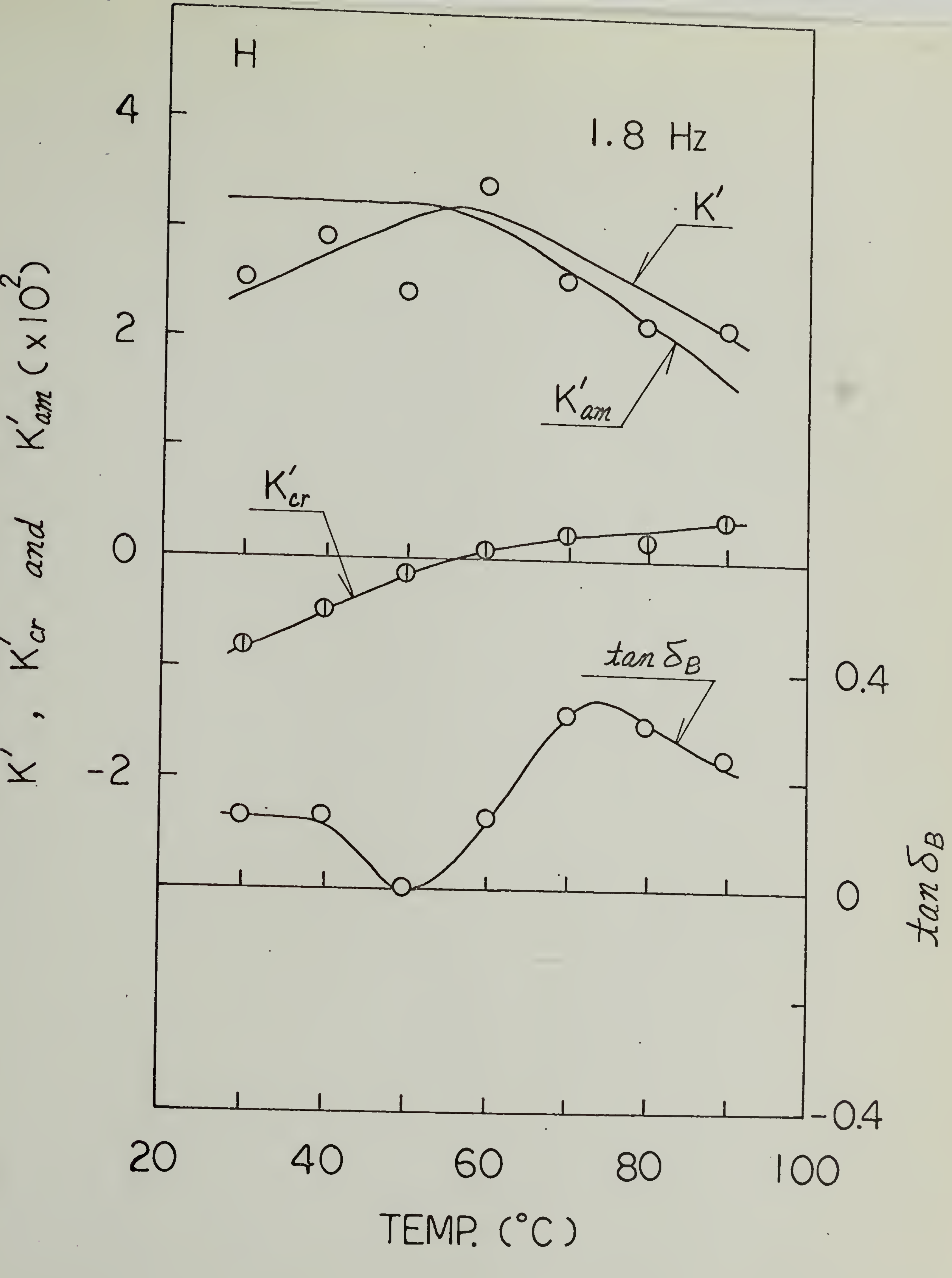
H
1.8 Hz
K′
K′am
K′cr
tan δB
K′ , K′cr and K′am (x10²)
tan δB
4
2
0
-2
0.4
0
-0.4
20
40
60
80
100
TEMP. (°C)

FIG. 87

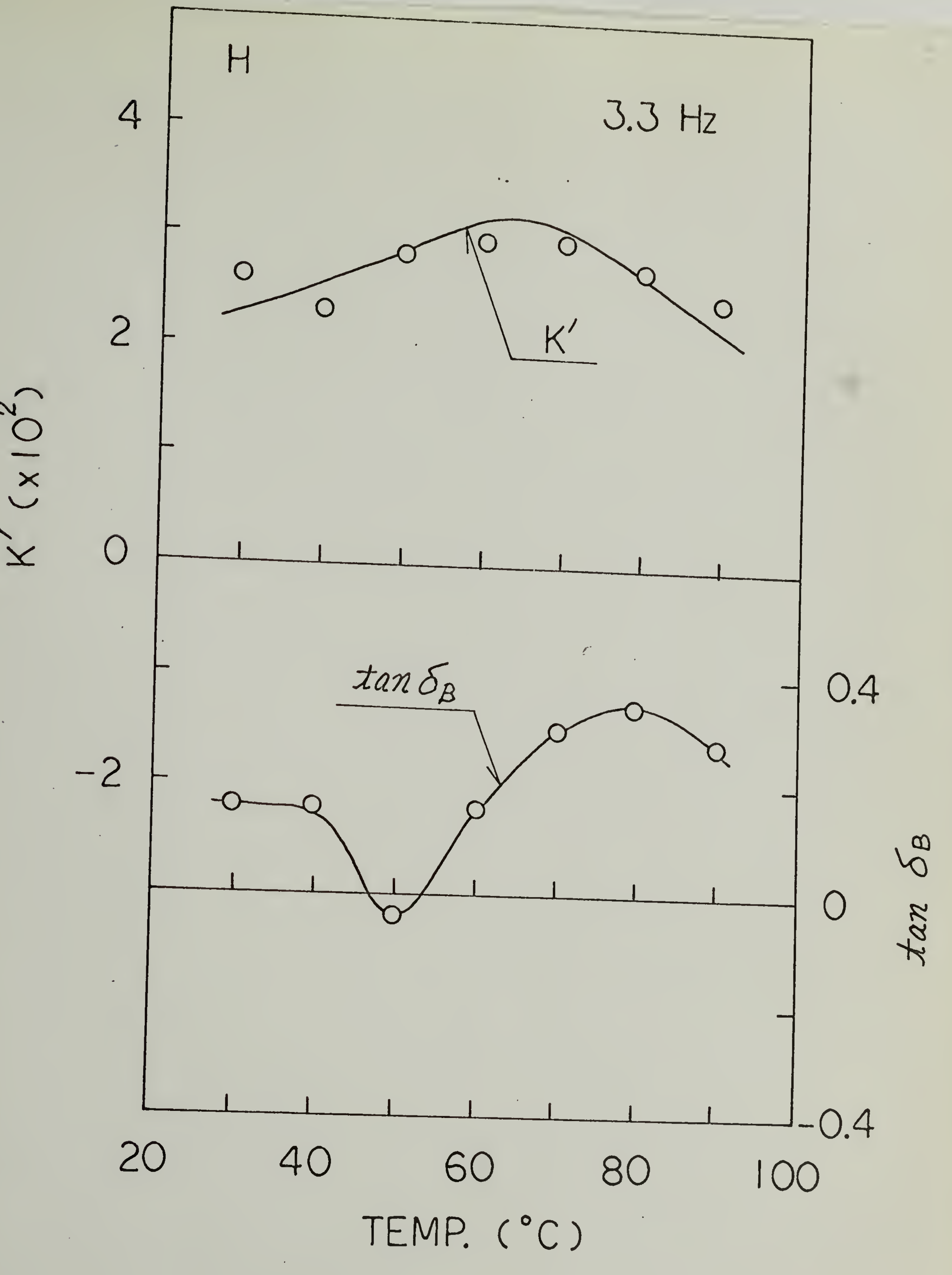

FIG. 88

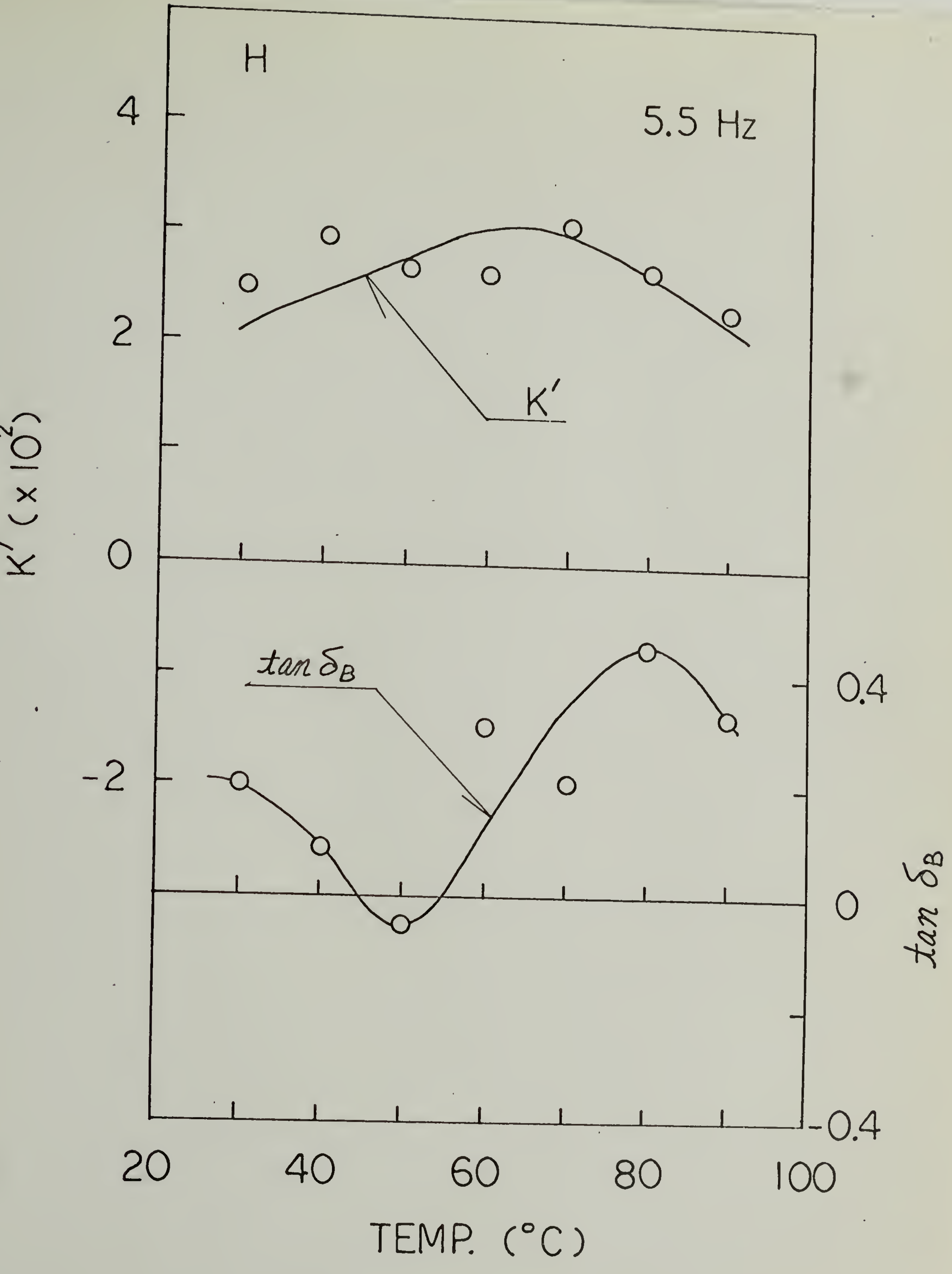

FIG. 89

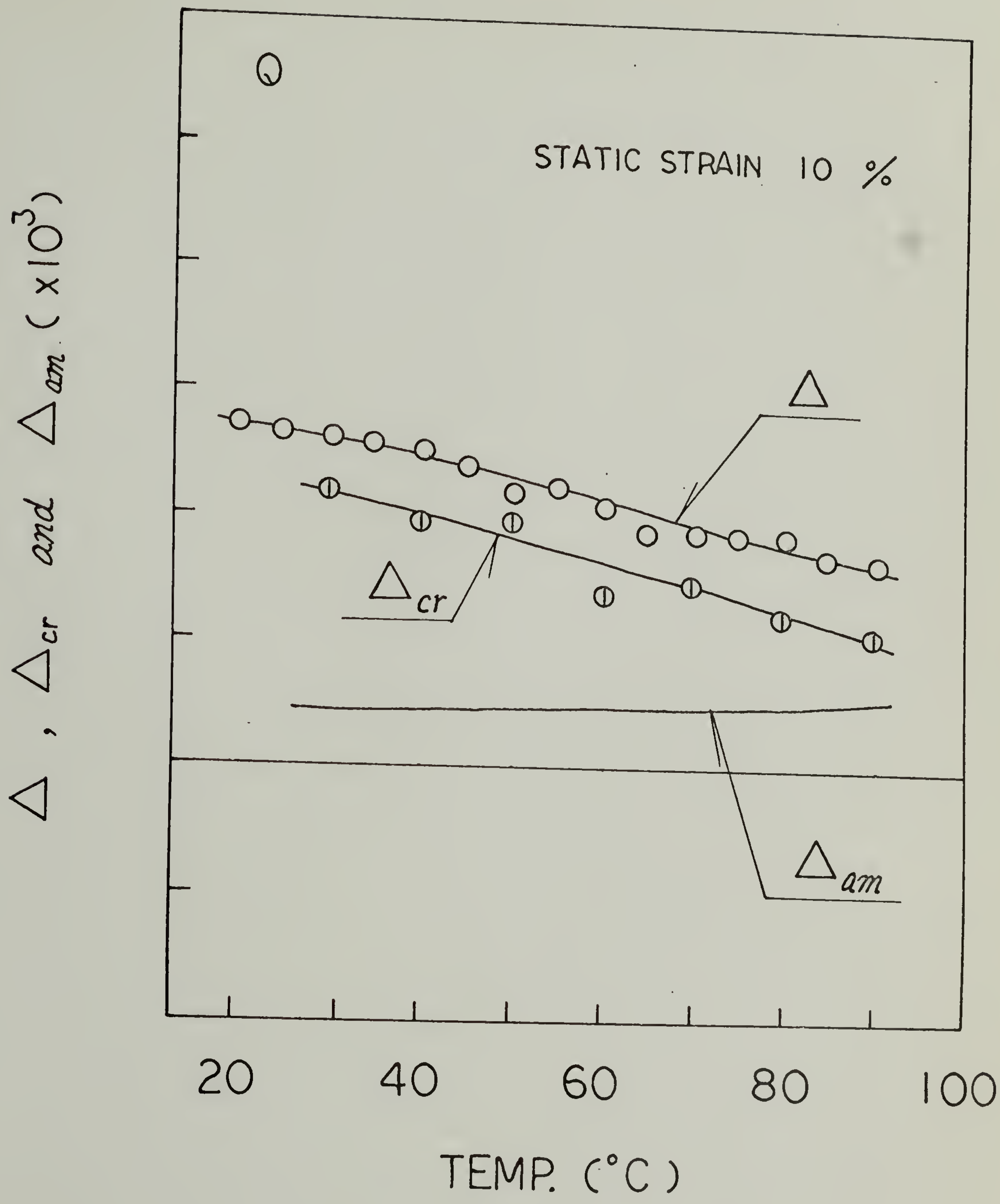
Q
STATIC STRAIN 10 %
Δ
Δ_{cr}
Δ_{am}
Δ , Δ_{cr} and Δ_{am} (x 10^3)
20
40
60
80
100
TEMP. (°C)

FIG. 90

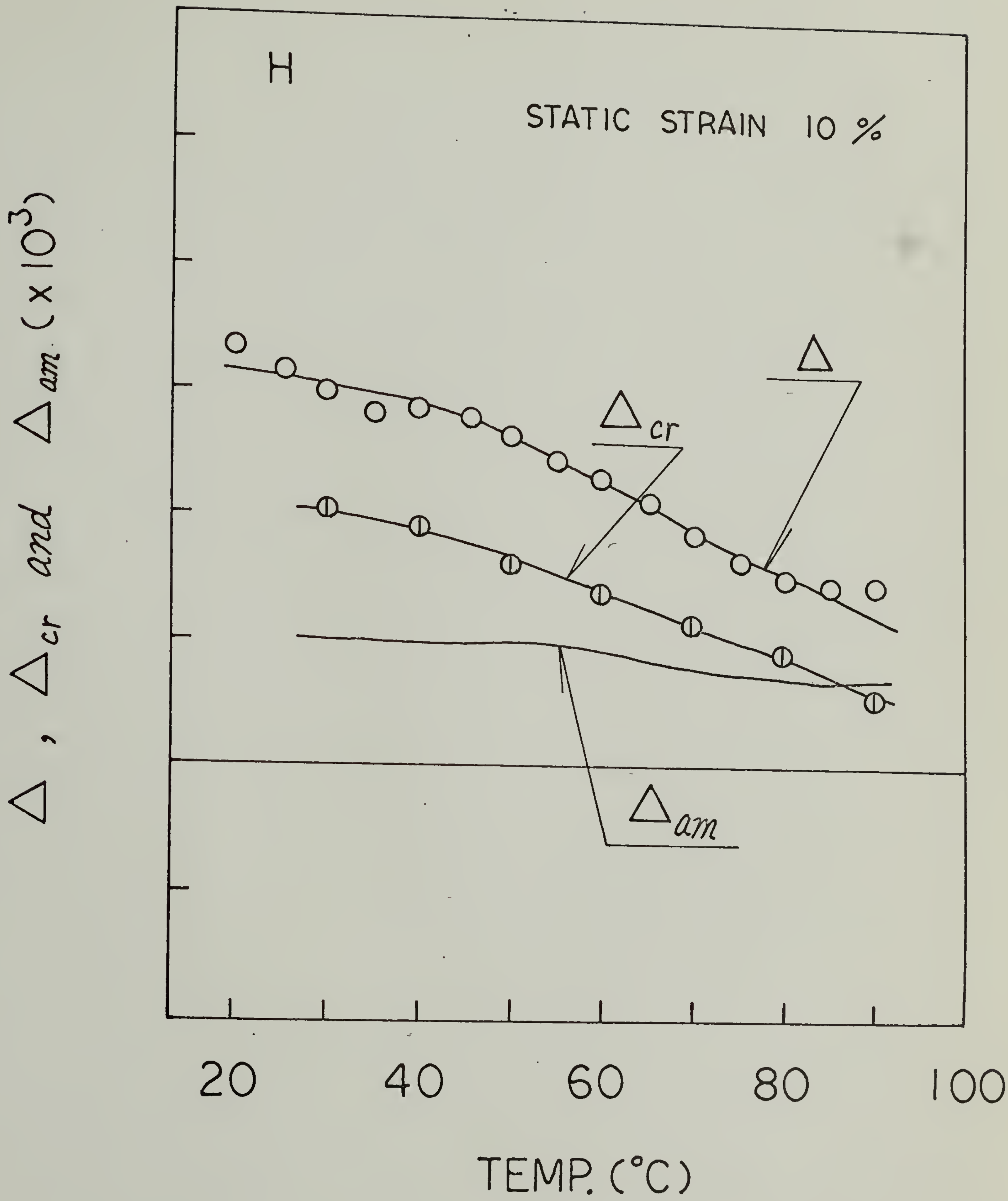
H
STATIC STRAIN 10 %
Δ
Δ_{cr}
Δ_{am}
Δ , Δ_{cr} and Δ_{am} ($\times 10^3$)
20
40
60
80
100
TEMP. (°C)

FIG. 91

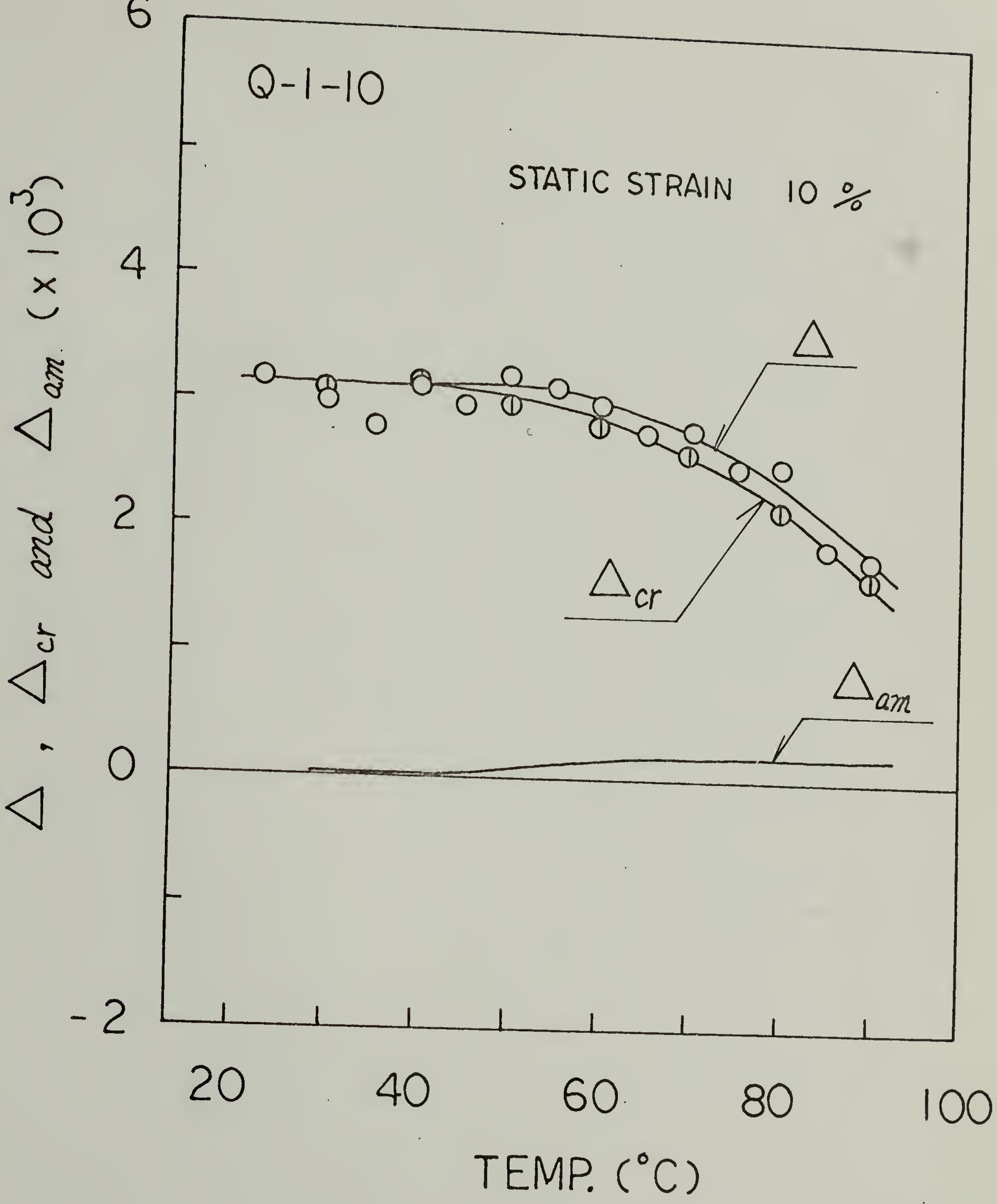
Q-1-10
STATIC STRAIN 10 %
Δ
Δ_cr
Δ_am
Δ , Δ_cr and Δ_am (x 10³)
6
4
2
0
- 2
20
40
60
80
100
TEMP. (°C)

FIG. 92

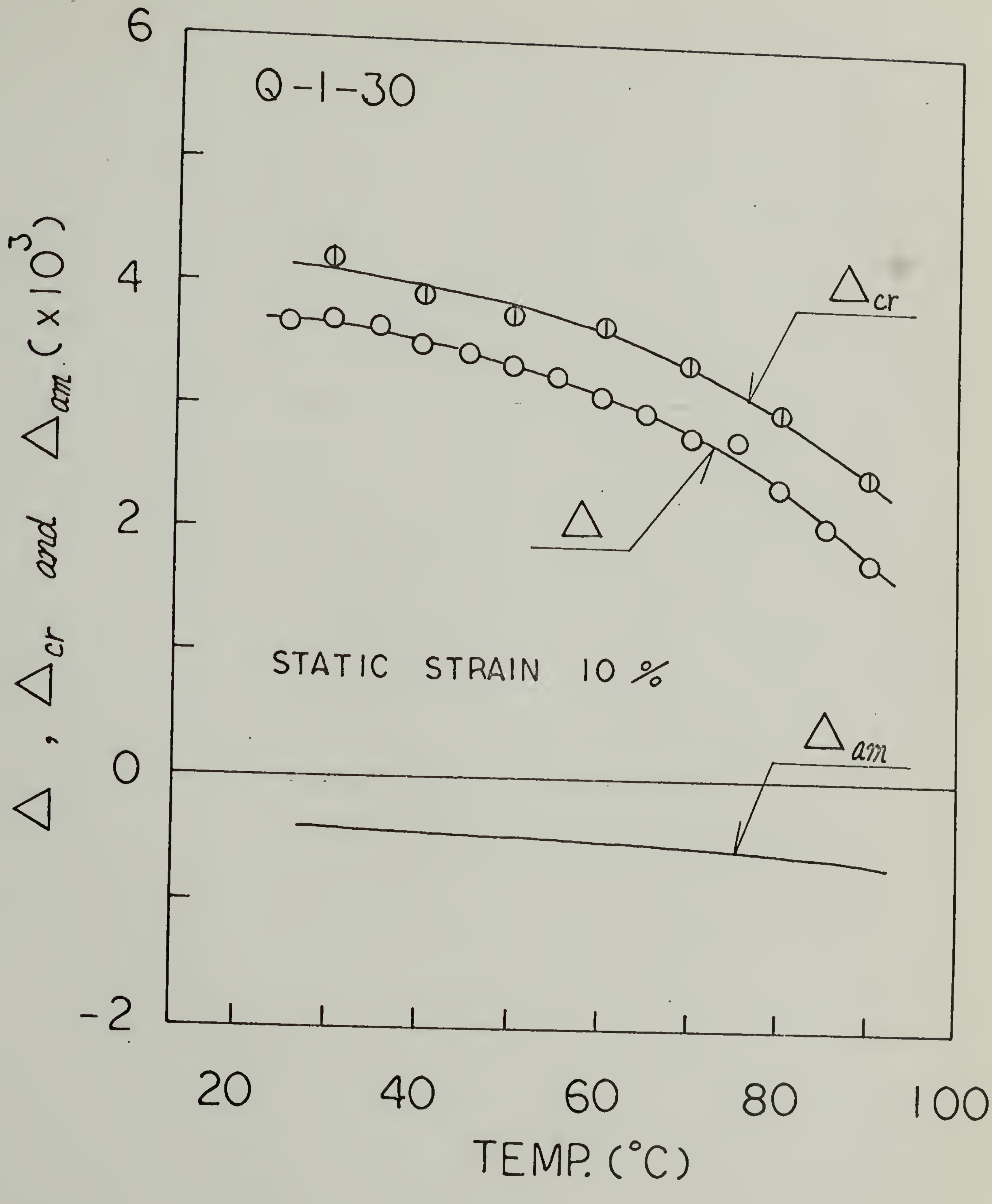
Q-1-30
Δ_{cr}
Δ
STATIC STRAIN 10 %
Δ_{am}
Δ , Δ_{cr} and Δ_{am} ($\times 10^3$)
6
4
2
0
-2
20
40
60
80
100
TEMP. (°C)

FIG. 93

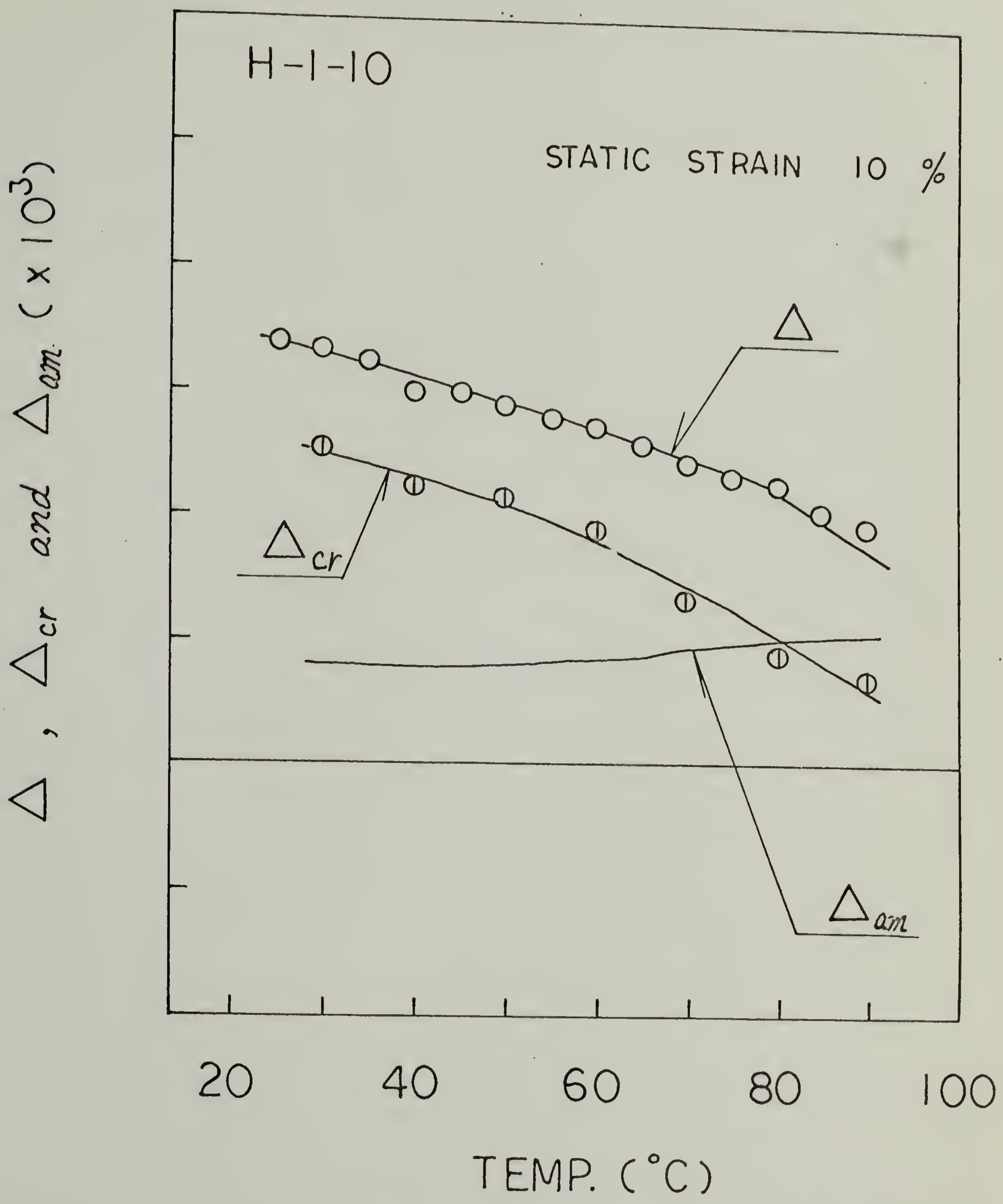
H-1-10
STATIC STRAIN 10 %
Δ
Δ_cr
Δ_am
Δ , Δ_cr and Δ_am (x 10³)
20
40
60
80
100
TEMP. (°C)

FIG. 94

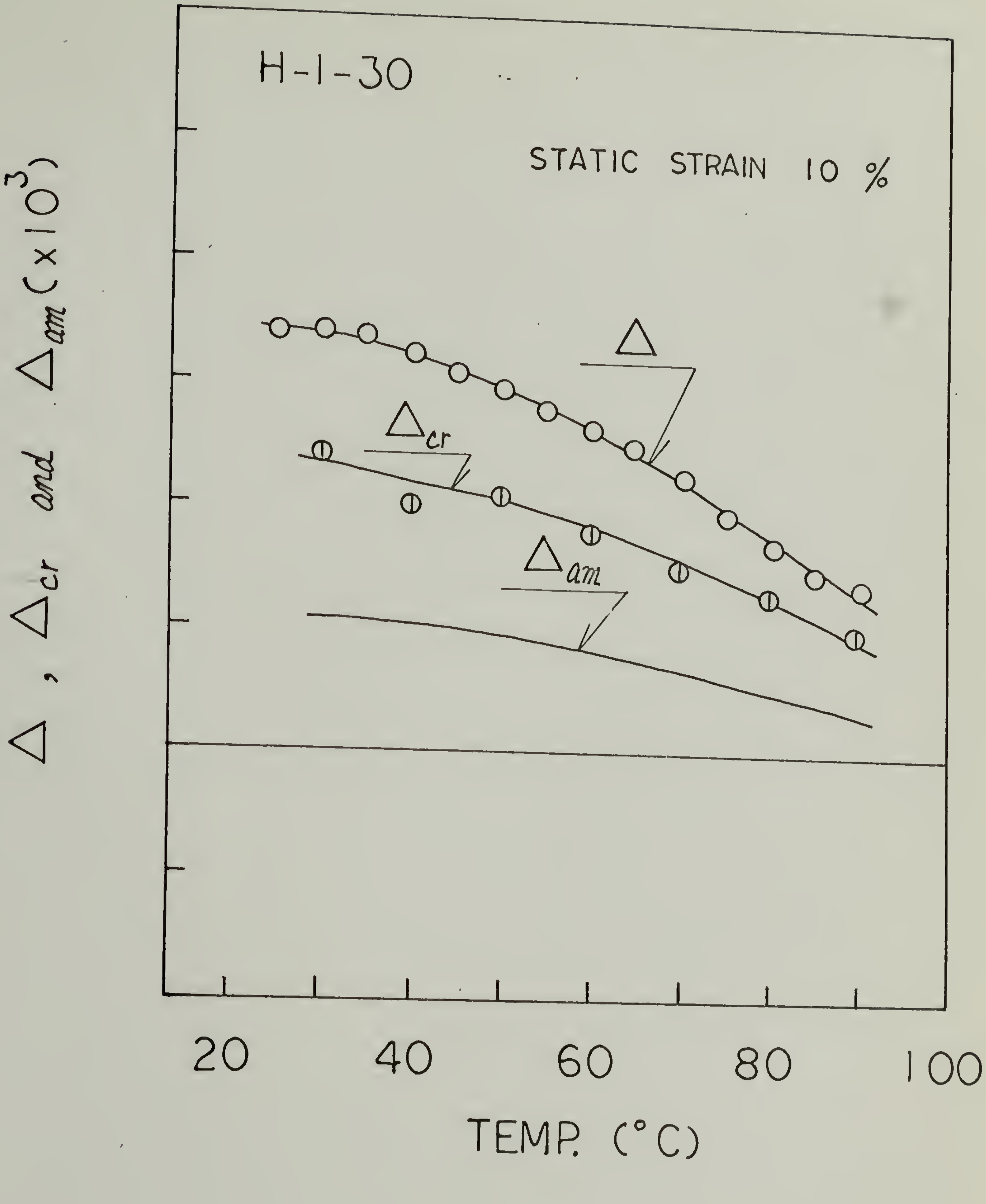
H-1-30
STATIC STRAIN 10 %
Δ
Δ_{cr}
Δ_{am}
Δ , Δ_{cr} and Δ_{am} ($\times 10^3$)
20
40
60
80
100
TEMP. (°C)

FIG. 95

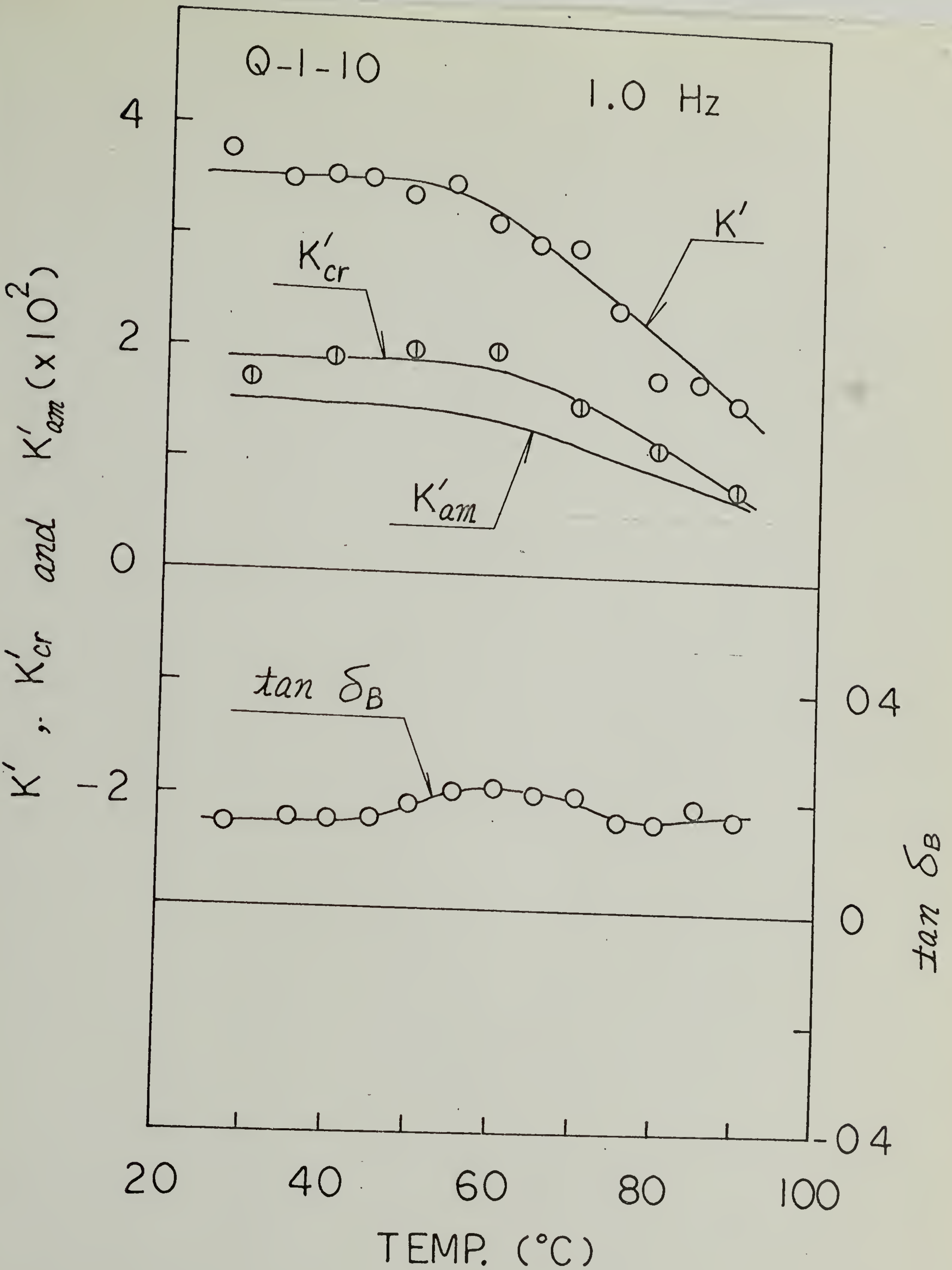
Q-1-10
1.0 Hz
K'
K'_{cr}
K'_{am}
tan δ_B
4
2
0
-2
0.4
0
-0.4
K', K'_{cr} and K'_{am} (x 10^2)
tan δ_B
20
40
60
80
100
TEMP. (°C)

FIG. 96

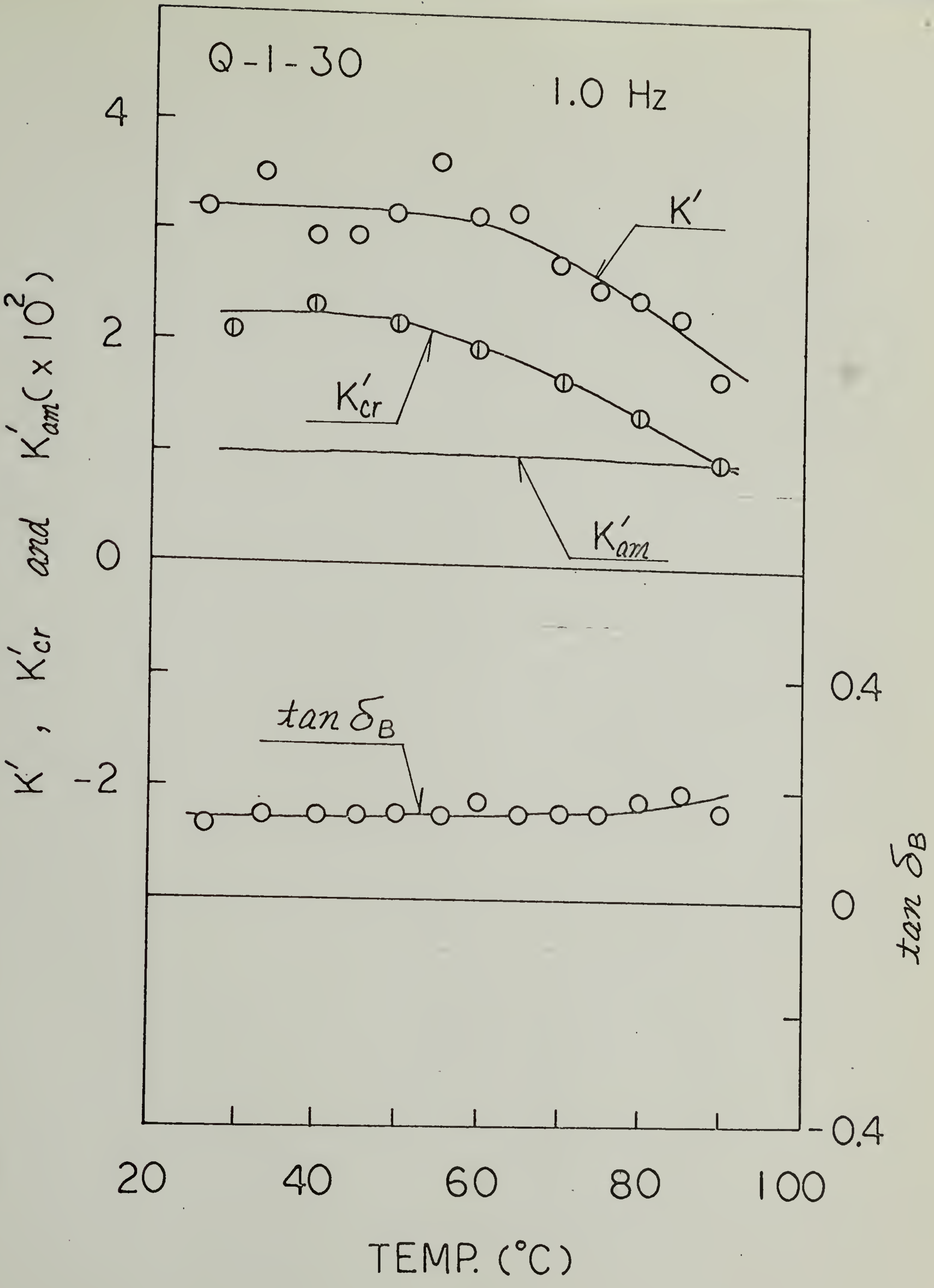
Q-1-30
1.0 Hz
K′
K′cr
K′am
tan δB
K′ , K′cr and K′am (x 10²)
4
2
0
-2
0.4
0
-0.4
tan δB
20
40
60
80
100
TEMP. (°C)

FIG. 97

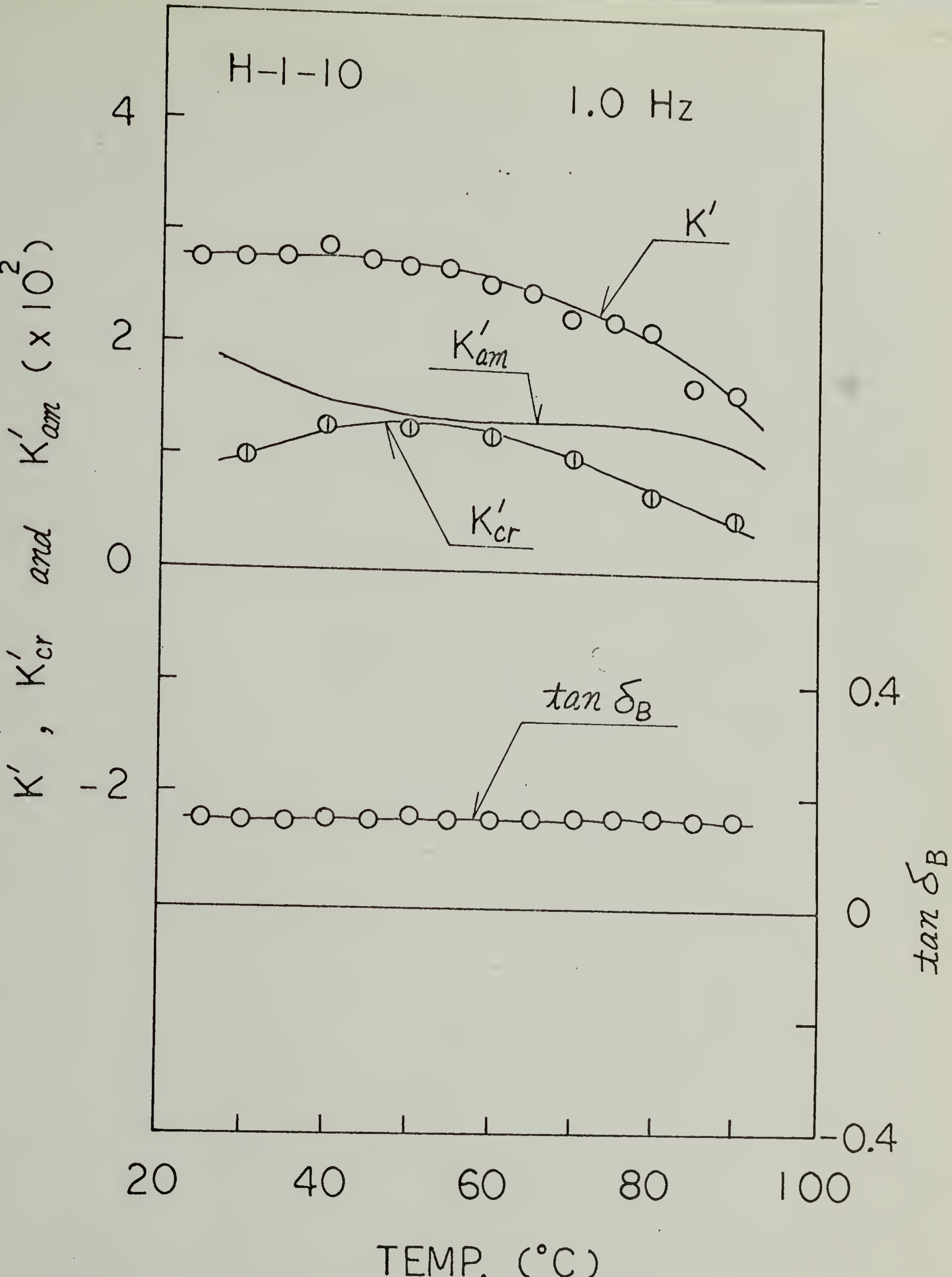
H-1-10
1.0 Hz
K'
K'am
K'cr
tan δB
K', K'cr and K'am (x 10^2)
4
2
0
-2
0.4
0
-0.4
tan δB
20
40
60
80
100
TEMP. (°C)

FIG. 98

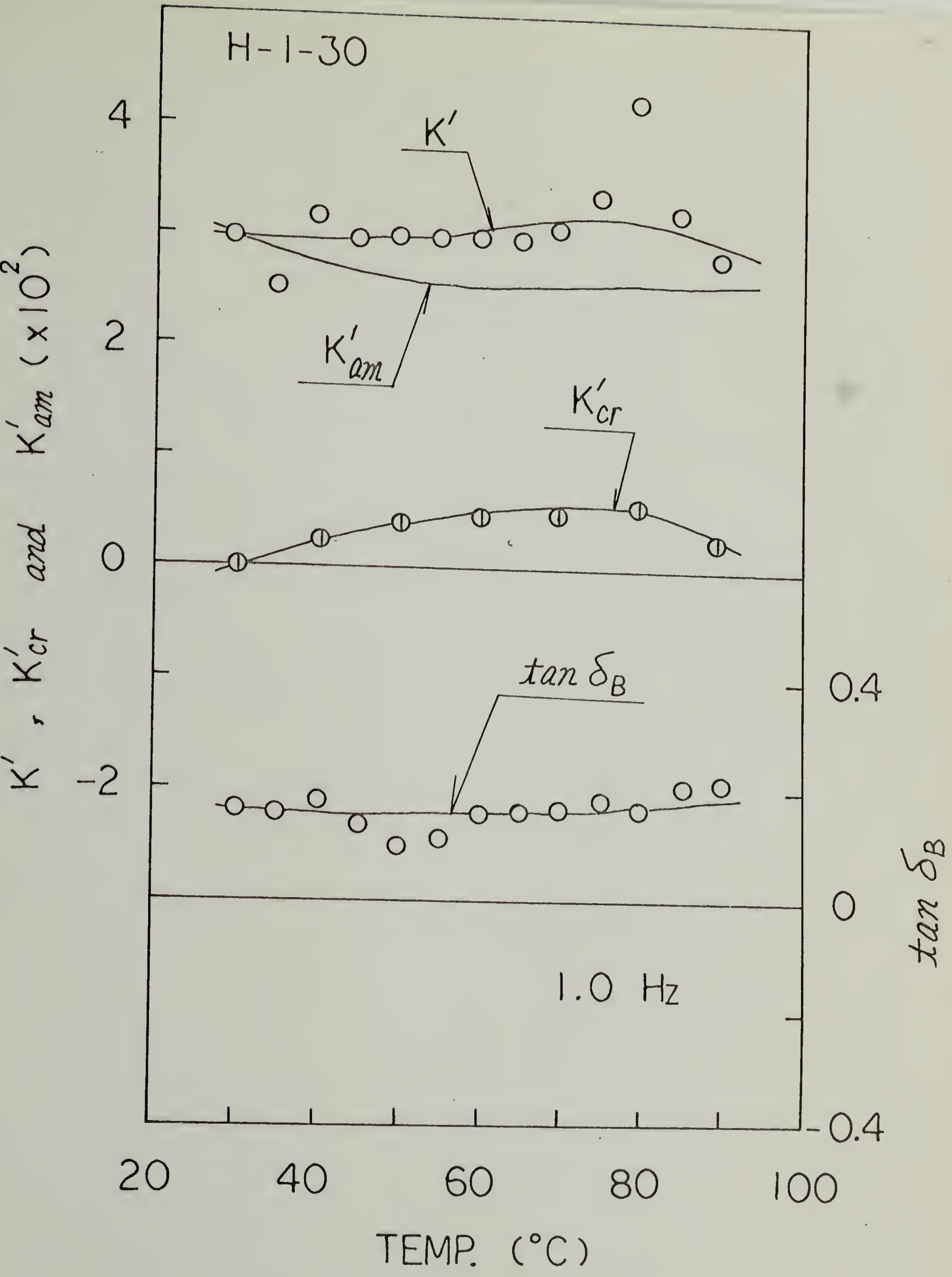
H-1-30
K'
K'am
K'cr
tan δB
1.0 Hz
K' , K'cr and K'am (x10²)
tan δB
4
2
0
-2
0.4
0
-0.4
20
40
60
80
100
TEMP. (°C)

FIG. 99

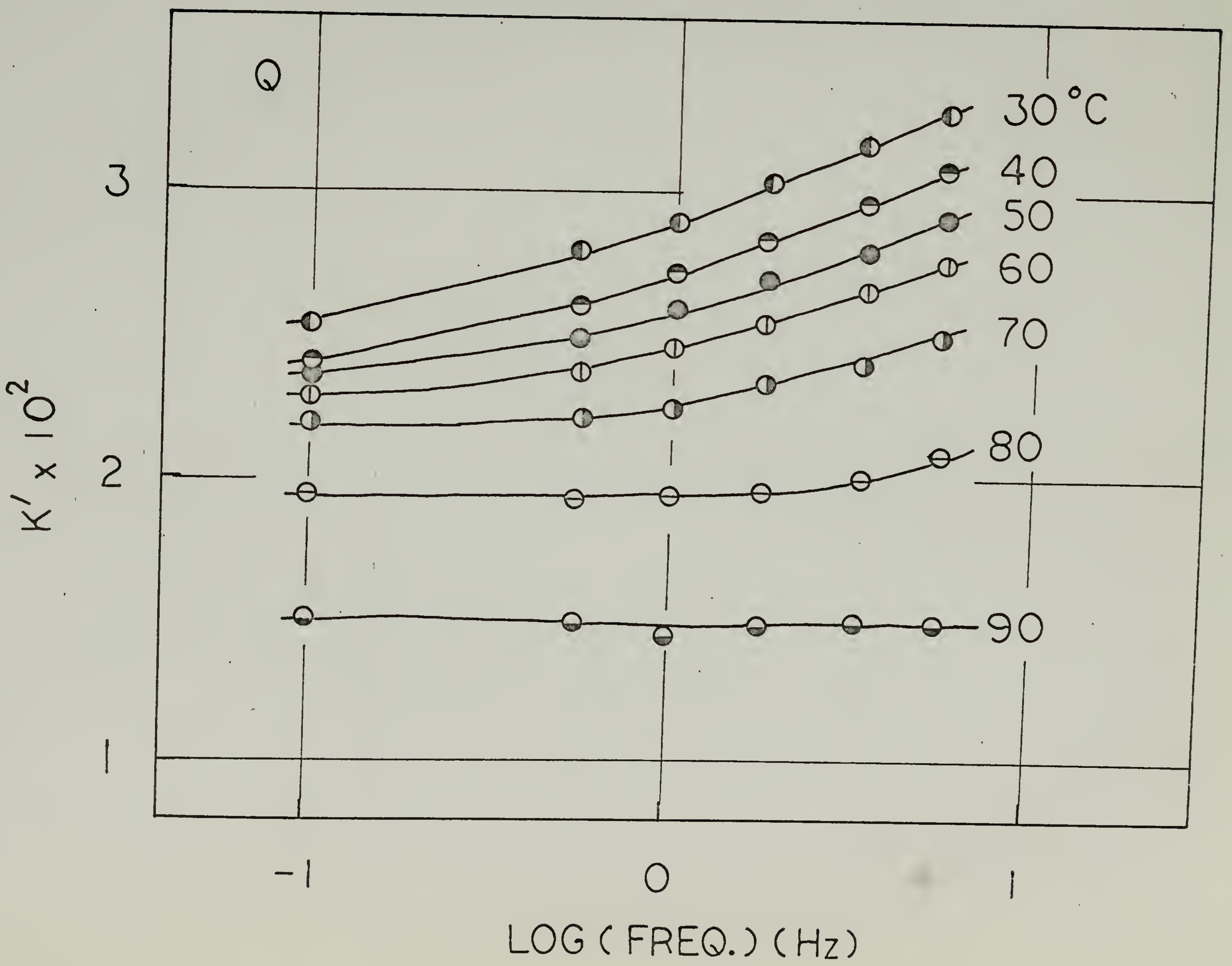

FIG. 100

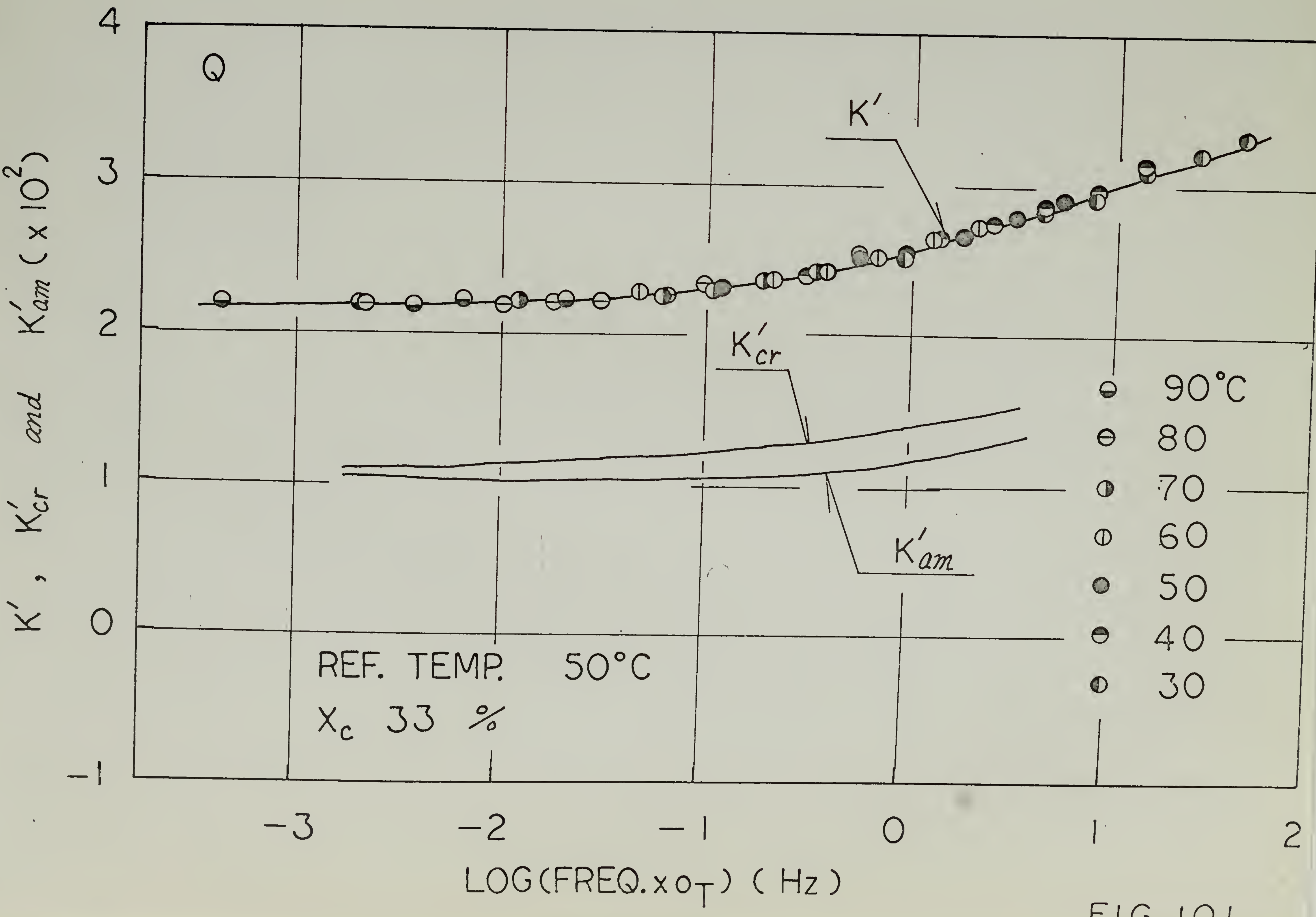
Q
K′
K'_{cr}
K'_{am}
90°C
80
70
60
50
40
30
REF. TEMP. 50°C
X_c 33 %
4
3
2
1
0
−1
−3
−2
−1
0
1
2
K', K'_{cr} and K'_{am} (x 10^2)
LOG(FREQ. x a_T) (Hz)

FIG. 101

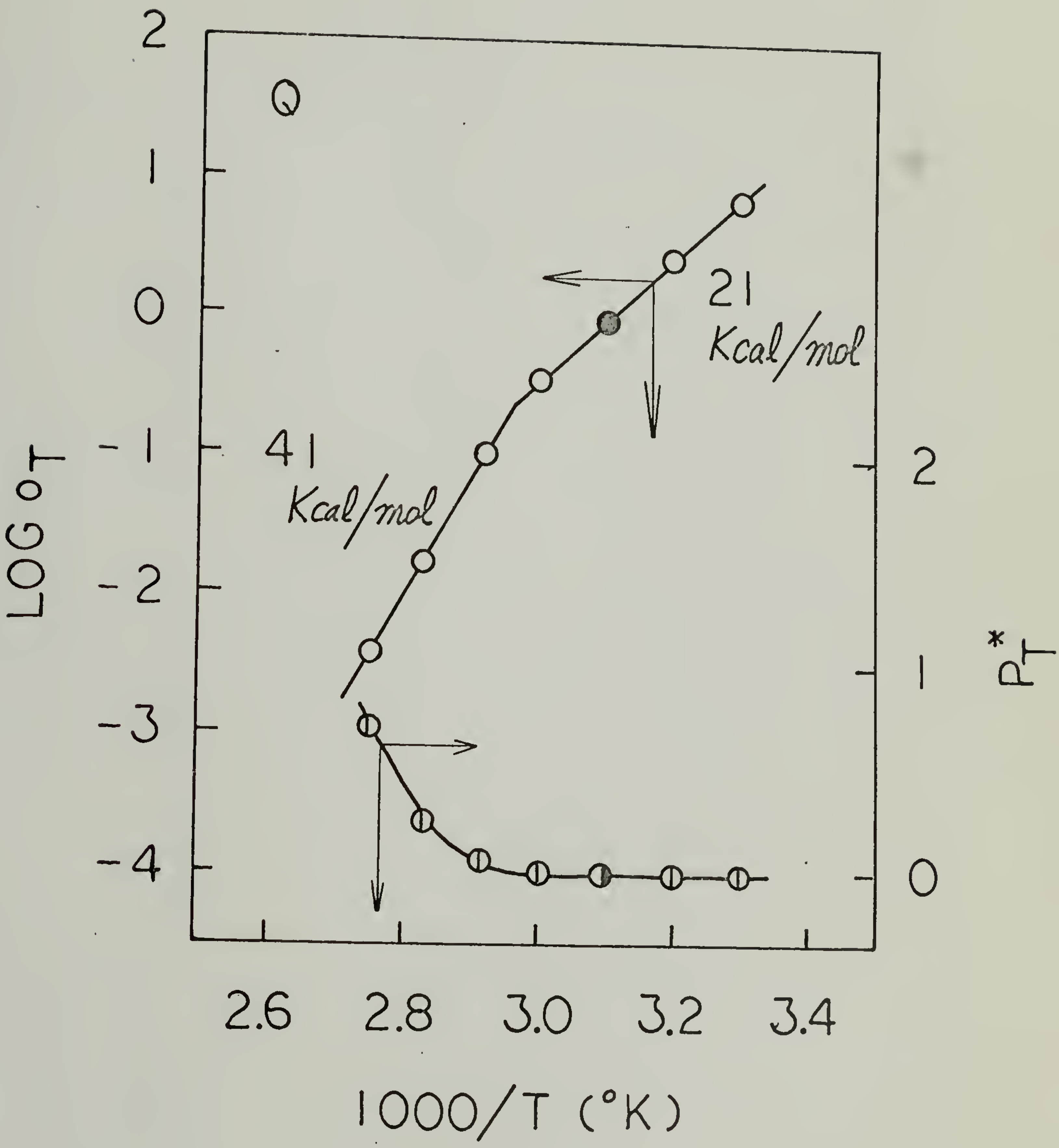
Q
2
1
0
-1
-2
-3
-4
LOG σT
21 Kcal/mol
41 Kcal/mol
2
1
0
P_T^*
2.6
2.8
3.0
3.2
3.4
1000/T (°K)

FIG. 102

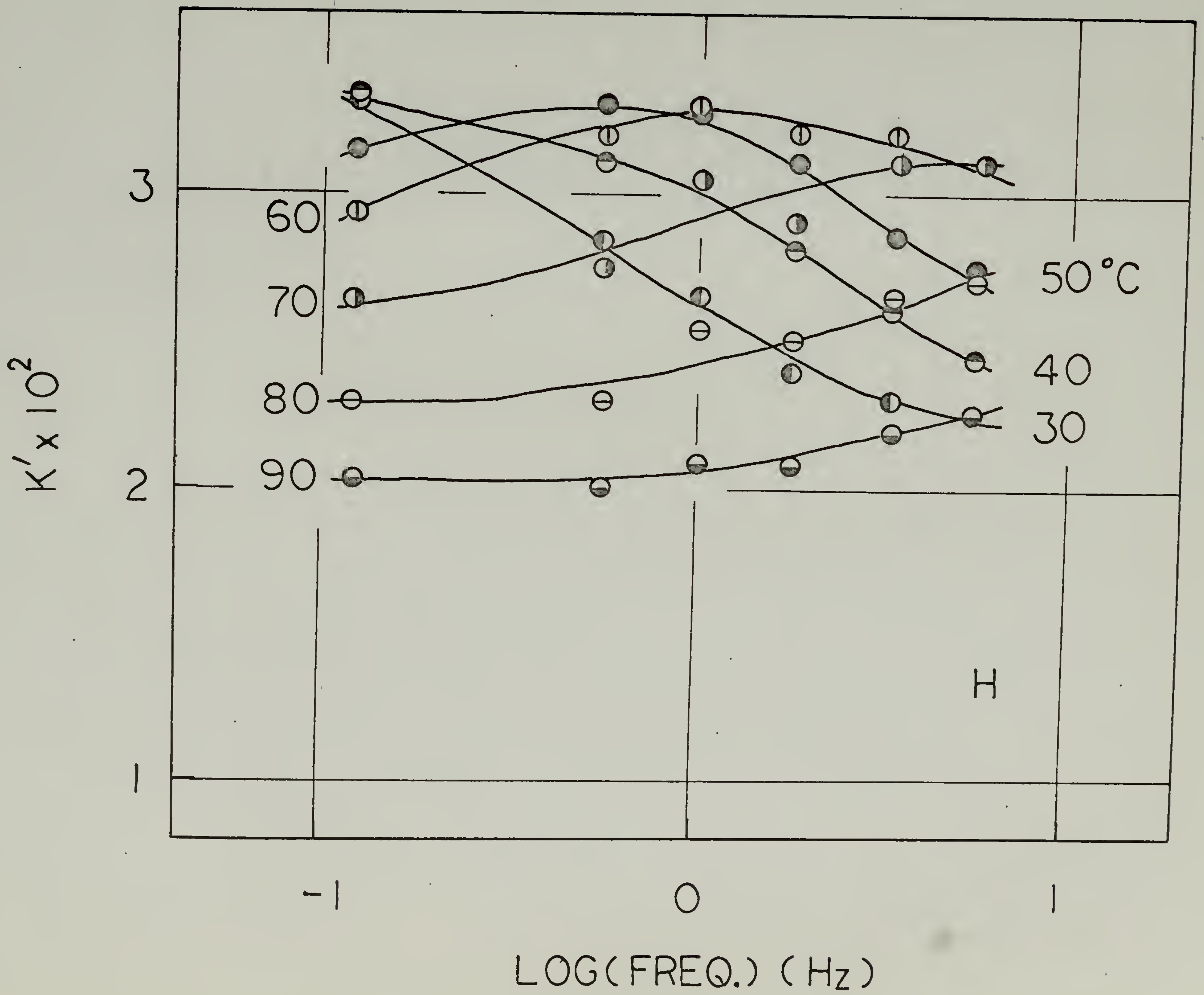

FIG. 103

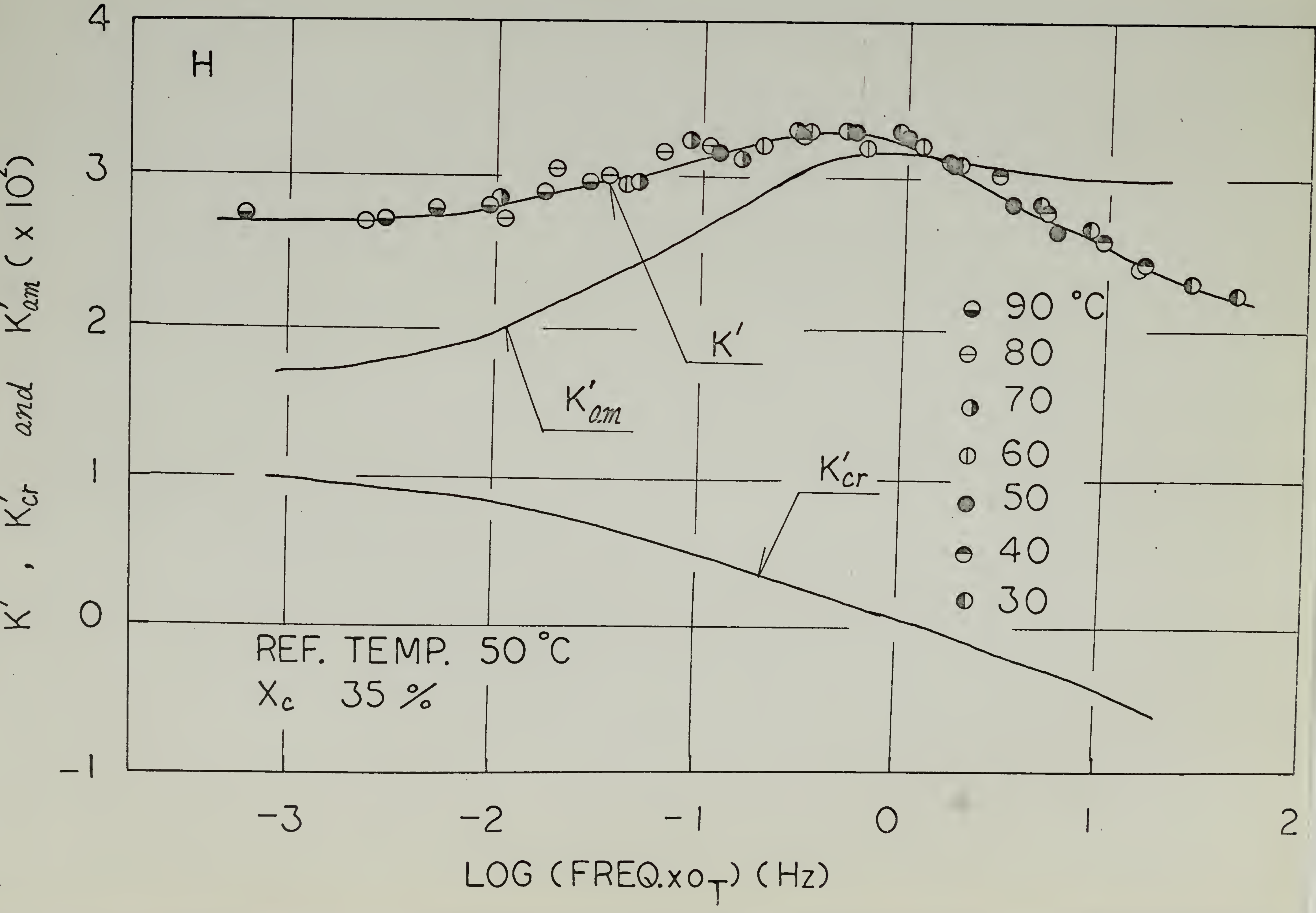
H
K' , K'cr and K'am (x 10²)
4
3
2
1
0
−1
−3
−2
−1
0
1
2
LOG (FREQ.xa_T) (Hz)
K'
K'am
K'cr
◒ 90 °C
⊖ 80
◑ 70
⦶ 60
● 50
⊖ 40
◐ 30
REF. TEMP. 50 °C
Xc 35 %

FIG.104

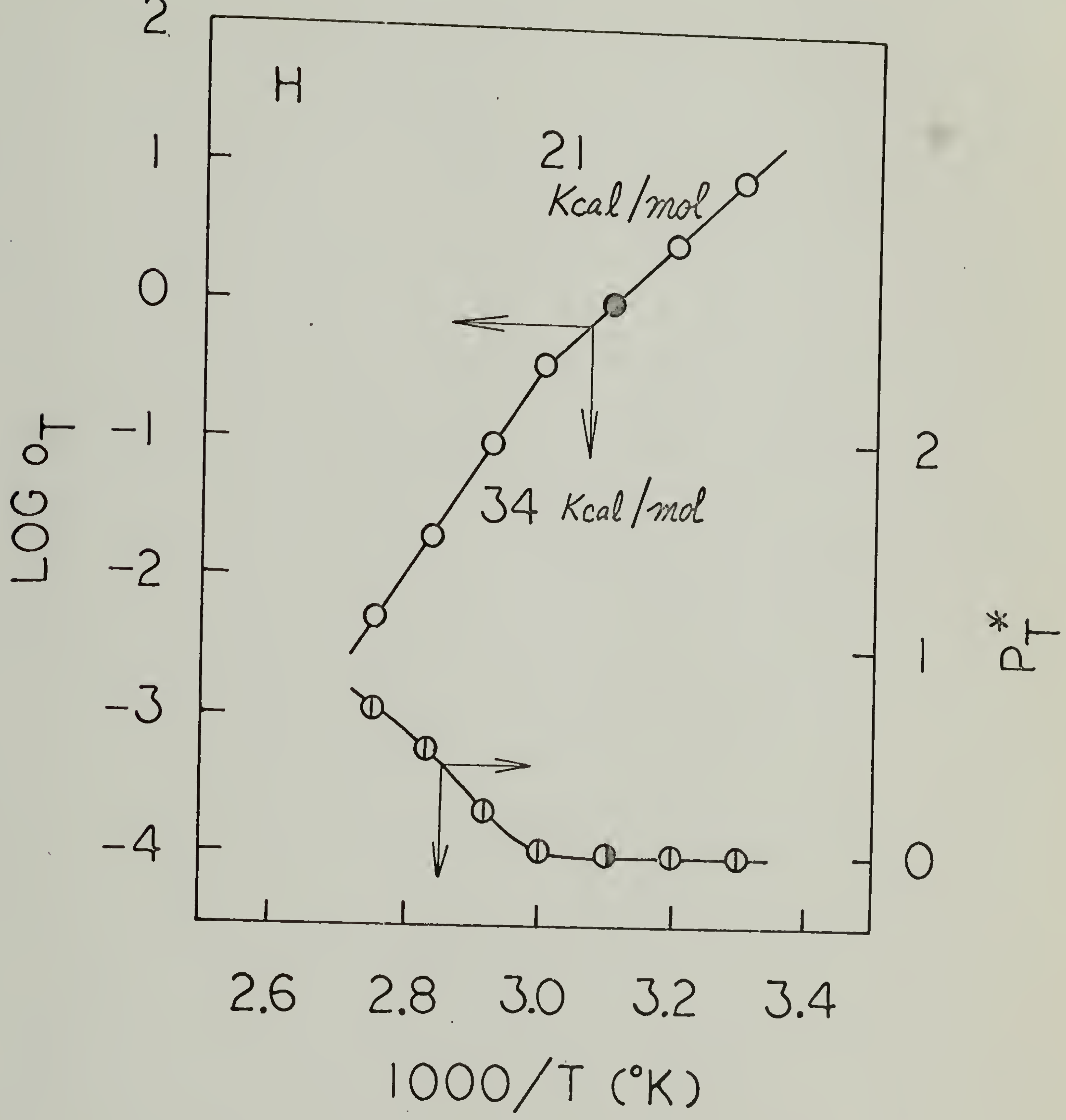
H
21
Kcal/mol
34 Kcal/mol
LOG σT
2
1
0
-1
-2
-3
-4
P*T
2
1
0
2.6
2.8
3.0
3.2
3.4
1000/T (°K)

FIG. 105

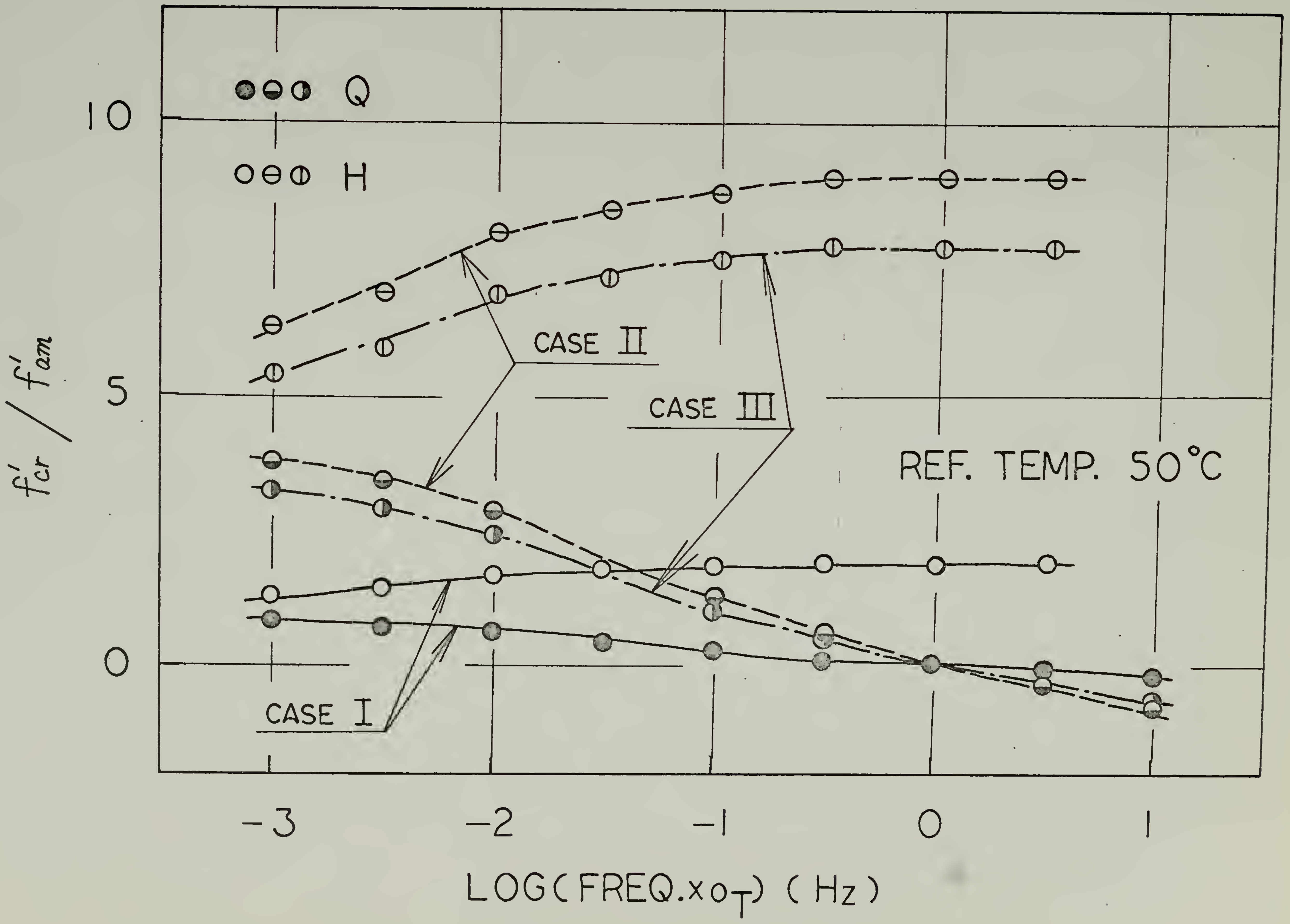
●◐◑ Q
○⊖⦶ H
10
5
0
f'_{cr} / f'_{am}
CASE II
CASE III
CASE I
REF. TEMP. 50°C
−3
−2
−1
0
1
LOG(FREQ.$\times a_T$) (Hz)

FIG.106